POLYTECHNIQUE MONTRÉAL

affiliée à l'Université de Montréal

Contributions to modeling, simulation, and analysis of three-phase dual active bridge converters for dc-grid integration

MAXIME BERGER

Département de génie électrique

Thèse présentée en vue de l'obtention du diplôme de *Philosophiæ Doctor*

Génie électrique

Août 2019

POLYTECHNIQUE MONTRÉAL

affiliée à l'Université de Montréal

Cette thèse intitulée :

Contributions to modeling, simulation, and analysis of three-phase dual active bridge converters for dc-grid integration

présentée par **MAXIME BERGER**

en vue de l'obtention du diplôme de *Philosophiæ Doctor*

a été dûment acceptée par le jury d'examen constitué de :

Houshang KARIMI, président
Ilhan KOCAR, membre et directeur de recherche
Jean MAHSEREDJIAN, membre et codirecteur de recherche
Handy FORTIN-BLANCHETTE, membre et codirecteur de recherche
Keyhan SHESHYEKANI, membre
Luiz A. C. LOPES, membre externe

ACKNOWLEDGEMENTS

First, I would like to thank M. Jacques Belley from Bombardier Transportation who believed in me twice for supporting both my master and my PhD projects. I will never forget the two amazing opportunities he gave me.

I would also like to thank M. Carl Lavertu from Bombardier Transportation for all his help during this adventure. He became more than a mentor for me, he became a friend. He cared for my success and gave many of his own personal time to help me. I consider myself privileged to learn from someone as knowledgable and as human as him every day.

I will always be grateful to my advisor Prof. Ilhan Kocar who supported me in many ways during my PhD. Ilhan gave me the opportunity to experience teaching twice and provided me support to travel and network with others. He has been very supportive, available and provided me all the guidance and advice I needed to realize my PhD project and develop my teaching skills.

Also, many thanks to Prof. Handy Fortin-Blanchette from École de technologie supérieure (ÉTS) who accepted to support me and trusted my determination to realize my project when I approached him at the end of his class. From many meetings in his office to late phone calls, he supported me all along the way. I like joking by saying that I would probably still be trying to program my FPGA modulator if it wasn't of Handy's advice to read Chapter 5 of the Pong P. Chu book.

Moreover, I can't pass over the collaboration with Prof. Jean Mahseredjian. He gave me the opportunity to enter the EMTP family during my master and I consider myself very fortunate of still being a part of this family 5 years later.

I would also like to thank my lover Brigitte for all her encouragement during the best and harder moments. She was and still is my best confidant and my best friend.

Despite the distance, I will always be grateful to my parents for their unconditional support that allows me to chase my dreams. They are an important part of what I became.

A special thanks also to Mme Isabelle Provost, M. Stéphane Goulet and M. Jean-Pierre Magalhaes Grave from Bombardier Transportation for all their help and support in different ways.

Finally, this project has been financially supported by Bombardier Transportation, FRQNT, CRSNG and the Trottier Institute for Sustainability in Engineering and Design.

RÉSUMÉ

Le convertisseur cc-cc bidirectionnel isolé triphasé à deux ponts actifs (3p-DAB) est largement étudié pour son utilisation dans les réseaux à courant continu de nouvelle génération. Son intégration nécessite une modélisation précise de ses caractéristiques petit et grand signal. De plus, sa caractérisation précise en mode dégradé d'opération est un sujet important pour le développement de réseaux fiables et résilients. L'application de stratégies de modélisation bien connues au convertisseur 3p-DAB, tant en fonctionnement normal que dégradé, n'est pas triviale du fait de sa structure cc-ca-cc, des différentes connexions possibles de transformateurs triphasés et du nombre plus élevé d'interrupteurs par rapport à d'autres topologies connues. L'absence de modèles petits signaux précis ainsi que de modèles grands signaux numériquement efficace du 3p-DAB est la principale motivation des développements présentés dans cette thèse. Trois contributions principales se dégagent de ce travail.

Cette thèse contribue d'abord à l'identification des limites de l'approche conventionnelle de moyennage en espace d'état (SSA) pour la détermination des impédances d'entrée Z_{D} et Z_{N} du convertisseur 3p-DAB. Ces deux fonctions de transfert sont nécessaires à l'application du théorème d'éléments supplémentaires (EET) de Middlebrook qui est largement utilisé par les concepteurs en électronique de puissance pour prévenir la dégradation des performances dynamiques ainsi que les conditions d'instabilité lors de l'ajout d'un filtre d'entrée. La détermination précise de Z_{D} et Z_{N} est également importante pour déduire les caractéristiques petit signal en boucle fermée du convertisseur à partir de son modèle en boucle ouverte. Bien qu'il soit démontré que l'approche généralisée de moyennage en espace d'état (GSSA) peut être utilisée pour surmonter les limites de la méthode SSA pour l'évaluation de Z_{D}, un nouveau modèle hybride combinant SSA et GSSA est proposé pour le calcul de Z_{N}.

La deuxième contribution de cette thèse est le développement d'un modèle moyenné généralisé (GAM) précis et efficace permettant la simulation de réseaux utilisant des convertisseurs 3p-DAB dans des logiciels d'analyses de transitoires électromagnétiques. Le modèle proposé est comparé en détail à d'autres techniques de modélisation, soit le modèle idéal en commutation, la technique des fonctions de commutation (SWF) et l'approche de moyennage en espace d'état (SSA). En somme, il est conclu que le modèle GAM fournit une solution optimale lorsqu'on

prend en compte la précision de la réponse transitoire, la réduction du temps de calcul et la largeur de bande de la réponse fréquentielle. Finalement, un réseau de simulation à grande échelle est développé dans le logiciel Electromagnetic Transient Program (EMTP) pour valider les performances du modèle GAM pour l'analyse du courant de défaut et de la tension de transitoire de rétablissement dans un système grande échelle.

La troisième contribution de cette thèse est la proposition et la caractérisation d'un nouveau mode dégradé pour le convertisseur 3p-DAB. Des travaux antérieurs ont montré que le 3p-DAB peut être utilisé dans un mode de défaillance de panne dit à phase gelée, c'est-à-dire lorsque les deux transistors d'une même phase sont forcés à l'état ouvert par les protections internes de leurs pilotes de grille. Puisque les diodes de roue libre sont laissées en autocommutation, la caractérisation analytique du convertisseur pour toutes les conditions de tension et de charge n'est pas triviale. Dans cette thèse, il est proposé d'ouvrir la phase en défaut de manière à éliminer l'interaction des diodes de roue libre au niveau de la phase défectueuse. En éliminant l'interaction de ces diodes, le 3p-DAB peut être opéré dans un mode de fonctionnement caractérisable pour toutes les conditions de tension et de charge. De plus, en raison de la circulation de courant réactif dans la phase défectueuse en fonctionnement à phase gelée, il est démontré que les contraintes de courant sont plus élevées et que la capacité de transfert de puissance du convertisseur est réduite par rapport au fonctionnement à phase ouverte proposé dans cette thèse.

ABSTRACT

The three-phase dual active bridge (3p-DAB) isolated-bidirectional dc-dc converter (IBDC) is widely investigated in next-generation dc-grids. Its successful integration requires an accurate representation of its small- and large-signal characteristics. Furthermore, accurate characterization of converters behavior in degraded-mode is an important topic for the development of reliable and resilient dc-grids. The application of well-known modeling strategies to 3p-DAB converters in both normal and degraded operations is not trivial due to its dc-ac-dc structure, the different possible three-phase transformer connections and the higher number of switches compared to other well-known IBDC topologies. The absence of accurate small-signal models as well as computational efficient large-signal models of the 3p-DAB has motivated the developments presented in this thesis. Three main contributions are emerging from this work.

This thesis first contributes to the identification of the limitations of the basic state-space averaging (SSA) approach for the determination of the driving point Z_{D} and null driving point Z_{N} input impedances for 3p-DAB converters. These two transfer functions are necessary for the application of Middlebrook's extra element theorem (EET) which is broadly used by practicing power electronic designers to avoid dynamic performance degradation or instability conditions in the presence of an additional input filter. The accurate determination of Z_{D} and Z_{N} is also important to derive the closed-loop small-signal characteristics of converters from its open-loop characteristics. While it is shown that the generalized state-space averaging (GSSA) approach can be used to overcome SSA limitations to evaluate Z_{D}, a new hybrid SSA and GSSA multi-input multi-output (MIMO) model, which combines SSA and GSSA, is proposed to evaluate Z_{N}.

The second contribution of this thesis is the development of an accurate and computational efficient generalized average model (GAM) which enables system-level simulation of dc-grids with 3p-DAB converters in electromagnetic transient type (EMT-type) programs. The proposed model is rigorously compared with alternative modeling techniques: ideal-model, switching-function (SWF) and state-space averaging (SSA). It is concluded that the GAM model provides an optimal solution when accuracy of transient response, reduction in computation time, and wideband response factors are considered. A large-scale test system is implemented in

Electromagnetic Transient Program (EMTP) to validate the performance of the GAM model for fault current and transient recovery voltage analysis in a practical size system.

The third contribution of this thesis is the proposal and the characterization of a new degraded mode for the 3p-DAB converter. Previous work has shown that the 3p-DAB can be operated in a frozen leg fault-tolerant mode, i.e. with the two transistors of the same phase being opened by their gate driver internal protections. Because the free-wheeling diodes are left self-commutated, the analytical characterization of the converter for all voltage and loading conditions is not trivial. In this thesis, it is proposed to open the faulty-phase such as it eliminates the interaction with the faulty-phase free-wheeling diodes. By removing the interaction of the free-wheeling diodes, the 3p-DAB falls in a characterizable operating mode for all voltage and loading conditions. Furthermore, because of the circulation of reactive current in the faulty-phase in frozen leg operation, it is demonstrated that the current stress is higher, and the power transfer capability is reduced over the proposed open-phase operation.

TABLE OF CONTENTS

ACKNOWLEDGEMENTS III

RÉSUMÉ IV

ABSTRACT VI

TABLE OF CONTENTS VIII

LIST OF TABLES XII

LIST OF FIGURES XIII

LIST OF SYMBOLS AND ABBREVIATIONS XVII

LIST OF APPENDICES XIX

CHAPTER 1 INTRODUCTION 1

1.1 Motivation 1

1.2 The three-phase dual active bridge (3p-DAB) 4

1.2.1 Control of the 3p-DAB 4

1.2.2 Variants of the 3p-DAB topology 5

1.3 Contributions 7

1.4 Methodology and limits 12

1.4.1 Methodology 12

1.4.2 Limits 13

1.5 Thesis outlines 14

CHAPTER 2 STEADY-STATE ANALYSIS 15

2.1 First harmonic approximation (FHA) in phasor-domain 15

2.1.1 Motivation 15

2.1.2 Model development 16

2.1.3 Model validation and analysis of the results 20

2.1.4 Application to the experimental prototype (model 4) 22
2.2 Piecewise-linear modeling (PLM) in time-domain 25
2.2.1 Motivation 25
2.2.2 Piecewise-linear current equations 25
2.2.3 Power transfer relationships 28
2.2.4 Zero-voltage switching (ZVS) boundaries 30
2.2.5 Capacitor ripple current and voltage 31
CHAPTER 3 SMALL-SIGNAL FREQUENCY-DOMAIN ANALYSIS 35
3.1 Small-signal model of the 3p-DAB 35
3.2 State-space averaging (SSA) 36
3.2.1 Model development 36
3.2.2 Derivation of the converter transfer functions 39
3.3 Generalized state-space averaging (GSSA) 42
3.3.1 Model development 42
3.4 Hybrid averaging and transfer functions evaluation 52
3.5 EMTP validation of the SSA, GSSA, and hybrid models 54
3.5.1 General procedure 54
3.5.2 Comparison of SSA, GSSA, and hybrid models 57
3.6 Controller sizing and closed-loop operation 57
3.6.1 Simplified closed-loop model for parameter sensitivity analysis with SSA 57
3.6.2 Complete closed-loop analysis for controller sizing 60
3.6.3 Closed-loop transfer functions 62
3.7 Input filter sizing 64
3.7.1 Input filter transfer functions 64

3.7.2 Modified transfer functions and stability analysis 65
3.7.3 Experimental results 69
CHAPTER 4 LARGE-SIGNAL TIME-DOMAIN SIMULATION 71
4.1 Switching-function (SWF) model 71
4.2 State-space averaging (SSA) model 72
4.3 Generalized averaging model (GAM) 74
4.4 Performance comparison 77
4.4.1 Closed-loop time-domain transient response 77
4.4.2 Simulation timing analysis 79
4.4.3 Transient short-circuit with multiple 3p-DAB 80
4.4.4 Closed-loop frequency-domain response 82
4.4.5 Transient analysis with a large-scale test system 84
4.4.6 Performance comparison 87
CHAPTER 5 OPEN-PHASE FAULT-TOLERANT OPERATION 90
5.1 Open-phase operation 90
5.2 Steady-state analysis 92
5.2.1 Transformer voltage and current waveforms 92
5.2.2 Power transfer relationship 96
5.2.3 Current stress in the faulty-bridge 98
5.2.4 ZVS soft-switching regions 100
5.3 Small-signal analysis 103
5.3.1 State-space averaging (SSA) model in open-phase 103
5.3.2 Generalized state-space averaging (GSSA) model in open-phase 107
5.3.3 Small-signal characteristics of the 3p-DAB in open-phase 110

5.4 Closed-loop transient analysis in open-phase 115

CHAPTER 6 CONCLUSIONS AND RECOMMENDATIONS 121

6.1 Summary of this thesis 121

6.2 Future work 124

6.2.1 Improvements to the developed small- and large-signal models 124

6.2.2 Diagnosis of switch failure for post-fault open-phase operation 126

BIBLIOGRAPHY 127

APPENDICES 134

LIST OF TABLES

Table 3.1: Transfer functions of the Y-Δ 3p-DAB converter obtained with SSA 41

Table 3.2: Closed-loop dynamic response analysis with SSA 59

Table 3.3: Input filter parameters 67

Table 4.1: Large-signal models comparison summary 88

Table 4.2: Summary of 3p-DAB models' implementation in EMTP 88

Table 5.1: Comparison of the transfer functions in normal and open-phase operations 106

LIST OF FIGURES

Figure 1.1 : Classification of isolated-bidirectional dc-dc converters (adapted from [11]) 1

Figure 1.2 : DAB topology for dc-grids interface 2

Figure 1.3 : Three-phase dual active bridge (3p-DAB) converter 2

Figure 1.4 : Control of the Y-Δ 3p-DAB converter under investigation 5

Figure 1.5 : Classification of approaches for time-domain simulation of the 3p-DAB 9

Figure 1.6 : Comparison of the fault-tolerant modes of the 3p-DAB 11

Figure 2.1 : Comparison of PLM and FHA waveforms for the Y-Δ transformer 16

Figure 2.2 : FHA model in physical quantities 16

Figure 2.3 : Typical waveforms with ZVS in the input bridge (Y-Δ transformer) 19

Figure 2.4 : Equivalent phasor diagrams 20

Figure 2.5 : Validation of the FHA design diagram for the Y-Y and Δ-Δ transformers 21

Figure 2.6 : Validation of the FHA design diagram for the Y-Δ transformer 21

Figure 2.7 : Application of FHA to the Y-Δ 3p-DAB prototype (model 4) 24

Figure 2.8 : Equivalent circuits for the application of PLM to the Y-Δ 3p-DAB 25

Figure 2.9 : Simplified representation of the Y-Δ 3p-DAB 27

Figure 2.10 : Waveforms for the calculation of the average output current 28

Figure 2.11 : Power transfer curves for the Y-Δ 3p-DAB prototype (model 4) 29

Figure 2.12 : ZVS regions for the Y-Δ 3p-DAB with the prototype (model 4) testing zone 31

Figure 2.13 : Calculation of the output voltage and current ripples 32

Figure 2.14 : Sizing of the output capacitor for the Y-Δ 3p-DAB prototype (model 4) 34

Figure 3.1 : Output voltage regulation small-signal block diagram (forward operation) 35

Figure 3.2 : Equivalent SSA small-signal circuits of the Y-Δ 3p-DAB converter 40

Figure 3.3 : Averaged switching-function dynamic phasors 49

Figure 3.4 : Hybrid MIMO small-signal model representation of the 3p-DAB in open-loop 53

Figure 3.5 : Equivalent circuits for the validation of the open-loop transfer functions 55

Figure 3.6 : Validation of the transfer functions with time-domain simulations (model 1) 56

Figure 3.7 : Simplified closed-loop diagram for parameters sensitivity analysis with SSA.....58

Figure 3.8 : Response to a step in the reference voltage from 12 V to 24 V (model 4).....60

Figure 3.9 : Complete closed-loop diagram for controller sizing 60

Figure 3.10 : Bode diagram for the sizing of the prototype controller (model 4).....61

Figure 3.11 : Bode diagram of the prototype controller (model 4) 61

Figure 3.12 : Transient response to a step in the reference voltage (prototype) 62

Figure 3.13 : Open-loop vs closed-loop transfer functions (model 4) 63

Figure 3.14 : Converter with input filter 65

Figure 3.15 : Input filter transfer functions magnitude 67

Figure 3.16 : Transient response after introduction of filters (model 4) 68

Figure 3.17 : Response to a step in the reference voltage from 0 V to 24 V (model 4).....68

Figure 3.18 : Unstable condition due to an additional input filter 69

Figure 3.19 : Input filter transfer functions magnitude (model 4) 69

Figure 3.20 : Response to a step in the reference voltage without input filter (prototype).....70

Figure 3.21 : Response to a step in the reference voltage with Filter D (prototype) 70

Figure 4.1 : SWF model of the Y-Δ 3p-DAB 72

Figure 4.2 : SSA model of the Y-Δ 3p-DAB 73

Figure 4.3 : GAM model of the Y-Δ 3p-DAB 74

Figure 4.4 : Simulation results for the validation of the large-signal models 78

Figure 4.5 : Computation time for different integration time-steps 79

Figure 4.6 : Protection control scheme for short-circuit analysis 80

Figure 4.7 : Simulation results for a short-circuit at the output of ten (10) 3p-DAB in parallel....81

Figure 4.8 : CPU calculation effort in % of the total computation time 81

Figure 4.9 : Analysis of the effect of D_o in fault analysis 82

Figure 4.10 : Equivalent circuits for the validation of the closed-loop frequency characteristics .83

Figure 4.11 : Closed-loop frequency response.....84

Figure 4.12 : Large-scale test system for the validation of the GAM model.....85

Figure 4.13 : Analysis of the fault current at fault application and during fault clearing 86

Figure 4.14 : Analysis of the voltage V5 during fault application and fault clearing.....86

Figure 5.1 : Protection scheme concept for frozen-leg operation (e.g. Fault on Q5, phase C).....91

Figure 5.2 : Protection scheme concept for open-phase operation (e.g. Fault on Q5, phase C) 91

Figure 5.3 : Reverse drain-source characteristic of the EPC2022 GaN FET (100V, 90A) [89]....92

Figure 5.4 : Simplified representation of the Y-Δ 3p-DAB with phase C open 94

Figure 5.5 : Theoretical waveforms for phase A (normal vs open-phase).....94

Figure 5.6 : Experimental waveforms for phase A in normal operation (prototype).....95

Figure 5.7 : Experimental waveforms for phase A in open-phase operation (prototype).....95

Figure 5.8 : Comparison of the power transfer capabilities (model 4/prototype).....98

Figure 5.9 : RMS current for different voltage and loading conditions (model 4/prototype).....99

Figure 5.10 : ZVS regions (normal vs open-phase) 101

Figure 5.11 : ZVS regions for all phases in open-phase 102

Figure 5.12 : Output power versus the control phase-shift with *d* as a parameter.....102

Figure 5.13 : Equivalent SSA small-signal circuits in open-phase operation.....104

Figure 5.14 : Impact of open-phase on the control-to-output transfer function (model 4) 112

Figure 5.15 : Impact of open-phase on the control phase-shift (model 4) 112

Figure 5.16 : Impact of open-phase on the input-to-output transfer function (model 4) 114

Figure 5.17 : Impact of open-phase on the input impedance (model 4).....115

Figure 5.18 : Closed-loop small-signal characteristics in open-phase (model 4) 116

Figure 5.19 : Closed-loop response for the normal operation case (prototype).....117

Figure 5.20 : Closed-loop response for the open-phase operation case (prototype).....117

Figure 5.21 : Simulation results for the transitions between the operating modes (model 4).....118

Figure 5.22 : Transition from normal to frozen leg (prototype).....119

Figure 5.23 : Transition from frozen leg to open-phase (prototype).....119

Figure 5.24 : Transition from normal to open-phase (prototype) 120

LIST OF SYMBOLS AND ABBREVIATIONS

1p-DAB	Single-phase dual active bridge
3p-DAB	Three-phase dual active bridge
AC	Alternating current
ADC	Analog-to-digital converter
CPL	Constant power load
CPU	Central processing unit
DAB	Dual active bridge
DC	Direct current
DPS	Dual-phase-shift
EET	Extra element theorem
EMC	Electromagnetic compatibility
EMT	Electromagnetic transient
EMTP	Electromagnetic transient program
EPS	Extended-phase-shift
ESR	Equivalent series resistance
FD	Fault-diagnosis
FET	Field effect transistor
FFT	Fast Fourier transform
FHA	First harmonic approximation
FPGA	Field programmable gate array
FT	Fault-tolerant
GaN	Gallium nitride
GAM	Generalized average model

GSSA	Generalized state-space averaging
IBDC	Isolated-bidirectional dc-dc converter
KVL	Kirchhoff's voltage law
MANA	Modified-augmented-nodal analysis
MIMO	Multi-input multi-output
MOV	Metal oxide varistor
OS	Overshoot
PI	Proportional integral
PLM	Piecewise-linear modeling
RAM	Random access memory
RMS	Root mean square
SiC	Silicon carbide
SPS	Single-phase-shift
SSA	State-space averaging
SST	Solid-state transformer
SWF	Switching-function
TAB	Triple active bridge
TPS	Triple-phase-shift
UPS	Uninterruptible power supply
ZVS	Zero-voltage switching

LIST OF APPENDICES

Appendix A – Converter model parameters.....134

Appendix B – Small-scale prototype 135

Appendix C – Piecewise-linear model in normal operation 140

Appendix D – Complement to the SSA model in normal operation.....152

Appendix E – Complement to the GSSA model in normal operation 154

Appendix F – Piecewise-linear model in open-phase operation.....158

CHAPTER 1 INTRODUCTION

1.1 Motivation

There is a surge of interest in academic and industrial research on dc-grids mainly due to their well-known advantages over ac-grids in several applications [1], [2]. DC distributions are being developed for applications such as transportation [3], [4], commercial and industrial buildings [5], [6], data centers [7], generating stations [8], and integration of distributed resources [9].
Power electronic interfaces play a key role in dc-grids [10], their primary functions being power flow control, galvanic isolation and voltage conversion between different grid voltage levels. Isolated-bidirectional dc-dc converters (IBDCs) are highly investigated for these applications because their structures naturally meet these three functions. IBDC topologies are classified into seven (7) categories depending on the number of switches that constitutes their switching stage (Figure 1.1).

Number of switches						
Two (2)	Three (3)	Four (4)	Five (5)	Six (6)	Eight (8)	Twelve (12)
dual-flyback, dual-Cuk Zeta-Sepic	forward-flyback	dual-push-pull push-pull-forward, push-pull-flyback dual-half-bridge	full-bridge-forward	half-full-bridge	single-phase-dual-active-bridge	**three-phase-dual-active-bridge**

Figure 1.1 : Classification of isolated-bidirectional dc-dc converters (adapted from [11])

Among these topologies, dual active bridge (DAB) isolated bidirectional dc-dc converters (Figure 1.2) are broadly considered due to their high flexibility, and their high efficiency owing to their inherent zero-voltage switching (ZVS) capabilities [12], [13]. DAB converters are proposed to be employed in many recent conversion applications such as distributed resources interface [14], uninterruptible power supply (UPS) systems [15], automotive [16], [17], passenger rail transportation [18], solid-state transformers (SST) [19], airborne wind turbines [20], and flexible load emulators [21].

Both single-phase (1p-DAB) and three-phase (3p-DAB) versions have been proposed and protected by a patent in the early 1990s [22]. These two topologies are now public domain and are gaining a broad interest especially with the introduction of emerging semiconductor technologies which tends to reduce the negative effects of having more switches when compared to other IBDC topologies. Regardless of the higher number of switches, the 3p-DAB (Figure 1.3) provides many

advantages over the 1p-DAB which is why it tends to be favored in many modern flexible dc-grids [23]. Due to its three-phase structure, the ripple frequency is increased, thus reducing the sizing of the filter capacitors. It also reduces the current through the switches and provides a better utilization of the transformer copper and core materials.

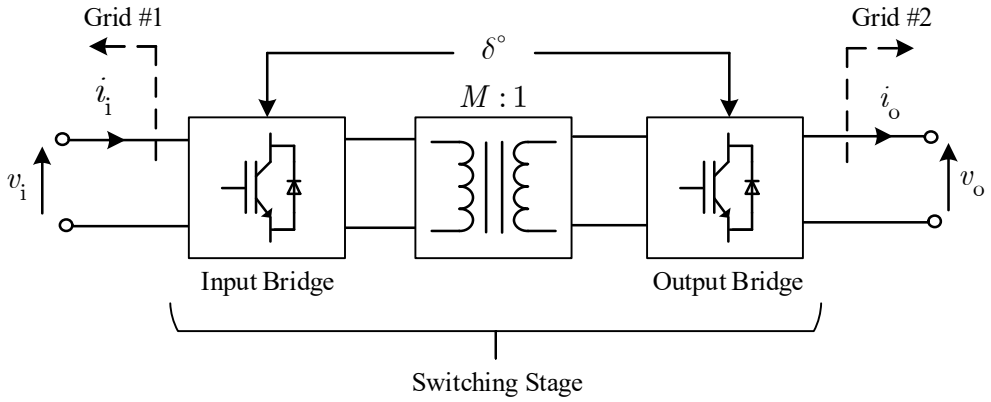

Figure 1.2 : DAB topology for dc-grids interface

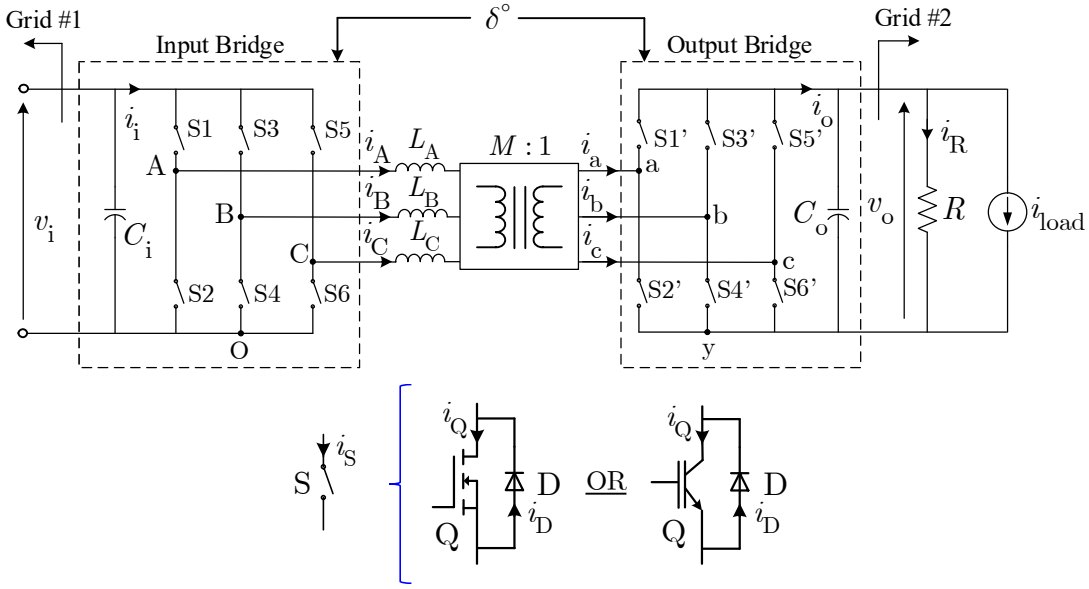

Figure 1.3 : Three-phase dual active bridge (3p-DAB) converter

The integration of power electronic converters in dc-grids brings many challenges in terms of power system control and stability [25]–[27]. Small-signal and large-signal analyses are necessary steps for successful integration of power electronics-based systems [28]. These analyses require the development of efficient and accurate models which can be implemented in modern computer programs.

Small-signal frequency-domain modeling of converters is important in controller and filter designs, as well as stability and dynamic performance assessments [29]. Converter open-loop small-signal characteristics are generally defined by a set of standard transfer functions: the control-to-output transfer function G_{vd}, the input-to-output transfer function G_{vg}, the driving point Z_D and null driving point Z_N input impedances, and the output impedance Z_o. For the stability analysis of multiple converters interacting with other network components, it is also required to determine the closed loop small-signal characteristics of the converter such as the loop gain T and the closed-loop input and output impedances [30].

As for traditional ac-grids, the integration of power electronics in dc-grids also requires time-domain system-level studies such as general transient behavior, voltage regulation performance with load variations, transient stability, and short-circuit [28], [31]–[33]. Since the behavior of a converter depends on both its topology and its controller, closed-loop modeling of converters is necessary for system-level studies [34].

Each converter topology has its own particularities which must be considered in the modeling process. As it will be emphasized in this thesis, the application of well-known modeling strategies to the 3p-DAB converter is not trivial due to its dc-ac-dc structure, the different possible three-phase transformer connections and the higher number of switches compared to other IBDC topologies. As it will also be shown in this thesis, there is currently a lack of accurate small-signal models for stability analysis of the 3p-DAB in the literature. It is also the case for efficient and accurate large-signal models of the 3p-DAB for system-level studies in electromagnetic transient type (EMT-type) programs.

Furthermore, there is also limited literature on degraded-mode operation of the 3p-DAB converter. Recently, its has been identified in [35] that the 3p-DAB converter can be operated in a frozen leg degraded-mode. However, the analytical characterization of the converter behavior under all voltage and loading conditions is not trivial. Accurate characterization of the converter behavior in degraded-mode is an important topic for the development of reliable and resilient dc-grids [36], [37].

1.2 The three-phase dual active bridge (3p-DAB)

1.2.1 Control of the 3p-DAB

The basic three-phase dual active bridge (3p-DAB) topology is shown in Figure 1.3. The transformer voltage ratio M is used to match the nominal voltage levels between the two grids. Due to its three-phase structure, the 3p-DAB also allows using different winding connections (Y-Y, Y-Δ, and Δ-Δ). It is, however, demonstrated in [24] that the Y-Δ transformer offers better performance in terms of stress on switches, transformer utilization, and filter capacitor requirements. The Y-Δ version (Figure 1.4 a)) has therefore been selected for investigation in this thesis.

Voltage control is performed by controlling the duty cycle of the primary and secondary bridges, and/or the phase-shift between the two bridges [38], [39]. Single-phase-shift (SPS) control has been the first proposed control method for the DAB converter. However, with SPS, both the 1p-DAB and the 3p-DAB have a limited ZVS soft-switching range under wide voltage and loading conditions [40]. For the 1p-DAB, extended-phase-shift (EPS) [41], dual-phase-shift (DPS) [42], and triple-phase-shift (TPS) [43] control strategies have been introduced to decrease the current stress, and improve the converter efficiency by extending its ZVS range. Due to the coupling between the three phases of the 3p-DAB, it has been shown that some TPS modulation methods [38] cannot be used without operating the 3p-DAB as a 1p-DAB converter. Even if it addresses the problem of poor partial load efficiency by extending the ZVS range, for the 3p-DAB, these strategies almost nullify the 3p-DAB advantages regarding the reduction of the output filter size [17]. The generic TPS modulation method of [43] has been used in [44] for the Y-Y 3p-DAB converter. While the results show a better efficiency at light load, it does not reduce the RMS current in the transformer as well as the maximum total losses at high load. It is not widely adopted in the literature and SPS still remains the most commonly used control method for the 3p-DAB.

The Y-Δ 3p-DAB converter under study in this thesis is therefore operated using SPS control with a fixed switching frequency $\omega_s = 2\pi f_s$ and a 180º (or 6-step) modulation method as shown in Figure 1.4 b) and c). The phase-shift δ between the gating signals applied to the two bridges is the variable used to regulate the voltage of either one of the two ports. For example, in forward operation ($0 \leq \delta \leq \pi/2$), the active power is transferred from the input bridge to the output bridge

such that v_o is regulated to reach its reference value V_o^{ref}. Reverse operation consists in reversing the sign of δ and regulating v_i to reach a reference value V_i^{ref}.

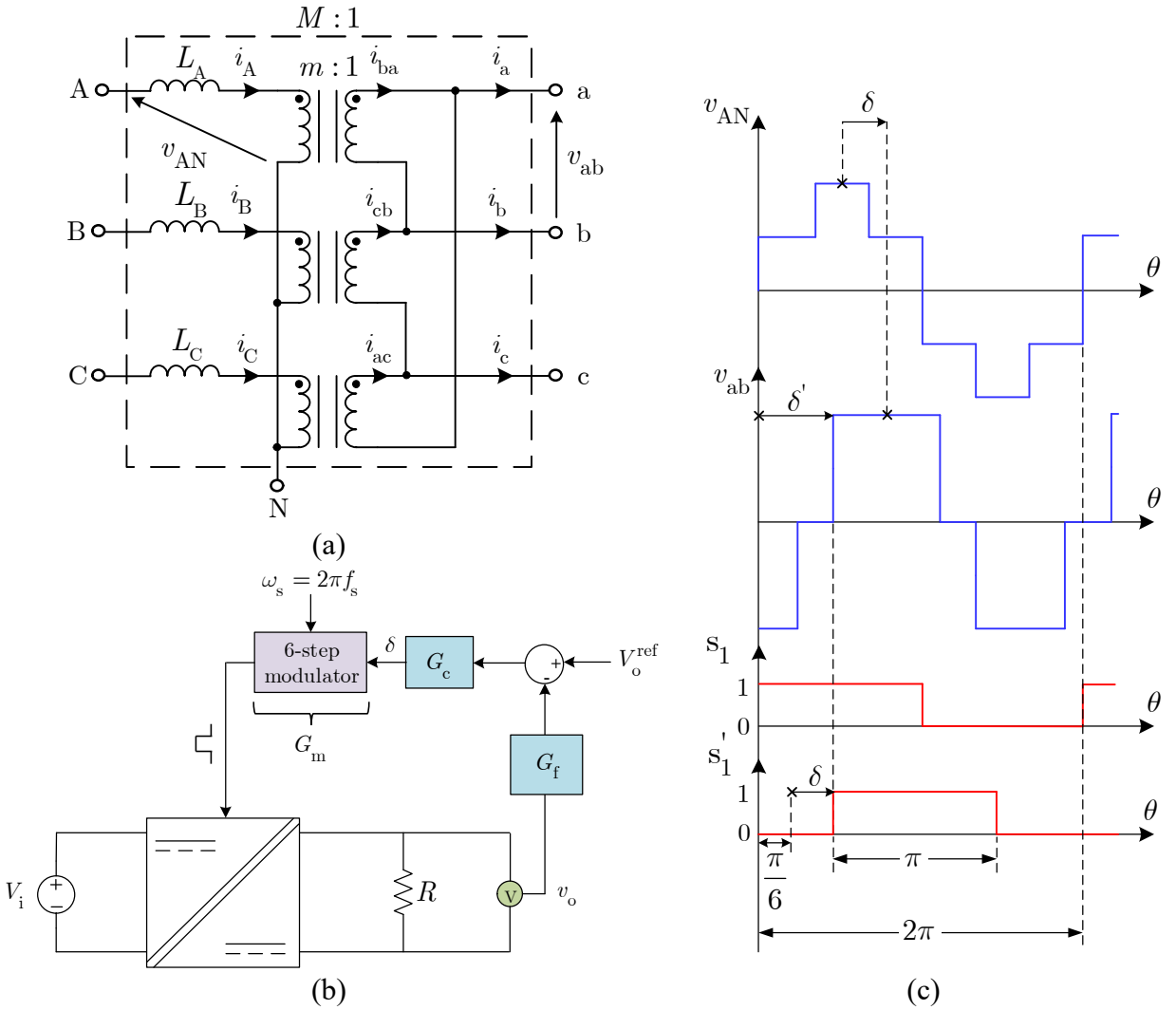

Figure 1.4 : Control of the Y-Δ 3p-DAB converter under investigation

1.2.2 Variants of the 3p-DAB topology

Different topologies of the 3p-DAB are also being proposed with different objectives. In [45], a six-leg inverter is used on the low-voltage side with the main objective of increasing the converter current capability while preserving standard modulation techniques and DAB advantages. The six-leg structure results in three decoupled voltages applied on the low-voltage side of the three-phase transformer.

Moreover, a 3p-DAB featuring a Y-Δ transformer and a current-tripler unit on the low-voltage side is proposed in [46] for increasing the converter conversion ratio while limiting the required transformer winding-ratio which has the negative effect of increasing the transformer leakage inductance and parasitic capacitance. The main drawback with the current-tripler version is that it does not offer ZVS on the low-voltage side. In [47] a current-fed topology is developed for achieving high efficiency over wide input voltage and loading ranges with a reduction in the circulation of reactive current in the Y-Y transformer.

The triple active bridge (TAB) topology using Y-YY and Y-YΔ transformer configurations is also analyzed and the Y-YΔ configuration is selected because it shows a better transformer utilization at high-power load [48], [49]. The TAB can be used to control the power flow between three different dc voltage sources, or to reduce the current through the output bridge switches by connecting the two output bridges in parallel.

1.3 Contributions

The main contributions of this thesis are summarized here. Each contribution is presented along with a literature review to clearly position this thesis with respect to previous work.

<u>Contribution #1</u>: Hybrid average modeling of three-phase dual active bridge converters for stability analysis [50]

The most popular technique to derive the analytical small-signal model of dc-dc converters is the state-space averaging (SSA) method [33], [51]. It is based on three main assumptions: 1) the switching ripple is small, 2) the ac variations are small, and 3) the modulation frequency ω_{m} is much smaller than the switching frequency ω_{s} [30]. It leads to a dc-averaged model of the converter. Due to the high-frequency ac-link in DAB converters, SSA has limitations in deriving an accurate small-signal model for DAB converters [52], [53]. SSA has been first applied to approximate the control-to-output G_{vd}, and the input-to-output G_{vg} transfer functions of the 3p-DAB in [54]. While it can be easily extended to the derivation of the output impedance Z_{o}, there is currently no resource in the literature to evaluate the driving point input impedance Z_{D} and the null driving point input impedance Z_{N} for 3p-DAB converters with SSA. These two transfer functions are necessary for the application of Middlebrook's extra element theorem (EET) [55] which is broadly used by power electronic designers to analyze dc-dc converters in the presence of an additional input filter.

To overcome the limitations of the SSA method for DAB converters, generalized state-space averaging (GSSA) models [56] have been developed in [53], [57] and [58]. These models are not extended to the derivation of Z_{D} and Z_{N}. The derivation of Z_{N} is particularly challenging for DAB converters modeled with GSSA. The methodology presented in [52] is the first attempt to derive both Z_{D} and Z_{N} for 1p-DAB converters modeled with GSSA. The methodology requires determining the closed-loop input impedance $Z_{\mathrm{in}}^{\mathrm{c}}$ with a dummy controller G_{c} before extracting Z_{N} by analytically removing the controller from the set of equations. The application of this methodology to 3p-DAB converters modeled with GSSA is neither shown nor trivial.

This thesis first contributes to the identification of the limitations of SSA in the modeling of 3p-DAB converters especially for the determination of Z_{D} and Z_{N}. While it will be shown that GSSA can be used to evaluate Z_{D}, a new hybrid SSA and GSSA multi-input multi-output (MIMO) model,

which combines SSA and GSSA, is proposed to evaluate Z_N. The proposed modeling approach is validated with time-domain simulations in Electromagnetic Transient Program (EMTP) [59]. Through the application of Middlebrook's EET for additional input filter [55], it is demonstrated that the proposed approach can effectively reduce the number of time-domain simulation runs as well as the number of experimental tests required to predict degradation of dynamic performance and instability conditions. The use of Middlebrook's theorem [55] not only guarantees stability, but also ensures that the introduction of an input filter does not substantially alter the converter transfer functions G_{vd}, G_{vg}, and Z_o [60]. SSA, GSSA, and hybrid methodologies are also thoroughly compared to provide a comprehensive review of their advantages, limitations, and overall performance.

Contribution #2: Large-signal modeling of three-phase dual active bridge converters for electromagnetic transient analysis in dc-grids [61]

As previously mentioned, large-signal modeling of the 3p-DAB converter is not trivial because of its dc-ac-dc structure, the various three-phase transformer connections and the higher number of switches compared to other IBDC topologies. The methodology presented in [62] is the first attempt to reduce the computation time for system-level studies with 3p-DAB converters in EMT-type programs. A discretized switching-function (SWF) model [63] in the αβ frame is implemented. It reduces the number of electrical nodes while preserving the switching-effect. However, it still requires time-steps in the range of $1/1000^{th}$ of the switching period to maintain numerical stability. The reduction in the computation time compared to the ideal-model approach is not shown and the reduction in the number of electrical nodes cannot be used alone as an indicator for the reduction in computation time.

The ideal-model approach is well known for the analysis of 3p-DAB converters and other topologies because its implementation using ideal switches is straightforward in circuit simulation tools. The ideal-model approach is a recognized reference for the validation of other models [28]. However, because the circuit topology is time-variant, the computation time is generally high for system-level studies. The SWF approach [63] has been proposed as an alternative methodology to ideal-model in which the converter circuit is replaced by controlled voltage and current sources. Since the circuit topology is now time-invariant, the SWF method reduces the computation

time [32]. However, because it keeps the switching-effect, small time-steps are still required. Averaged models [51], [56] are well known for neglecting the switching-effect and allowing the use of larger time-steps which significantly reduce the computation time.

In this thesis, a generalized averaging model (GAM) for time-domain simulation of 3p-DAB converters is developed, implemented and compared with the ideal, SWF [63] and SSA [51] methods in EMTP. In Figure 1.5, the simulation approaches investigated in this thesis are marked with a star (*). The ideal-model is used as a reference. Detailed-mode simulation in which detailed semiconductor models are used is not considered because such level of sophistication is generally not necessary for system-level studies.

This thesis contributes to provide a solution to the challenges in implementing a computational efficient and accurate model that enables time-domain system-level simulation of dc-grids with 3p-DAB converters. The reduced complexity and computation time of the proposed GAM model allow the efficient validation of future system-level control schemes in dc-grids. By comparing the performance of the developed GAM model in terms of transient response, computation time and frequency response with alternative modeling techniques, it also provides a complete comprehensive understanding of the advantages and limitations of the GAM approach applied to the 3p-DAB. A large-scale test system is also implemented to validate the performance of the GAM model for fault current and transient recovery voltage analysis in a practical size system.

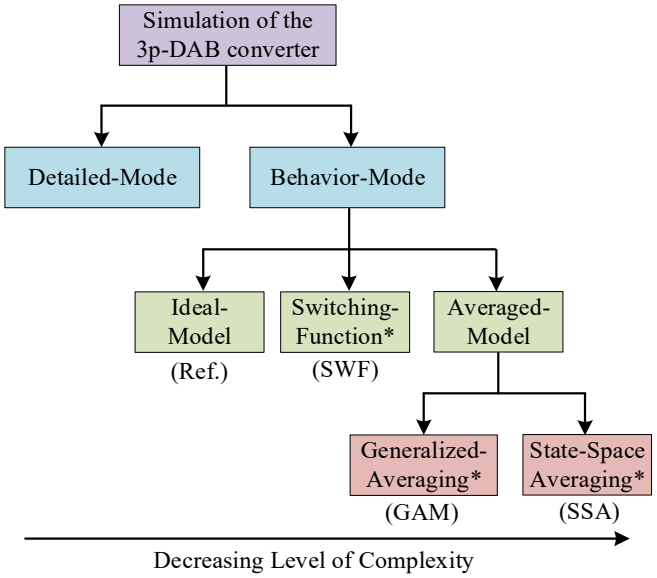

Figure 1.5 : Classification of approaches for time-domain simulation of the 3p-DAB

<u>Contribution #3</u>: Open-phase fault-tolerant operation of the three-phase dual active bridge converter [*paper conditionally accepted with major mandatory changes in IEEE Transactions on Power Electronics*]

In ac-grids, ac transformers are well known for their high reliability even in the presence of temporary or permanent overload conditions [64]. In dc-grids, the overall grid reliability can be significantly affected by the reliability of individual power electronic converters. The reliability of power electronic systems is in fact negatively affected by the higher number of components, including more vulnerable parts such as semiconductors and electrolytic capacitors. Failure of one of the components or subsystems generally lead to shutdown of the whole converter unit because most converters are not built with redundancy [37], [65].

Other than thermal management [66], oversizing of components, redundancy of converters, and fault-tolerant (FT) methods are recognized methodologies to improve the reliability of converters. Among these approaches, oversizing of components is the most used in the industry. However, while oversizing components such as filter capacitors is generally not a problem other than a probable reduction in the power density, oversizing semiconductors can negatively affect the efficiency and increase the overall cost of the converter. Besides, while it may reduce the occurrence of failures, it does not mean that the converter can resume operation upon fault detection. Instead of oversizing components, the traditional redundancy approach consists in adding extra parallel converters or modules, and/or adding redundant cells inside the converter structure for rapid reconfiguration of the faulty converter section. The redundancy approach is an expensive solution. FT operation is recognized to be more cost-effective than the redundancy approach [36]. FT operation means that a fault in a component or subsystem does not cause the overall system to malfunction [67]. In other words, degraded operation under post-fault conditions implies that the converter can continue operating with reduced performance metrics [37].

Because of its higher number of switches, it would be fair to argue that the reliability of the 3p-DAB converter is reduced when compared to other IBDC topologies, including the 1p-DAB. However, it has been shown that the 3p-DAB converter can be operated in a frozen leg degraded-mode, i.e. with the two transistors of the same phase being deliberately opened by their gate driver internal protections, leaving their free-wheeling diodes self-commutated (Figure 1.6 a)) [35]. Because the free-wheeling diodes are left self-commutated, the analytical characterization of the

converter behavior in this degraded-mode is not trivial and leads to multiple cases to analyze which are functions of the converter voltage and loading conditions. The frozen leg operation of the 3p-DAB also leads to increased transformer current as well as a reduced power transfer capability for light and heavier load conditions. These loading conditions are characterized in [35] but are not generalized to all voltage and loading conditions. Moreover, due to the complexity in deriving an analytical model, the impacts on the ZVS capabilities, controller sizing, dynamic response, and stability are not validated.

In response to this challenge, the research contributions of this thesis are as follows. First, it is proposed to open the faulty-phase side such as it eliminates the interaction of the faulty-leg free-wheeling diodes (Figure 1.6 a)). As a result, it is possible to characterize the steady-state and transient operations of the 3p-DAB with one phase open for all voltage and loading conditions. It allows evaluating the major impacts of open-phase fault-tolerant operation as well as presenting key design considerations for a successful open-phase FT operation. Furthermore, the results also revealed that open-phase operation can provide increased power transfer capability and reduced circulating current as compared to frozen leg proposed in [35].

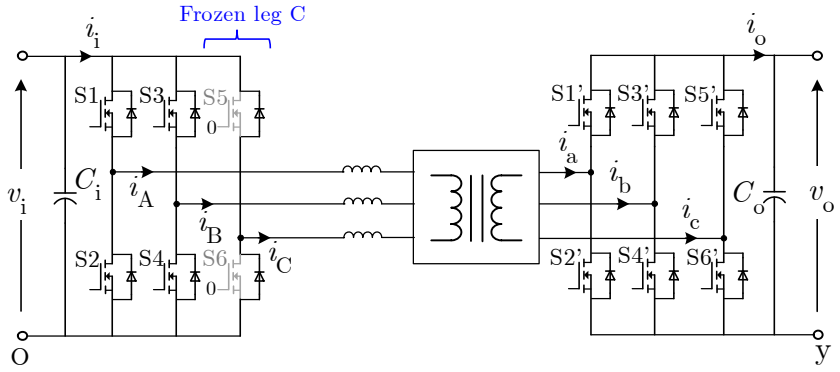

(a) Frozen leg fault-tolerant operation [35]

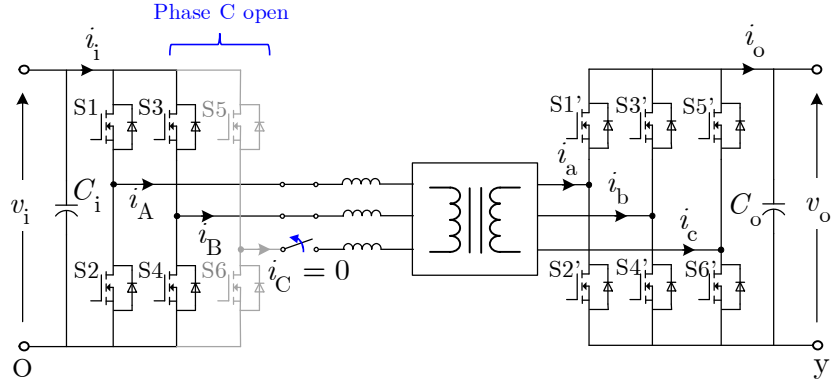

(b) Proposed open-phase fault-tolerant operation

Figure 1.6 : Comparison of the fault-tolerant modes of the 3p-DAB

1.4 Methodology and limits

1.4.1 Methodology

The design and integration process of power electronic converters such as the 3p-DAB requires investigations with different abstraction levels [68]. The main objective of this thesis is to develop and validate accurate models for integration analyses of 3p-DAB converters in dc-grids. A hierarchical modeling, simulation, testing and analysis methodology is used. Time-domain simulation in EMTP and experimental results on a small-scale closed-loop EPC2022 gallium nitride (GaN)-based Y-Δ 3p-DAB converter are also provided. Four (4) different converter design parameter sets are used in this thesis. This is explained by the evolution of the project over time and the necessity to address comments in the publication process prior to the writing of this thesis. Their main parameters are summarized in Appendix A and additional details on the design and fabrication of the small-scale prototype are provided in Appendix B.

The methodology is summarized as follows:

1. ***Steady-state analysis*:** A generalized phasor-domain method based on the first harmonic approximation (FHA) method [12] combined with Mordey's V-curve theory for synchronous machines [69] is first proposed for gaining understanding and physical insight. Then, the piecewise-linear modeling (PLM) approach [12], [24] is used for the determination of the parameters of the converter models, and for designing the small-scale prototype. PLM is also used for evaluating the converter operating point, the power transfer relationships, the ZVS boundaries, and for the sizing of the output capacitor. PLM is a necessary step for the development and implementation of small- and large-signal models.
2. ***Small-signal frequency-domain analysis*:** State-space averaging (SSA) and generalized state-space averaging (GSSA) small-signal models are derived for the calculation of all the open-loop transfer functions of the Y-Δ 3p-DAB converter (G_{vd}, G_{vg}, Z_D, Z_N, and Z_o). Both models are then compared and validated with time-domain simulations in EMTP. While GSSA is used to evaluate Z_D, a hybrid SSA and GSSA multi-input multi-output (MIMO) model is proposed to evaluate Z_N. The developed models are used for the design of the closed-loop controller, and for dynamic performance and stability assessments using MATLAB/Simulink.

3. ***Large-signal time-domain modeling and simulation*:** A generalized averaging model (GAM) of the Y-Δ 3p-DAB converter is developed, implemented and compared in closed-loop with the ideal, switching-function (SWF) and SSA methods applied to the 3p-DAB in EMTP. The performance of the GAM model is analyzed in terms of transient response, computation time and frequency response. A large-scale test system is also implemented to validate the performance of the GAM model for system-level transient fault current and transient recovery voltage analyses.
4. ***Open-phase fault-tolerant analysis*:** Steady-state analysis based on the PLM approach is performed to characterize the converter in open-phase operation and evaluate the impacts on the converter steady-state characteristics. Open-phase operation is also compared with frozen leg [35] and normal operations. Moreover, small-signal frequency-domain analysis using SSA and GSSA methodologies is performed to design a suitable closed-loop controller for both normal and open-phase operations as well as to assess the impacts on the converter stability and dynamic performance.

1.4.2 Limits

In this thesis, the converter under study is the Y-Δ 3p-DAB operated using single-phase-shift (SPS) control with a fixed switching frequency ω_s and a 180º (or 6-step) modulation scheme. The results are not extended to other emerging modulation methods. The converter is assumed lossless for steady-state, small-signal and large-signal analyses. Information on loss analysis for the 3p-DAB converter can be found in [68], [70]–[72]. The transformer magnetizing inductance and the presence of snubber capacitances are neglected. The switches are assumed ideal. The dead-time between the upper and lower switches is also neglected because it increases drastically the complexity in modeling the 3p-DAB converter [73]. The result is the assumption of an ideal transition of the current from the free-wheeling diodes to the transistors during the ZVS turn-on events. Furthermore, only forward operation and the Y-Δ transformer are considered but the generalization to other transformer connections is discussed. The load is assumed to be purely resistive.

1.5 Thesis outlines

The structure of this thesis is mainly oriented to follow the methodology and to expose the development specific to each of the contributions defined in section 1.3.

In **Chapter 2** – **Steady-State Analysis**, steady-state modeling of the 3p-DAB converter is used for sizing and for providing a general understanding of the converter operating principles. It is a necessary step to small-signal (**Chapter 3**) and large-signal (**Chapter 4)** analyses.

In **Chapter 3 – Small-Signal Frequency-Domain Analysis**, small-signal models of the 3p-DAB are developed, validated and implemented. They are used for closed-loop controller design, as well as small-signal stability assessment and dynamic performance analysis in MATLAB/Simulink.

In **Chapter 4 – Large-Signal Time-Domain Simulation**, a generalized average model (GAM) is developed, validated and implemented. It enables closed-loop system-level simulation of dc-grids with 3p-DAB converters in EMTP.

In **Chapter 5 – Open-Phase Fault-Tolerant Operation**, steady-state, small-signal and transient analyses are performed to enable the successful operation of 3p-DAB converters in open-phase fault-tolerant condition.

In **Chapter 6 – Conclusions and Recommendations**, the main conclusions of this thesis are presented along with recommendations for future area of research in modeling, simulation, and analysis of the 3p-DAB converter in both normal and fault-tolerant operations.

CHAPTER 2 STEADY-STATE ANALYSIS

In this chapter, steady-state modeling of the 3p-DAB converter is performed for supporting the selection of the parameters of the converter models as well as for assisting the selection of the components for the small-scale prototype. It also presents the main steps for the calculation of the converter operating point, the power transfer relationships, and the zero-voltage switching (ZVS) regions. This step is necessary for the development of small- and large-signal models as well as for the analysis of the converter in degraded-mode.

2.1 First harmonic approximation (FHA) in phasor-domain

2.1.1 Motivation

The steady-state analysis of the DAB is generally performed using the piecewise-linear modeling (PLM) approach. As it will be seen in section 2.2, this approach is a demanding task for 3p-DAB converters. To simplify the analysis, the 3p-DAB can also be analyzed using the first harmonic approximation (FHA) in the phasor-domain [12], [74]. It consists in replacing the input and output bridges by voltage sources at the switching frequency ω_s and the transformer by its equivalent leakage reactance X_s. Using this model, the power transfer relationship of the 3p-DAB is similar to the power-angle relationship of synchronous machines. This method can also be used to approximate the input and output bridge ZVS ranges.

In this thesis, a generalized FHA phasor-domain modeling method for steady-state analysis of 3p-DAB with single-phase-shift (SPS) control has been developed. A set of general and simplified equations has been developed and a useful diagram for first converter design has been developed in physical and per-unit quantities. The FHA method has been generalized for different transformer connections and validated using time-domain simulations.

The FHA method combined with the use of the developed diagram allows approximating the RMS and peak currents as well as the ZVS regions for given converter specifications. It also provides a means to understand the general operating principles of the 3p-DAB converter. Unlike PLM, the FHA method results in a single set of equations which does not depend on the transformer connection and the control phase-shift δ operating range.

2.1.2 Model development

The transformer is first replaced by its equivalent primary-referred leakage reactance $X_s = \omega_s L_s$. As seen in Figure 2.1, the voltages applied by the input and output bridges, v_{AN} and v'_{an} respectively, are modeled by equivalent phasor-domain voltage sources $\mathbf{V}_{AN}$ and $\mathbf{V}'_{an}$ at the switching frequency ω_s. The equivalent transformer current $\mathbf{I}_A$ obtained from the phasor-domain analysis is close to the time-domain current i_A which is almost sinusoidal owing to the three-phase structure. The resulting FHA phasor-domain circuit and phasor diagram are given in Figure 2.2.

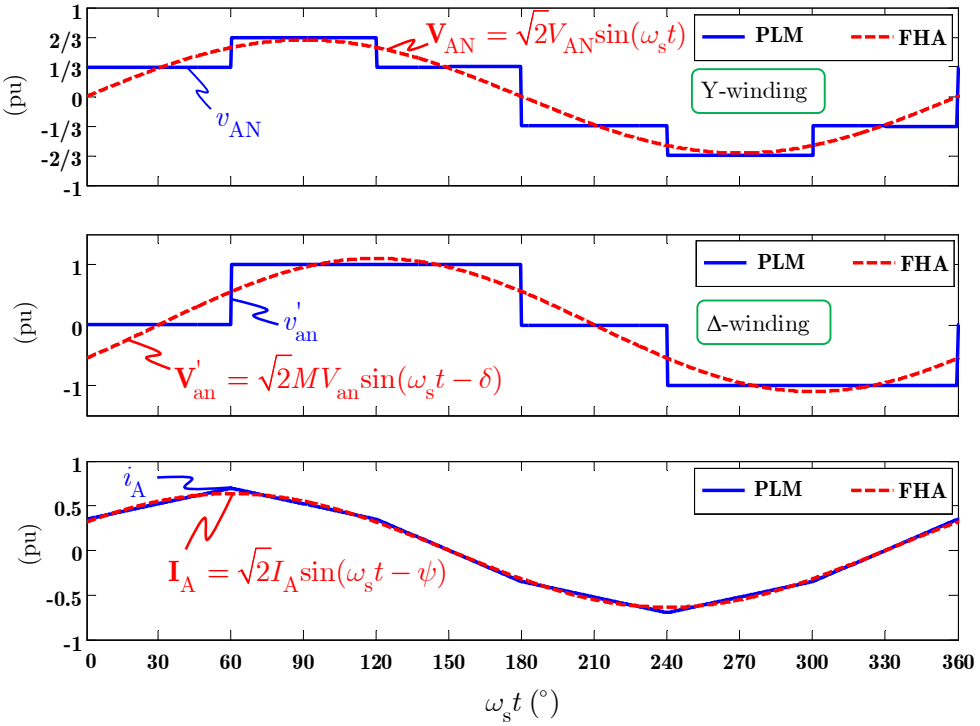

Figure 2.1 : Comparison of PLM and FHA waveforms for the Y-Δ transformer

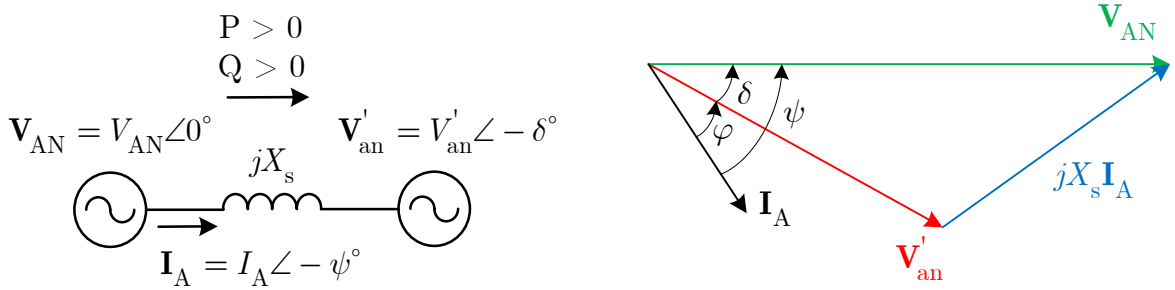

(a) Equivalent single-phase circuit (b) Equivalent phasor diagram

Figure 2.2 : FHA model in physical quantities

The phasor-diagram is defined in generating convention such that active and reactive powers are positive when flowing from $\mathbf{V}_{\mathrm{AN}}$ to $\mathbf{V}_{\mathrm{an}}^{'}$. The input voltage phasor $\mathbf{V}_{\mathrm{AN}}$ is taken as the reference, which implies that the modulator is synchronizing the output bridge with respect to the input bridge. $\mathbf{V}_{\mathrm{AN}}$ is comparable to the synchronous generator internal field excitation in the equivalent machine model. The output bridge voltage $\mathbf{V}_{\mathrm{an}}^{'}$ is equivalent to the network voltage. The phase-shift δ is equivalent to the power angle of the synchronous machine such that, a positive value of δ means that the active power is transferred from $\mathbf{V}_{\mathrm{AN}}$ to $\mathbf{V}_{\mathrm{an}}^{'}$ (forward operation). Conversely, a negative value of δ means that the active power is transferred from $\mathbf{V}_{\mathrm{an}}^{'}$ to $\mathbf{V}_{\mathrm{AN}}$ (reverse operation). The angle φ is the angle between the transformer line current $\mathbf{I}_{\mathrm{A}}$ and the output bridge voltage $\mathbf{V}_{\mathrm{an}}^{'}$ such that the value of $\cos(\varphi)$ is similar to the power factor of the synchronous machine with respect to the network. The angle ψ is the angle between the transformer line current $\mathbf{I}_{\mathrm{A}}$ and the input bridge voltage $\mathbf{V}_{\mathrm{AN}}$. Based on these definitions, the active and reactive power equations for the input and output bridges are written as,

$$P_{\mathrm{i}} = 3V_{\mathrm{AN}}I_{\mathrm{A}}\cos(\psi),\ Q_{\mathrm{i}} = 3V_{\mathrm{AN}}I_{\mathrm{A}}\sin(\psi) \tag{2.1}$$

$$P_{\mathrm{o}} = 3V_{\mathrm{an}}^{'}I_{\mathrm{A}}\cos(\varphi),\ Q_{\mathrm{o}} = 3V_{\mathrm{an}}^{'}I_{\mathrm{A}}\sin(\varphi) \tag{2.2}$$

For the equivalent single-phase circuit of Figure 2.2 a), it is also well known that the power transfer equation (or power-angle equation) is given by,

$$P = P_{\mathrm{i}} = P_{\mathrm{o}} = \frac{3V_{\mathrm{AN}}V_{\mathrm{an}}^{'}}{X_{\mathrm{s}}}\sin(\delta) \tag{2.3}$$

Because both the voltage and the current are non-sinusoidal, it is expected that both the fundamental and harmonic components contribute to the active power flow. However, as the harmonic order increases, the equivalent reactance of the transformer also increases, which reduces the power transfer capability of the transformer at higher harmonics. This mainly explains why FHA can be used to evaluate the power transfer relationship of 3p-DAB converters in a similar way to the power-angle relationship of synchronous machines connected to an equivalent network at the fundamental frequency ω_{s}.

In the 3p-DAB, reactive current needs to circulate through the transistors free-wheeling diodes to provide ZVS at turn-on of the transistors. On the phasor diagram of Figure 2.2 b), it means that $\mathbf{I}_{\mathrm{A}}$

must lie between the input voltage $\mathbf{V}_{\mathrm{AN}}$ and the output voltage $\mathbf{V}'_{\mathrm{an}}$ [12]. In other words, $\mathbf{I}_{\mathrm{A}}$ must lag $\mathbf{V}_{\mathrm{AN}}$ for ZVS at the input bridge (see example in Figure 2.3), and similarly, $\mathbf{I}_{\mathrm{A}}$ must lead $\mathbf{V}'_{\mathrm{an}}$ for ZVS at the output bridge. Physically, it means that both bridges are providing reactive power to the transformer leakage reactance X_{s}. The equivalent phasor diagrams at the ZVS boundaries for the input and output bridges are given in Figure 2.4 a) and b) respectively. Mathematically, it means that $\psi = 0^{\circ}$ (i.e. $\cos(\psi) = 1$) at the ZVS boundary of the input bridge and $\varphi = 0^{\circ}$ (i.e. $\cos(\varphi) = 1$) at the ZVS boundary of the output bridge. Using the phasor diagrams of Figure 2.4 a) and b), the ZVS boundaries for both bridges are evaluated. For the input bridge it yields to,

$$I_{\mathrm{A}} = \frac{\sqrt{(V'_{\mathrm{an}})^2 - (V_{\mathrm{AN}})^2}}{X_{\mathrm{s}}} \tag{2.4}$$

and for the output bridge it leads to,

$$I_{\mathrm{A}} = \frac{\sqrt{(V_{\mathrm{AN}})^2 - (V'_{\mathrm{an}})^2}}{X_{\mathrm{s}}} \tag{2.5}$$

As for the synchronous machine, the maximum power transfer in (2.3) occurs when $\delta = 90^{\circ}$. In this condition, the equivalent phasor diagram is shown in Figure 2.4 c), and the current I_{A} at the maximum power transfer boundary is evaluated as,

$$I_{\mathrm{A}} = \frac{\sqrt{(V_{\mathrm{AN}})^2 + (V'_{\mathrm{an}})^2}}{X_{\mathrm{s}}} \tag{2.6}$$

Another useful relationship is the equation which relates the transformer current I_{A} to the input V_{AN} and output V'_{an} voltages for different phase-shift angles δ. It is given by,

$$I_{\mathrm{A}} = \frac{\sqrt{(V_{\mathrm{AN}}\cos(\delta) - V'_{\mathrm{an}})^2 + (V_{\mathrm{AN}}\sin(\delta))^2}}{X_{\mathrm{s}}} \tag{2.7}$$

Finally, the equation which relates the transformer current I_{A} to the input V_{AN} and output V'_{an} voltages for different output power set-points P_{o} is established. This relationship is equivalent to Mordey's V-Curve for synchronous machines [69] which is widely used for design and testing of synchronous machines. It can be demonstrated that the resulting relationship for the 3p-DAB is given by,

$$I_{\mathrm{A}}=\frac{1}{3V_{\mathrm{an}}^{'}}\cdot\sqrt{\left[\frac{3V_{\mathrm{an}}^{'}}{X_{\mathrm{s}}}\left(\sqrt{(V_{\mathrm{AN}})^{2}-\left(\frac{P_{\mathrm{o}}X_{\mathrm{s}}}{3V_{\mathrm{an}}^{'}}\right)^{2}}-V_{\mathrm{an}}^{'}\right)\right]^{2}+(P_{\mathrm{o}})^{2}} \tag{2.8}$$

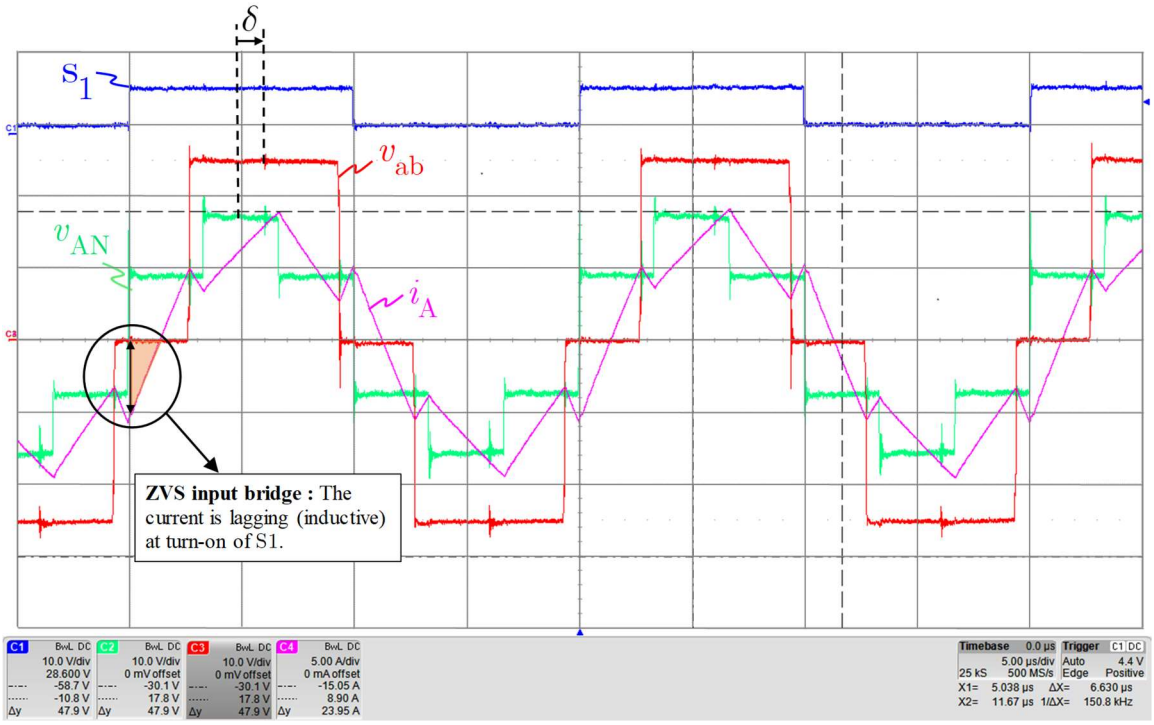

Figure 2.3 : Typical waveforms with ZVS in the input bridge (Y-Δ transformer)

Equations (2.4)–(2.8) need to be written in terms of the dc input and output voltages (V_{i} and V_{o}) to be useful for the analysis of 3p-DAB converters. Fourier decomposition of the waveforms for Y- and Δ-windings is used to obtain the amplitude of the phasors $\mathbf{V}_{\mathrm{AN}}$ and $\mathbf{V}_{\mathrm{an}}^{'}$ in terms of V_{i} and V_{o} respectively,

$$V_{\mathrm{AN}}=\frac{2}{\sqrt{2}\pi}V_{\mathrm{i}} \tag{2.9}$$

$$V_{\mathrm{an}}^{'}=MV_{\mathrm{an}}=M\frac{2}{\sqrt{2}\pi}V_{\mathrm{o}} \tag{2.10}$$

The peak current can be approximated by,

$$I_{\mathrm{A}}^{\mathrm{pk}}=\sqrt{2}I_{\mathrm{A}} \tag{2.11}$$

From the input bridge current, the output bridge current can also be obtained with,

$$I_{\mathrm{a}}=MI_{\mathrm{A}} \tag{2.12}$$

Moreover, the per-unit model is a generalization of the physical quantities model which allows more flexibility in the analysis of the 3p-DAB converter. The per-unit model is obtained from the physical quantities model by using the following base,

$$V_{\mathrm{b}} = V_{\mathrm{an}}^{'}, \quad I_{\mathrm{b}} = \frac{V_{\mathrm{an}}^{'}}{X_{\mathrm{s}}}, \quad S_{\mathrm{b}} = V_{\mathrm{b}} I_{\mathrm{b}} = \frac{(V_{\mathrm{an}}^{'})^2}{X_{\mathrm{s}}}, \quad Z_{\mathrm{b}} = X_{\mathrm{s}} \tag{2.13}$$

For convenience, the ratio between the input and output voltages is also expressed as,

$$D = \frac{V_{\mathrm{AN}}}{V_{\mathrm{an}}^{'}} = \frac{V_{\mathrm{i}}}{M V_{\mathrm{o}}} \tag{2.14}$$

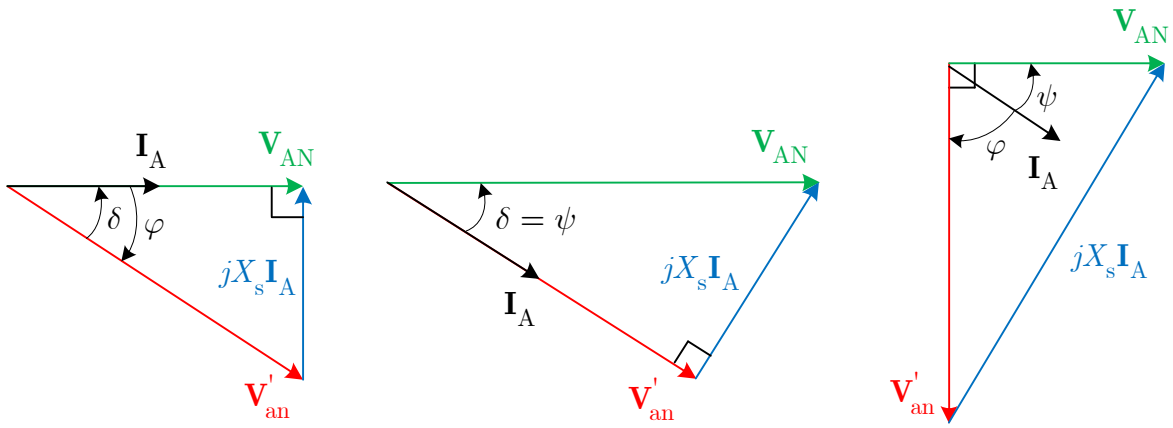

(a) At ZVS boundary input bridge

(b) At ZVS boundary output bridge

(c) At maximum power transfer

Figure 2.4 : Equivalent phasor diagrams

2.1.3 Model validation and analysis of the results

The equations of the generalized FHA model are validated for three different transformer connections (Y-Y, Δ-Δ, and Y-Δ) using time-domain simulations in EMTP. The results are shown in Figure 2.5 for the Y-Y and Δ-Δ transformers and Figure 2.6 for the Y-Δ transformer.

From the results obtained in Figure 2.5 and Figure 2.6, it is concluded that the FHA modeling method is accurate to evaluate the constant output power P_{o} equation given in (2.8). It is also precise to determine the constant phase-shift δ equation given in (2.7) which also includes the maximum power transfer equation at $\delta = 90^{\circ}$ given in (2.6). The maximum error between the FHA model and time-domain simulations for the calculation of the RMS current is lower than 1%. For

the calculation of the peak current, the maximum error is 10%. This is explained by the fact that the current is not perfectly sinusoidal in the transformer.

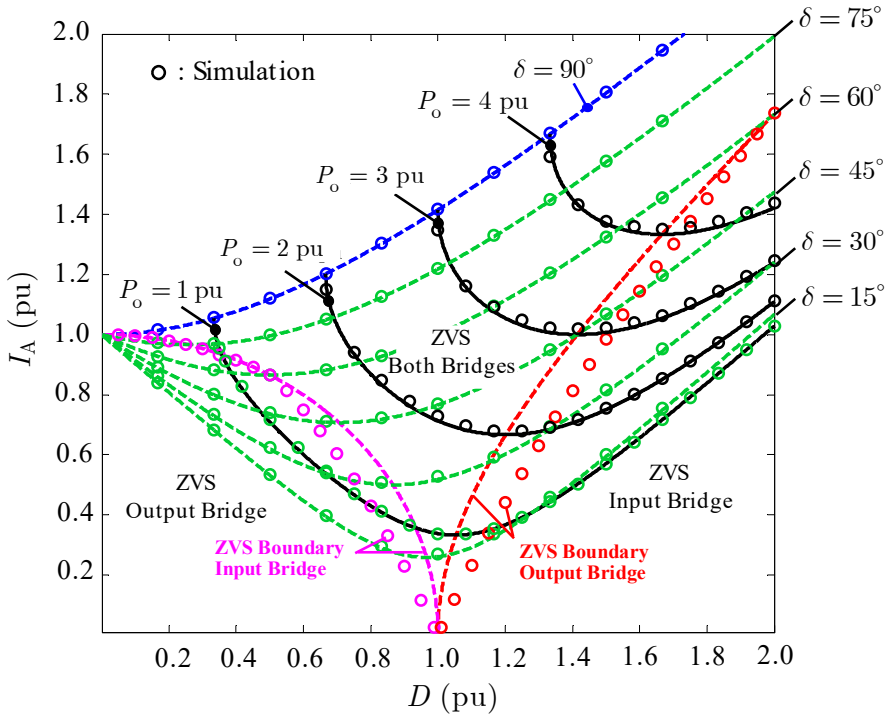

Figure 2.5 : Validation of the FHA design diagram for the Y-Y and Δ-Δ transformers

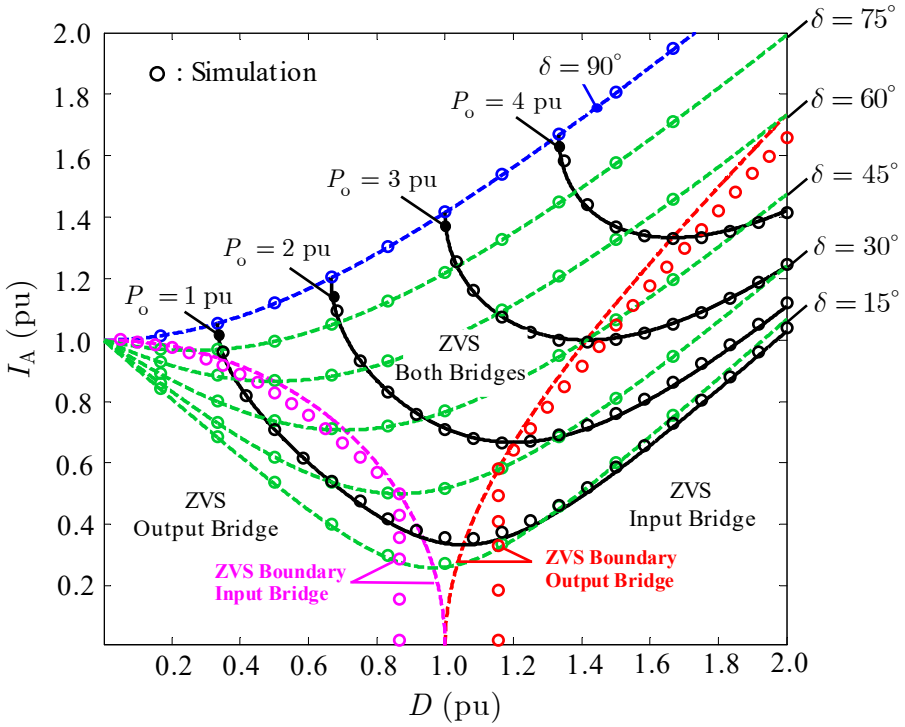

Figure 2.6 : Validation of the FHA design diagram for the Y-Δ transformer

It is also observed in Figure 2.5 and Figure 2.6 that the FHA modeling approach is less accurate to evaluate the input and output bridges ZVS boundaries at low output power. The maximum error between FHA and time-domain simulations is 15 % for the Y-Δ transformer, and 8 % for the Y-Y and Δ-Δ transformers. However, two important observations must be made. First, FHA leads to a conservative evaluation of the ZVS regions. This means that the ZVS regions evaluated using FHA are smaller than expected with time-domain simulations. Second, FHA gives a good estimation at high output power. The identification of the ZVS regions is generally more critical at high output power. The error between FHA and time-domain simulations is explained by the fact that harmonic distortion in the transformer current leads to errors in the evaluation of the current zero-crossing; ZVS occurs in the input bridge if $i_{\mathrm{A}} < 0$ at turn-on of $\mathrm{S1}$ as shown in Figure 2.3, and ZVS occurs in the output bridge if $i_{\mathrm{a}} > 0$ at turn-on of S1'.

2.1.4 Application to the experimental prototype (model 4)

The FHA method combined with the use of the developed diagram allows approximating the RMS and peak currents as well as the ZVS regions for given converter specifications. It is an important step for the development of a hardware prototype and, to a lesser extent, to the implementation of simulation models. For this reason, the Y-Δ 3p-DAB prototype (model 4) is used in this section as a design example. For a constant output voltage $V_{\mathrm{o}} = 24\ \mathrm{V}$, the design diagrams for two different switching frequencies $f_{\mathrm{s}} = 50\ \mathrm{kHz}$ and $f_{\mathrm{s}} = 100\ \mathrm{kHz}$ are given in Figure 2.7. The testing zone represents the operating zone for which simulations and experiments have been conducted.

Important conclusions regarding the 3p-DAB operating principles can also be drawn from the results in Figure 2.7. First, it is possible to see that, for the same amount of active power transferred, minimum RMS current operation occurs at the output bridge ZVS boundary. High reactive circulating current increases the transformer losses and decreases the transformer utilization, such that, for the same output power, it is desirable to reduce the amount of reactive current while keeping ZVS at both bridges. Furthermore, from a design standpoint, the leakage inductance L_{s} should be selected such that maximum power transfer is possible for the entire voltage operating ranges. For instance, in Figure 2.7 a), for $V_{\mathrm{o}} = 24\ \mathrm{V}$ and $f_{\mathrm{s}} = 50\ \mathrm{kHz}$, it is concluded that the converter can be operated at $P_{\mathrm{o}} = 250\ \mathrm{W}$ for the entire range of input voltage V_{i} (18 V to 30 V)

without reaching the maximum power transfer limit $\delta = 90^{\circ}$. It is not the case if $f_{\mathrm{s}} = 100\ \mathrm{kHz}$ as seen in Figure 2.7 b). This is because the power transfer capability of the 3p-DAB decreases as the switching frequency f_{s} increases and as the input voltage V_{i} decreases. This can be seen by rewriting (2.3) using (2.9) and (2.10),

$$P_{\mathrm{o}} = \frac{6\sqrt{3}}{\pi^2}\left(\frac{mV_{\mathrm{i}}V_{\mathrm{o}}}{\omega_{\mathrm{s}}L_{\mathrm{s}}}\right)\sin(\delta) \tag{2.15}$$

In Figure 2.7, it is also possible to perform a preliminary assessment of the ZVS boundaries for both bridges. First, it can be observed that, under low load conditions, ZVS is not guaranteed at the input bridge for low input voltage V_{i}, and at the output bridge for high input voltage V_{i}. At higher power set-points P_{o}, the ZVS range increases up to a point where the main limitation on the converter design becomes the maximum phase-shift angle $\delta = 90^{\circ}$. Also note that, for the same output power P_{o}, the region where both bridges are ZVS tends to increase at low power as the switching frequency f_{s} is increased.

The maximum RMS current expected for the hardware prototype is $I_{\mathrm{A}} = 12.5\ \mathrm{A}$ ($I_{\mathrm{A}}^{\mathrm{pk}} = 17.7\ \mathrm{A}$) in the input bridge, and $I_{\mathrm{a}} = 10.8\ \mathrm{A}$ ($I_{\mathrm{a}}^{\mathrm{pk}} = 15.3\ \mathrm{A}$) in the output bridge.

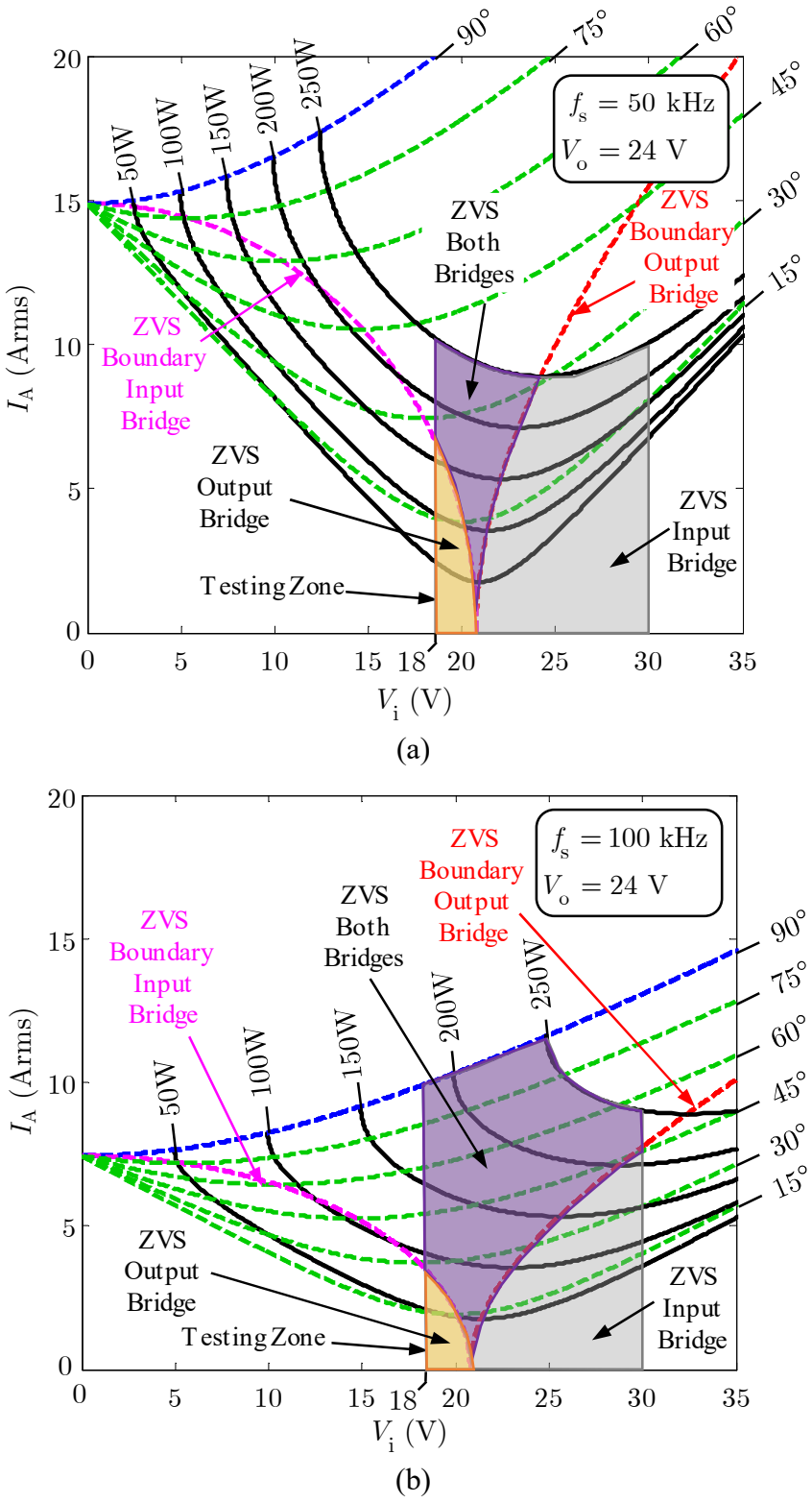

Figure 2.7 : Application of FHA to the Y-Δ 3p-DAB prototype (model 4)

2.2 Piecewise-linear modeling (PLM) in time-domain

2.2.1 Motivation

The steady-state analysis of DAB converters is often performed using the piecewise-linear (PLM) approach in time-domain. It consists in defining the transformer series inductor current equations for each operating mode over one half-cycle, i.e for the interval $\theta = [0, \pi]$. This approach is a demanding task for the 3p-DAB converter because it requires the derivation of the current equations for up to six modes, where the equations for each of the six modes also vary with the control phase-shift δ operating range, and the transformer connection (Y-Δ, Δ-Y or Y-Δ, and Δ-Δ).

The PLM approach allows evaluating with precision the ZVS boundaries, both the ripple currents and voltages of the filter capacitors, as well as the power transfer relationships. It also allows evaluating the RMS and peak currents through the transformer and the switches, but the resulting equations are more convenient using the FHA method presented in section 2.1.

2.2.2 Piecewise-linear current equations

The first step in applying the PLM approach for the 3p-DAB consists in solving the three-phase currents using the equivalent circuits shown in Figure 2.8.

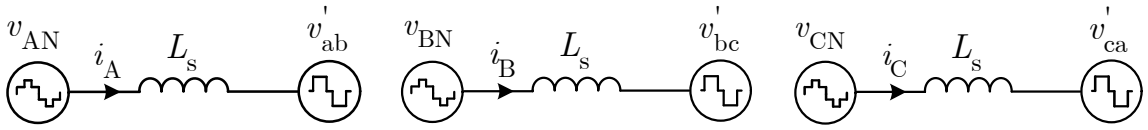

(a) Phase A (b) Phase B (c) Phase C

Figure 2.8 : Equivalent circuits for the application of PLM to the Y-Δ 3p-DAB

By making the assumption that constant dc voltages are applied on both sides of the series inductor for a given generic interval $\theta = [\theta_o, \theta_1]$, it is possible to calculate the current flowing through each phase using the following relationships,

$$i_A(\theta) = \frac{1}{\omega_s L_s}\left(v_{AN} - v'_{ab}\right)\cdot(\theta - \theta_o) + i_A(\theta_o) \tag{2.16}$$

$$i_{\mathrm{B}}(\theta)=\frac{1}{\omega_{\mathrm{s}}L_{\mathrm{s}}}\left(v_{\mathrm{BN}}-v_{\mathrm{bc}}^{'}\right)\cdot(\theta-\theta_{\mathrm{o}})+i_{\mathrm{B}}(\theta_{\mathrm{o}}) \tag{2.17}$$

$$i_{\mathrm{C}}(\theta)=\frac{1}{\omega_{\mathrm{s}}L_{\mathrm{s}}}\left(v_{\mathrm{CN}}-v_{\mathrm{ca}}^{'}\right)\cdot(\theta-\theta_{\mathrm{o}})+i_{\mathrm{C}}(\theta_{\mathrm{o}}) \tag{2.18}$$

For the 3p-DAB, the derivation of the phase current equations must be done for two different ranges which depend on the control phase-shift δ and the transformer connection. For the specific case of the Y-Δ 3p-DAB, range 1 is defined as $0\le\delta\le\pi/6$ and range 2 is defined as $\pi/6\le\delta\le\pi/2$.

To apply (2.16)–(2.18), it is necessary to determine the primary voltages v_{AN}, v_{BN} and v_{CN} as functions of the dc input voltage v_{i}, and the primary-referred secondary voltages $v_{\mathrm{ab}}^{'}$, $v_{\mathrm{bc}}^{'}$ and $v_{\mathrm{ca}}^{'}$ in terms of the dc output voltage v_{o}. To do so, the equivalent circuit of Figure 2.9 is used.

The voltages applied by the input bridge on the primary-side are given by,

$$v_{\mathrm{AN}}=v_{\mathrm{AO}}-v_{\mathrm{NO}} \tag{2.19}$$

$$v_{\mathrm{BN}}=v_{\mathrm{BO}}-v_{\mathrm{NO}} \tag{2.20}$$

$$v_{\mathrm{CN}}=v_{\mathrm{CO}}-v_{\mathrm{NO}} \tag{2.21}$$

Assuming that the voltages v_{AN}, v_{BN} and v_{CN} are balanced, and adding (2.19) to (2.21) together, it leads to,

$$v_{\mathrm{NO}}=\frac{v_{\mathrm{AO}}+v_{\mathrm{BO}}+v_{\mathrm{CO}}}{3} \tag{2.22}$$

with,

$$v_{\mathrm{AO}}=\mathrm{s}_1 v_{\mathrm{i}} \tag{2.23}$$

$$v_{\mathrm{BO}}=\mathrm{s}_3 v_{\mathrm{i}} \tag{2.24}$$

$$v_{\mathrm{CO}}=\mathrm{s}_5 v_{\mathrm{i}} \tag{2.25}$$

and s_1, s_3, and s_5 being the input bridge switching-functions which are defined in Appendix C. Inserting (2.23)–(2.25) into (2.22), it results that,

$$v_{\mathrm{NO}}=\frac{\left(\mathrm{s}_1+\mathrm{s}_3+\mathrm{s}_5\right)v_{\mathrm{i}}}{3} \tag{2.26}$$

From (2.26), it is concluded that the voltage v_{NO} on the primary-side only depends on the input bridge switching-functions and the converter input voltage. Furthermore, inserting (2.23)–(2.26) into (2.19)–(2.21) leads to,

$$v_{\mathrm{AN}} = \frac{\left(2\mathrm{s}_1 - \mathrm{s}_3 - \mathrm{s}_5\right) v_{\mathrm{i}}}{3} \tag{2.27}$$

$$v_{\mathrm{BN}} = \frac{\left(2\mathrm{s}_3 - \mathrm{s}_1 - \mathrm{s}_5\right) v_{\mathrm{i}}}{3} \tag{2.28}$$

$$v_{\mathrm{CN}} = \frac{\left(2\mathrm{s}_5 - \mathrm{s}_1 - \mathrm{s}_3\right) v_{\mathrm{i}}}{3} \tag{2.29}$$

A similar analysis can be carried out on the secondary-side which leads to,

$$v'_{\mathrm{ab}} = m v_{\mathrm{ab}} = m\left(\mathrm{s}'_1 - \mathrm{s}'_3\right) v_{\mathrm{o}} \tag{2.30}$$

$$v'_{\mathrm{bc}} = m v_{\mathrm{bc}} = m\left(\mathrm{s}'_3 - \mathrm{s}'_5\right) v_{\mathrm{o}} \tag{2.31}$$

$$v'_{\mathrm{ca}} = m v_{\mathrm{ca}} = m\left(\mathrm{s}'_5 - \mathrm{s}'_1\right) v_{\mathrm{o}} \tag{2.32}$$

with s'_1, s'_3 and s'_5 being the output bridge switching-functions (Appendix C). Knowing the values of the switching-functions (either 0 or 1) for each mode over $\theta = [0, \pi]$, and making the assumption that the input and output voltages are both constant, i.e. that $v_{\mathrm{i}} = V_{\mathrm{i}}$ and $v_{\mathrm{o}} = V_{\mathrm{o}}$, the equations for the phase currents given by (2.16)–(2.18) can be solved using (2.27)–(2.32). The resulting current equations for each of the three phases are given in Appendix C. These equations are necessary to evaluate the power transfer relationships, the ZVS boundaries as well as the capacitor ripple current and voltage.

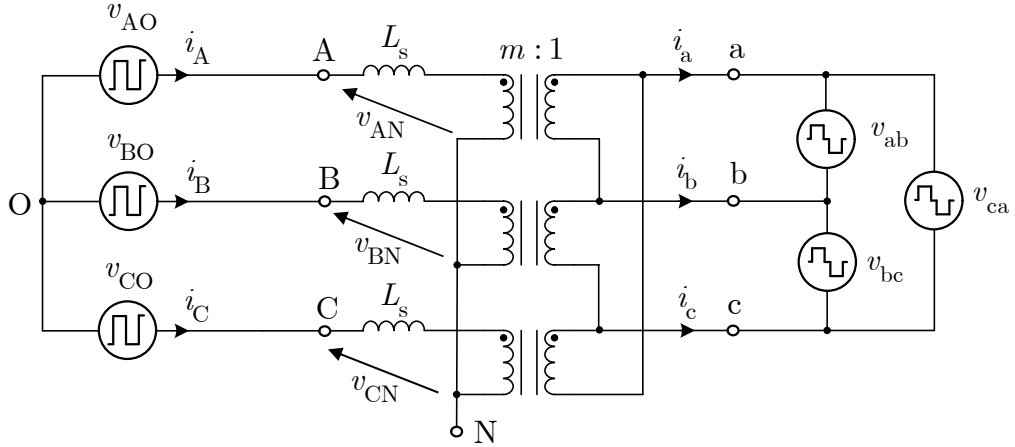

Figure 2.9 : Simplified representation of the Y-Δ 3p-DAB

2.2.3 Power transfer relationships

The procedure to derive the power transfer relationships of the 3p-DAB requires averaging the input or output currents which are expressed in terms of the primary transformer currents as well as the input and output bridge switching-functions given in Appendix C,

$$i_{\mathrm{i}} = \mathrm{s}_1 i_{\mathrm{A}} + \mathrm{s}_3 i_{\mathrm{B}} + \mathrm{s}_5 i_{\mathrm{C}} \tag{2.33}$$

$$i_{\mathrm{o}} = m\left[(\mathrm{s}_1' - \mathrm{s}_3')i_{\mathrm{A}} + (\mathrm{s}_3' - \mathrm{s}_5')i_{\mathrm{B}} + (\mathrm{s}_5' - \mathrm{s}_1')i_{\mathrm{C}}\right] \tag{2.34}$$

Due to the symmetrical operation of the 3p-DAB, the analysis only needs to be performed over the interval $\theta = [0, \pi/3]$ i.e. for modes I and II. The analysis is performed here on the output current i_{o} for the two different control phase-shift δ ranges (Figure 2.10). A similar analysis can be done on the input current i_{i}.

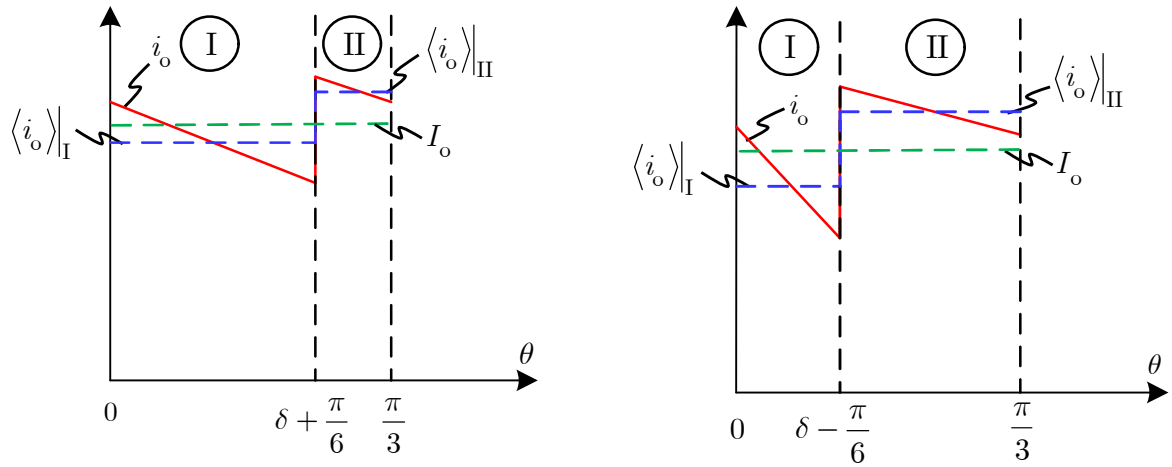

(a) Range 1 ($0 \le \delta \le \pi/6$) (b) Range 2 ($\pi/6 \le \delta \le \pi/2$)

Figure 2.10 : Waveforms for the calculation of the average output current

The procedure to calculate the average output currents for mode I $\langle i_{\mathrm{o}} \rangle|_{\mathrm{I}}$ and mode II $\langle i_{\mathrm{o}} \rangle|_{\mathrm{II}}$ is given in Appendix C. Knowing the average output currents for these two modes, the total average output current I_{o} is calculated following the methodology presented in [54] and [75]. For range 1, I_{o} is calculated as follows,

$$I_{\mathrm{o}} = \frac{3}{\pi}\left[(\delta + \frac{\pi}{6}) \cdot \langle i_{\mathrm{o}} \rangle|_{\mathrm{I}} + (\frac{\pi}{6} - \delta) \cdot \langle i_{\mathrm{o}} \rangle|_{\mathrm{II}}\right] \tag{2.35}$$

which, using (C.42) and (C.49), yields to,

$$I_{\mathrm{o}}=\frac{mV_{\mathrm{i}}}{\omega_{\mathrm{s}}L_{\mathrm{s}}}\delta \tag{2.36}$$

such that the output power is given by,

$$P_{\mathrm{o}}=V_{\mathrm{o}}I_{\mathrm{o}}=\frac{mV_{\mathrm{i}}V_{\mathrm{o}}}{\omega_{\mathrm{s}}L_{\mathrm{s}}}\delta \tag{2.37}$$

Applying a similar procedure in range 2, using (C.50) and (C.51), results in,

$$P_{\mathrm{o}}=\frac{mV_{\mathrm{i}}V_{\mathrm{o}}}{\omega_{\mathrm{s}}L_{\mathrm{s}}}\left[\frac{3}{2}\left(\delta-\frac{\delta^2}{\pi}\right)-\frac{\pi}{24}\right] \tag{2.38}$$

Equations (2.37) and (2.38) are known to be the power transfer relationships of the Y-Δ 3p-DAB converter. They are necessary for the calculation of the operating point for the application of the state-space averaging (SSA) method (section 3.2) for the small-signal analysis of 3p-DAB converters. By comparing (2.37) and (2.38) with (2.15) which was obtained using FHA, it is concluded that, according to both the FHA and PLM models, the output power P_{o} increases as $mV_{\mathrm{i}}V_{\mathrm{o}}$ increases and $\omega_{\mathrm{s}}L_{\mathrm{s}}$ decreases. It also shows that if m, V_{i}, V_{o}, ω_{s} and L_{s} are all constants, then, the only way to regulate the output power of the 3p-DAB is by controlling the phase-shift δ. The power transfer relationships for the Y-Δ 3p-DAB prototype (model 4) are plotted in Figure 2.11. The FHA model is also compared with the PLM approach. It shows that FHA is also precise for determining the power transfer relationship.

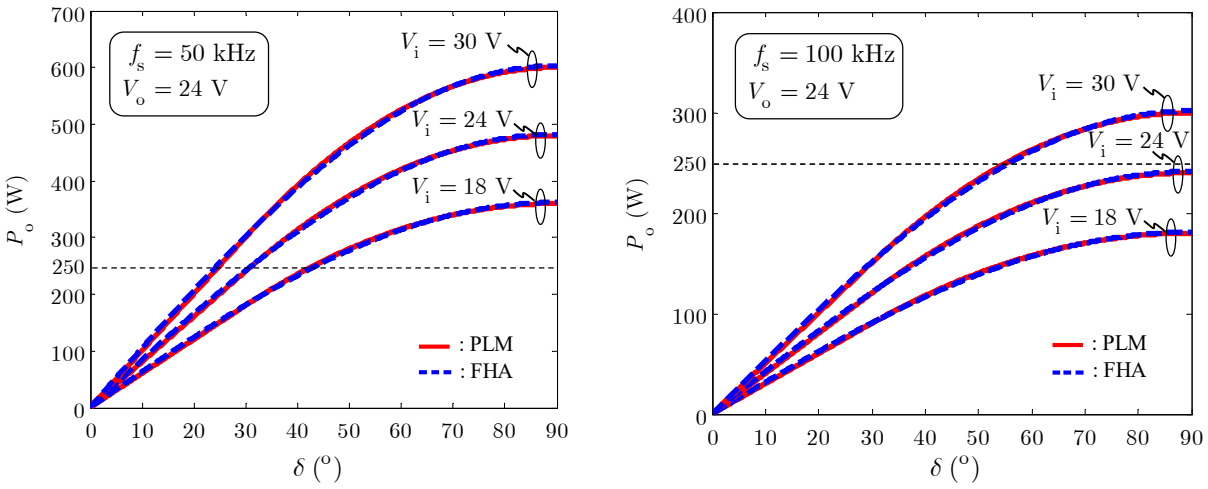

(a) For $f_{\mathrm{s}} = 50$ kHz (b) For $f_{\mathrm{s}} = 100$ kHz

Figure 2.11 : Power transfer curves for the Y-Δ 3p-DAB prototype (model 4)

2.2.4 Zero-voltage switching (ZVS) boundaries

The 3p-DAB makes use of reactive circulating current through the transistor free-wheeling diodes of each bridge to provide ZVS. As mentioned before, ZVS occurs at the input bridge if $i_{\mathrm{A}} < 0$ at turn-on of S1, and ZVS occurs in the output bridge if $i_{\mathrm{a}} > 0$ at turn-on of S1'. The procedure to evaluate the theoretical ZVS boundaries for the 3p-DAB has been presented in [12] and [24]. In the case of the Y-Δ 3p-DAB, for the input bridge, it consists in solving the equation $i_{\mathrm{A}}(0) = 0$ and, for the output bridge, it consists in solving the following equation,

$$i_{\mathrm{a}}(\delta+\frac{\pi}{6}) = m\left[i_{\mathrm{A}}(\delta+\frac{\pi}{6}) - i_{\mathrm{C}}(\delta+\frac{\pi}{6})\right] = 0 \tag{2.39}$$

Using (C.6) and (C.24) for determining $i_{\mathrm{A}}(0)$, the ZVS boundaries for the input bridge are obtained. For range 1 ($0 \le \delta \le \pi/6$), the input bridge is operated with ZVS when,

$$d > \frac{3}{2} \tag{2.40}$$

and, for range 2 ($\pi/6 \le \delta \le \pi/2$), the input bridge is operated with ZVS if,

$$d > \frac{9\pi - 18\delta}{4\pi} \tag{2.41}$$

with the voltage conversion ratio d defined as,

$$d = \frac{V_{\mathrm{i}}}{mV_{\mathrm{o}}} \tag{2.42}$$

Similarly, for range 1, it can be demonstrated that the output bridge is operated with ZVS for,

$$d < 2 \tag{2.43}$$

and for range 2, when,

$$d < \frac{4\pi}{3\pi - 6\delta} \tag{2.44}$$

From (2.40) and (2.43), it can be concluded that, in range 1, the ZVS regions do not depend on the control phase-shift δ, but do depend on the voltage conversion ratio d. In range 2, the ZVS regions are functions of both the control phase-shift δ, and the voltage conversion ratio d. The ZVS regions for the Y-Δ 3p-DAB are given in Figure 2.12. The testing zone for the prototype is also added for information. The results in Figure 2.12 show that it is advantageous from a soft-switching standpoint to operate the 3p-DAB with a voltage conversion ratio d ranging between 1.5 and 2. This is possible in applications where the tolerances on the input and output voltages are small.

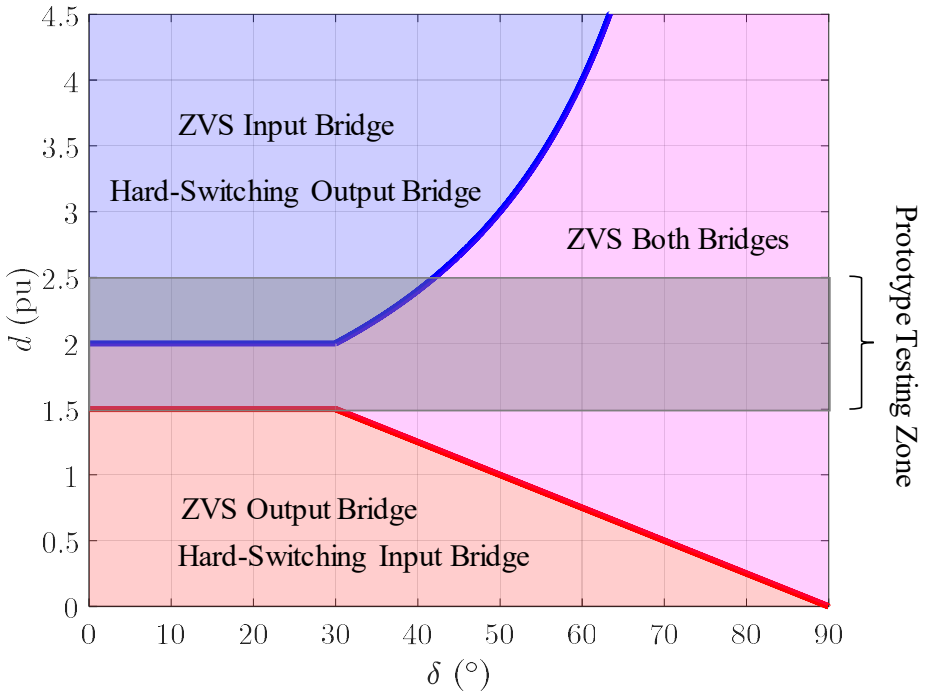

Figure 2.12 : ZVS regions for the Y-Δ 3p-DAB with the prototype (model 4) testing zone

2.2.5 Capacitor ripple current and voltage

In the previous sections, the ripples in the input and output voltages have been neglected, such that the ripples in the input and output currents were also neglected. In forward operation, the calculation of the ripple voltage Δv_{o} and the ripple current Δi_{o} is important for sizing the output filter capacitor C_{o}. The value of C_{o} is often selected based on the maximum ripple voltage $\Delta v_{\mathrm{o}}^{\max}$ specified for a given application. The value of C_{o} also has an important impact on the dynamic performance as well as the stability of the converter such that $\Delta v_{\mathrm{o}}^{\max}$ is not the only selection criterion. The influence of C_{o} on the converter dynamic will be discussed in Chapter 3.

The analysis of the ripple current is performed using the equivalent circuit of Figure 2.13 a). In the equivalent circuit of Figure 2.13 a), the 3p-DAB is modeled as a current source i_{o} defined using the equations for i_{o} provided in Appendix C. From Figure 2.13 b), it must also be noted that the ripples are theoretically at a frequency of $6f_{\mathrm{s}}$. This is an important conclusion which will be used in the formulation of the small- and large-signal models in Chapter 3 and Chapter 4 respectively.

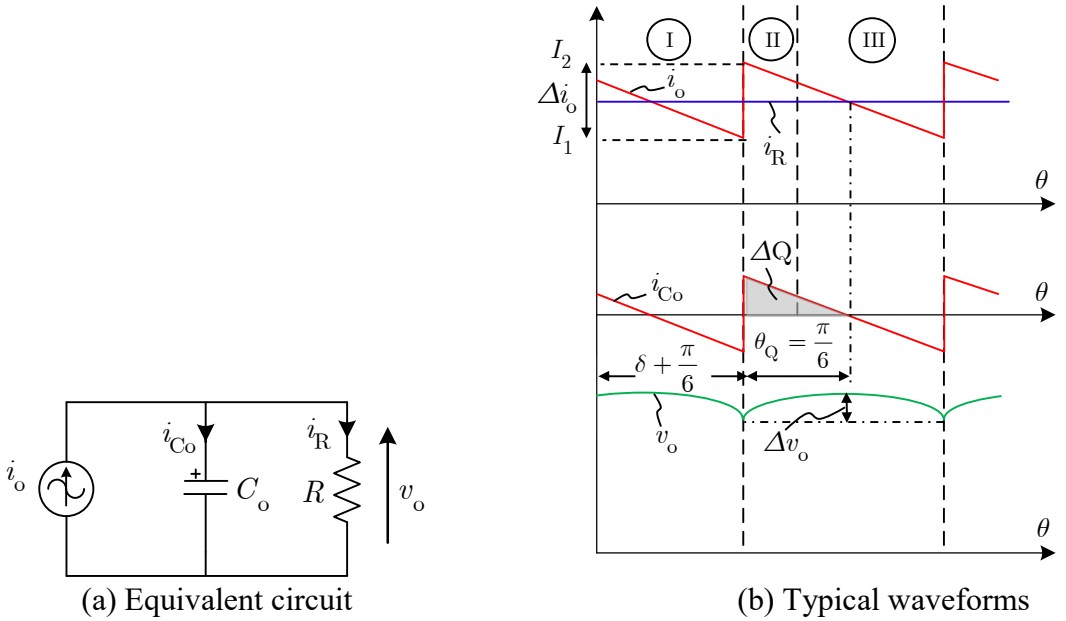

(a) Equivalent circuit (b) Typical waveforms

Figure 2.13 : Calculation of the output voltage and current ripples

The procedure will be presented here for range 1 ($0 \le \delta \le \pi/6$) because it leads to simpler analytical expressions. The procedure consists in first neglecting the ripple voltage Δv_o for the evaluation of the ripple current Δi_o. By analyzing the waveforms of Figure 2.13 b), the ripple current is defined as,

$$\Delta i_o = \left| I_2 - I_1 \right| \tag{2.45}$$

From (C.40), it can be demonstrated that the current I_1 is given by,

$$I_1 = \frac{m}{9\omega_s L_s}\left[\left(9\delta + \frac{3\pi}{2}\right)V_i - 3\pi m V_o\right] \tag{2.46}$$

and, from the application of (C.43), it can be shown that the current I_2 is given by,

$$I_2 = m\left(i_A(\delta+\frac{\pi}{6}) - i_B(\delta+\frac{\pi}{6})\right) \tag{2.47}$$

where $i_A(\delta+\pi/6)$ is obtained using (C.1) and (C.6), and $i_B(\delta+\pi/6)$ is evaluated using (C.7) and (C.12). This leads to,

$$I_2 = \frac{m}{9\omega_s L_s}\left[\left(9\delta - \frac{3\pi}{2}\right)V_i + 3\pi m V_o\right] \tag{2.48}$$

Therefore, inserting (2.46) and (2.48) into (2.45), and simplifying, the ripple current is evaluated,

$$\Delta i_{\mathrm{o}} = \frac{m}{6 f_{\mathrm{s}} L_{\mathrm{s}}} \left| 2m V_{\mathrm{o}} - V_{\mathrm{i}} \right| \tag{2.49}$$

From (2.49), it is concluded that the ripple current Δi_{o} is inversely proportional to the factor $6 f_{\mathrm{s}}$ which corresponds, as mentioned before, to the ripple frequency. This is in fact one of the main advantages of the 3p-DAB over the 1p-DAB since it allows reducing the sizing of the output filter capacitor C_{o}. Increasing the series inductance L_{s} can also reduce the ripple voltage but this is generally not used for this purpose since increasing L_{s} reduces the power transfer capability of the converter as seen in section 2.2.3.

The ripple current Δi_{o} is then used to evaluate the ripple voltage Δv_{o}. It requires analyzing the capacitor current i_{Co} waveform (Figure 2.13 b)). First, it is well known that,

$$\Delta \mathrm{Q} = i_{\mathrm{Co}} \Delta t = C_{\mathrm{o}} \Delta v_{\mathrm{o}} \tag{2.50}$$

where $\Delta \mathrm{Q}$ is the quantity of charge absorbed/released by the capacitor at each interval of duration $\theta_{\mathrm{Q}} = 2\pi f_{\mathrm{s}} T_{\mathrm{Q}} = \pi/6$, as defined in Figure 2.13 b). This represents the area under the curve of i_{Co}, such that, Δv_{o} can be calculated by,

$$\Delta v_{\mathrm{o}} = \frac{\frac{\Delta i_{\mathrm{o}}}{2} \cdot T_{\mathrm{Q}}}{2\mathrm{C}_{\mathrm{o}}} = \frac{\frac{\Delta i_{\mathrm{o}}}{2} \cdot \frac{1}{12 f_{\mathrm{s}}}}{2\mathrm{C}_{\mathrm{o}}} = \frac{\Delta i_{\mathrm{o}}}{48 f_{\mathrm{s}} \mathrm{C}_{\mathrm{o}}} \tag{2.51}$$

Inserting (2.49) into (2.51), it yields that,

$$\Delta v_{\mathrm{o}} = \frac{m}{288 f_{\mathrm{s}}^2 L_{\mathrm{s}} C_{\mathrm{o}}} \cdot \left| 2m V_{\mathrm{o}} - V_{\mathrm{i}} \right| \tag{2.52}$$

Knowing the maximum peak-to-peak ripple voltage specified $\Delta v_{\mathrm{o}}^{\max}$, the output capacitor C_{o} can be calculated as,

$$C_{\mathrm{o}} = \frac{m}{288 f_{\mathrm{s}}^2 L_{\mathrm{s}} \Delta v_{\mathrm{o}}^{\max}} \cdot \left| 2m V_{\mathrm{o}} - V_{\mathrm{i}} \right| \tag{2.53}$$

Equation (2.53) is important since it allows calculating the minimum capacitor value C_{o} required to meet the maximum peak-to-peak ripple voltage specified $\Delta v_{\mathrm{o}}^{\max}$. In practice, $\Delta v_{\mathrm{o}}^{\max}$ is given in percentage of the output voltage V_{o}. A similar analysis can be performed for the 3p-DAB operated in range 2 ($\pi/6 \leq \delta \leq \pi/2$).

The prototype (model 4) is used as a design example to demonstrate the use of the developed set of equations. For instance, for a maximum peak-to-peak ripple voltage specified $\Delta v_{\mathrm{o}}^{\max} = 0.2\%$, the results are shown in Figure 2.14 for $f_{\mathrm{s}} = 50$ kHz and $f_{\mathrm{s}} = 100$ kHz.

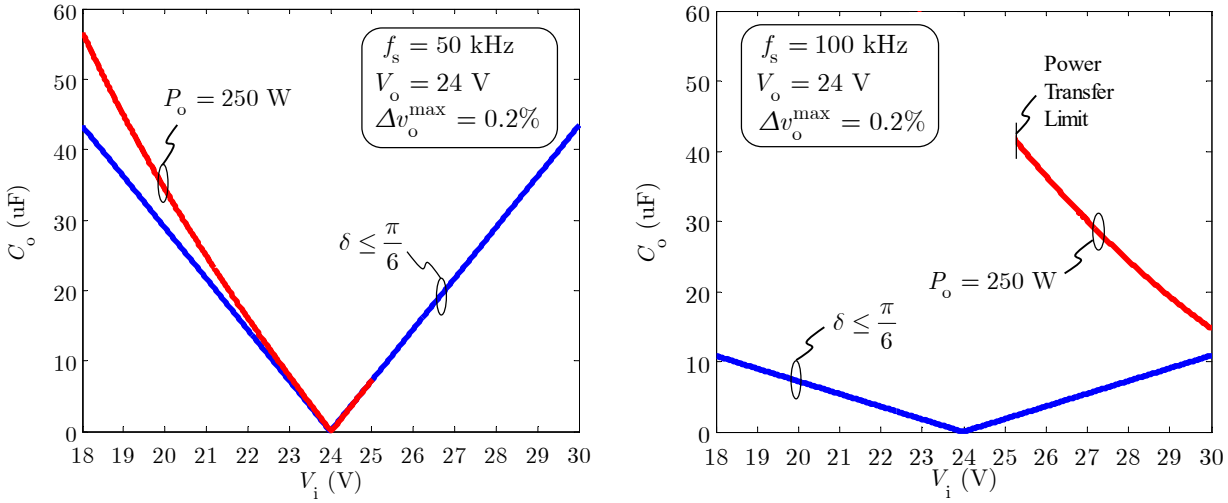

Figure 2.14 : Sizing of the output capacitor for the Y-Δ 3p-DAB prototype (model 4)

CHAPTER 3 SMALL-SIGNAL FREQUENCY-DOMAIN ANALYSIS

In this chapter, small-signal models are developed to determine all the transfer functions of the 3p-DAB converter. It allows designing a suitable controller for closed-loop operation as well as assessing dynamic performance and stability of the 3p-DAB within its environment. This step is particularly important to ensure that the addition of an input filter does not degrade the dynamic performance of the converter, or in worst-case lead to unstable conditions. This step is also a prerequisite for the implementation of the developed large-signal models in Chapter 4 since large-signal system-level analysis requires closed-loop modeling of converters.

3.1 Small-signal model of the 3p-DAB

Converter open-loop small-signal characteristics are generally defined by a set of standard transfer functions: the control-to-output transfer function G_{vd}, the input-to-output transfer function G_{vg}, the driving point Z_{D} and null driving point Z_{N} input impedances, and the output impedance Z_{o} [30]. The equivalent small-signal block diagram for output voltage regulation of the Y-Δ 3p-DAB converter in forward operation is shown in Figure 3.1.

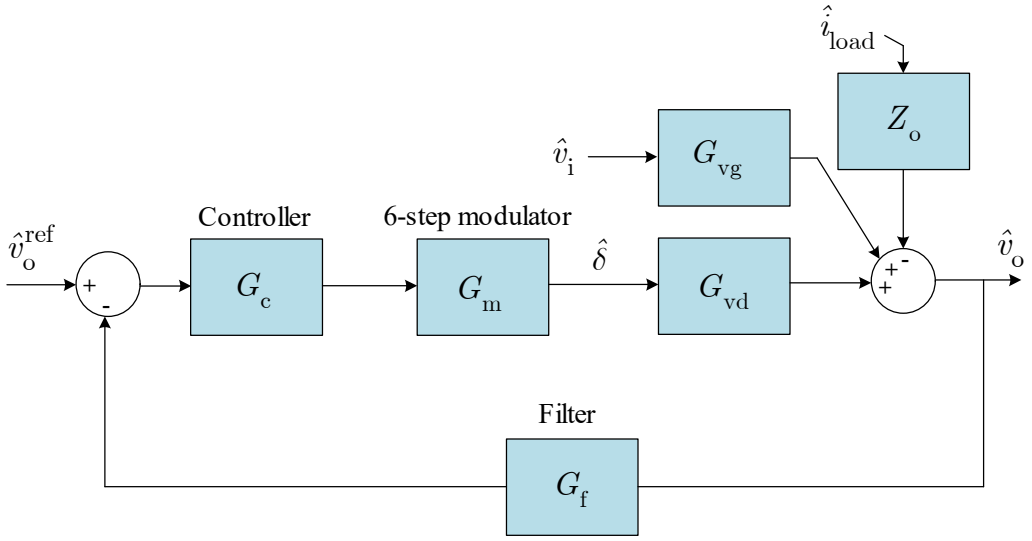

Figure 3.1 : Output voltage regulation small-signal block diagram (forward operation)

For the 3p-DAB, the open-loop transfer functions are defined as follows,

$$G_{\mathrm{vd}}(s) = \left.\frac{\hat{v}_{\mathrm{o}}(s)}{\hat{\delta}(s)}\right|_{\hat{v}_{\mathrm{i}}(s)=0} \tag{3.1}$$

$$G_{\mathrm{vg}}(s)=\left.\frac{\hat{v}_{\mathrm{o}}(s)}{\hat{v}_{\mathrm{i}}(s)}\right|_{\hat{\delta}(s)=0} \tag{3.2}$$

$$Z_{\mathrm{D}}(s)=\left.\frac{\hat{v}_{\mathrm{i}}(s)}{\hat{i}_{\mathrm{i}}(s)}\right|_{\hat{\delta}(s)=0} \tag{3.3}$$

$$Z_{\mathrm{N}}(s)=\left.\frac{\hat{v}_{\mathrm{i}}(s)}{\hat{i}_{\mathrm{i}}(s)}\right|_{\hat{v}_{\mathrm{o}}(s)=0} \tag{3.4}$$

$$Z_{\mathrm{o}}(s)=-\left.\frac{\hat{v}_{\mathrm{o}}(s)}{\hat{i}_{\mathrm{load}}(s)}\right|_{\hat{v}_{\mathrm{i}}(s)=0,\ \hat{\delta}(s)=0} \tag{3.5}$$

In this chapter, the objective is to define each one of these transfer functions such that it allows evaluating the influence of the converter parameters on the small-signal characteristics of the 3p-DAB.

3.2 State-space averaging (SSA)

3.2.1 Model development

The general procedure to derive G_{vd} and G_{vg} for the Y-Y 3p-DAB using SSA has been presented in [54]. It assumes that the transformer currents are changing much faster than the dc voltages in addition to the assumption of balanced operation. This approach is used here to determine G_{vd} and G_{vg} for the Y-Δ 3p-DAB converter. It is also extended to derive Z_{D}, Z_{N}, and Z_{o}.

The idea behind the SSA modeling technique for 3p-DAB converters is to describe the converter behavior by the following dc-averaged and linearized state-space model,

$$\frac{d}{dt}\hat{\mathbf{x}}(t)=\hat{\mathbf{A}}\hat{\mathbf{x}}(t)+\hat{\mathbf{B}}\hat{\mathbf{u}}(t) \tag{3.6}$$

$$\hat{\mathbf{y}}(t)=\hat{\mathbf{C}}\hat{\mathbf{x}}(t)+\hat{\mathbf{D}}\hat{\mathbf{u}}(t) \tag{3.7}$$

where, to obtain all the desired transfer functions, it is proposed here to use more generalized set of vectors of state, inputs and outputs,

$$\hat{\mathbf{x}}(t)=\hat{v}_{\mathrm{o}}(t),\ \ \hat{\mathbf{u}}(t)=\begin{bmatrix}\hat{\delta}(t)\\ \hat{v}_{\mathrm{i}}(t)\end{bmatrix},\ \ \hat{\mathbf{y}}(t)=\begin{bmatrix}\hat{v}_{\mathrm{o}}(t)\\ \hat{i}_{\mathrm{i}}(t)\end{bmatrix} \tag{3.8}$$

The objective is to determine the averaged and linearized state-space matrices in (3.6) and (3.7). For the 3p-DAB, there are two sets of state-space matrices depending on the operating range defined by the phase-shift δ. In both cases, the output capacitor C_{o} voltage equation is first given by,

$$C_{\mathrm{o}} \frac{\mathrm{d}v_{\mathrm{o}}(t)}{\mathrm{d}t} = i_{\mathrm{o}}(t) - \frac{v_{\mathrm{o}}(t)}{R} \tag{3.9}$$

where the output current i_{o} is a function of the transformer currents i_{A}, i_{B} and i_{C} as defined in (2.34). By neglecting the input capacitor C_{i}, the input current i_{i} is also written in terms of the transformer currents i_{A}, i_{B} and i_{C} as defined in (2.33). It is simply written here as,

$$i_{\mathrm{i}}(t) = f\Big(i_{\mathrm{A}}(t), i_{\mathrm{B}}(t), i_{\mathrm{C}}(t)\Big) \tag{3.10}$$

The input i_{i} and output i_{o} currents are then averaged as described in Appendix C. Note that, due to the symmetrical operation of the 3p-DAB, the procedure only needs to be performed for modes I and II. Then, as described in Appendix D, by inserting the average values of i_{o} and i_{i} obtained in Appendix C into (3.9) and (3.10) respectively, it results in the following set of intermediate state-space equations,

$$\frac{\mathrm{d}v_{\mathrm{o}}(t)}{\mathrm{d}t} = \mathbf{A}_{\mathrm{I}} v_{\mathrm{o}}(t) + \mathbf{B}_{\mathrm{I}} v_{\mathrm{i}}(t) \tag{3.11}$$

$$\frac{\mathrm{d}v_{\mathrm{o}}(t)}{\mathrm{d}t} = \mathbf{A}_{\mathrm{II}} v_{\mathrm{o}}(t) + \mathbf{B}_{\mathrm{II}} v_{\mathrm{i}}(t) \tag{3.12}$$

$$i_{\mathrm{i}}(t) = \mathbf{C}_{\mathrm{I}} v_{\mathrm{o}}(t) + \mathbf{D}_{\mathrm{I}} v_{\mathrm{i}}(t) \tag{3.13}$$

$$i_{\mathrm{i}}(t) = \mathbf{C}_{\mathrm{II}} v_{\mathrm{o}}(t) + \mathbf{D}_{\mathrm{II}} v_{\mathrm{i}}(t) \tag{3.14}$$

with the intermediate matrices $\mathbf{A}_{\mathrm{I}}$, $\mathbf{A}_{\mathrm{II}}$, $\mathbf{B}_{\mathrm{I}}$, $\mathbf{B}_{\mathrm{II}}$, $\mathbf{C}_{\mathrm{I}}$, $\mathbf{C}_{\mathrm{II}}$, $\mathbf{D}_{\mathrm{I}}$ and $\mathbf{D}_{\mathrm{II}}$ being given for each range in Appendix D. As shown in Appendix D, the averaged state-space matrices $\mathbf{A}$, $\mathbf{B}$, $\mathbf{C}$ and $\mathbf{D}$ are then obtained by averaging their respective matrices for modes I and II. For range 1, it results in,

$$\frac{\mathrm{d}v_{\mathrm{o}}(t)}{\mathrm{d}t} = \underbrace{\frac{-1}{RC_{\mathrm{o}}}}_{\mathbf{A}} v_{\mathrm{o}}(t) + \underbrace{\left(\frac{m}{\omega_{\mathrm{s}} L_{\mathrm{s}} C_{\mathrm{o}}} \delta(t)\right)}_{\mathbf{B}} v_{\mathrm{i}}(t) \tag{3.15}$$

$$i_{\mathrm{i}}(t)=\underbrace{\frac{m\delta(t)}{\omega_{\mathrm{s}}L_{\mathrm{s}}}}_{\mathbf{C}}v_{\mathrm{o}}(t) \tag{3.16}$$

and for range 2,

$$\frac{\mathrm{d}v_{\mathrm{o}}(t)}{\mathrm{d}t}=\underbrace{\frac{-1}{RC_{\mathrm{o}}}}_{\mathbf{A}}v_{\mathrm{o}}(t)+\underbrace{\left(\frac{m}{\omega_{\mathrm{s}}L_{\mathrm{s}}C_{\mathrm{o}}}\left[\frac{3}{2}\left(\delta(t)-\frac{\delta(t)^2}{\pi}\right)-\frac{\pi}{24}\right]\right)}_{\mathbf{B}}v_{\mathrm{i}}(t) \tag{3.17}$$

$$i_{\mathrm{i}}(t)=\underbrace{\frac{m}{\omega_{\mathrm{s}}L_{\mathrm{s}}}\left[\frac{3}{2}\left(\delta(t)-\frac{\delta^2(t)}{\pi}\right)-\frac{\pi}{24}\right]}_{\mathbf{C}}v_{\mathrm{o}}(t) \tag{3.18}$$

Note that the matrix $\mathbf{D}$ is null in both cases. Taylor's linearization technique is used to linearize the non-linear terms in $\mathbf{B}$ and $\mathbf{C}$. The operating point is calculated using (2.37) and (2.38). Then, changing into a small-signal model with the following perturbations,

$$\begin{aligned}\delta(t)&=\delta+\hat{\delta}(t)\ ,\ v_{\mathrm{i}}(t)=V_{\mathrm{i}}+\hat{v}_{\mathrm{i}}(t)\\ v_{\mathrm{o}}(t)&=V_{\mathrm{o}}+\hat{v}_{\mathrm{o}}(t)\ ,\ i_{\mathrm{i}}(t)=I_{\mathrm{i}}+\hat{i}_{\mathrm{i}}(t)\end{aligned} \tag{3.19}$$

it results in the following small-signal state-space equations. For range 1,

$$\frac{\mathrm{d}\hat{v}_{\mathrm{o}}(t)}{\mathrm{d}t}=\underbrace{\left(\frac{-1}{RC_{\mathrm{o}}}\right)}_{\hat{\mathbf{A}}}\hat{v}_{\mathrm{o}}(t)+\underbrace{\left[\frac{mV_{\mathrm{i}}}{\omega_{\mathrm{s}}L_{\mathrm{s}}C_{\mathrm{o}}}\ \frac{m\delta}{\omega_{\mathrm{s}}L_{\mathrm{s}}C_{\mathrm{o}}}\right]}_{\hat{\mathbf{B}}}\begin{bmatrix}\hat{\delta}(t)\\ \hat{v}_i(t)\end{bmatrix} \tag{3.20}$$

$$\begin{bmatrix}\hat{v}_{\mathrm{o}}(t)\\ \hat{i}_{\mathrm{i}}(t)\end{bmatrix}=\underbrace{\begin{bmatrix}1\\ \frac{m\delta}{\omega_{\mathrm{s}}L_{\mathrm{s}}}\end{bmatrix}}_{\hat{\mathbf{C}}}\hat{v}_{\mathrm{o}}(t)+\underbrace{\begin{bmatrix}0 & 0\\ \frac{mV_{\mathrm{o}}}{\omega_{\mathrm{s}}L_{\mathrm{s}}} & 0\end{bmatrix}}_{\hat{\mathbf{D}}}\begin{bmatrix}\hat{\delta}(t)\\ \hat{v}_{\mathrm{i}}(t)\end{bmatrix} \tag{3.21}$$

and for range 2,

$$\frac{\mathrm{d}\hat{v}_{\mathrm{o}}(t)}{\mathrm{d}t}=\underbrace{\left(\frac{-1}{RC_{\mathrm{o}}}\right)}_{\hat{\mathbf{A}}}\hat{v}_{\mathrm{o}}(t)+\underbrace{\left(\frac{m}{\omega_{\mathrm{s}}L_{\mathrm{s}}C_{\mathrm{o}}}\right)\left[\left[\frac{3}{2}\left(1-\frac{2\delta}{\pi}\right)\right]V_{\mathrm{i}}\quad\left[\frac{3}{2}\left(\delta-\frac{\delta^2}{\pi}\right)-\frac{\pi}{24}\right]\right]}_{\hat{\mathbf{B}}}\begin{bmatrix}\hat{\delta}(t)\\ \hat{v}_i(t)\end{bmatrix} \tag{3.22}$$

$$\begin{bmatrix}\hat{v}_{\mathrm{o}}(t)\\ \hat{i}_{\mathrm{i}}(t)\end{bmatrix}=\underbrace{\begin{bmatrix}1\\ \dfrac{m}{\omega_{\mathrm{s}}L_{\mathrm{s}}}\left[\dfrac{3}{2}\left(\delta-\dfrac{\delta^2}{\pi}\right)-\dfrac{\pi}{24}\right]\end{bmatrix}}_{\hat{\mathbf{C}}}\hat{v}_{\mathrm{o}}(t)+\underbrace{\begin{bmatrix}0 & 0\\ \dfrac{mV_{\mathrm{o}}}{\omega_{\mathrm{s}}L_{\mathrm{s}}}\left[\dfrac{3}{2}\left(1-\dfrac{2\delta}{\pi}\right)\right] & 0\end{bmatrix}}_{\hat{\mathbf{D}}}\begin{bmatrix}\hat{\delta}(t)\\ \hat{v}_{\mathrm{i}}(t)\end{bmatrix} \tag{3.23}$$

3.2.2 Derivation of the converter transfer functions

The SSA model allows drawing equivalent small-signal circuits for the 3p-DAB in an analogous way to simpler topologies. By transferring (3.20)–(3.23) into the frequency-domain, two equivalent circuits are defined in Figure 3.2. These equivalent circuits are then used to derive the converter transfer functions G_{vd}, G_{vg}, Z_{D}, Z_{N} and Z_{o}. The resulting transfer functions are given in Table 3.1. Furthermore, by posing that $\hat{v}_{\mathrm{o}}(s)\rightarrow 0$ in the equivalent circuits of Figure 3.2, the perturbation $\hat{\delta}(s)$ that needs to be injected for the evaluation of Z_{N} can be defined as follows. For range 1, it results in,

$$G_{\delta\mathrm{i}}(s)=\left.\frac{\hat{\delta}(s)}{\hat{v}_{\mathrm{i}}(s)}\right|_{\hat{v}_{\mathrm{o}}(s)=0}=-\frac{\delta}{V_{\mathrm{i}}} \tag{3.24}$$

and for range 2, it leads to,

$$G_{\delta\mathrm{i}}(s)=\left.\frac{\hat{\delta}(s)}{\hat{v}_{\mathrm{i}}(s)}\right|_{\hat{v}_{\mathrm{o}}(s)=0}=-\frac{\dfrac{3}{2}\left(\delta-\dfrac{\delta^2}{\pi}\right)-\dfrac{\pi}{24}}{\left[\dfrac{3}{2}\left(1-\dfrac{2\delta}{\pi}\right)\right]V_{\mathrm{i}}} \tag{3.25}$$

Equations (3.24) and (3.25) will be used in section 3.4 for the application of the proposed hybrid averaging methodology. However, an important remark here is that the required perturbation $\hat{\delta}(s)$ on the command must be 180° phase-shifted from the injected perturbation $\hat{v}_{\mathrm{i}}$ on the input voltage in order to have $\hat{v}_{\mathrm{o}}(s)\rightarrow 0$.

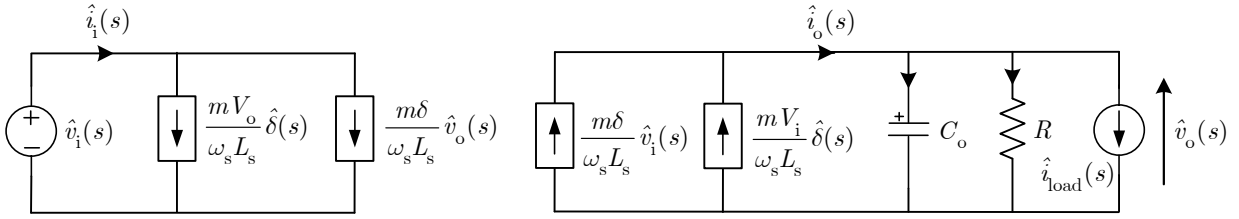

(a) For range 1

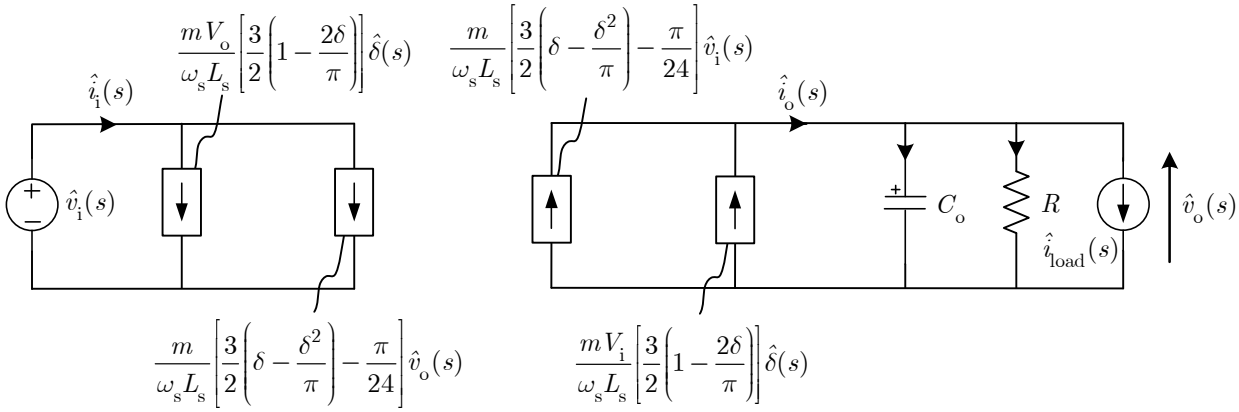

(b) For range 2

Figure 3.2 : Equivalent SSA small-signal circuits of the Y-Δ 3p-DAB converter

Table 3.1: Transfer functions of the Y-Δ 3p-DAB converter obtained with SSA

Range 1 ($0 \le \delta \le \pi/6$)	Range 2 ($\pi/6 \le \delta \le \pi/2$)
$G_{\mathrm{vd}}(s)=\left(\frac{mRV_{\mathrm{i}}}{\omega_{\mathrm{s}}L_{\mathrm{s}}}\right)\frac{1}{sRC_{\mathrm{o}}+1}$ (3.26)	$G_{\mathrm{vd}}(s)=\left(\frac{mRV_{\mathrm{i}}}{\omega_{\mathrm{s}}L_{\mathrm{s}}}\left[\frac{3}{2}\left(1-\frac{2\delta}{\pi}\right)\right]\right)\frac{1}{sRC_{\mathrm{o}}+1}$ (3.27)
$G_{\mathrm{vg}}(s)=\left(\frac{mR\delta}{\omega_{\mathrm{s}}L_{\mathrm{s}}}\right)\frac{1}{sRC_{\mathrm{o}}+1}$ (3.28)	$G_{\mathrm{vg}}(s)=\left(\frac{mR}{\omega_{\mathrm{s}}L_{\mathrm{s}}}\left[\frac{3}{2}\left(\delta-\frac{\delta^2}{\pi}\right)-\frac{\pi}{24}\right]\right)\frac{1}{sRC_{\mathrm{o}}+1}$ (3.29)
$Z_{\mathrm{D}}(s)=\left(\frac{\omega_{\mathrm{s}}L_{\mathrm{s}}}{m\delta}\right)^2\frac{sRC_{\mathrm{o}}+1}{R}$ (3.30)	$Z_{\mathrm{D}}(s)=\frac{sRC_{\mathrm{o}}+1}{R\left(\frac{m}{\omega_{\mathrm{s}}L_{\mathrm{s}}}\left[\frac{3}{2}\left(\delta-\frac{\delta^2}{\pi}\right)-\frac{\pi}{24}\right]\right)^2}$ (3.31)
$Z_{\mathrm{N}}(s)=-\frac{\omega_{\mathrm{s}}L_{\mathrm{s}}V_{\mathrm{i}}}{mV_{\mathrm{o}}\delta}$ (3.32)	$Z_{\mathrm{N}}(s)=-\left(\frac{\omega_{\mathrm{s}}L_{\mathrm{s}}V_{\mathrm{i}}}{mV_{\mathrm{o}}}\right)\frac{1}{\left[\frac{3}{2}\left(\delta-\frac{\delta^2}{\pi}\right)-\frac{\pi}{24}\right]}$ (3.33)
$Z_{\mathrm{o}}(s)=-\frac{R}{sRC_{\mathrm{o}}+1}$ (3.34)	

3.3 Generalized state-space averaging (GSSA)

3.3.1 Model development

The generalized state-space averaging (GSSA) [56] methodology is widely used for the small-signal analysis of dc-dc converters. It is based on the concept of dynamic phasors which is well known for the analysis of power electronic converters and electric machines in power systems [76]–[80]. The concept of GSSA is to expand the converter state-variables and its switching-functions using a k^{th} coefficient Fourier series decomposition. The general procedure consists in 1) writing the converter differential equations using the state-space representation and the definition of the switching-functions, 2) deriving the index-k^{th} state-space equations by averaging the switching-functions and the state-space equations using Fourier series properties [53], [56], and 3) deriving the small-signal model by linearizing the equations around the operating point. Unlike SSA, it results in a single model that does not depend on the phase-shift δ operating range. The transformer connection is considered through the definition of the switching-functions, the calculation of the winding ratio, and the definition of the input and output currents.

3.3.1.1 Converter differential equations using state-space representation and the definition of the switching-functions

For the 3p-DAB, the output capacitor voltage v_{o} and the transformer primary currents i_{A}, i_{B}, and i_{C} are taken here as state-variables. Unlike SSA which is only valid for the balanced case, GSSA is valid for the unbalanced case, i.e. that L_{A}, L_{B} and L_{C} are not necessarily identical. First, inserting (2.34) into (3.9), the output capacitor voltage equation is obtained,

$$\frac{\mathrm{d}v_{\text{o}}}{\mathrm{d}t} = \frac{m}{C_{\text{o}}}\left[(\mathrm{s}_1^{'} - \mathrm{s}_3^{'})i_{\text{A}} + (\mathrm{s}_3^{'} - \mathrm{s}_5^{'})i_{\text{B}} + (\mathrm{s}_5^{'} - \mathrm{s}_1^{'})i_{\text{C}}\right] - \frac{v_{\text{o}}}{RC_{\text{o}}} \tag{3.35}$$

Then, the differential equations for the three-phase currents are derived. For example, for phase A, the current flowing through inductor L_{A} is expressed as,

$$L_{\text{A}}\frac{\mathrm{d}i_{\text{A}}}{\mathrm{d}t} = v_{\text{AN}} - v_{\text{ab}}^{'} \tag{3.36}$$

with v_{AN} being dependent on the input bridge switching-functions as defined in (2.27) and $v_{\text{ab}}^{'}$ being dependent on the output bridge switching-functions as defined in (2.30). It yields to,

$$\frac{\mathrm{d}i_{\mathrm{A}}}{\mathrm{d}t}=\frac{1}{3L_{\mathrm{A}}}\left[\left(2\mathrm{s}_1-\mathrm{s}_3-\mathrm{s}_5\right)v_{\mathrm{i}}-3m\left(\mathrm{s}_1^{'}-\mathrm{s}_3^{'}\right)v_{\mathrm{o}}\right] \tag{3.37}$$

Similarly, for phases B and C, it results in,

$$\frac{\mathrm{d}i_{\mathrm{B}}}{\mathrm{d}t}=\frac{1}{3L_{\mathrm{B}}}\left[\left(2\mathrm{s}_3-\mathrm{s}_1-\mathrm{s}_5\right)v_{\mathrm{i}}-3m\left(\mathrm{s}_3^{'}-\mathrm{s}_5^{'}\right)v_{\mathrm{o}}\right] \tag{3.38}$$

$$\frac{\mathrm{d}i_{\mathrm{C}}}{\mathrm{d}t}=\frac{1}{3L_{\mathrm{C}}}\left[\left(2\mathrm{s}_5-\mathrm{s}_1-\mathrm{s}_3\right)v_{\mathrm{i}}-3m\left(\mathrm{s}_5^{'}-\mathrm{s}_1^{'}\right)v_{\mathrm{o}}\right] \tag{3.39}$$

Finally, it is also convenient to add the input current i_{i} equation given in (2.33) in the GSSA model formulation.

3.3.1.2 Deriving the index k[th] state-space equations by averaging the switching-functions and the state-space equations using Fourier series properties.

As previously mentioned, the main idea behind GSSA is to expand the converter state-variables and its switching-functions using a k^{th} coefficient Fourier series decomposition. It is assumed that only a few Fourier coefficients $X_{\mathrm{k}}(t)$ provides an acceptable approximation of the original waveform, and that the coefficients vary slowly with time [33]. The k^{th} coefficients (or index-k phasors) of the generic variable x at time t are determined by the application of the Fourier series definition to continuous-time periodic signals with a sliding averaging window defined by the interval $\left[t-T_{\mathrm{s}},T_{\mathrm{s}}\right]$. It results in the following definition,

$$X_{\mathrm{k}}(t)=\left\langle x\right\rangle_{\mathrm{k}}(t)=\frac{1}{T_{\mathrm{s}}}\int_{t-T_{\mathrm{s}}}^{t}x(\tau)\cdot e^{-jk\omega_{\mathrm{s}}\tau}d\tau \tag{3.40}$$

with $\left\langle x\right\rangle_{\mathrm{k}}(t)$ being the complex Fourier coefficients which are functions of time t since the interval under consideration slides with respect to time. It results in a dynamic model of the dominant Fourier series coefficients in which the coefficients $\left\langle x\right\rangle_{\mathrm{k}}(t)$ are the state-variables. The index $k=0$ component is the dc-component and is expressed as $\left\langle x\right\rangle_0$. The other coefficients are the dynamic phasors $\left\langle x\right\rangle_{\mathrm{k}}$ (for $k\neq 0$) and are complex values which are expressed as follows,

$$\left\langle x\right\rangle_{\mathrm{k}}=\left\langle x\right\rangle_{\mathrm{k}}^{\mathrm{R}}+j\left\langle x\right\rangle_{\mathrm{k}}^{\mathrm{I}}=\left\langle x\right\rangle_{\text{-k}}^{*} \tag{3.41}$$

with $\left\langle x\right\rangle_{\mathrm{k}}$, $\left\langle x\right\rangle_{\mathrm{k}}^{\mathrm{R}}$ and $\left\langle x\right\rangle_{\mathrm{k}}^{\mathrm{I}}$ being all functions of time and $\left\langle x\right\rangle_{\text{-k}}^{*}$ being the complex conjugate of $\left\langle x\right\rangle_{\mathrm{k}}$. Similarly, the converter switching-functions are also expanded. For the generic switching-

function $q(t)$, the index $k=0$ component is expressed as $\langle q \rangle_0$, and the dynamic phasors $\langle q \rangle_k$ (for $k \neq 0$) are also complex values which are expressed as follows,

$$\langle q \rangle_k = \langle q \rangle_k^R + j \langle q \rangle_k^I = \langle q \rangle_{-k}^* \tag{3.42}$$

If only the index $k=0$ and $k=\pm 1$ terms are considered, the resulting Fourier series decomposition for the generic variable x and the generic switching-function q are given by,

$$x(t) \approx \langle x \rangle_0 + \langle x \rangle_{-1} e^{-j\omega_s t} + \langle x \rangle_1 e^{j\omega_s t} \tag{3.43}$$

$$q(t) \approx \langle q \rangle_0 + \langle q \rangle_{-1} e^{-j\omega_s t} + \langle q \rangle_1 e^{j\omega_s t} \tag{3.44}$$

To average the converter differential equations using the Fourier series decomposition, two important Fourier series properties are used [56].

Property 1 – *Differentiation with respect to time*

This property is formulated as follows,

$$\frac{d\langle x \rangle_k(t)}{dt} = \langle dx/dt \rangle_k(t) - jk\omega_s \langle x \rangle_k(t) \tag{3.45}$$

where $\langle dx/dt \rangle_k(t)$ represents the average of the differential of the state-variable x in the converter differential equations.

Property 2 – *Average of product*

This property is formulated as follows,

$$\langle qx \rangle_k = \sum_{i=-\infty}^{+\infty} \langle q \rangle_{k-i} \langle x \rangle_{k-i} \tag{3.46}$$

For $k=0$, it results in,

$$\langle qx \rangle_0 = \langle q \rangle_0 \langle x \rangle_0 + 2\left(\langle x \rangle_1^R \langle q \rangle_1^R + \langle x \rangle_1^I \langle q \rangle_1^I \right) \tag{3.47}$$

and, for $k=1$, it results in,

$$\langle qx \rangle_1^R = \langle q \rangle_0 \langle x \rangle_1^R + \langle x \rangle_0 \langle q \rangle_1^R \tag{3.48}$$

$$\left\langle qx \right\rangle_1^{\mathrm{I}} = \left\langle q \right\rangle_0 \left\langle x \right\rangle_1^{\mathrm{I}} + \left\langle x \right\rangle_0 \left\langle q \right\rangle_1^{\mathrm{I}} \tag{3.49}$$

In the case of the 3p-DAB converter, the index $k = \pm 1$ terms of v_{i} and v_{o} are neglected here because it is assumed that the dynamic of v_{i} and v_{o} is much slower than the dynamic of the transformer currents. Mathematically, it means that,

$$\left\langle v_{\mathrm{i}} \right\rangle_1^{\mathrm{R}} = \left\langle v_{\mathrm{i}} \right\rangle_1^{\mathrm{I}} = \left\langle v_{\mathrm{o}} \right\rangle_1^{\mathrm{R}} = \left\langle v_{\mathrm{o}} \right\rangle_1^{\mathrm{I}} = 0 \tag{3.50}$$

The model only includes the index $k = 0$ terms of i_{i}, v_{i} and v_{o} such that,

$$v_{\mathrm{i}} = \left\langle v_{\mathrm{i}} \right\rangle_0, \; i_{\mathrm{i}} = \left\langle i_{\mathrm{i}} \right\rangle_0, \; v_{\mathrm{o}} = \left\langle v_{\mathrm{o}} \right\rangle_0 \tag{3.51}$$

Moreover, the transformer currents are assumed to be purely ac, such that the model considers that the dc-components of i_{A}, i_{B} and i_{C} are zero,

$$\left\langle i_{\mathrm{A}} \right\rangle_0 = \left\langle i_{\mathrm{B}} \right\rangle_0 = \left\langle i_{\mathrm{C}} \right\rangle_0 = 0 \tag{3.52}$$

Since the three-phase structure leads to a ripple voltage at $k = 6$, which, by design, should be adequately filtered by C_{o} as discussed in section 2.2.5, harmonics at $k > 1$ are neglected such that only the index $k = \pm 1$ terms (fundamental dynamic phasors) of i_{A}, i_{B} and i_{C} are considered here,

$$\begin{aligned}
i_{\mathrm{A}} &= \left\langle i_{\mathrm{A}} \right\rangle_1 = \left\langle i_{\mathrm{A}} \right\rangle_1^{\mathrm{R}} + j \left\langle i_{\mathrm{A}} \right\rangle_1^{\mathrm{I}} = \left\langle i_{\mathrm{A}} \right\rangle_{-1}^{*} \\
i_{\mathrm{B}} &= \left\langle i_{\mathrm{B}} \right\rangle_1 = \left\langle i_{\mathrm{B}} \right\rangle_1^{\mathrm{R}} + j \left\langle i_{\mathrm{B}} \right\rangle_1^{\mathrm{I}} = \left\langle i_{\mathrm{B}} \right\rangle_{-1}^{*} \\
i_{\mathrm{C}} &= \left\langle i_{\mathrm{C}} \right\rangle_1 = \left\langle i_{\mathrm{C}} \right\rangle_1^{\mathrm{R}} + j \left\langle i_{\mathrm{C}} \right\rangle_1^{\mathrm{I}} = \left\langle i_{\mathrm{C}} \right\rangle_{-1}^{*}
\end{aligned} \tag{3.53}$$

Furthermore, for the input bridge, the index $k = 0$ component of the switching-function $\mathrm{s_x}$ is expressed as $\left\langle \mathrm{s_x} \right\rangle_0$, and the $k = \pm 1$ terms of $\mathrm{s_x}$ are expressed as follows,

$$\left\langle \mathrm{s_x} \right\rangle_1 = \left\langle \mathrm{s_x} \right\rangle_1^{\mathrm{R}} + j \left\langle \mathrm{s_x} \right\rangle_1^{\mathrm{I}} = \left\langle \mathrm{s_x} \right\rangle_{-1}^{*} \tag{3.54}$$

with x = 1, 3, or 5 as defined in Appendix C.

Similarly, for the output bridge, the index $k = 0$ component of the switching-function $\mathrm{s}_{\mathrm{x}}^{'}$ is expressed as $\left\langle \mathrm{s}_{\mathrm{x}}^{'} \right\rangle_0$, and the $k = \pm 1$ terms of $\mathrm{s}_{\mathrm{x}}^{'}$ are expressed as follows,

$$\left\langle \mathrm{s}_{\mathrm{x}}^{'} \right\rangle_1 = \left\langle \mathrm{s}_{\mathrm{x}}^{'} \right\rangle_1^{\mathrm{R}} + j\left\langle \mathrm{s}_{\mathrm{x}}^{'} \right\rangle_1^{\mathrm{I}} = \left\langle \mathrm{s}_{\mathrm{x}}^{'} \right\rangle_{-1}^{*} \tag{3.55}$$

By taking the average on both sides of (3.35) and (2.33), and using property 1 (*differentiation with respect to time*), the index-0 averaged model equations are obtained,

$$\frac{\mathrm{d}\left\langle v_{\mathrm{o}} \right\rangle_0}{\mathrm{d}t} = \frac{m}{C_{\mathrm{o}}}\left[\left\langle \mathrm{s}_1^{'} i_{\mathrm{A}} \right\rangle_0 - \left\langle \mathrm{s}_3^{'} i_{\mathrm{A}} \right\rangle_0 + \left\langle \mathrm{s}_3^{'} i_{\mathrm{B}} \right\rangle_0 - \left\langle \mathrm{s}_5^{'} i_{\mathrm{B}} \right\rangle_0 + \left\langle \mathrm{s}_5^{'} i_{\mathrm{C}} \right\rangle_0 - \left\langle \mathrm{s}_1^{'} i_{\mathrm{C}} \right\rangle_0\right] - \frac{\left\langle v_{\mathrm{o}} \right\rangle_0}{RC_{\mathrm{o}}} \tag{3.56}$$

$$\left\langle i_{\mathrm{i}} \right\rangle_0 = \left\langle \mathrm{s}_1 i_{\mathrm{A}} \right\rangle_0 + \left\langle \mathrm{s}_3 i_{\mathrm{B}} \right\rangle_0 + \left\langle \mathrm{s}_5 i_{\mathrm{C}} \right\rangle_0 \tag{3.57}$$

Similarly, by taking the average on both sides of (3.37)–(3.39), and using property 1 (*differentiation with respect to time*), the index-1 averaged model equations are derived,

$$\frac{\mathrm{d}\left\langle i_{\mathrm{A}} \right\rangle_1}{\mathrm{d}t} = \frac{1}{3L_{\mathrm{A}}}\left[2\left\langle \mathrm{s}_1 v_{\mathrm{i}} \right\rangle_1 - \left\langle \mathrm{s}_3 v_{\mathrm{i}} \right\rangle_1 - \left\langle \mathrm{s}_5 v_{\mathrm{i}} \right\rangle_1 - 3m\left(\left\langle \mathrm{s}_1^{'} v_{\mathrm{o}} \right\rangle_1 - \left\langle \mathrm{s}_3^{'} v_{\mathrm{o}} \right\rangle_1\right)\right] - j\omega_{\mathrm{s}}\left\langle i_{\mathrm{A}} \right\rangle_1 \tag{3.58}$$

$$\frac{\mathrm{d}\left\langle i_{\mathrm{B}} \right\rangle_1}{\mathrm{d}t} = \frac{1}{3L_{\mathrm{B}}}\left[2\left\langle \mathrm{s}_3 v_{\mathrm{i}} \right\rangle_1 - \left\langle \mathrm{s}_1 v_{\mathrm{i}} \right\rangle_1 - \left\langle \mathrm{s}_5 v_{\mathrm{i}} \right\rangle_1 - 3m\left(\left\langle \mathrm{s}_3^{'} v_{\mathrm{o}} \right\rangle_1 - \left\langle \mathrm{s}_5^{'} v_{\mathrm{o}} \right\rangle_1\right)\right] - j\omega_{\mathrm{s}}\left\langle i_{\mathrm{B}} \right\rangle_1 \tag{3.59}$$

$$\frac{\mathrm{d}\left\langle i_{\mathrm{C}} \right\rangle_1}{\mathrm{d}t} = \frac{1}{3L_{\mathrm{C}}}\left[2\left\langle \mathrm{s}_5 v_{\mathrm{i}} \right\rangle_1 - \left\langle \mathrm{s}_1 v_{\mathrm{i}} \right\rangle_1 - \left\langle \mathrm{s}_3 v_{\mathrm{i}} \right\rangle_1 - 3m\left(\left\langle \mathrm{s}_5^{'} v_{\mathrm{o}} \right\rangle_1 - \left\langle \mathrm{s}_1^{'} v_{\mathrm{o}} \right\rangle_1\right)\right] - j\omega_{\mathrm{s}}\left\langle i_{\mathrm{C}} \right\rangle_1 \tag{3.60}$$

Applying property 2 (*average of product*) to (3.56)–(3.60) and writing the system of equations using the state-space formulation, it leads to the following GSSA model,

$$\frac{d\left\langle \mathbf{x}(t) \right\rangle}{dt} = \mathbf{A}\left\langle \mathbf{x}(t) \right\rangle + \mathbf{B}\left\langle \mathbf{u}(t) \right\rangle \tag{3.61}$$

$$\left\langle \mathbf{y}(t) \right\rangle = \mathbf{C}\left\langle \mathbf{x}(t) \right\rangle + \mathbf{D}\left\langle \mathbf{u}(t) \right\rangle \tag{3.62}$$

with,

$$\left\langle \mathbf{x}(t) \right\rangle = \left[\left\langle v_{\mathrm{o}} \right\rangle_0 \left\langle i_{\mathrm{A}} \right\rangle_1^{\mathrm{R}} \left\langle i_{\mathrm{A}} \right\rangle_1^{\mathrm{I}} \left\langle i_{\mathrm{B}} \right\rangle_1^{\mathrm{R}} \left\langle i_{\mathrm{B}} \right\rangle_1^{\mathrm{I}} \left\langle i_{\mathrm{C}} \right\rangle_1^{\mathrm{R}} \left\langle i_{\mathrm{C}} \right\rangle_1^{\mathrm{I}}\right]^T \tag{3.63}$$

$$\left\langle \mathbf{y}(t) \right\rangle = \left[\left\langle v_{\mathrm{o}} \right\rangle_0 \left\langle i_{\mathrm{i}} \right\rangle_0\right]^{\mathrm{T}}, \left\langle \mathbf{u}(t) \right\rangle = \left[\left\langle \delta \right\rangle_0 \left\langle v_{\mathrm{i}} \right\rangle_0\right]^{\mathrm{T}} \tag{3.64}$$

and,

$$\mathbf{A}=\begin{bmatrix} \dfrac{-1}{RC_{\mathrm{o}}} & \dfrac{2m}{C_{\mathrm{o}}}\left\langle S_{13}^{'}\right\rangle_1^{\mathrm{R}} & \dfrac{2m}{C_{\mathrm{o}}}\left\langle S_{13}^{'}\right\rangle_1^{\mathrm{I}} & \dfrac{2m}{C_{\mathrm{o}}}\left\langle S_{35}^{'}\right\rangle_1^{\mathrm{R}} & \dfrac{2m}{C_{\mathrm{o}}}\left\langle S_{35}^{'}\right\rangle_1^{\mathrm{I}} & \dfrac{2m}{C_{\mathrm{o}}}\left\langle S_{51}^{'}\right\rangle_1^{\mathrm{R}} & \dfrac{2m}{C_{\mathrm{o}}}\left\langle S_{51}^{'}\right\rangle_1^{\mathrm{I}} \\ -\dfrac{m}{L_{\mathrm{A}}}\left\langle S_{13}^{'}\right\rangle_1^{\mathrm{R}} & 0 & \omega_{\mathrm{s}} & 0 & 0 & 0 & 0 \\ -\dfrac{m}{L_{\mathrm{A}}}\left\langle S_{13}^{'}\right\rangle_1^{\mathrm{I}} & -\omega_{\mathrm{s}} & 0 & 0 & 0 & 0 & 0 \\ -\dfrac{m}{L_{\mathrm{B}}}\left\langle S_{35}^{'}\right\rangle_1^{\mathrm{R}} & 0 & 0 & 0 & \omega_{\mathrm{s}} & 0 & 0 \\ -\dfrac{m}{L_{\mathrm{B}}}\left\langle S_{35}^{'}\right\rangle_1^{\mathrm{I}} & 0 & 0 & -\omega_{\mathrm{s}} & 0 & 0 & 0 \\ -\dfrac{m}{L_{\mathrm{C}}}\left\langle S_{51}^{'}\right\rangle_1^{\mathrm{R}} & 0 & 0 & 0 & 0 & 0 & \omega_{\mathrm{s}} \\ -\dfrac{m}{L_{\mathrm{C}}}\left\langle S_{51}^{'}\right\rangle_1^{\mathrm{I}} & 0 & 0 & 0 & 0 & -\omega_{\mathrm{s}} & 0 \end{bmatrix} \tag{3.65}$$

$$\begin{aligned} \left\langle S_{13}^{'}\right\rangle_1^{\mathrm{R}} &= \left\langle \mathrm{s}_1^{'}\right\rangle_1^{\mathrm{R}} - \left\langle \mathrm{s}_3^{'}\right\rangle_1^{\mathrm{R}},\ \left\langle S_{13}^{'}\right\rangle_1^{\mathrm{I}} = \left\langle \mathrm{s}_1^{'}\right\rangle_1^{\mathrm{I}} - \left\langle \mathrm{s}_3^{'}\right\rangle_1^{\mathrm{I}} \\ \left\langle S_{35}^{'}\right\rangle_1^{\mathrm{R}} &= \left\langle \mathrm{s}_3^{'}\right\rangle_1^{\mathrm{R}} - \left\langle \mathrm{s}_5^{'}\right\rangle_1^{\mathrm{R}},\ \left\langle S_{35}^{'}\right\rangle_1^{\mathrm{I}} = \left\langle \mathrm{s}_3^{'}\right\rangle_1^{\mathrm{I}} - \left\langle \mathrm{s}_5^{'}\right\rangle_1^{\mathrm{I}} \\ \left\langle S_{51}^{'}\right\rangle_1^{\mathrm{R}} &= \left\langle \mathrm{s}_5^{'}\right\rangle_1^{\mathrm{R}} - \left\langle \mathrm{s}_1^{'}\right\rangle_1^{\mathrm{R}},\ \left\langle S_{51}^{'}\right\rangle_1^{\mathrm{I}} = \left\langle \mathrm{s}_5^{'}\right\rangle_1^{\mathrm{I}} - \left\langle \mathrm{s}_1^{'}\right\rangle_1^{\mathrm{I}} \end{aligned} \tag{3.66}$$

$$\mathbf{B}=\begin{bmatrix} 0 & 0 \\ 0 & \dfrac{1}{3L_{\mathrm{A}}}\left[2\left\langle \mathrm{s}_1\right\rangle_1^{\mathrm{R}} - \left\langle \mathrm{s}_3\right\rangle_1^{\mathrm{R}} - \left\langle \mathrm{s}_5\right\rangle_1^{\mathrm{R}}\right] \\ 0 & \dfrac{1}{3L_{\mathrm{A}}}\left[2\left\langle \mathrm{s}_1\right\rangle_1^{\mathrm{I}} - \left\langle \mathrm{s}_3\right\rangle_1^{\mathrm{I}} - \left\langle \mathrm{s}_5\right\rangle_1^{\mathrm{I}}\right] \\ 0 & \dfrac{1}{3L_{\mathrm{B}}}\left[2\left\langle \mathrm{s}_3\right\rangle_1^{\mathrm{R}} - \left\langle \mathrm{s}_1\right\rangle_1^{\mathrm{R}} - \left\langle \mathrm{s}_5\right\rangle_1^{\mathrm{R}}\right] \\ 0 & \dfrac{1}{3L_{\mathrm{B}}}\left[2\left\langle \mathrm{s}_3\right\rangle_1^{\mathrm{I}} - \left\langle \mathrm{s}_1\right\rangle_1^{\mathrm{I}} - \left\langle \mathrm{s}_5\right\rangle_1^{\mathrm{I}}\right] \\ 0 & \dfrac{1}{3L_{\mathrm{C}}}\left[2\left\langle \mathrm{s}_5\right\rangle_1^{\mathrm{R}} - \left\langle \mathrm{s}_1\right\rangle_1^{\mathrm{R}} - \left\langle \mathrm{s}_3\right\rangle_1^{\mathrm{R}}\right] \\ 0 & \dfrac{1}{3L_{\mathrm{C}}}\left[2\left\langle \mathrm{s}_5\right\rangle_1^{\mathrm{I}} - \left\langle \mathrm{s}_1\right\rangle_1^{\mathrm{I}} - \left\langle \mathrm{s}_3\right\rangle_1^{\mathrm{I}}\right] \end{bmatrix} \tag{3.67}$$

$$\mathbf{C}=\begin{bmatrix} 1 & 0 & 0 & 0 & 0 & 0 & 0 \\ 0 & 2\left\langle \mathrm{s}_1\right\rangle_1^{\mathrm{R}} & 2\left\langle \mathrm{s}_1\right\rangle_1^{\mathrm{I}} & 2\left\langle \mathrm{s}_3\right\rangle_1^{\mathrm{R}} & 2\left\langle \mathrm{s}_3\right\rangle_1^{\mathrm{I}} & 2\left\langle \mathrm{s}_5\right\rangle_1^{\mathrm{R}} & 2\left\langle \mathrm{s}_5\right\rangle_1^{\mathrm{I}} \end{bmatrix} \tag{3.68}$$

$$\mathbf{D}=\begin{bmatrix} 0 & 0 \\ 0 & 0 \end{bmatrix} \tag{3.69}$$

To solve (3.61)–(3.69), the index $k = 1$ average of the input and output bridge switching-functions must be derived. From (3.40), it can be written that [53],

$$\left\langle \mathrm{s_x} \right\rangle_1 (t) = \frac{1}{T_\mathrm{s}} \int_{t-T_\mathrm{s}}^{t} \mathrm{s_x}(\tau) \cdot \cos(\omega_\mathrm{s}\tau)\, d\tau - j\frac{1}{T_\mathrm{s}} \int_{t-T_\mathrm{s}}^{t} \mathrm{s_x}(\tau) \cdot \sin(\omega_\mathrm{s}\tau)\, d\tau \tag{3.70}$$

$$\left\langle \mathrm{s_x'} \right\rangle_1 (t) = \frac{1}{T_\mathrm{s}} \int_{t-T_\mathrm{s}}^{t} \mathrm{s_x'}(\tau) \cdot \cos(\omega_\mathrm{s}\tau)\, d\tau - j\frac{1}{T_\mathrm{s}} \int_{t-T_\mathrm{s}}^{t} \mathrm{s_x'}(\tau) \cdot \sin(\omega_\mathrm{s}\tau)\, d\tau \tag{3.71}$$

with x = 1, 3, or 5 as defined in Appendix C. For phase A, the switching-functions $\mathrm{s}_1(\tau)$ and $\mathrm{s}_1'(\tau)$ are defined as follows.

$$\mathrm{s}_1(\tau) = \begin{cases} 1, & 0 \le \tau < \dfrac{T_\mathrm{s}}{2} \\ 0, & \dfrac{T_\mathrm{s}}{2} \le \tau < T_\mathrm{s} \end{cases} \tag{3.72}$$

$$\mathrm{s}_1'(\tau) = \begin{cases} 1, & \dfrac{T_\mathrm{s}}{2\pi}\left(\left\langle \delta \right\rangle_0 + \dfrac{\pi}{6}\right) \le \tau < \dfrac{T_\mathrm{s}}{2}\left(1 + \dfrac{1}{\pi}\left(\left\langle \delta \right\rangle_0 + \dfrac{\pi}{6}\right)\right) \\ 0, & 0 \le \tau < \dfrac{T_\mathrm{s}}{2\pi}\left(\left\langle \delta \right\rangle_0 + \dfrac{\pi}{6}\right) \ \cup \ \dfrac{T_\mathrm{s}}{2}\left(1 + \dfrac{1}{\pi}\left(\left\langle \delta \right\rangle_0 + \dfrac{\pi}{6}\right)\right) \le \tau < T_\mathrm{s} \end{cases} \tag{3.73}$$

Using (3.72) to solve (3.70), it yields that,

$$\left\langle \mathrm{s}_1 \right\rangle_1 = \left\langle \mathrm{s}_1 \right\rangle_1^\mathrm{R} + j\left\langle \mathrm{s}_1 \right\rangle_1^\mathrm{I} = -j\frac{1}{\pi} \tag{3.74}$$

Similarly, using (3.73) to solve (3.71), it results in,

$$\left\langle \mathrm{s}_1' \right\rangle_1 = \left\langle \mathrm{s}_1' \right\rangle_1^\mathrm{R} + j\left\langle \mathrm{s}_1' \right\rangle_1^\mathrm{I} = \frac{1}{\pi}\sin\left(\left\langle \delta \right\rangle_0 + \frac{7\pi}{6}\right) + j\frac{1}{\pi}\cos\left(\left\langle \delta \right\rangle_0 + \frac{7\pi}{6}\right) \tag{3.75}$$

Note here that the average of the input bridge switching-functions does not depend on the control phase-shift $\left\langle \delta \right\rangle_0$ but it is the case for the output bridge. Similarly, for phase B, it is results in,

$$\left\langle \mathrm{s}_3 \right\rangle_1 = \left\langle \mathrm{s}_3 \right\rangle_1^\mathrm{R} + j\left\langle \mathrm{s}_3 \right\rangle_1^\mathrm{I} = -\frac{\sqrt{3}}{2\pi} + j\frac{1}{2\pi} \tag{3.76}$$

$$\left\langle \mathrm{s}_3' \right\rangle_1 = \left\langle \mathrm{s}_3' \right\rangle_1^\mathrm{R} + j\left\langle \mathrm{s}_3' \right\rangle_1^\mathrm{I} = \frac{1}{\pi}\sin\left(\left\langle \delta \right\rangle_0 + \frac{11\pi}{6}\right) + j\frac{1}{\pi}\cos\left(\left\langle \delta \right\rangle_0 + \frac{11\pi}{6}\right) \tag{3.77}$$

and for phase C, it results in,

$$\left\langle \mathrm{s}_5 \right\rangle_1 = \left\langle \mathrm{s}_5 \right\rangle_1^{\mathrm{R}} + j\left\langle \mathrm{s}_5 \right\rangle_1^{\mathrm{I}} = \frac{\sqrt{3}}{2\pi} + j\frac{1}{2\pi} \tag{3.78}$$

$$\left\langle \mathrm{s}_5^{'} \right\rangle_1 = \left\langle \mathrm{s}_5^{'} \right\rangle_1^{\mathrm{R}} + j\left\langle \mathrm{s}_5^{'} \right\rangle_1^{\mathrm{I}} = \frac{1}{\pi}\sin\left(\left\langle \delta \right\rangle_0 + \frac{\pi}{2}\right) + j\frac{1}{\pi}\cos\left(\left\langle \delta \right\rangle_0 + \frac{\pi}{2}\right) \tag{3.79}$$

Figure 3.3 shows the averaged switching-function dynamic phasors for the Y-Δ 3p-DAB. All the phasors are equal in magnitude ($1/\pi$), but the output bridge switching-function phasors (red) are $\left\langle \delta \right\rangle_0 + \pi/6$ lagging the input bridge switching-function phasors (blue).

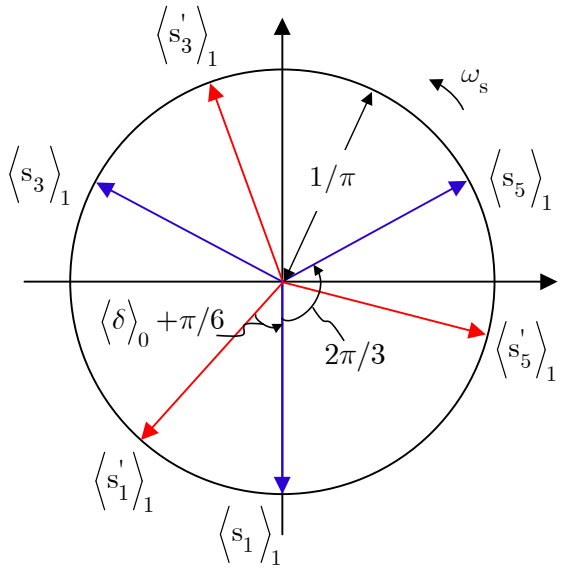

Figure 3.3 : Averaged switching-function dynamic phasors

3.3.1.3 Linearized small-signal model and operating point

To derive the small-signal model, it is necessary to linearize the system of equations defined by (3.61)–(3.69) and (3.74)–(3.79) by applying the following perturbations around the operating point,

$$\begin{aligned}
&\left\langle \delta \right\rangle_0 = \delta + \left\langle \hat{\delta} \right\rangle_0, \left\langle v_\mathrm{o} \right\rangle_0 = V_\mathrm{o} + \left\langle \hat{v}_\mathrm{o} \right\rangle_0, \\
&\left\langle v_\mathrm{i} \right\rangle_0 = V_\mathrm{i} + \left\langle \hat{v}_\mathrm{i} \right\rangle_0, \left\langle i_\mathrm{i} \right\rangle_0 = I_\mathrm{i} + \left\langle \hat{i}_\mathrm{i} \right\rangle_0, \\
&\left\langle i_\mathrm{A} \right\rangle_1^{\mathrm{R}} = \left\langle I_\mathrm{A} \right\rangle_1^{\mathrm{R}} + \left\langle \hat{i}_\mathrm{A} \right\rangle_1^{\mathrm{R}}, \left\langle i_\mathrm{A} \right\rangle_1^{\mathrm{I}} = \left\langle I_\mathrm{A} \right\rangle_1^{\mathrm{I}} + \left\langle \hat{i}_\mathrm{A} \right\rangle_1^{\mathrm{I}}, \\
&\left\langle i_\mathrm{B} \right\rangle_1^{\mathrm{R}} = \left\langle I_\mathrm{B} \right\rangle_1^{\mathrm{R}} + \left\langle \hat{i}_\mathrm{B} \right\rangle_1^{\mathrm{R}}, \left\langle i_\mathrm{B} \right\rangle_1^{\mathrm{I}} = \left\langle I_\mathrm{B} \right\rangle_1^{\mathrm{I}} + \left\langle \hat{i}_\mathrm{B} \right\rangle_1^{\mathrm{I}}, \\
&\left\langle i_\mathrm{C} \right\rangle_1^{\mathrm{R}} = \left\langle I_\mathrm{C} \right\rangle_1^{\mathrm{R}} + \left\langle \hat{i}_\mathrm{C} \right\rangle_1^{\mathrm{R}}, \left\langle i_\mathrm{C} \right\rangle_1^{\mathrm{I}} = \left\langle I_\mathrm{C} \right\rangle_1^{\mathrm{I}} + \left\langle \hat{i}_\mathrm{C} \right\rangle_1^{\mathrm{I}}
\end{aligned} \tag{3.80}$$

The vector of the state-variable operating points $\mathbf{X}$ is given by,

$$\mathbf{X}=\left[V_{\mathrm{o}}\ \ \left\langle I_{\mathrm{A}}\right\rangle_1^{\mathrm{R}}\ \left\langle I_{\mathrm{A}}\right\rangle_1^{\mathrm{I}}\ \left\langle I_{\mathrm{B}}\right\rangle_1^{\mathrm{R}}\ \left\langle I_{\mathrm{B}}\right\rangle_1^{\mathrm{I}}\ \left\langle I_{\mathrm{C}}\right\rangle_1^{\mathrm{R}}\ \left\langle I_{\mathrm{C}}\right\rangle_1^{\mathrm{I}}\right]^{\mathrm{T}} \tag{3.81}$$

and it is obtained by solving the following equation,

$$\mathbf{X}=-\mathbf{A}^{-1}\mathbf{B}\mathbf{U} \tag{3.82}$$

with $\mathbf{A}$ and $\mathbf{B}$ being given in (3.65) and (3.67) respectively, and $\mathbf{U}=\left[0\ \ V_{\mathrm{i}}\right]^{\mathrm{T}}$.

It is also proposed here to calculate the operating point δ of the control phase-shift by solving (2.37) or (2.38).

The main steps to linearize the system of equations are summarized in Appendix E. The result is a *k*-dependent averaged small-signal model written as,

$$\frac{d\left\langle\hat{\mathbf{x}}(t)\right\rangle}{dt}=\hat{\mathbf{A}}\left\langle\hat{\mathbf{x}}(t)\right\rangle+\hat{\mathbf{B}}\left\langle\hat{\mathbf{u}}(t)\right\rangle \tag{3.83}$$

$$\left\langle\hat{\mathbf{y}}(t)\right\rangle=\hat{\mathbf{C}}\left\langle\hat{\mathbf{x}}(t)\right\rangle+\hat{\mathbf{D}}\left\langle\hat{\mathbf{u}}(t)\right\rangle \tag{3.84}$$

with the following averaged state-variable vector,

$$\left\langle\hat{\mathbf{x}}\right\rangle=\left[\left\langle\hat{v}_{\mathrm{o}}\right\rangle_0\ \left\langle\hat{i}_{\mathrm{A}}\right\rangle_1^{\mathrm{R}}\ \left\langle\hat{i}_{\mathrm{A}}\right\rangle_1^{\mathrm{I}}\ \left\langle\hat{i}_{\mathrm{B}}\right\rangle_1^{\mathrm{R}}\ \left\langle\hat{i}_{\mathrm{B}}\right\rangle_1^{\mathrm{I}}\ \left\langle\hat{i}_{\mathrm{C}}\right\rangle_1^{\mathrm{R}}\ \left\langle\hat{i}_{\mathrm{C}}\right\rangle_1^{\mathrm{I}}\right]^{T} \tag{3.85}$$

and the following vectors of input and output,

$$\left\langle\hat{\mathbf{u}}\right\rangle=\left[\left\langle\hat{\delta}\right\rangle_0\ \left\langle\hat{v}_{\mathrm{i}}\right\rangle_0\right]^{T},\ \ \left\langle\hat{\mathbf{y}}\right\rangle=\left[\left\langle\hat{v}_{\mathrm{o}}\right\rangle_0\ \left\langle\hat{i}_{\mathrm{i}}\right\rangle_0\right]^{T} \tag{3.86}$$

The averaged state-space matrices are given by,

$$\hat{\mathbf{A}}=\begin{bmatrix}\dfrac{-1}{RC_{\mathrm{o}}} & A_{12} & A_{13} & A_{14} & A_{15} & A_{16} & A_{17}\\ A_{21} & 0 & \omega_{\mathrm{s}} & 0 & 0 & 0 & 0\\ A_{31} & -\omega_{\mathrm{s}} & 0 & 0 & 0 & 0 & 0\\ A_{41} & 0 & 0 & 0 & \omega_{\mathrm{s}} & 0 & 0\\ A_{51} & 0 & 0 & -\omega_{\mathrm{s}} & 0 & 0 & 0\\ A_{61} & 0 & 0 & 0 & 0 & 0 & \omega_{\mathrm{s}}\\ A_{71} & 0 & 0 & 0 & 0 & -\omega_{\mathrm{s}} & 0\end{bmatrix} \tag{3.87}$$

$$\hat{\mathbf{B}} = \begin{bmatrix} B_{11} & B_{12} & B_{13} & B_{14} & B_{15} & B_{16} & B_{17} \\ 0 & 0 & \dfrac{-1}{\pi L_{\mathrm{A}}} & \dfrac{-\sqrt{3}}{2\pi L_{\mathrm{B}}} & \dfrac{1}{2\pi L_{\mathrm{B}}} & \dfrac{\sqrt{3}}{2\pi L_{\mathrm{C}}} & \dfrac{1}{2\pi L_{\mathrm{C}}} \end{bmatrix}^{T} \tag{3.88}$$

$$\hat{\mathbf{C}} = \begin{bmatrix} 1 & 0 & 0 & 0 & 0 & 0 & 0 \\ 0 & 0 & -\dfrac{2}{\pi} & -\dfrac{\sqrt{3}}{\pi} & \dfrac{1}{\pi} & \dfrac{\sqrt{3}}{\pi} & \dfrac{1}{\pi} \end{bmatrix} \tag{3.89}$$

$$\hat{\mathbf{D}} = \begin{bmatrix} 0 & 0 \\ 0 & 0 \end{bmatrix} \tag{3.90}$$

with,

$$\begin{gathered} A_{12} = \frac{2}{C_{\mathrm{o}}} S_1,\ A_{13} = \frac{2}{C_{\mathrm{o}}} S_2,\ A_{14} = \frac{2}{C_{\mathrm{o}}} S_3, \\ A_{15} = \frac{2}{C_{\mathrm{o}}} S_4,\ A_{16} = \frac{2}{C_{\mathrm{o}}} S_5,\ A_{17} = \frac{2}{C_{\mathrm{o}}} S_6 \end{gathered} \tag{3.91}$$

$$\begin{gathered} A_{21} = -\frac{1}{L_{\mathrm{A}}} S_1,\ A_{31} = -\frac{1}{L_{\mathrm{A}}} S_2,\ A_{41} = -\frac{1}{L_{\mathrm{B}}} S_3 \\ A_{51} = -\frac{1}{L_{\mathrm{B}}} S_4,\ A_{61} = -\frac{1}{L_{\mathrm{C}}} S_5,\ A_{71} = -\frac{1}{L_{\mathrm{C}}} S_6 \end{gathered} \tag{3.92}$$

$$\begin{gathered} B_{12} = -\frac{V_{\mathrm{o}}}{L_{\mathrm{A}}} S_2,\ B_{13} = \frac{V_{\mathrm{o}}}{L_{\mathrm{A}}} S_1,\ B_{14} = -\frac{V_{\mathrm{o}}}{L_{\mathrm{B}}} S_4 \\ B_{15} = \frac{V_{\mathrm{o}}}{L_{\mathrm{B}}} S_3,\ B_{16} = -\frac{V_{\mathrm{o}}}{L_{\mathrm{C}}} S_6,\ B_{17} = \frac{V_{\mathrm{o}}}{L_{\mathrm{C}}} S_5 \end{gathered} \tag{3.93}$$

$$B_{11} = \frac{2}{C_{\mathrm{o}}} \sum_{n=1}^{6} B_{11}(n) \tag{3.94}$$

where the $B_{11}(n)$ terms are defined by,

$$\begin{gathered} B_{11}(1) = S_2 \left\langle I_{\mathrm{A}} \right\rangle_1^{\mathrm{R}},\ B_{11}(2) = -S_1 \left\langle I_{\mathrm{A}} \right\rangle_1^{\mathrm{I}}, \\ B_{11}(3) = S_4 \left\langle I_{\mathrm{B}} \right\rangle_1^{\mathrm{R}},\ B_{11}(4) = -S_3 \left\langle I_{\mathrm{B}} \right\rangle_1^{\mathrm{I}} \\ B_{11}(5) = S_6 \left\langle I_{\mathrm{C}} \right\rangle_1^{\mathrm{R}},\ B_{11}(6) = -S_5 \left\langle I_{\mathrm{C}} \right\rangle_1^{\mathrm{I}} \end{gathered} \tag{3.95}$$

and the S_1 to S_6 terms are defined by,

$$
\begin{aligned}
S_1 &= \frac{m}{\pi}\left[\sin\left(\delta+\frac{7\pi}{6}\right)-\sin\left(\delta+\frac{11\pi}{6}\right)\right] \\
S_2 &= \frac{m}{\pi}\left[\cos\left(\delta+\frac{7\pi}{6}\right)-\cos\left(\delta+\frac{11\pi}{6}\right)\right] \\
S_3 &= \frac{m}{\pi}\left[\sin\left(\delta+\frac{11\pi}{6}\right)-\sin\left(\delta+\frac{\pi}{2}\right)\right] \\
S_4 &= \frac{m}{\pi}\left[\cos\left(\delta+\frac{11\pi}{6}\right)-\cos\left(\delta+\frac{\pi}{2}\right)\right] \\
S_5 &= \frac{m}{\pi}\left[\sin\left(\delta+\frac{\pi}{2}\right)-\sin\left(\delta+\frac{7\pi}{6}\right)\right] \\
S_6 &= \frac{m}{\pi}\left[\cos\left(\delta+\frac{\pi}{2}\right)-\cos\left(\delta+\frac{7\pi}{6}\right)\right]
\end{aligned}
\tag{3.96}
$$

3.4 Hybrid averaging and transfer functions evaluation

The system of equations defined by the GSSA model (3.83)–(3.96) is proposed to be combined with (3.24) and (3.25) from the SSA model, such that, the system is represented as a coupled multi-input multi-output (MIMO) system in the frequency-domain (Figure 3.4). This representation is called "hybrid" because it combines both the SSA and GSSA models. For the evaluation of the transfer function Z_{N}, the SSA model is used to approximate the required perturbation $\left\langle \hat{\delta}(s) \right\rangle_0$ to be injected in the GSSA model to impose $\left\langle \hat{v}_{\mathrm{o}}(s) \right\rangle_0 \to 0$.

The general procedure to obtain all the transfer functions is decomposed into four (4) steps:

1) The GSSA model (3.83)–(3.96) is solved using MATLAB to obtain the transfer functions defined in (3.97), i.e. G_{vd}, G_{vg}, G_{id}, and Z_{D}.

$$
\begin{bmatrix} \left\langle \hat{v}_{\mathrm{o}}(s) \right\rangle_0 \\ \left\langle \hat{i}_{\mathrm{i}}(s) \right\rangle_0 \end{bmatrix} = \begin{bmatrix} G_{\mathrm{vd}}(s) & G_{\mathrm{vg}}(s) \\ G_{\mathrm{id}}(s) & 1 \,/\, Z_{\mathrm{D}}(s) \end{bmatrix} \begin{bmatrix} \left\langle \hat{\delta}(s) \right\rangle_0 \\ \left\langle \hat{v}_{\mathrm{i}}(s) \right\rangle_0 \end{bmatrix}
\tag{3.97}
$$

2) The SSA model is solved to obtain the transfer functions $G_{\delta i}$ defined by (3.24) or (3.25), depending on the operating range of the control phase-shift δ. Note that, the SSA model is also used to obtain Z_o directly.

3) Knowing all the transfer functions in Figure 3.4, the MIMO system is implemented in MATLAB/Simulink. The GSSA part is implemented as defined in (3.97).

4) The transfer function Z_N is evaluated by solving the hybrid system represented in Figure 3.4 using the Linear Analysis tool of MATLAB/Simulink.

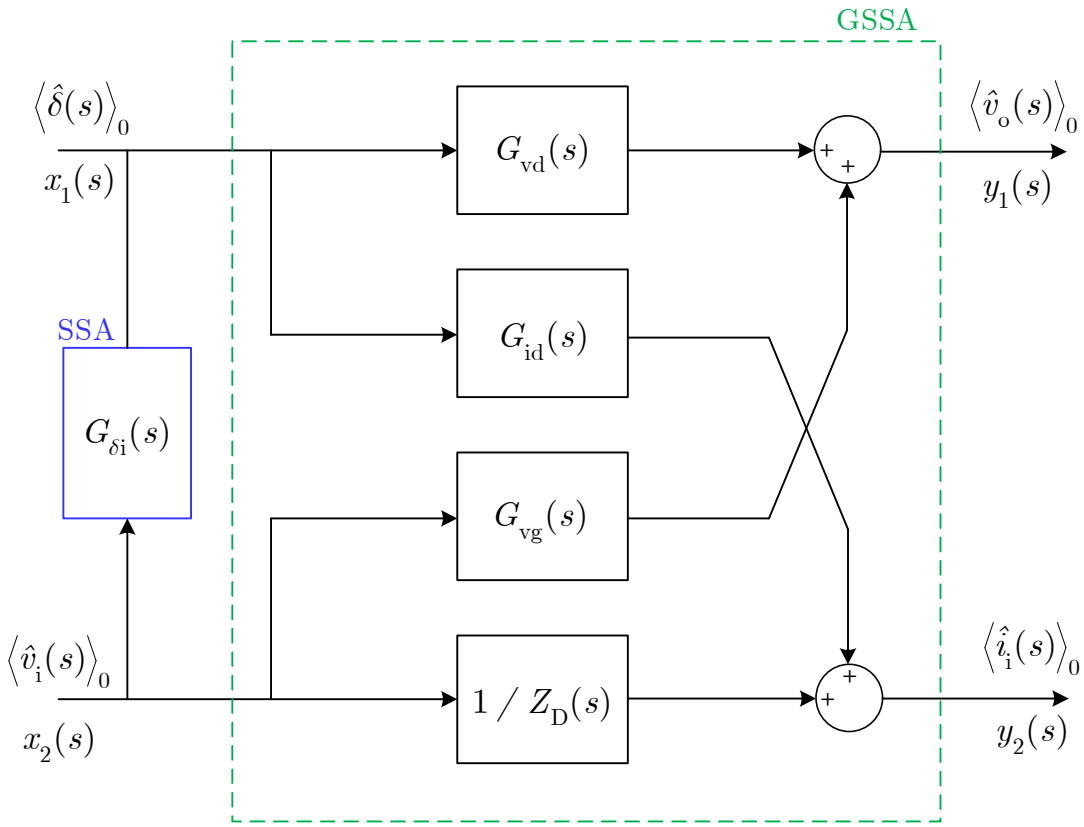

Figure 3.4 : Hybrid MIMO small-signal model representation of the 3p-DAB in open-loop

3.5 EMTP validation of the SSA, GSSA, and hybrid models

3.5.1 General procedure

The SSA, GSSA and hybrid models are validated with time-domain simulations in EMTP. The equivalent circuits for the validation of all the transfer functions are shown in Figure 3.5. The injected perturbations are defined as follows,

$$\hat{v}_{\mathrm{i}}(t) = v_{\mathrm{pert}}\cos(2\pi f_{\mathrm{pert}}t) \tag{3.98}$$

$$\hat{\delta}(t) = \delta_{\mathrm{pert}}\cos(2\pi f_{\mathrm{pert}}t + \theta_{\mathrm{pert}}) \tag{3.99}$$

$$\hat{i}_{\mathrm{load}}(t) = i_{\mathrm{pert}}\cos(2\pi f_{\mathrm{pert}}t) \tag{3.100}$$

The amplitude of the perturbations is kept small around the operating point (< 5%). The frequency of the perturbations is varied between 50 Hz to 48 kHz, for a switching frequency $f_{\mathrm{s}} = 50$ kHz. The simulation time-step is fixed to $\Delta t =$ 0.01 µs. The simulation parameters for model 1 (Appendix A) are used, and the results are shown in Figure 3.6.

For the validation of G_{vd} in Figure 3.5 a), a perturbation $\hat{\delta}(t)$ of amplitude δ_{pert} on the control phase-shift $\delta(t)$ is applied with $\theta_{\mathrm{pert}} = 0^{\circ}$. The output voltage $v_{\mathrm{o}}(t)$ is measured, and its magnitude at the perturbation frequency f_{pert}, noted here v_{mes}, is extracted by Fast Fourier Transform (FFT) analysis using the ScopeView tool in EMTP. The gain of the transfer function G_{vd} is obtained by calculating,

$$\left|G_{\mathrm{vd}}\right| = 20\log\left(\frac{v_{\mathrm{mes}}}{\delta_{\mathrm{pert}}}\right) \tag{3.101}$$

For the validation of G_{vg} and Z_{D} in Figure 3.5 b), a perturbation $\hat{v}_{\mathrm{i}}(t)$ of amplitude v_{pert} on the input voltage $v_{\mathrm{i}}(t)$ is applied, and the output voltage $v_{\mathrm{o}}(t)$ and the input current $i_{\mathrm{i}}(t)$ are both measured. The magnitude of both $v_{\mathrm{o}}(t)$ and $i_{\mathrm{i}}(t)$ at the perturbation frequency f_{pert}, noted here v_{mes} and i_{mes} respectively, are also extracted by FFT analysis. The gain of the transfer functions G_{vg} and Z_{D} is obtained by calculating,

$$\left|G_{\mathrm{vg}}\right| = 20\log\left(\frac{v_{\mathrm{mes}}}{v_{\mathrm{pert}}}\right) \tag{3.102}$$

$$\left|Z_{\mathrm{D}}\right| = 20\log\left(\frac{v_{\mathrm{pert}}}{i_{\mathrm{mes}}}\right) \tag{3.103}$$

For the validation of Z_N in Figure 3.5 c), a perturbation $\hat{v}_i(t)$ of amplitude v_{pert} on the input voltage $v_i(t)$ is applied while a perturbation $\hat{\delta}(t)$ of amplitude δ_{pert} on the control phase-shift $\delta(t)$ is applied with $\theta_{pert} = 180^\circ$ as required by (3.24) and (3.25). The goal of the perturbation $\hat{\delta}(t)$ is to maintain $\hat{v}_o = 0$. The input current $i_i(t)$ is measured, and its magnitude at the perturbation frequency f_{pert}, noted here i_{mes}, is also obtained by FFT analysis. The gain of the transfer function Z_N is obtained by calculating,

$$\left|Z_N\right| = 20\log\left(\frac{v_{pert}}{i_{mes}}\right) \tag{3.104}$$

Finally, for the validation of Z_o in Figure 3.5 d), a perturbation $\hat{i}_{load}(t)$ of amplitude i_{pert} on the load current $i_{load}(t)$ is applied. The output voltage $v_o(t)$ is measured, and its magnitude at the perturbation frequency f_{pert}, noted here v_{mes}, is also extracted by FFT analysis. The gain of the transfer function Z_o is obtained by calculating,

$$\left|Z_o\right| = 20\log\left(\frac{v_{mes}}{i_{pert}}\right) \tag{3.105}$$

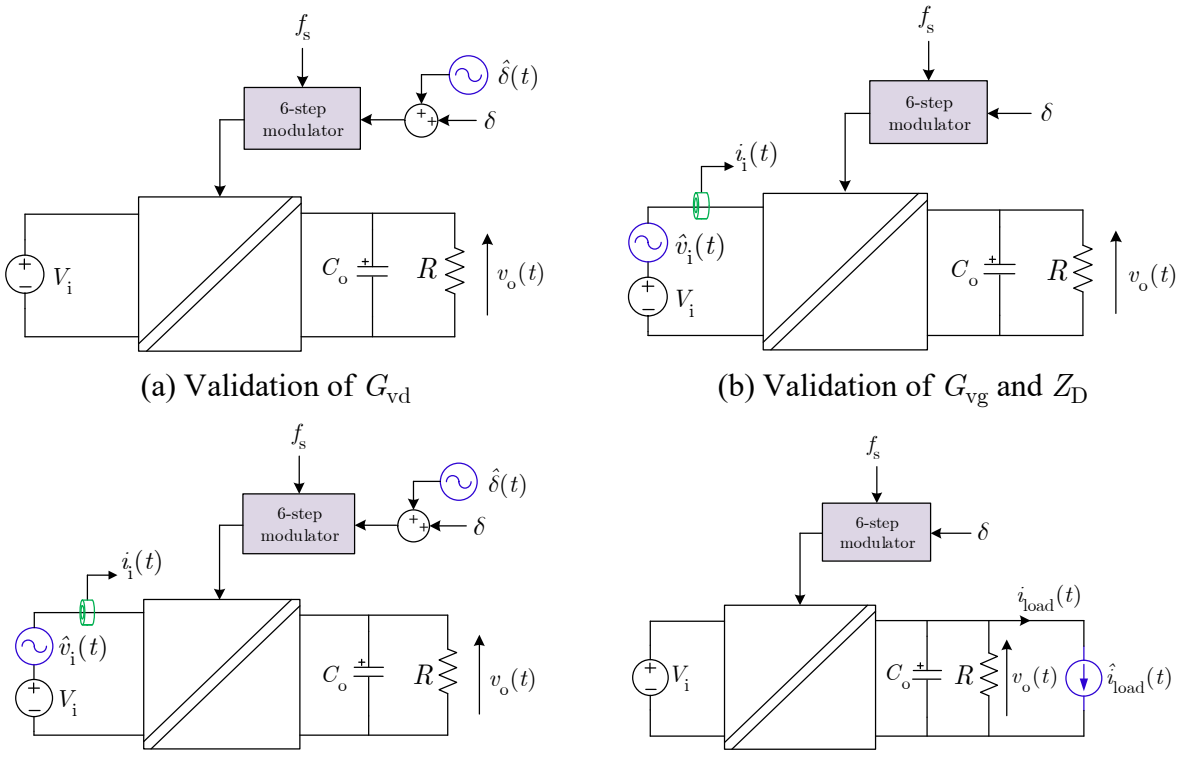

(a) Validation of G_{vd}

(b) Validation of G_{vg} and Z_D

(c) Validation of Z_N

(d) Validation of Z_o

Figure 3.5 : Equivalent circuits for the validation of the open-loop transfer functions

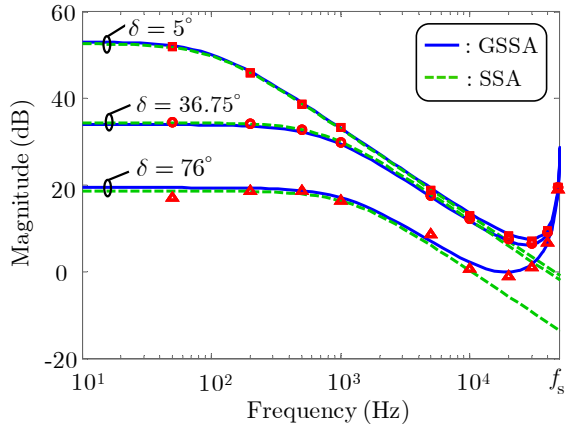

(a) Validation of $|G_{vd}|$

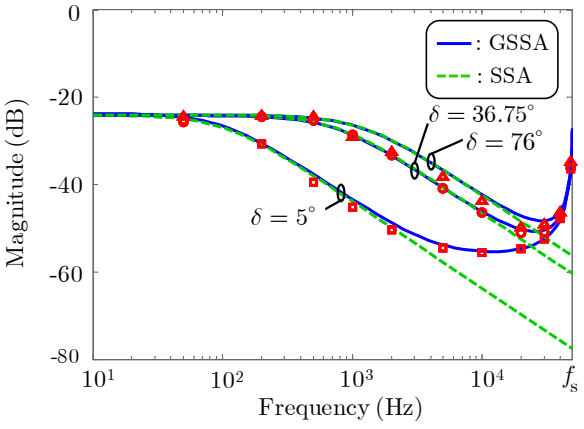

(b) Validation of $|G_{vg}|$

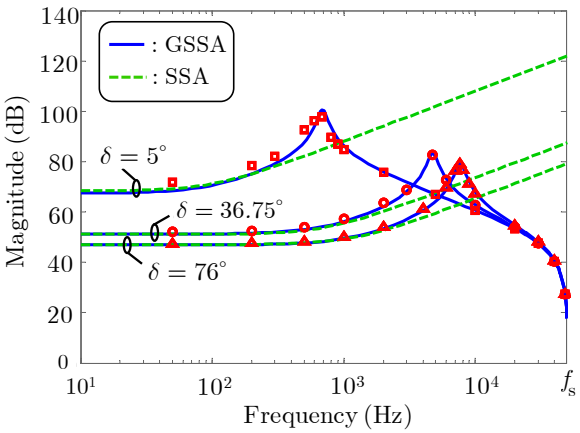

(c) Validation of $|Z_D|$

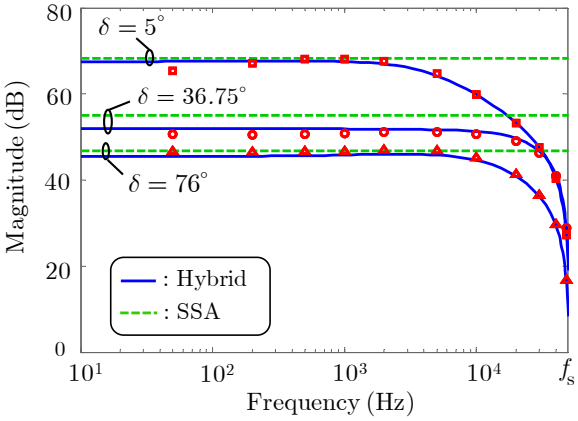

(d) Validation of $|Z_N|$

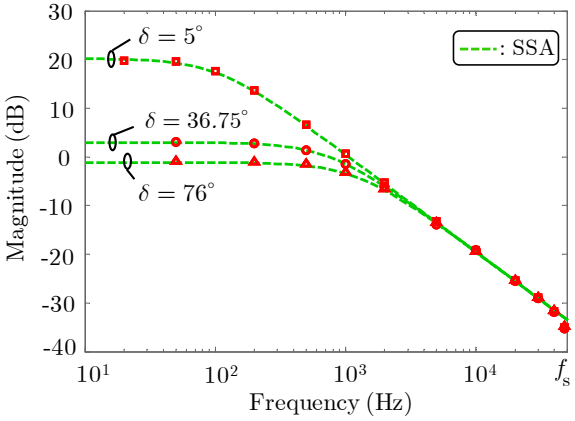

(e) Validation of $|Z_o|$

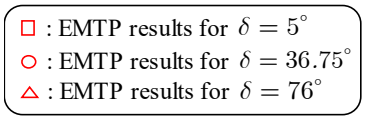

Figure 3.6 : Validation of the transfer functions with time-domain simulations (model 1)

3.5.2 Comparison of SSA, GSSA, and hybrid models

From Figure 3.6 a) and b), it is first observed that both the GSSA and SSA models are accurate to evaluate G_{vd}, and G_{vg} for frequencies up to around 1/5$^{\mathrm{th}}$ of the switching frequency f_{s}. The precision of the SSA model decreases as the frequency of the perturbation is increased toward f_{s}. This is because SSA does not consider the dynamic of both the transformer currents and the switching-functions. By analyzing Figure 3.6. c) and d), it is also concluded that the SSA model does not correctly model Z_{D} and Z_{N}, but the proposed hybrid model provides a mean to evaluate Z_{N} which is not possible by using GSSA only.

Overall, from the simulation results in Figure 3.6, it is also concluded that the GSSA and hybrid models, together, are accurate to determine G_{vd}, G_{vg}, Z_{N}, and Z_{D} over the validation frequency range. However, for G_{vd} and G_{vg}, the GSSA model tends to slightly lose accuracy at high-power while, for Z_{D}, the accuracy is slightly reduced at low power. For Z_{N}, the hybrid model is also a little less accurate at low frequencies. This is mainly explained by errors on the calculation of the operating point with GSSA. From Figure 3.6 e), it is also concluded that the SSA model is accurate for the evaluation of the output impedance Z_{o}. Being able to model the 3p-DAB from low frequencies up to the switching frequency f_{s} is important because it allows to 1) design a controller with an increased bandwidth, and 2) predict stability as well as the dynamic behavior of the converter over a broad range of frequencies (DC to f_{s}).

Although SSA is less precise, it allows representing the converter equivalent model using standard circuit theory. These circuits are easier to manipulate to determine analytical expressions of the converter transfer functions. Thus, SSA gives a better insight of system parameters sensitivity. However, SSA also results in two sets of state-space matrices depending on the control phase-shift δ operating range.

3.6 Controller sizing and closed-loop operation

3.6.1 Simplified closed-loop model for parameter sensitivity analysis with SSA

As mentioned before, SSA provides a better intuition than GSSA of system parameters sensitivity. The closed-loop system of Figure 3.1 is simplified here for the analysis of the converter parameter

sensitivity with SSA. It neglects the modulator gain K_{m} and it assumes that the converter dynamic is dominant over the dynamic of the measurement filter G_{f}. The simplified closed-loop diagram is shown in Figure 3.7.

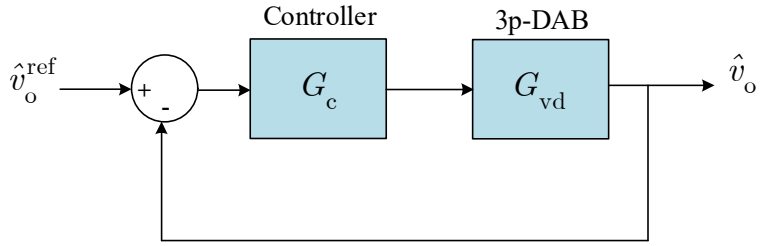

Figure 3.7 : Simplified closed-loop diagram for parameters sensitivity analysis with SSA

The controller G_{c} used here is a simple PI-type with the transfer function given as,

$$G_{\mathrm{c}}(s) = \frac{sK_{\mathrm{p}} + K_{\mathrm{i}}}{s} \tag{3.106}$$

The general form of the transfer function G_{vd} with the SSA model is also written as,

$$G_{\mathrm{vd}}(s) = \frac{K_{\mathrm{vd}}}{sRC_{\mathrm{o}} + 1} \tag{3.107}$$

The closed-loop transfer function from the reference to the output is given by,

$$H(s) = \frac{\hat{v}_{\mathrm{o}}}{\hat{v}_{\mathrm{o}}^{\mathrm{ref}}} = \frac{1}{1 + G_{\mathrm{c}}G_{\mathrm{vd}}} \tag{3.108}$$

which yields to,

$$H(s) = \frac{\hat{v}_{\mathrm{o}}}{\hat{v}_{\mathrm{o}}^{\mathrm{ref}}} = \frac{s\left(sRC_{\mathrm{o}} + 1\right)\left(1/K_{\mathrm{vd}}K_{\mathrm{i}}\right)}{\left(\frac{RC_{\mathrm{o}}}{K_{\mathrm{vd}}K_{\mathrm{i}}}\right)s^2 + \left(\frac{1 + K_{\mathrm{vd}}K_{\mathrm{p}}}{K_{\mathrm{vd}}K_{\mathrm{i}}}\right)s + 1} \tag{3.109}$$

By making the assumption that $K_{\mathrm{vd}}K_{\mathrm{p}} >> 1$, the analysis of the 2nd order denominator, which has the general form $\tau^2 s^2 + 2\zeta\tau s + 1,$ leads to an approximate damping coefficient ζ of,

$$\zeta \approx \frac{K_{\mathrm{p}}}{\sqrt{K_{\mathrm{i}}}} \frac{\sqrt{K_{\mathrm{vd}}}}{2\sqrt{RC_{\mathrm{o}}}} \tag{3.110}$$

and an approximate time-constant τ of,

$$\tau \approx \frac{1}{\sqrt{K_{\mathrm{i}}}} \sqrt{\frac{RC_{\mathrm{o}}}{K_{\mathrm{vd}}}} \tag{3.111}$$

with K_{vd} given for range 1 by,

$$K_{\mathrm{vd}} = \frac{mRV_{\mathrm{i}}}{\omega_{\mathrm{s}} L_{\mathrm{s}}} \tag{3.112}$$

and for range 2 by,

$$K_{\mathrm{vd}} = \frac{mRV_{\mathrm{i}}}{\omega_{\mathrm{s}} L_{\mathrm{s}}} \left[\frac{3}{2} \left(1 - \frac{2\delta}{\pi} \right) \right] \tag{3.113}$$

Inserting (3.112) and (3.113) into (3.110) and (3.111), it yields to the damping coefficients ζ and the time-constants τ provided in Table 3.2. Knowing that the overshoot (OS) and the time-to-first-peak t_{p} of the time-domain response are both related to the damping coefficient ζ and the time-constant τ, it is possible to assess the impact of the parameters on the closed-loop response using basic control theory,

$$t_{\mathrm{p}} = \frac{\pi\tau}{\sqrt{1-\zeta^2}} \tag{3.114}$$

$$\mathrm{OS} = e^{\frac{-\pi\zeta}{\sqrt{1-\zeta^2}}} \tag{3.115}$$

Theoretically, the closed-loop dynamic can be controlled through the controller parameters K_{p}, K_{i} as well as the converter design parameters m, V_{i}, ω_{s}, L_{s}, and C_{o}. In practice, it is more convenient to use only K_{p}, K_{i} and C_{o} since m, V_{i}, ω_{s} and L_{s} all affect the steady-state operating point. For example, as shown in Figure 3.8, for a given PI-controller, increasing the output capacitor C_{o} increases the response time t_{p} as well as the overshoot (OS). This can be explained by the fact that increasing C_{o} decreases ζ and increases τ with all other parameters being held constant (Table 3.2).

Table 3.2: Closed-loop dynamic response analysis with SSA

Range 1 ($0 \le \delta \le \pi/6$)		Range 2 ($\pi/6 \le \delta \le \pi/2$)	
$\zeta \approx \frac{K_{\mathrm{p}}}{2\sqrt{K_{\mathrm{i}}}} \sqrt{\frac{mV_{\mathrm{i}}}{\omega_{\mathrm{s}} L_{\mathrm{s}} C_{\mathrm{o}}}}$	(3.116)	$\zeta \approx \frac{K_{\mathrm{p}}}{2\sqrt{K_{\mathrm{i}}}} \sqrt{\frac{mV_{\mathrm{i}}}{\omega_{\mathrm{s}} L_{\mathrm{s}} C_{\mathrm{o}}}} \sqrt{\frac{3}{2}\left(1 - \frac{2\delta}{\pi}\right)}$	(3.117)
$\tau \approx \frac{1}{\sqrt{K_{\mathrm{i}}}} \sqrt{\frac{\omega_{\mathrm{s}} L_{\mathrm{s}} C_{\mathrm{o}}}{mV_{\mathrm{i}}}}$	(3.118)	$\tau \approx \frac{1}{\sqrt{K_{\mathrm{i}}}} \sqrt{\frac{\omega_{\mathrm{s}} L_{\mathrm{s}} C_{\mathrm{o}}}{mV_{\mathrm{i}}}} \frac{1}{\sqrt{\frac{3}{2}\left(1 - \frac{2\delta}{\pi}\right)}}$	(3.119)

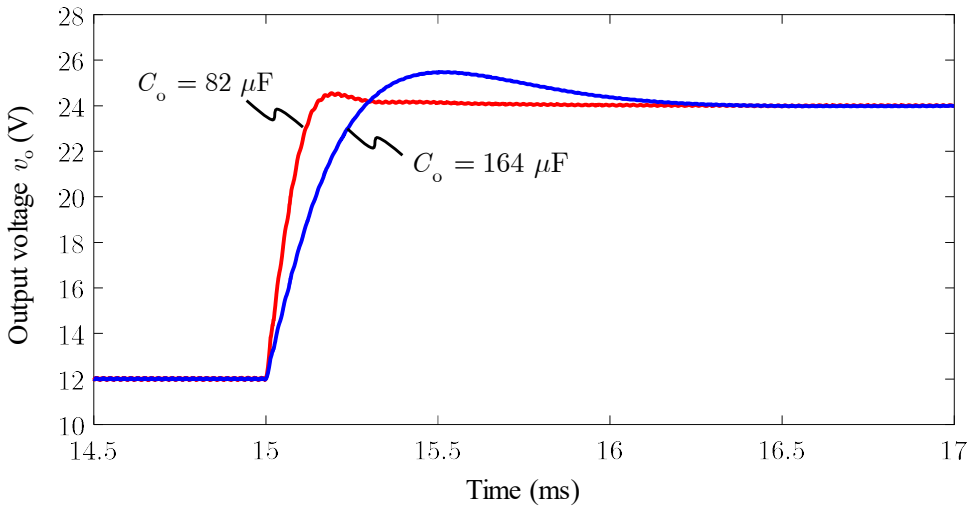

Figure 3.8 : Response to a step in the reference voltage from 12 V to 24 V (model 4)

3.6.2 Complete closed-loop analysis for controller sizing

For controller sizing, the complete closed-loop small-signal diagram of Figure 3.9 must be used because the modulator introduces a gain K_m and the dynamic of the feedback measurement filter G_f may not be negligible.

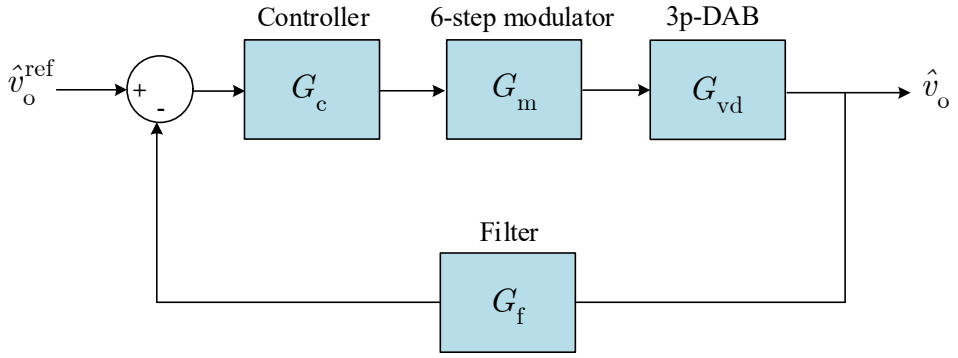

Figure 3.9 : Complete closed-loop diagram for controller sizing

Using Nyquist's theorem, the analysis is performed on the loop gain $T = G \cdot G_c$ with G defined as,

$$G = G_{vd} G_m G_f \tag{3.120}$$

For the prototype (model 4), the bode diagram of the system transfer functions is shown in Figure 3.10. The objective is to calculate the PI-controller parameters K_p and K_i to meet desired dynamic performance defined by a cross-over frequency $\omega_{\varphi m} = 2\pi f_{\varphi m}$ and a phase-margin φ_m. The general transfer function of the PI-controller is given in (3.106). The bode diagram of the controller

G_c and the open-loop transfer function $G \cdot G_c$ is shown in Figure 3.11. The resulting transient response to a step in the output voltage reference v_o^{ref} from 0 to 24 V is shown in Figure 3.12. The resulting time-to-peak t_p is equal to 0.5 ms, and the resulting overshoot is equal to 9 %.

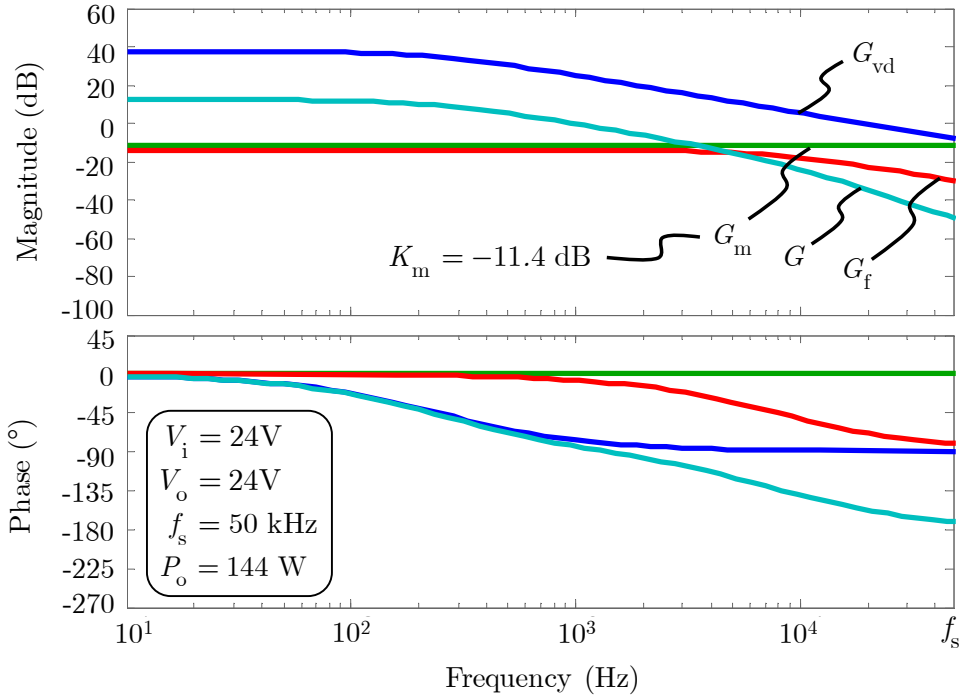

Figure 3.10 : Bode diagram for the sizing of the prototype controller (model 4)

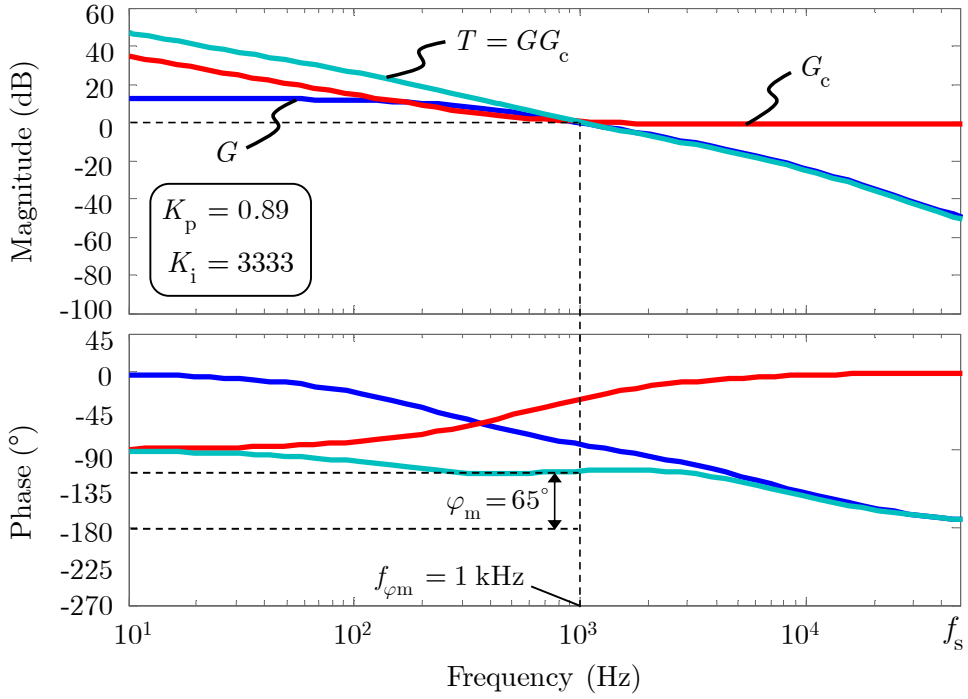

Figure 3.11 : Bode diagram of the prototype controller (model 4)

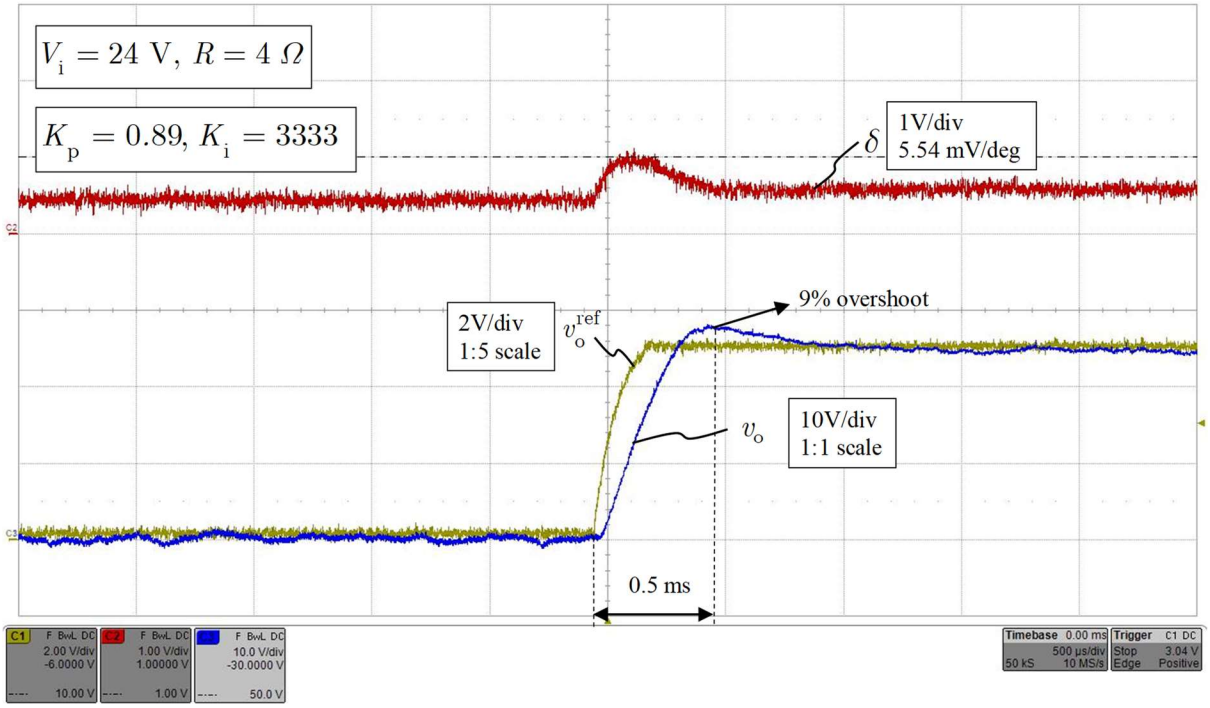

Figure 3.12 : Transient response to a step in the reference voltage (prototype)

3.6.3 Closed-loop transfer functions

The analysis of the converter closed-loop transfer functions is important for systems integration. One of the advantages of being able to evaluate Z_D and Z_N is the fact that it allows calculating the closed-loop input impedance of the 3p-DAB knowing its loop gain T for a given controller [30],

$$\frac{1}{Z_{in}^{c}(s)} = \frac{\hat{i}_i(s)}{\hat{v}_i(s)}\bigg|_{\substack{\hat{v}_o^{ref}(s)=0 \\ \hat{i}_{load}(s)=0}} = \frac{1}{Z_N(s)}\left(\frac{T(s)}{1+T(s)}\right) + \frac{1}{Z_D(s)}\left(\frac{1}{1+T(s)}\right) \tag{3.121}$$

Furthermore, knowing the open-loop transfer functions G_{vd}, G_{vg} and Z_o, and the loop gain T, the remaining closed-loop transfer functions can also be evaluated with [30],

$$G_{vd}^{c}(s) = \frac{\hat{v}_o(s)}{\hat{v}_o^{ref}(s)}\bigg|_{\substack{\hat{v}_i(s)=0 \\ \hat{i}_{load}(s)=0}} = \frac{1}{G_f(s)}\frac{T(s)}{1+T(s)} \tag{3.122}$$

$$Z_o^{c}(s) = -\frac{\hat{v}_o(s)}{\hat{i}_{load}(s)}\bigg|_{\substack{\hat{v}_o^{ref}(s)=0 \\ \hat{v}_i(s)=0}} = \frac{Z_o(s)}{1+T(s)} \tag{3.123}$$

$$G_{vg}^{c}(s) = \frac{\hat{v}_o(s)}{\hat{v}_i(s)}\bigg|_{\substack{\hat{v}_o^{ref}(s)=0 \\ \hat{i}_{load}(s)=0}} = \frac{G_{vg}(s)}{1+T(s)} \tag{3.124}$$

Analyzing (3.121)–(3.124), it must be concluded that it is important to model accurately the open-loop transfer functions G_{vd}, G_{vg}, Z_D, Z_N and Z_o to evaluate the closed-loop characteristics of the converter. This is because even slight errors in determining G_{vd}, G_{vg}, Z_D, Z_N and Z_o are multiplied together in (3.121)–(3.124) through the loop gain T. As an application example, the closed-loop transfer functions for the prototype (model 4) are compared with the open-loop transfer functions in Figure 3.13.

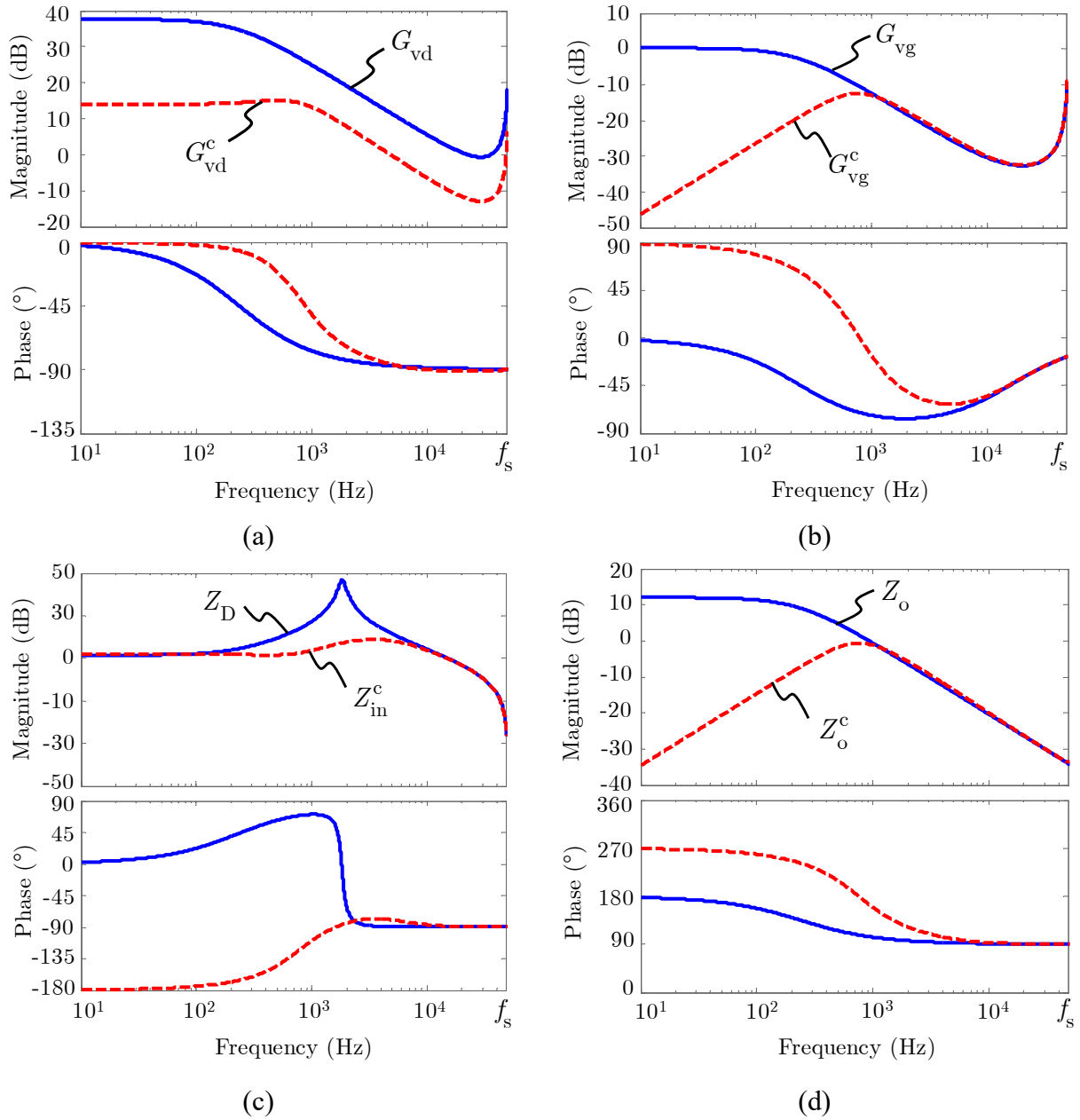

Figure 3.13 : Open-loop vs closed-loop transfer functions (model 4)

3.7 Input filter sizing

3.7.1 Input filter transfer functions

In practice, a low-pass filter is generally added at the input of dc-dc converters to meet electromagnetic compatibility (EMC) requirements. The common practice is to use a 2nd order LC-filter as shown in Figure 3.14. Four (4) transfer functions are considered from a systems integration standpoint. They are given as follows. The input impedance Z_{f} is given by,

$$Z_{\mathrm{f}}(s)=\frac{\hat{v}_{\mathrm{s}}(s)}{\hat{i}_{\mathrm{s}}(s)}=\frac{s^2L_{\mathrm{g}}C_{\mathrm{i}}+s\left(R_{\mathrm{g}}+R_{\mathrm{i}}\right)C_{\mathrm{i}}+1}{sC_{\mathrm{i}}} \tag{3.125}$$

The output impedance Z_{g} is given by,

$$Z_{\mathrm{g}}(s)=-\frac{\hat{v}_{\mathrm{i}}(s)}{\hat{i}_{\mathrm{i}}(s)}=-\frac{s^2R_{\mathrm{i}}L_{\mathrm{g}}C_{\mathrm{i}}+s\left(R_{\mathrm{g}}R_{\mathrm{i}}C_{\mathrm{i}}+L_{\mathrm{g}}\right)+R_{\mathrm{g}}}{s^2L_{\mathrm{g}}C_{\mathrm{i}}+s\left(R_{\mathrm{g}}+R_{\mathrm{i}}\right)C_{\mathrm{i}}+1} \tag{3.126}$$

The input-to-output voltage transfer function G_{o} is given by,

$$G_{\mathrm{o}}(s)=\frac{\hat{v}_{\mathrm{i}}(s)}{\hat{v}_{\mathrm{s}}(s)}=\frac{sR_{\mathrm{i}}C_{\mathrm{i}}+1}{s^2L_{\mathrm{g}}C_{\mathrm{i}}+s\left(R_{\mathrm{g}}+R_{\mathrm{i}}\right)C_{\mathrm{i}}+1} \tag{3.127}$$

The back-current transfer function H_{i} is given by,

$$H_{\mathrm{i}}(s)=\frac{\hat{i}_{\mathrm{s}}(s)}{\hat{i}_{\mathrm{i}}(s)}=\frac{Z_{\mathrm{g}}(s)}{R_{\mathrm{g}}+sL_{\mathrm{g}}} \tag{3.128}$$

The input filter is generally selected based on desired characteristics of G_{o}, H_{i} and Z_{f}. The input-to-output voltage transfer function G_{o} is important because it shows how voltage noise coming from the source will propagates at the converter input, which can further propagate at the output of the converter through its closed-loop input-to-output transfer function $G_{\mathrm{vg}}^{\mathrm{c}}$. The transfer function H_{i} is also of interest because it allows to design a filter which reduces the propagation of noise current generated by the converter back to the source. In some applications, it may also be desirable to have a minimum input impedance at given frequencies to avoid circulating currents at these frequencies which could further impact other systems in the network.

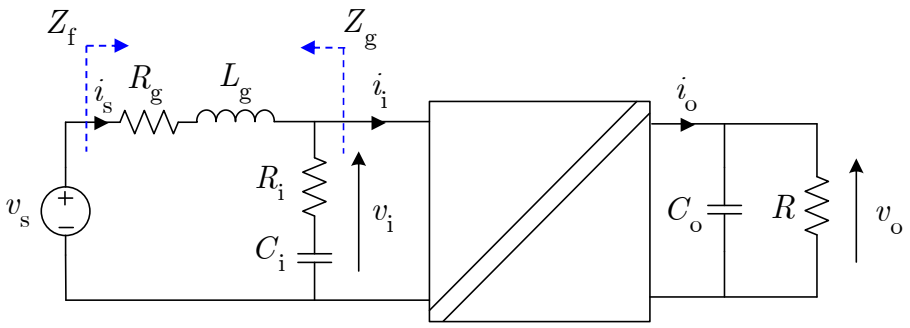

Figure 3.14 : Converter with input filter

3.7.2 Modified transfer functions and stability analysis

The output impedance Z_g is generally the consequence of design choices on Z_f, G_o and H_i. However, Z_g affects the dynamic performance of the converter and the overall system may even become unstable if it is not properly considered during design. In fact, the input filter affects the open-loop transfer functions of the converter, mainly the control-to-output transfer function G_{vd}, the input-to-output transfer function G_{vg}, and the output impedance Z_o [30]. Consequently, the closed-loop behavior of the converter is also impacted.

According to Middlebrook's EET [30], [55], the magnitude of the output impedance of the input filter Z_g should meet (3.129) to both ensure stability and that the input filter does not substantially alter the converter open-loop transfer functions,

$$\left|Z_g(s)\right| \ll \left|Z_N(s)\right|, \quad \left|Z_g(s)\right| \ll \left|Z_D(s)\right| \tag{3.129}$$

Middlebrook's EET is a widely used stability criterion. It is used not only to guarantee stability, but also to ensure that the introduction of an input filter does not substantially alter the converter open-loop transfer functions G_{vd}, G_{vg} and Z_o. Its application greatly reduces the required number of both time-domain simulations and experiments to 1) predict stability, and 2) design a system with an acceptable and predictable transient response. It is known to be a conservative approach which means that, even if (3.129) is violated, the system still can be stable [60]. Knowing all the converter transfer functions, it is frequent practice to analyze the modified converter loop gain. This is a key step to ensure the predictability of the converter dynamic. Under the presence of an additional input filter, the converter control-to-output transfer function is modified following [30],

$$G_{\mathrm{vd}}^{\mathrm{new}}(s)=G_{\mathrm{vd}}(s)\left(\frac{1+Z_{\mathrm{g}}(s)/Z_{\mathrm{N}}(s)}{1+Z_{\mathrm{g}}(s)/Z_{\mathrm{D}}(s)}\right) \tag{3.130}$$

which leads to the modified loop gain calculated as,

$$T^{\mathrm{new}}(s)=T(s)\left(\frac{1+Z_{\mathrm{g}}(s)/Z_{\mathrm{N}}(s)}{1+Z_{\mathrm{g}}(s)/Z_{\mathrm{D}}(s)}\right) \tag{3.131}$$

The correction factor K_{corr} is also defined as [30],

$$K_{\mathrm{corr}}(s)=\left(\frac{1+Z_{\mathrm{g}}(s)/Z_{\mathrm{N}}(s)}{1+Z_{\mathrm{g}}(s)/Z_{\mathrm{D}}(s)}\right) \tag{3.132}$$

From (3.129)–(3.132), it is again concluded that, being able to evaluate Z_{D} and Z_{N}, allows evaluating the impacts of the input filter on the converter dynamic. The utilization of the developed models is demonstrated through the application of Middlebrook's extra element theorem for additional input filter. Three filters are designed. The magnitude of all their transfer functions is shown in Figure 3.15. The filter parameters are shown in Table 3.3. The value of the input capacitor C_{i} is kept constant and the inductor L_{g} is increased such that the filter cut-off frequency f_{g} is decreased.

According to (3.129) and analyzing Figure 3.15 d), Filter A is not expected to largely deteriorate the dynamic response, but Filter B and Filter C are expected to substantially impact the dynamic performance. By analyzing the results in Figure 3.16 and Figure 3.17, it is concluded that Filter B and Filter C have an important impact on the transient performance of the converter. Filter C even lead to instability, that is, an oscillating behavior. In dc systems, unstable conditions are often characterized by a constant AC component superimposed on the DC value [81]. In practical applications, saturation of the controller introduces non-linear behavior which often leads to oscillating waveforms exhibiting saturation plateau. The results in Figure 3.18 show an example of waveforms on a 3p-DAB converter with an input filter which does not meet Middlebrook's theorem. The phase-shift δ (purple) oscillates and saturates at 90°. The output voltage v_{o} (cyan) is oscillating around its reference $v_{\mathrm{o}}^{\mathrm{ref}}$ (yellow). The input voltage v_{i} (green) also exhibits unwanted oscillations due to the constant power (i.e. negative incremental resistance) behavior of the converter input impedance.

Table 3.3: Input filter parameters

Parameter	Symbol	Filter A	Filter B	Filter C
Input Inductor	L_g	47 µH	188 µH	376 µH
Inductor ESR	R_g	20.8 mΩ	83.2 mΩ	166 mΩ
Input Capacitor	C_i	82 µF	82 µF	82 µF
Capacitor ESR	R_i	120 mΩ	120 mΩ	120 mΩ
Cut-off frequency	f_g	2.56 kHz	1.28 kHz	905 Hz

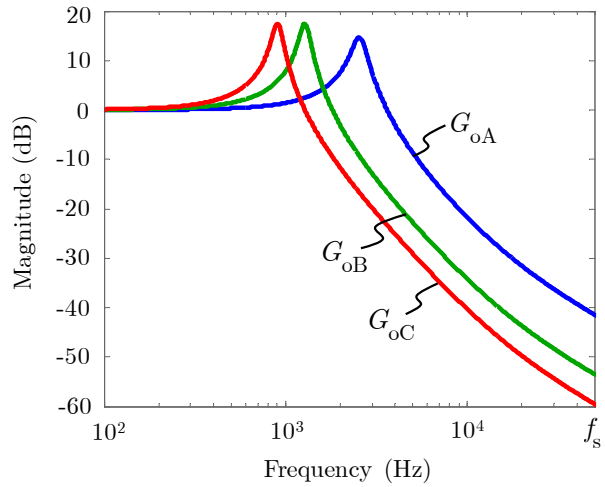

(a) Input-to-output voltage transfer function

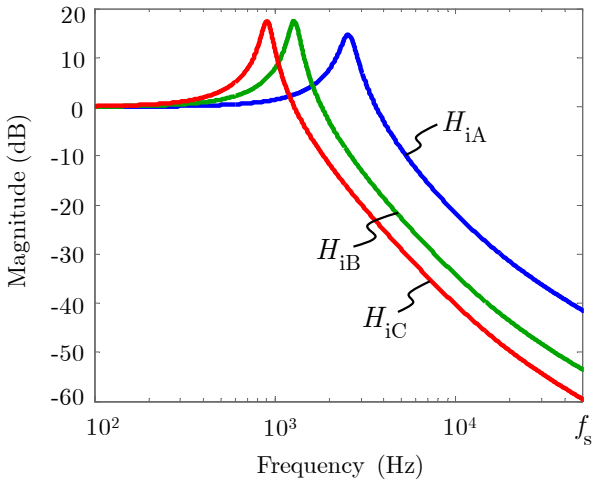

(b) Back-current transfer function

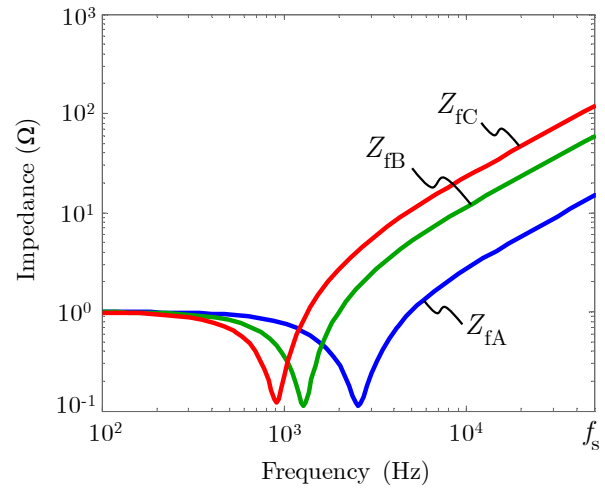

(c) Filter input impedance

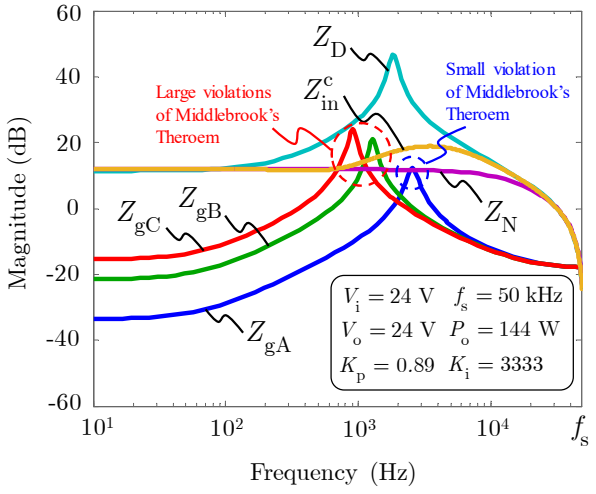

(d) Filter output impedance vs converter input impedance (Middlebrook's theorem)

Figure 3.15 : Input filter transfer functions magnitude

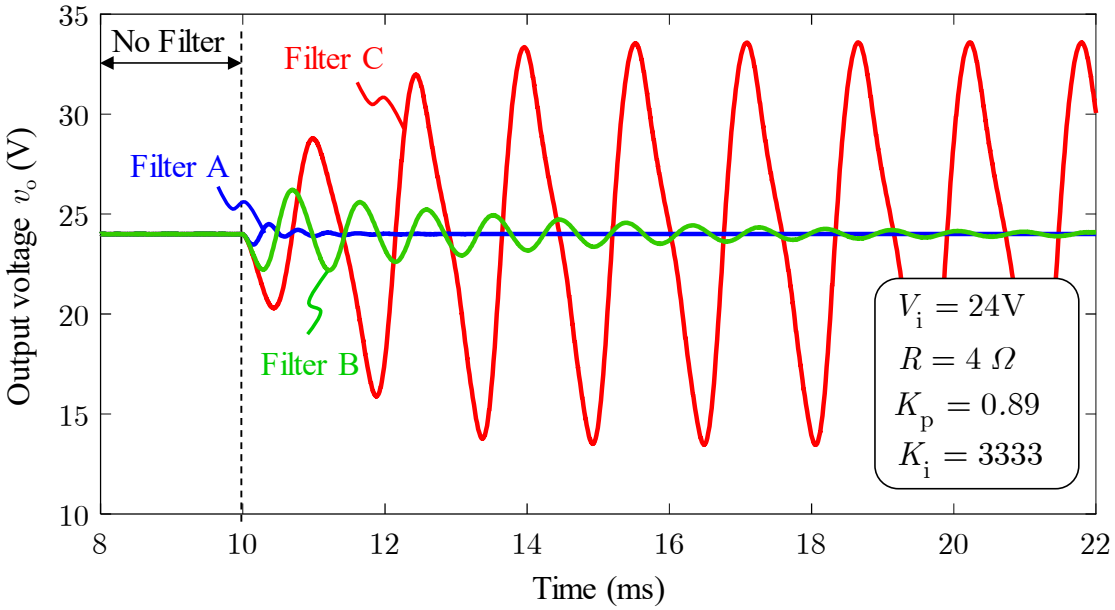

Figure 3.16 : Transient response after introduction of filters (model 4)

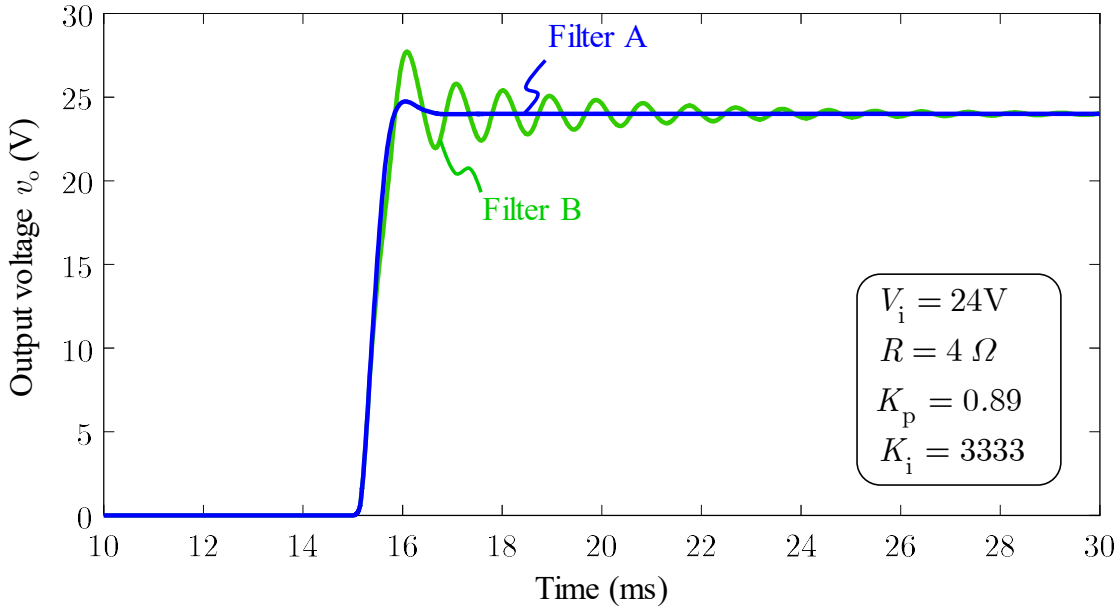

Figure 3.17 : Response to a step in the reference voltage from 0 V to 24 V (model 4)

Figure 3.18 : Unstable condition due to an additional input filter

3.7.3 Experimental results

The impact of an additional input filter on the transient response is verified with the experimental prototype. An input filter (Filter D) with the parameters given in Figure 3.19 a) is designed. It is added at the input of the closed-loop 3p-DAB prototype operated at the operating point given in Figure 3.19 a). As seen in Figure 3.19 a), the magnitude of the filter output impedance Z_{gD} is violating Middlebrook's EET (3.129) with respect to the null driving point impedance Z_N. This means that the correction factor (Figure 3.19 b)) will impact both the magnitude and the phase of the converter transfer functions according to (3.130)–(3.132), thus, its transient response. The experimental results in Figure 3.20 and Figure 3.21 confirm the degradation in the transient response. The overshoot OS increases from 8% without input filter to 16% with Filter D.

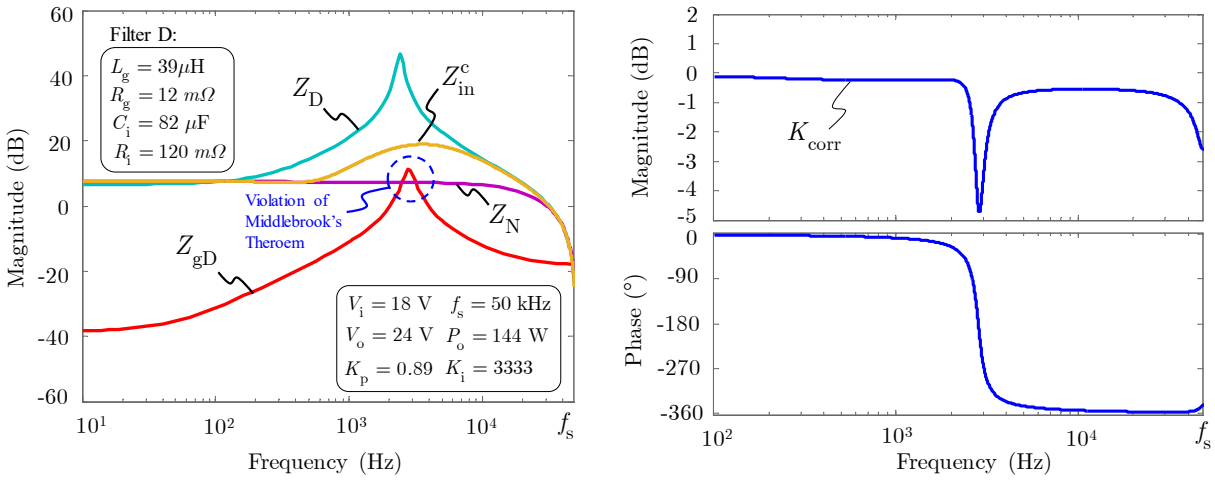

(a) Middlebrook's theorem application (b) Correction factor with Filter D

Figure 3.19 : Input filter transfer functions magnitude (model 4)

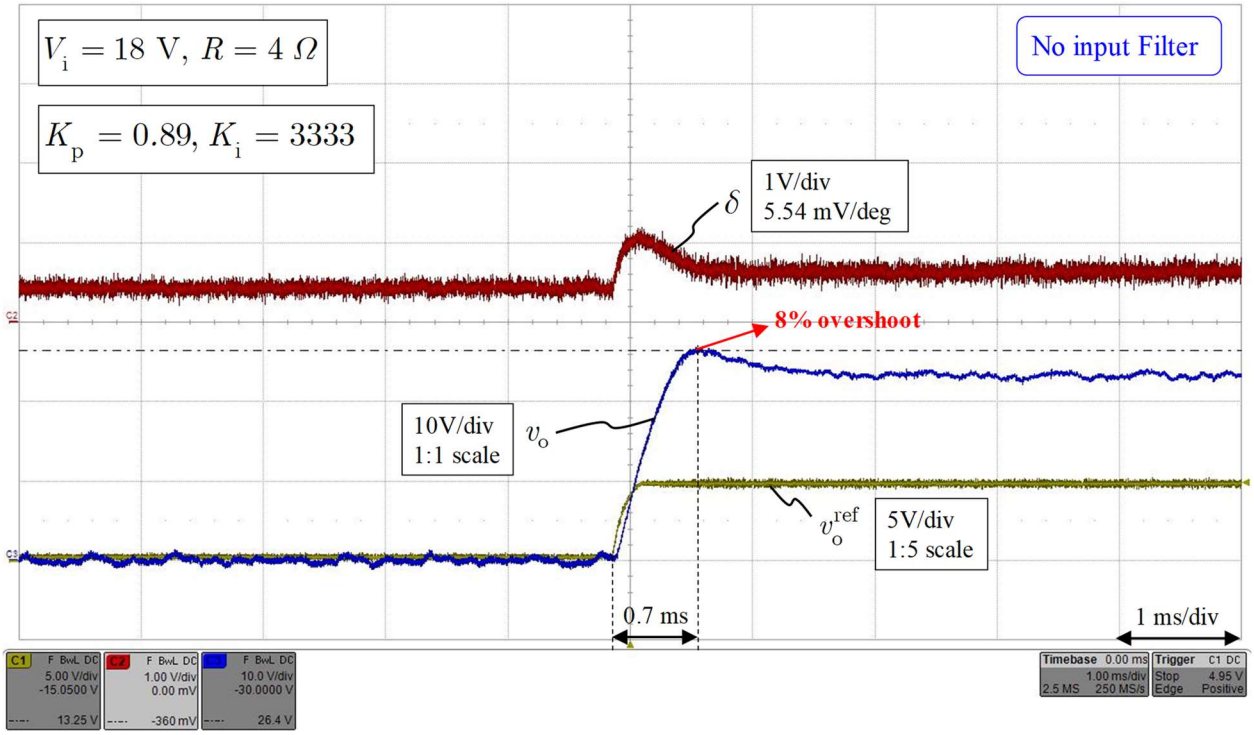

Figure 3.20 : Response to a step in the reference voltage without input filter (prototype)

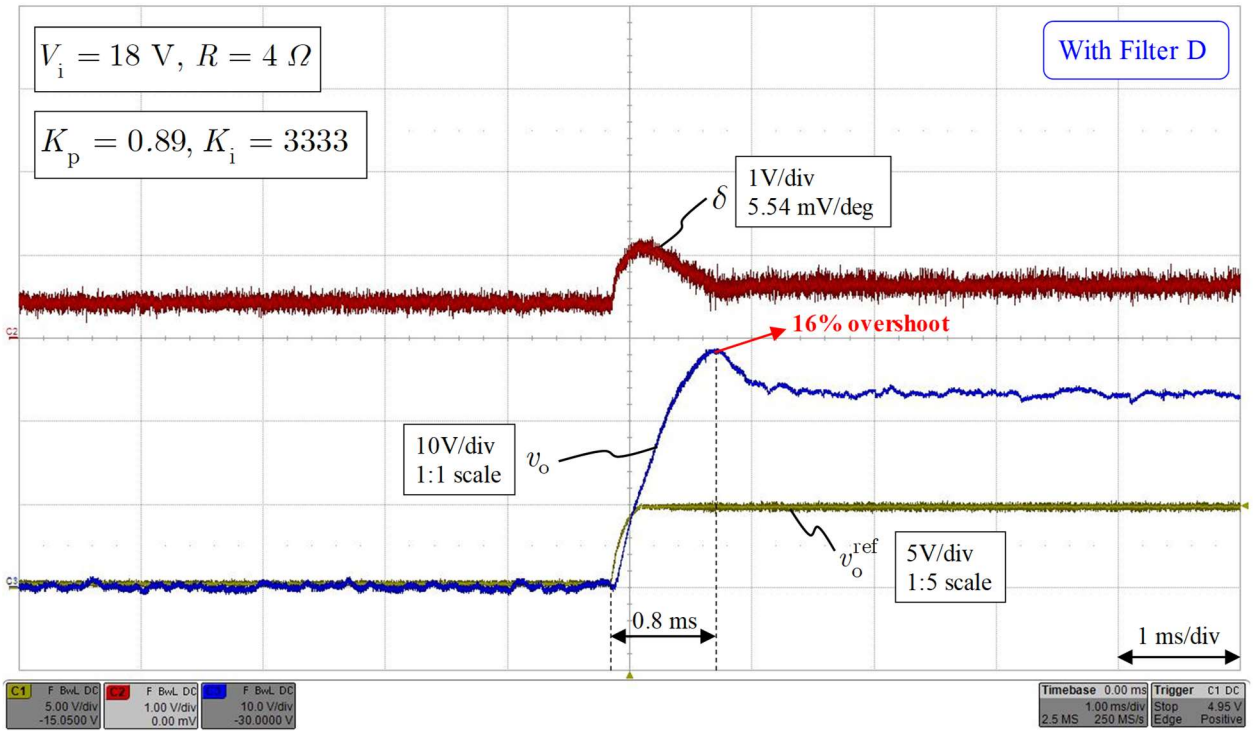

Figure 3.21 : Response to a step in the reference voltage with Filter D (prototype)

CHAPTER 4 LARGE-SIGNAL TIME-DOMAIN SIMULATION

In this chapter, large-signal models are developed to enable system-level simulation of dc-grids with 3p-DAB converters in EMT-type programs. Switching-functions (SWF), state-space averaging (SSA) and generalized averaging (GAM) models of the Y-Δ 3p-DAB converter are developed, implemented and compared with the ideal-model approach in EMTP. While the implementation of the SWF and SSA models is presented for comparison purpose, the main contribution of this chapter is the development and the implementation of the GAM model.

4.1 Switching-function (SWF) model

The concept of switching-functions has been first introduced in [63] for the simulation of three-phase inverters in PSpice. For the 3p-DAB, it consists in replacing each leg of each bridge by an equivalent controlled current source seen from the dc-side (Figure 4.1 a)), and an equivalent controlled voltage source seen from the ac-side (Figure 4.1 b)). The three-phase transformer is directly modeled using EMTP ideal transformer model, which allows to easily consider the winding-connection, the ratio m and the series inductances L_{A}, L_{B} and L_{C}. The input and output diodes D_{i} and D_{o} are used to model the effect of the input and output bridges anti-parallel diodes on negative voltage. These diodes prevent the voltage from becoming negative at either one of the two dc ports. Their importance is discussed in section 4.4.3.

The switching-functions are defined by the gating signals coming from the output of the modulator as defined in Appendix C. In Figure 4.1 c), the switching-functions for phase A are provided as an example. Phases B and C are ±120º phase-shifted from phase A. For any transformer connection, the input current source is calculated using (2.33) and the output current source is calculated as follows.

$$i_{\mathrm{o}} = \mathrm{s}_1^{'} i_{\mathrm{a}} + \mathrm{s}_3^{'} i_{\mathrm{b}} + \mathrm{s}_5^{'} i_{\mathrm{c}} \tag{4.1}$$

The transformer primary and secondary voltage sources are defined as,

$$v_{\mathrm{A}} = \left(2\mathrm{s}_1 - 1\right)\frac{v_{\mathrm{i}}}{2}, v_{\mathrm{B}} = \left(2\mathrm{s}_3 - 1\right)\frac{v_{\mathrm{i}}}{2}, v_{\mathrm{C}} = \left(2\mathrm{s}_5 - 1\right)\frac{v_{\mathrm{i}}}{2} \tag{4.2}$$

$$v_{\mathrm{a}} = \left(2\mathrm{s}_1^{'} - 1\right)\frac{v_{\mathrm{o}}}{2}, v_{\mathrm{b}} = \left(2\mathrm{s}_3^{'} - 1\right)\frac{v_{\mathrm{o}}}{2}, v_{\mathrm{c}} = \left(2\mathrm{s}_5^{'} - 1\right)\frac{v_{\mathrm{o}}}{2} \tag{4.3}$$

All the switching-functions, currents and voltages in (4.1)–(4.3) are updated at each time-step Δt. The dependence to time has been removed for the sake of clarity of the presented material. The control phase-shift δ is hidden in (4.3) though the calculation of the output bridge switching-functions s'_1, s'_3 and s'_5. In open-loop, the phase-shift δ is fixed while in closed-loop it is calculated by implementing the controller structure shown in Figure 1.4 b). The implementation of the SWF model also requires to completely model the modulator.

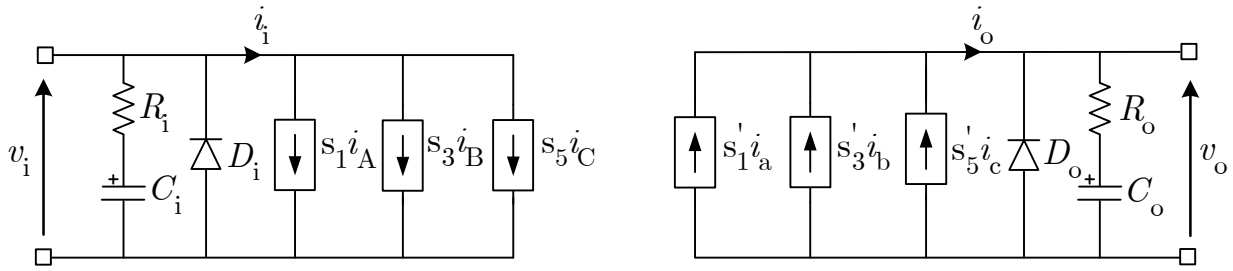

(a) Equivalent switching-function model of the 3p-DAB seen from the dc-grids

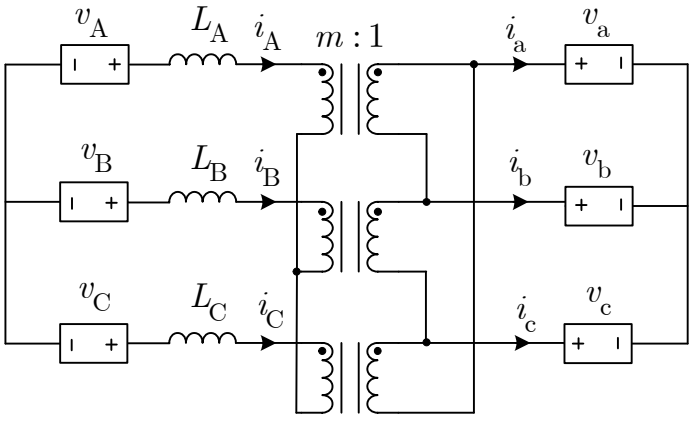

(b) Equivalent Y-Δ transformer model

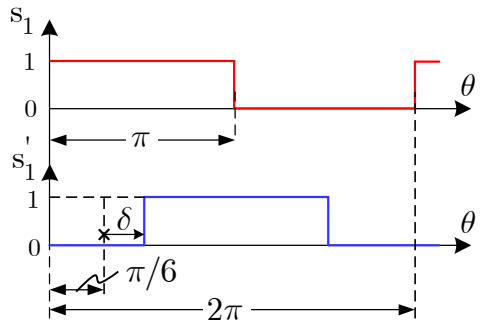

(c) Switching-functions for phase A

Figure 4.1 : SWF model of the Y-Δ 3p-DAB

4.2 State-space averaging (SSA) model

The state-space averaging (SSA) method [51] has been first applied in [54] to approximate the control-to-output G_{vd} and the input-to-output G_{vg} transfer functions of the Y-Y 3p-DAB converter. Since there is no resource in the literature regarding the use of SSA for large-signal analysis of 3p-DAB converters in EMT-type programs, the approach used in this thesis is presented in the next paragraphs.

Following the averaging steps described in section 3.2, the index-0 (dc) model of the converter is obtained. As it is derived using the piecewise-linear modeling (PLM) approach, it results in two sets of equations which depend on the phase-shift δ operating range. Using (2.37) and (2.38) which assumes a lossless converter, the resulting averaged input current $\langle i_{\mathrm{i}} \rangle_0$ and output current $\langle i_{\mathrm{o}} \rangle_0$ are calculated at each time-step Δt. They are used to control the current sources of Figure 4.2. For range 1 ($0 \leq \delta \leq \pi/6$), the input and output currents are given by,

$$\langle i_{\mathrm{i}} \rangle_0 = \left(\frac{m}{\omega_{\mathrm{s}} L_{\mathrm{s}}} \right) \cdot \langle \delta \rangle_0 \cdot \langle v_{\mathrm{o}} \rangle_0 \tag{4.4}$$

$$\langle i_{\mathrm{o}} \rangle_0 = \left(\frac{m}{\omega_{\mathrm{s}} L_{\mathrm{s}}} \right) \cdot \langle \delta \rangle_0 \cdot \langle v_{\mathrm{i}} \rangle_0 \tag{4.5}$$

and for range 2 ($\pi/6 \leq \delta \leq \pi/2$), they are calculated by,

$$\langle i_{\mathrm{i}} \rangle_0 = \left(\frac{m}{\omega_{\mathrm{s}} L_{\mathrm{s}}} \right) \left[\frac{3}{2} \left(\langle \delta \rangle_0 - \frac{\left(\langle \delta \rangle_0 \right)^2}{\pi} \right) - \frac{\pi}{24} \right] \langle v_{\mathrm{o}} \rangle_0 \tag{4.6}$$

$$\langle i_{\mathrm{o}} \rangle_0 = \left(\frac{m}{\omega_{\mathrm{s}} L_{\mathrm{s}}} \right) \left[\frac{3}{2} \left(\langle \delta \rangle_0 - \frac{\left(\langle \delta \rangle_0 \right)^2}{\pi} \right) - \frac{\pi}{24} \right] \langle v_{\mathrm{i}} \rangle_0 \tag{4.7}$$

As for the SWF model, in open-loop, the phase-shift $\langle \delta \rangle_0$ is fixed while, in closed-loop, it is calculated by implementing the controller structure presented in Figure 1.4 b).

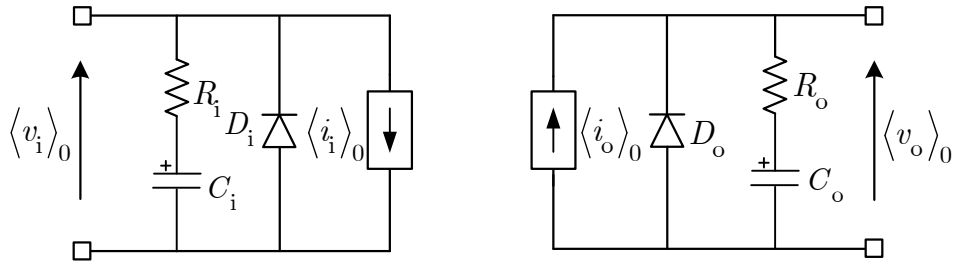

Figure 4.2 : SSA model of the Y-Δ 3p-DAB

4.3 Generalized averaging model (GAM)

The generalized averaging model (GAM) is based on the averaged index-0 (dc) and the index-1 (fundamental frequency) system of equations (3.61)–(3.69) developed in section 3.3.1.2. As for the SSA model, seen from the dc-grids, the GAM approach leads to the equivalent index-0 model shown in Figure 4.3 a). The index-0 model is governed by a system of equations which is function of the index-1 model (Figure 4.3 b) to g)). The index-1 model includes the ac dynamic of both the transformer currents and the switching-functions. The index-1 model can be solved in EMTP by either using control system equations or the network solver with controlled voltage sources and inductors to implement the equivalent circuits shown in Figure 4.3 b) to g).

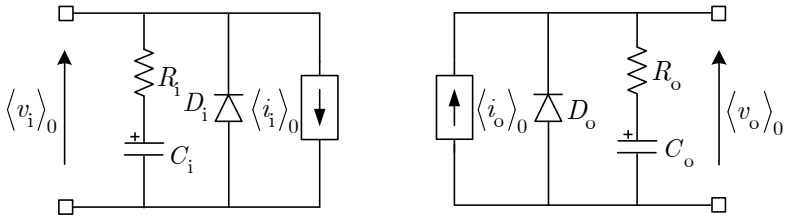

(a) Index-0 (dc) model

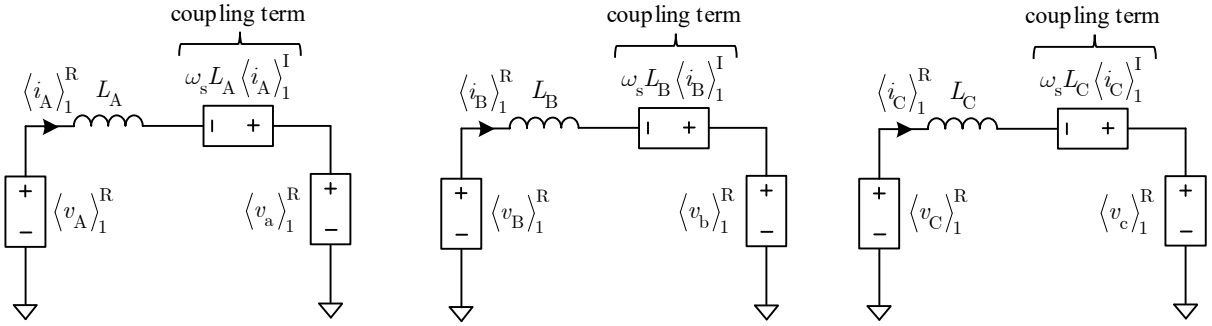

(b) Phase A – Real Part (c) Phase B – Real Part (d) Phase C – Real Part

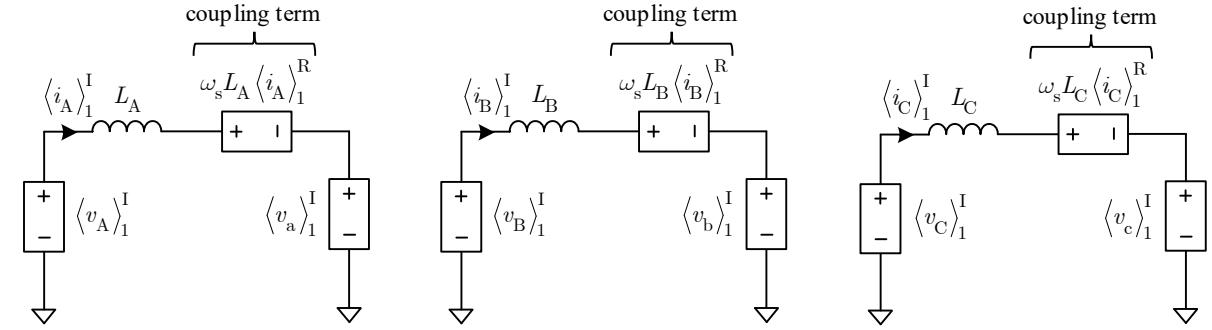

(e) Phase A – Imaginary Part (f) Phase B – Imaginary Part (g) Phase C – Imaginary Part

Figure 4.3 : GAM model of the Y-Δ 3p-DAB

In this thesis, the index-1 model has been implemented using the control system equations. The large-signal model of the 3p-DAB converter is given here using the following state-space notation,

$$\frac{d\left\langle \mathbf{x} \right\rangle}{dt} = \mathbf{A}\left\langle \mathbf{x} \right\rangle + \mathbf{B}\left\langle \mathbf{u} \right\rangle \tag{4.8}$$

$$\left\langle \mathbf{y} \right\rangle = \mathbf{C}\left\langle \mathbf{x} \right\rangle + \mathbf{D}\left\langle \mathbf{u} \right\rangle \tag{4.9}$$

with,

$$\left\langle \mathbf{x} \right\rangle = \left[\left\langle i_{\mathrm{A}} \right\rangle_1^{\mathrm{R}} \left\langle i_{\mathrm{A}} \right\rangle_1^{\mathrm{I}} \left\langle i_{\mathrm{B}} \right\rangle_1^{\mathrm{R}} \left\langle i_{\mathrm{B}} \right\rangle_1^{\mathrm{I}} \left\langle i_{\mathrm{C}} \right\rangle_1^{\mathrm{R}} \left\langle i_{\mathrm{C}} \right\rangle_1^{\mathrm{I}} \right]^T \tag{4.10}$$

$$\left\langle \mathbf{u} \right\rangle = \left[\left\langle v_{\mathrm{i}} \right\rangle_0 \left\langle v_{\mathrm{o}} \right\rangle_0 \right]^{\mathrm{T}}, \left\langle \mathbf{y} \right\rangle = \left[\left\langle i_{\mathrm{i}} \right\rangle_0 \left\langle i_{\mathrm{o}} \right\rangle_0 \right]^{\mathrm{T}} \tag{4.11}$$

The resulting system of equations defined by (4.8)–(4.18) is implemented in EMTP by using the control blocks and solved based on [82]. The calculated values of the input current $\left\langle i_{\mathrm{i}} \right\rangle_0$ and the output current $\left\langle i_{\mathrm{o}} \right\rangle_0$ are used to control the current sources of Figure 4.3 a). The system matrices $\mathbf{A}$, $\mathbf{B}$, $\mathbf{C}$ and $\mathbf{D}$ are time-dependent and given by,

$$\mathbf{A} = \begin{bmatrix} 0 & \omega_{\mathrm{s}} & 0 & 0 & 0 & 0 \\ -\omega_{\mathrm{s}} & 0 & 0 & 0 & 0 & 0 \\ 0 & 0 & 0 & \omega_{\mathrm{s}} & 0 & 0 \\ 0 & 0 & -\omega_{\mathrm{s}} & 0 & 0 & 0 \\ 0 & 0 & 0 & 0 & 0 & \omega_{\mathrm{s}} \\ 0 & 0 & 0 & 0 & -\omega_{\mathrm{s}} & 0 \end{bmatrix}, \mathbf{B} = \begin{bmatrix} B_{11} & B_{12} \\ B_{21} & B_{22} \\ B_{31} & B_{32} \\ B_{41} & B_{42} \\ B_{51} & B_{52} \\ B_{61} & B_{62} \end{bmatrix}$$

$$\mathbf{C} = \begin{bmatrix} C_{11} & C_{12} & C_{13} & C_{14} & C_{15} & C_{16} \\ C_{21} & C_{22} & C_{23} & C_{24} & C_{25} & C_{26} \end{bmatrix}, \mathbf{D} = \begin{bmatrix} 0 & 0 \\ 0 & 0 \end{bmatrix} \tag{4.12}$$

with,

$$\begin{aligned} B_{12} &= \frac{m}{L_{\mathrm{A}}}\left(\left\langle \mathrm{s}_3^{'} \right\rangle_1^{\mathrm{R}} - \left\langle \mathrm{s}_1^{'} \right\rangle_1^{\mathrm{R}} \right), B_{22} = \frac{m}{L_{\mathrm{A}}}\left(\left\langle \mathrm{s}_3^{'} \right\rangle_1^{\mathrm{I}} - \left\langle \mathrm{s}_1^{'} \right\rangle_1^{\mathrm{I}} \right) \\ B_{32} &= \frac{m}{L_{\mathrm{B}}}\left(\left\langle \mathrm{s}_5^{'} \right\rangle_1^{\mathrm{R}} - \left\langle \mathrm{s}_3^{'} \right\rangle_1^{\mathrm{R}} \right), B_{42} = \frac{m}{L_{\mathrm{B}}}\left(\left\langle \mathrm{s}_5^{'} \right\rangle_1^{\mathrm{I}} - \left\langle \mathrm{s}_3^{'} \right\rangle_1^{\mathrm{I}} \right) \\ B_{52} &= \frac{m}{L_{\mathrm{C}}}\left(\left\langle \mathrm{s}_1^{'} \right\rangle_1^{\mathrm{R}} - \left\langle \mathrm{s}_5^{'} \right\rangle_1^{\mathrm{R}} \right), B_{62} = \frac{m}{L_{\mathrm{C}}}\left(\left\langle \mathrm{s}_1^{'} \right\rangle_1^{\mathrm{I}} - \left\langle \mathrm{s}_5^{'} \right\rangle_1^{\mathrm{I}} \right) \end{aligned} \tag{4.13}$$

$$B_{11}=\frac{1}{3L_{\mathrm{A}}}\left[2\left\langle \mathrm{s}_1\right\rangle_1^{\mathrm{R}}-\left\langle \mathrm{s}_3\right\rangle_1^{\mathrm{R}}-\left\langle \mathrm{s}_5\right\rangle_1^{\mathrm{R}}\right],\ B_{21}=\frac{1}{3L_{\mathrm{A}}}\left[2\left\langle \mathrm{s}_1\right\rangle_1^{\mathrm{I}}-\left\langle \mathrm{s}_3\right\rangle_1^{\mathrm{I}}-\left\langle \mathrm{s}_5\right\rangle_1^{\mathrm{I}}\right]$$
$$B_{31}=\frac{1}{3L_{\mathrm{B}}}\left[2\left\langle \mathrm{s}_3\right\rangle_1^{\mathrm{R}}-\left\langle \mathrm{s}_1\right\rangle_1^{\mathrm{R}}-\left\langle \mathrm{s}_5\right\rangle_1^{\mathrm{R}}\right],\ B_{41}=\frac{1}{3L_{\mathrm{B}}}\left[2\left\langle \mathrm{s}_3\right\rangle_1^{\mathrm{I}}-\left\langle \mathrm{s}_1\right\rangle_1^{\mathrm{I}}-\left\langle \mathrm{s}_5\right\rangle_1^{\mathrm{I}}\right] \tag{4.14}$$
$$B_{51}=\frac{1}{3L_{\mathrm{C}}}\left[2\left\langle \mathrm{s}_5\right\rangle_1^{\mathrm{R}}-\left\langle \mathrm{s}_1\right\rangle_1^{\mathrm{R}}-\left\langle \mathrm{s}_3\right\rangle_1^{\mathrm{R}}\right],\ B_{61}=\frac{1}{3L_{\mathrm{C}}}\left[2\left\langle \mathrm{s}_5\right\rangle_1^{\mathrm{I}}-\left\langle \mathrm{s}_1\right\rangle_1^{\mathrm{I}}-\left\langle \mathrm{s}_3\right\rangle_1^{\mathrm{I}}\right]$$

$$C_{21}=2m\left(\left\langle \mathrm{s}_1^{'}\right\rangle_1^{\mathrm{R}}-\left\langle \mathrm{s}_3^{'}\right\rangle_1^{\mathrm{R}}\right),\ C_{22}=2m\left(\left\langle \mathrm{s}_1^{'}\right\rangle_1^{\mathrm{I}}-\left\langle \mathrm{s}_3^{'}\right\rangle_1^{\mathrm{I}}\right)$$
$$C_{23}=2m\left(\left\langle \mathrm{s}_3^{'}\right\rangle_1^{\mathrm{R}}-\left\langle \mathrm{s}_5^{'}\right\rangle_1^{\mathrm{R}}\right),\ C_{24}=2m\left(\left\langle \mathrm{s}_3^{'}\right\rangle_1^{\mathrm{I}}-\left\langle \mathrm{s}_5^{'}\right\rangle_1^{\mathrm{I}}\right) \tag{4.15}$$
$$C_{25}=2m\left(\left\langle \mathrm{s}_5^{'}\right\rangle_1^{\mathrm{R}}-\left\langle \mathrm{s}_1^{'}\right\rangle_1^{\mathrm{R}}\right),\ C_{26}=2m\left(\left\langle \mathrm{s}_5^{'}\right\rangle_1^{\mathrm{I}}-\left\langle \mathrm{s}_1^{'}\right\rangle_1^{\mathrm{I}}\right)$$

$$C_{11}=2\left\langle \mathrm{s}_1\right\rangle_1^{\mathrm{R}},\ C_{12}=2\left\langle \mathrm{s}_1\right\rangle_1^{\mathrm{I}},\ C_{13}=2\left\langle \mathrm{s}_3\right\rangle_1^{\mathrm{R}}$$
$$C_{14}=2\left\langle \mathrm{s}_3\right\rangle_1^{\mathrm{I}},\ C_{15}=2\left\langle \mathrm{s}_5\right\rangle_1^{\mathrm{R}},\ C_{16}=2\left\langle \mathrm{s}_5\right\rangle_1^{\mathrm{I}} \tag{4.16}$$

As shown in section 3.3.1.2, for the input bridge, the averaged switching-functions are constant because they do not depend on the control phase-shift. They are expressed here as,

$$\left\langle \mathrm{s}_1\right\rangle_1=\frac{1}{\pi}e^{-j\frac{\pi}{2}},\ \left\langle \mathrm{s}_3\right\rangle_1=\frac{1}{\pi}e^{j\frac{\pi}{6}},\ \left\langle \mathrm{s}_5\right\rangle_1=\frac{1}{\pi}e^{j\frac{5\pi}{6}} \tag{4.17}$$

For the output bridge, they depend on the instantaneous value of the control phase-shift $\left\langle \delta\right\rangle_0$ and are referenced with respect to the input bridge. They are expressed here using Euler's formula,

$$\left\langle \mathrm{s}_1^{'}\right\rangle_1=\left\langle \mathrm{s}_1\right\rangle_1 e^{-j\left(\frac{\pi}{6}+\left\langle \delta\right\rangle_0\right)},\left\langle \mathrm{s}_3^{'}\right\rangle_1=\left\langle \mathrm{s}_3\right\rangle_1 e^{-j\left(\frac{\pi}{6}+\left\langle \delta\right\rangle_0\right)},\left\langle \mathrm{s}_5^{'}\right\rangle_1=\left\langle \mathrm{s}_5\right\rangle_1 e^{-j\left(\frac{\pi}{6}+\left\langle \delta\right\rangle_0\right)} \tag{4.18}$$

For solving the index-1 model using the network solver (instead of the control equations solver) as in Figure 4.3 b) to g), the voltage sources are the following,

$$\left\langle v_{\mathrm{A}}\right\rangle_1^{\mathrm{R}}=\frac{1}{3}\left[2\left\langle \mathrm{s}_1\right\rangle_1^{\mathrm{R}}-\left\langle \mathrm{s}_3\right\rangle_1^{\mathrm{R}}-\left\langle \mathrm{s}_5\right\rangle_1^{\mathrm{R}}\right]\cdot\left\langle v_{\mathrm{i}}\right\rangle_0,\quad \left\langle v_{\mathrm{a}}\right\rangle_1^{\mathrm{R}}=m\left[\left\langle \mathrm{s}_1^{'}\right\rangle_1^{\mathrm{R}}-\left\langle \mathrm{s}_3^{'}\right\rangle_1^{\mathrm{R}}\right]\cdot\left\langle v_{\mathrm{o}}\right\rangle_0 \tag{4.19}$$

$$\left\langle v_{\mathrm{A}}\right\rangle_1^{\mathrm{I}}=\frac{1}{3}\left[2\left\langle \mathrm{s}_1\right\rangle_1^{\mathrm{I}}-\left\langle \mathrm{s}_3\right\rangle_1^{\mathrm{I}}-\left\langle \mathrm{s}_5\right\rangle_1^{\mathrm{I}}\right]\cdot\left\langle v_{\mathrm{i}}\right\rangle_0,\quad \left\langle v_{\mathrm{a}}\right\rangle_1^{\mathrm{I}}=m\left[\left\langle \mathrm{s}_1^{'}\right\rangle_1^{\mathrm{I}}-\left\langle \mathrm{s}_3^{'}\right\rangle_1^{\mathrm{I}}\right]\cdot\left\langle v_{\mathrm{o}}\right\rangle_0 \tag{4.20}$$

$$\left\langle v_{\mathrm{B}}\right\rangle_1^{\mathrm{R}}=\frac{1}{3}\left[2\left\langle \mathrm{s}_3\right\rangle_1^{\mathrm{R}}-\left\langle \mathrm{s}_1\right\rangle_1^{\mathrm{R}}-\left\langle \mathrm{s}_5\right\rangle_1^{\mathrm{R}}\right]\cdot\left\langle v_{\mathrm{i}}\right\rangle_0,\quad \left\langle v_{\mathrm{b}}\right\rangle_1^{\mathrm{R}}=m\left[\left\langle \mathrm{s}_3^{'}\right\rangle_1^{\mathrm{R}}-\left\langle \mathrm{s}_5^{'}\right\rangle_1^{\mathrm{R}}\right]\cdot\left\langle v_{\mathrm{o}}\right\rangle_0 \tag{4.21}$$

$$\left\langle v_{\mathrm{B}}\right\rangle_1^{\mathrm{I}}=\frac{1}{3}\left[2\left\langle \mathrm{s}_3\right\rangle_1^{\mathrm{I}}-\left\langle \mathrm{s}_1\right\rangle_1^{\mathrm{I}}-\left\langle \mathrm{s}_5\right\rangle_1^{\mathrm{I}}\right]\cdot\left\langle v_{\mathrm{i}}\right\rangle_0,\quad \left\langle v_{\mathrm{b}}\right\rangle_1^{\mathrm{I}}=m\left[\left\langle \mathrm{s}_3^{'}\right\rangle_1^{\mathrm{I}}-\left\langle \mathrm{s}_5^{'}\right\rangle_1^{\mathrm{I}}\right]\cdot\left\langle v_{\mathrm{o}}\right\rangle_0 \tag{4.22}$$

$$\left\langle v_{\mathrm{C}}\right\rangle_1^{\mathrm{R}}=\frac{1}{3}\left[2\left\langle \mathrm{s}_5\right\rangle_1^{\mathrm{R}}-\left\langle \mathrm{s}_1\right\rangle_1^{\mathrm{R}}-\left\langle \mathrm{s}_3\right\rangle_1^{\mathrm{R}}\right]\cdot\left\langle v_{\mathrm{i}}\right\rangle_0,\quad \left\langle v_{\mathrm{c}}\right\rangle_1^{\mathrm{R}}=m\left[\left\langle \mathrm{s}_5^{'}\right\rangle_1^{\mathrm{R}}-\left\langle \mathrm{s}_1^{'}\right\rangle_1^{\mathrm{R}}\right]\cdot\left\langle v_{\mathrm{o}}\right\rangle_0 \tag{4.23}$$

$$\left\langle v_{\mathrm{C}}\right\rangle_1^{\mathrm{I}}=\frac{1}{3}\left[2\left\langle \mathrm{s}_5\right\rangle_1^{\mathrm{I}}-\left\langle \mathrm{s}_1\right\rangle_1^{\mathrm{I}}-\left\langle \mathrm{s}_3\right\rangle_1^{\mathrm{I}}\right]\cdot\left\langle v_{\mathrm{i}}\right\rangle_0,\quad \left\langle v_{\mathrm{c}}\right\rangle_1^{\mathrm{I}}=m\left[\left\langle \mathrm{s}_5^{'}\right\rangle_1^{\mathrm{I}}-\left\langle \mathrm{s}_1^{'}\right\rangle_1^{\mathrm{I}}\right]\cdot\left\langle v_{\mathrm{o}}\right\rangle_0 \tag{4.24}$$

4.4 Performance comparison

In this section, the performance of the GAM model is compared with the SWF, SSA and ideal-model approaches. The main results are provided in sections 4.4.1 to 4.4.5. They are analyzed together in section 4.4.6.

4.4.1 Closed-loop time-domain transient response

The transient response of the GAM model is first compared with equivalent closed-loop ideal, SWF and SSA models in EMTP. As for the validation of the small-signal models in section 3.5.1, model 1 parameters given in Appendix A are used. The integration time-step Δt is equal to 0.01 µs for both the reference (Ref.) and SWF models, and is equal to 0.1 µs for both the GAM and SSA models.

To compare the models, large-signal step-function perturbations are applied as shown in Figure 4.4 a). The resulting output voltages v_{o} for each model are compared in Figure 4.4 b). Figure 4.4 c) and Figure 4.4 d) demonstrate that the SWF and GAM models consider the transient oscillations at the switching frequency f_{s} but not the SSA model. Figure 4.4 e) shows that all the models consider the transient oscillations at the cross-over frequency $f_{\varphi\mathrm{m}}$ while Figure 4.4 f) indicates that only the SWF model includes the ripple at $6f_{\mathrm{s}}$. The component at $6f_{\mathrm{s}}$ is generally negligible in large signal studies because it is generally significantly attenuated by the output capacitor C_{o}. Cases where the ripple at $6f_{\mathrm{s}}$ is not negligible are not investigated in this thesis.

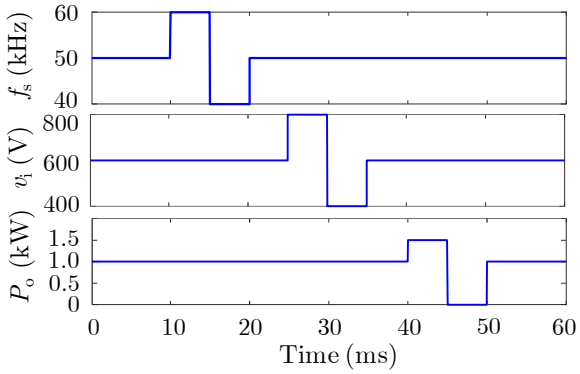

(a) Large-signal perturbations

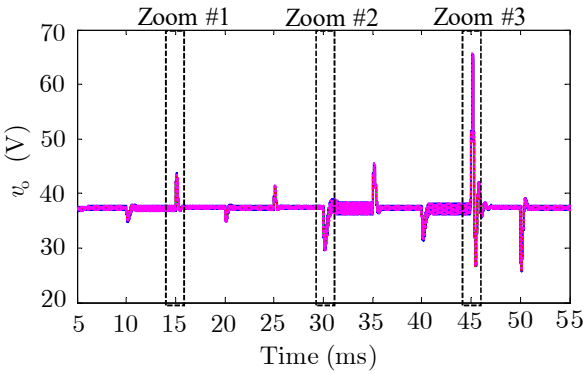

(b) Simulation results

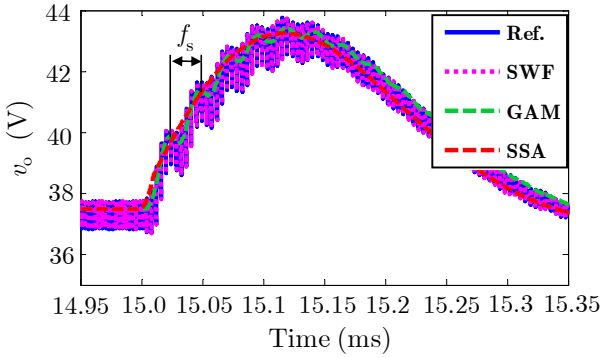

(c) Zoom #1

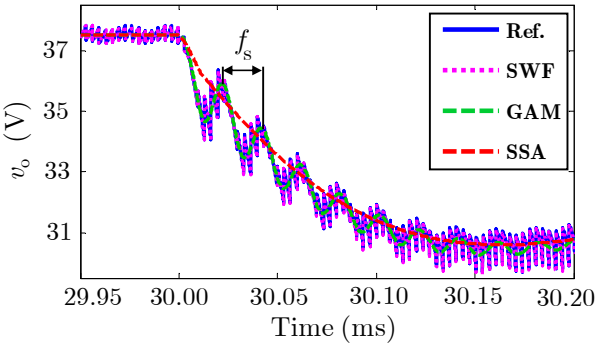

(d) Zoom #2

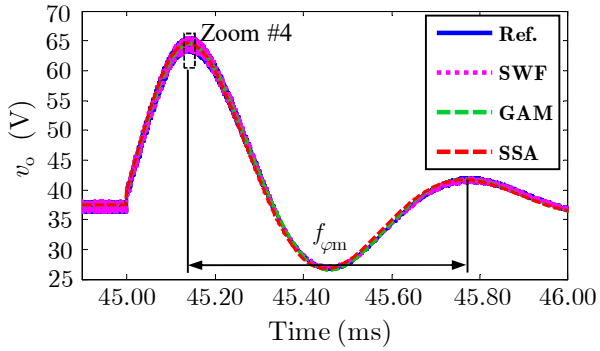

(e) Zoom #3

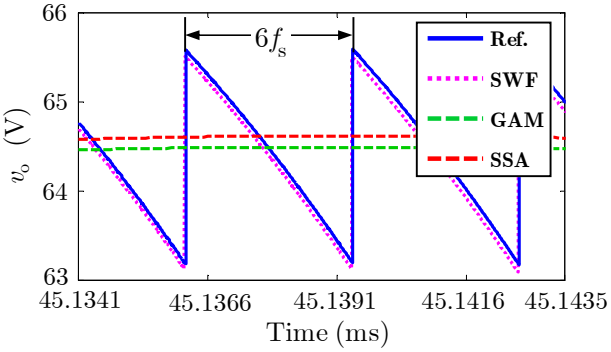

(f) Zoom #4

Figure 4.4 : Simulation results for the validation of the large-signal models

4.4.2 Simulation timing analysis

In system-level analysis, the simulation time-step Δt is generally selected based on the frequency spectra of the targeted power system studies. In the case of many power electronic converters, even for the analysis of low-frequency phenomena, if the switching-effect is modeled, it is necessary to reduce the time-step Δt to typically 1/100$^{\text{th}}$ of the switching period $T_s = 1/f_s$ (rule of thumb). In the case of the 3p-DAB, since the ripple is at $6f_s$, it requires having a time-step smaller than around 1/600$^{\text{th}}$ of the switching period T_s. This problem has been highlighted in [62] for the specific case of the 3p-DAB converter.

Since the computation time t_{cpu} highly depends on the integration time-step Δt, multiple simulation runs as in Figure 4.4 have been performed to thoroughly compare the models. The results are shown in Figure 4.5. An Intel® Core™ processor i7-4700HQ (2.4 GHz) with 12 GB of RAM, and EMTP-RV software version 3.4 is used. The total simulation time $t_{\text{sim}} = 60$ ms.

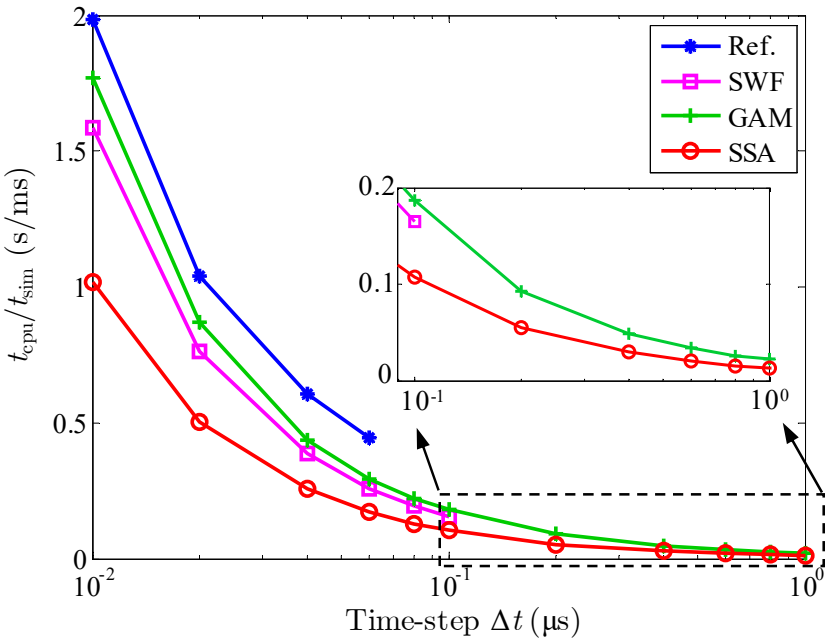

Figure 4.5 : Computation time for different integration time-steps

4.4.3 Transient short-circuit with multiple 3p-DAB

A bolted fault of 20 ms duration is applied at the output of ten (10) 3p-DAB converters connected in parallel. An output VI-characteristic with the parameters of model 1 given in Appendix A is implemented to consider a common converter fault protection scheme [4]. It is implemented as shown in Figure 4.6. The resulting transient short-circuit current for each model are compared in Figure 4.7. The maximum integration time-step obtained in Figure 4.5 is used for each model, i.e., $\Delta t = 0.06$ µs for the reference (Ref.) model, $\Delta t = 0.1$ µs for the SWF model, and $\Delta t = 1$ µs for both the GAM and SSA models. A breakdown analysis of the CPU effort is also shown in Figure 4.8.

Moreover, as mentioned before, diodes D_{i} and D_{o} are used to model the clamping effect of the freewheeling diodes on prospective negative voltage at the dc ports. These diodes are always present in practical applications. As an example, the importance of D_{o} in fault analysis is shown in Figure 4.9 by comparing the ideal-model results with the SWF, GAM and SSA results without D_{o}. Due to oscillations caused by interaction between C_{o} and the fault path inductance, the voltage v_{o} can become negative during transient events such that the transistor free-wheeling diodes are activated, therefore influencing the transient response. An example of the importance of D_{i} is shown experimentally in [83].

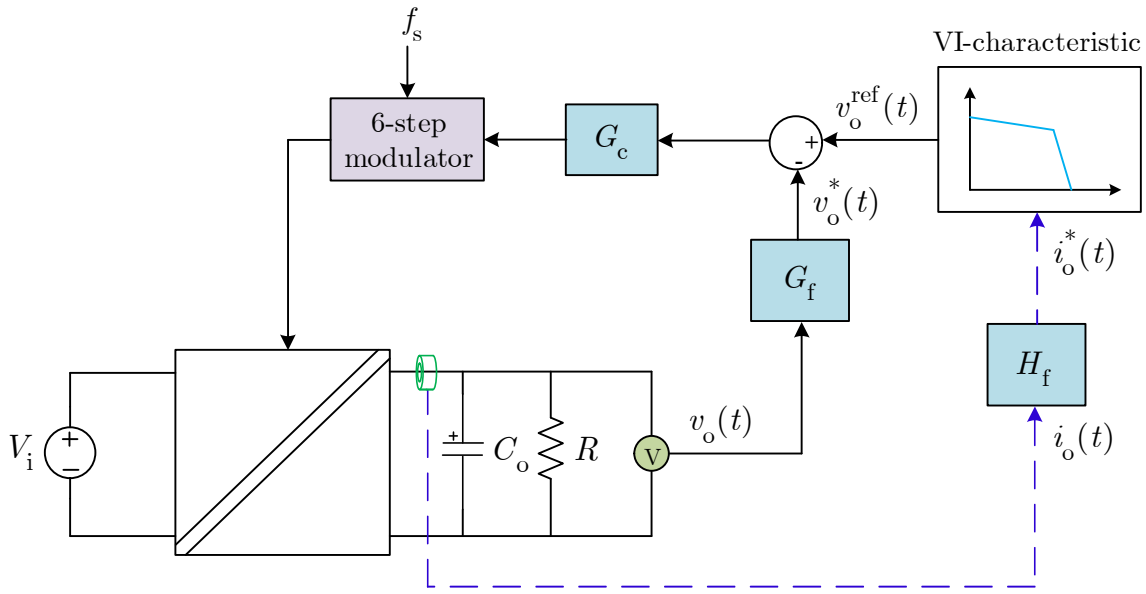

Figure 4.6 : Protection control scheme for short-circuit analysis

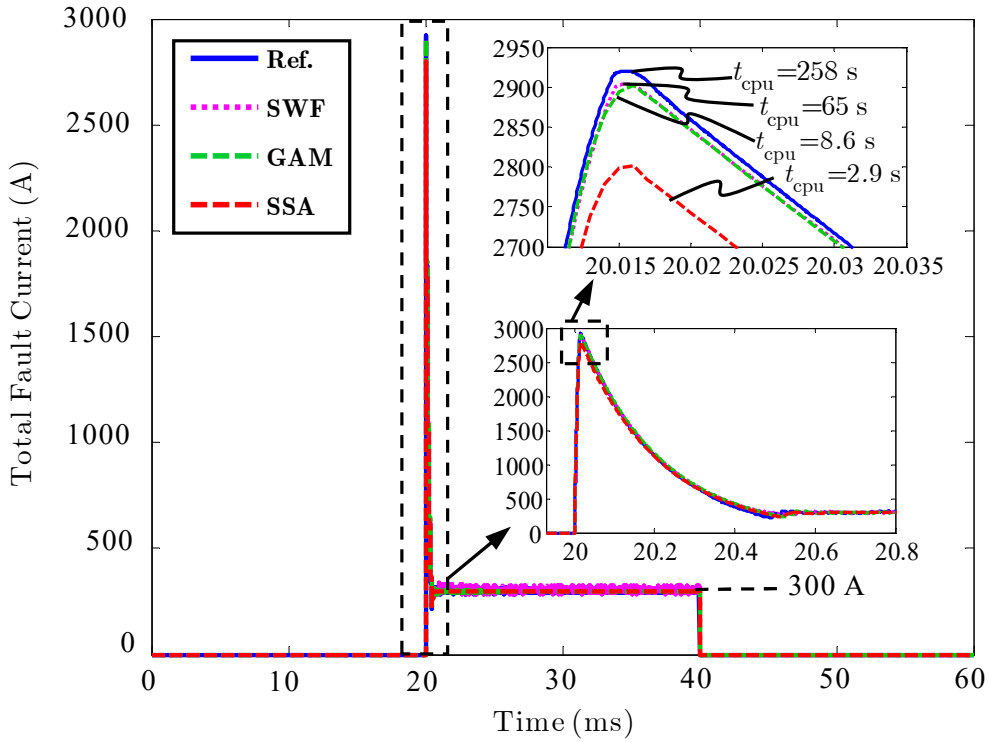

Figure 4.7 : Simulation results for a short-circuit at the output of ten (10) 3p-DAB in parallel.

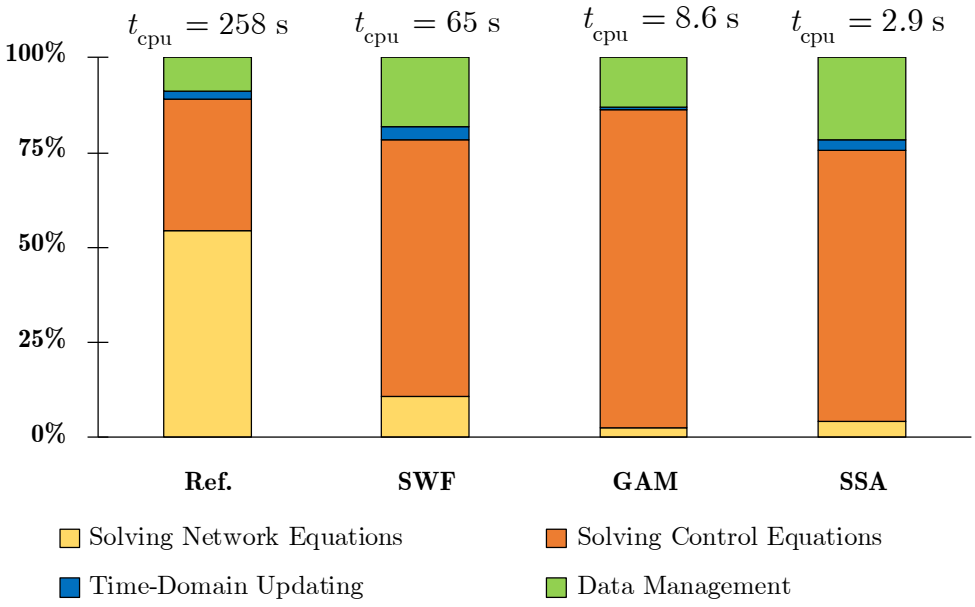

Figure 4.8 : CPU calculation effort in % of the total computation time

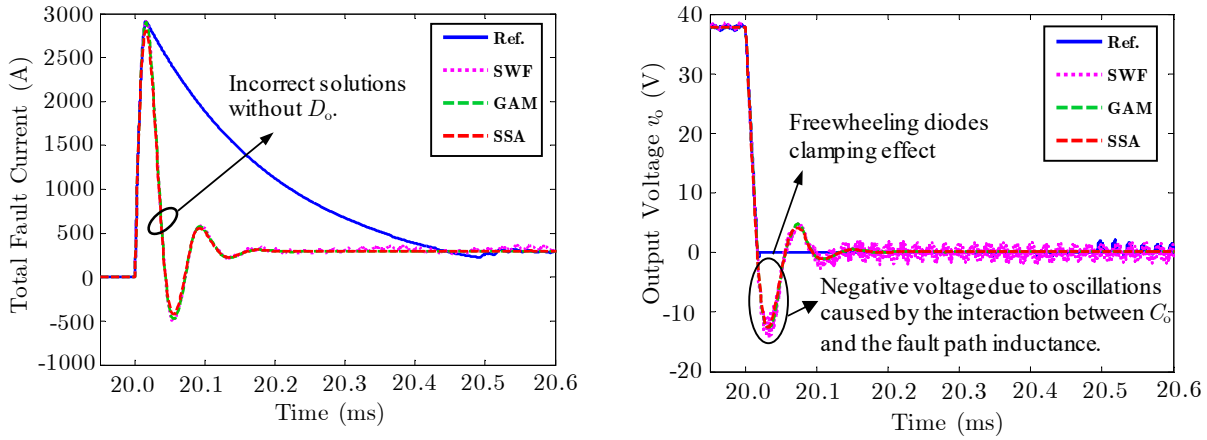

(a) Total fault current

(b) Output voltage at one of the converter terminals

Figure 4.9 : Analysis of the effect of D_o in fault analysis

4.4.4 Closed-loop frequency-domain response

In Figure 4.4 e), the main frequency component of the oscillations in the closed-loop response is close to the cross-over frequency of the designed PI-controller, i.e. $f_{\varphi m} = 1.5$ kHz. However, as mentioned before, for system-level studies, the frequency content is a function of the aimed power system analysis. This means that, instead of being step-functions, the large-signal perturbations may contain a large spectrum of frequencies.

Therefore, the precision of the models at different frequencies is assessed here. For system-level analysis, the input impedance Z_{in}^{c}, the output impedance Z_{o}^{c}, the input-to-output voltage relationship G_{vg}^{c}, and the back-current gain G_{load}^{c} are the main closed-loop transfer functions of interest. The closed-loop input impedance Z_{in}^{c} is defined in (3.121), the closed-loop output impedance Z_{o}^{c} is defined in (3.123), and the closed-loop input-to-output voltage relationship G_{vg}^{c} is defined in (3.124). The back-current gain G_{load}^{c} is defined as follows,

$$G_{load}^{c}(s) = \left.\frac{\hat{i}_i(s)}{\hat{i}_{load}(s)}\right|_{\substack{\hat{v}_o^{ref}(s)=0 \\ \hat{v}_i^{o}(s)=0}} \tag{4.25}$$

The transfer functions G_{vg}^{c} and G_{load}^{c} are particularly interesting because they show how perturbations at the input of the converter propagate at the output and vice versa. The input and

output impedances, defined by Z_{in}^{c} and Z_{o}^{c} respectively, are also relevant because, by definition, they show the local reaction of the converter to perturbations at either one of the ports.

The models are validated by applying sine wave perturbations at different frequencies in the simulation models. The magnitude of the output signals is extracted by FFT analysis using the ScopeView tool in EMTP. The equivalent circuits for the validation of the closed-loop frequency characteristics of the large-signal models are shown in Figure 4.10. The results are shown in Figure 4.11.

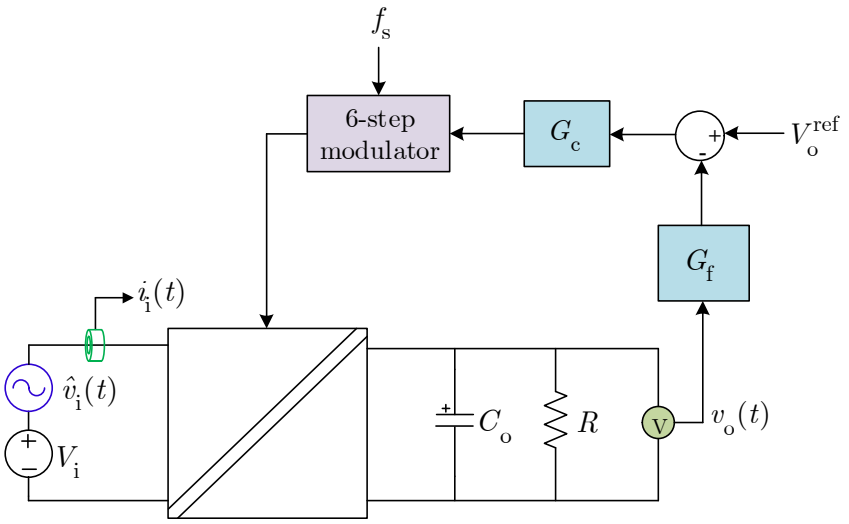

(a) Equivalent circuit for the validation of G_{vg}^{c} and Z_{in}^{c}

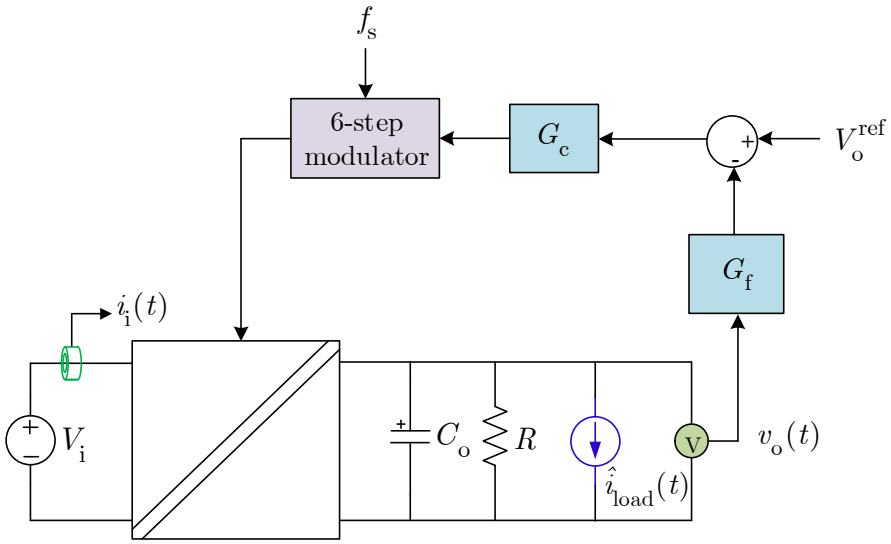

(b) Equivalent circuit for the validation of $G_{\text{load}}^{\text{c}}$ and Z_{o}^{c}

Figure 4.10 : Equivalent circuits for the validation of the closed-loop frequency characteristics

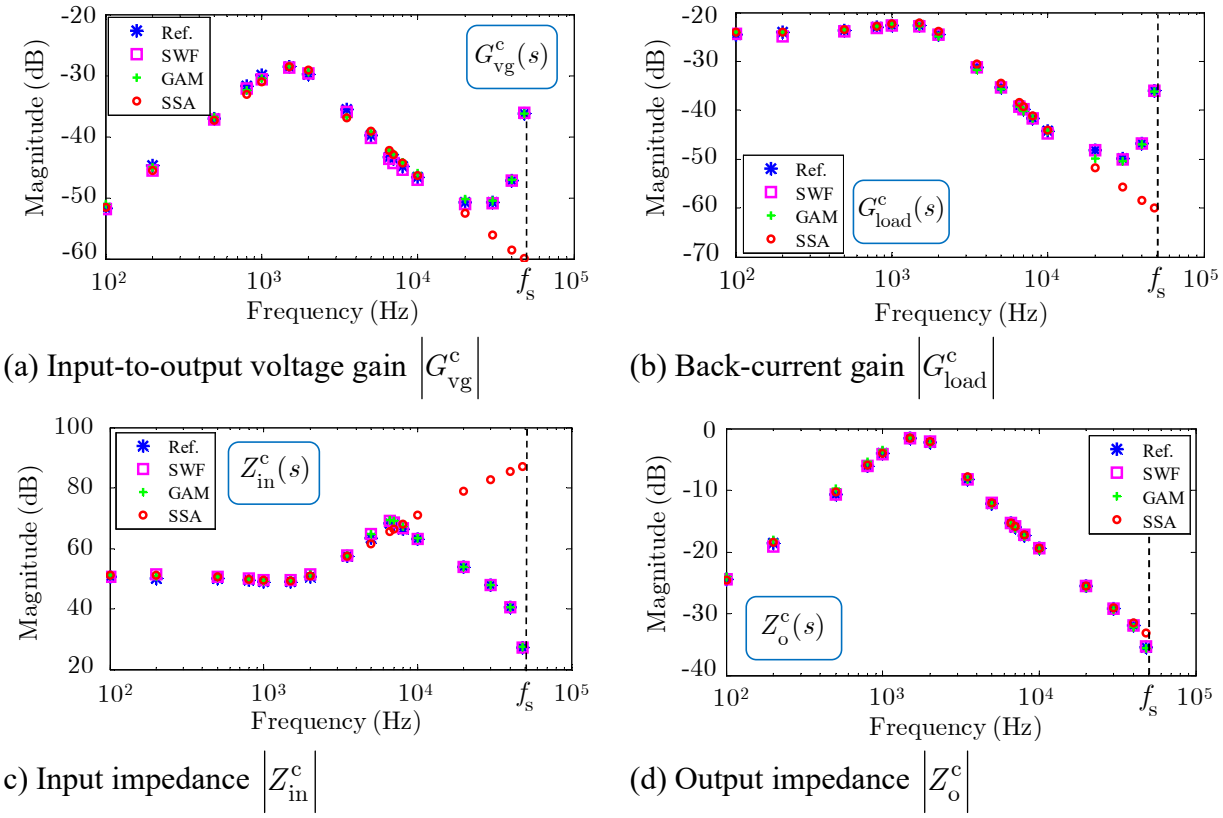

(a) Input-to-output voltage gain $\left|G^{c}_{vg}\right|$

(b) Back-current gain $\left|G^{c}_{load}\right|$

c) Input impedance $\left|Z^{c}_{in}\right|$

(d) Output impedance $\left|Z^{c}_{o}\right|$

Figure 4.11 : Closed-loop frequency response

4.4.5 Transient analysis with a large-scale test system

The effectiveness and accuracy of the GAM model to study a large-scale system are now validated through a short-circuit test case in which the transient fault current as well as the transient recovery voltage at fault clearing are analyzed. A single line diagram of the test system is shown in Figure 4.12. It is composed of a primary voltage ring bus at 750 V, two intermediate voltage buses at 380 V, and a low voltage ring bus at 110 V. The system is divided into ten (10) identical regions with a total of twenty (20) 3p-DAB converters. All the converters are designed with an LC input filter using the methodology presented in section 3.7. The parameters of the 3p-DAB converters used in this test case are provided in Appendix A (DABXA = model 2, and DABXB = model 3, with X = 1 to 10). Cables are modeled with equivalent RL circuits (not shown in Figure 4.12). Detailed models of battery, circuit breaker detection and arcing, fuse detection and arcing, as well as metal oxide varistors (MOV) are used. Detailed information on these models can be found in [4], [83]–[85].

At t = 20 ms, a 1 mΩ fault is applied in region 6 of the 110 V bus as shown in Figure 4.12. The short-circuit current and the sequence of events are shown in Figure 4.13 while the analysis of the transient voltage (V5 in Figure 4.12) is provided in Figure 4.14. These results confirm that the developed GAM model can be used for accurate grid-level analyses such as fault current evaluation and transient recovery voltage assessment.

Furthermore, for the reference (ref.) model, the integration time-step is Δt = 0.06 µs and the total computation time is t_{cpu} = 4565 s for a total simulation time t_{sim} = 50 ms. This is the largest time-step that can be used to maintain numerical stability. For the GAM model, the integration time-step Δt is increased to 1 µs such that the total computation time is significantly reduced to t_{cpu} = 45 s.

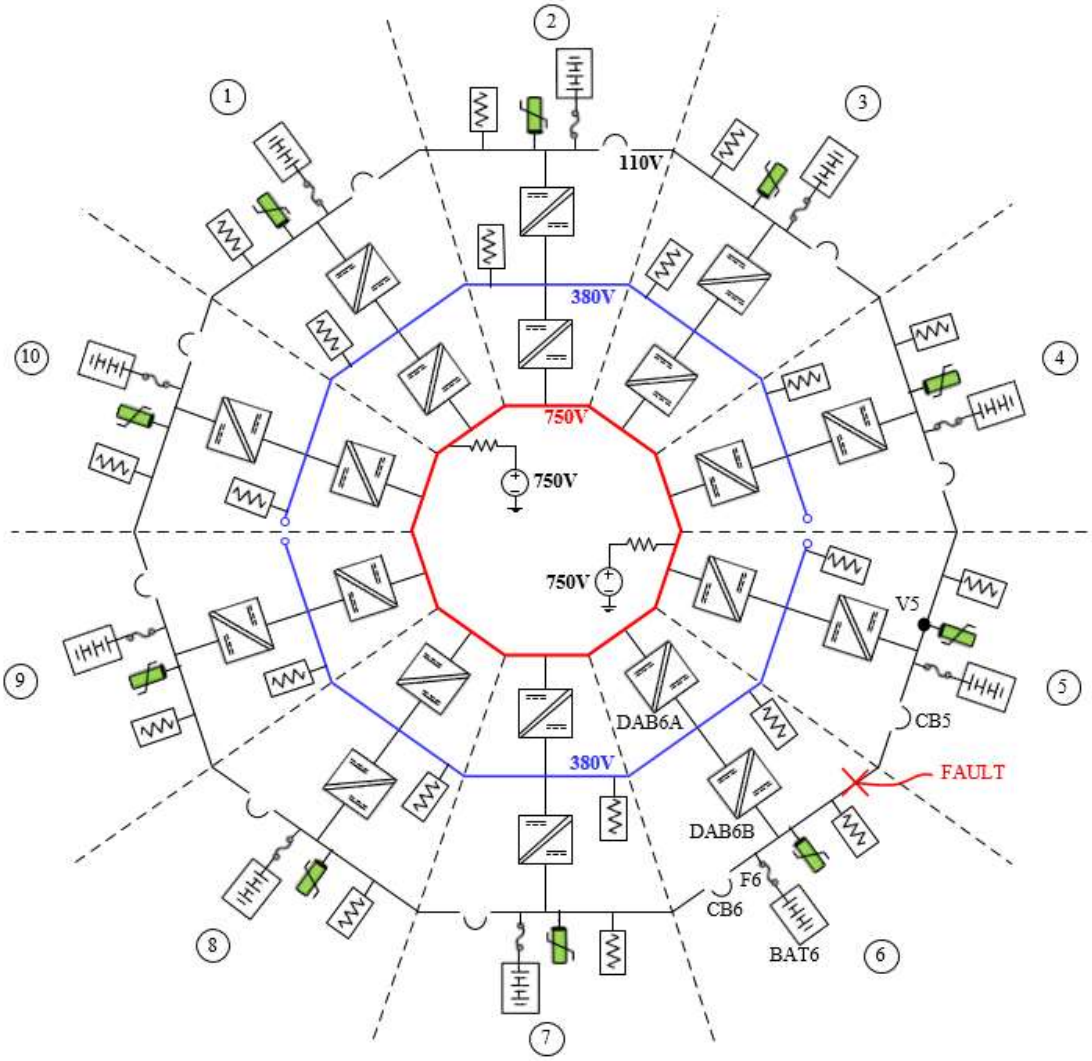

Figure 4.12 : Large-scale test system for the validation of the GAM model

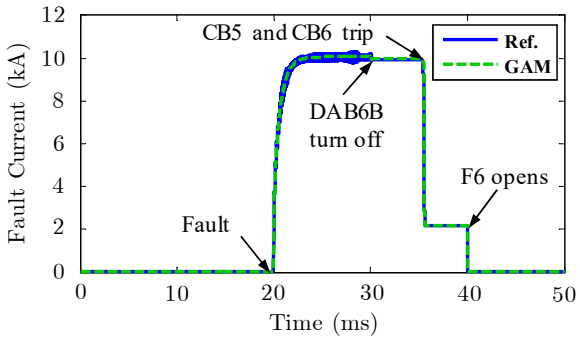

(a) Fault current for the complete simulation run

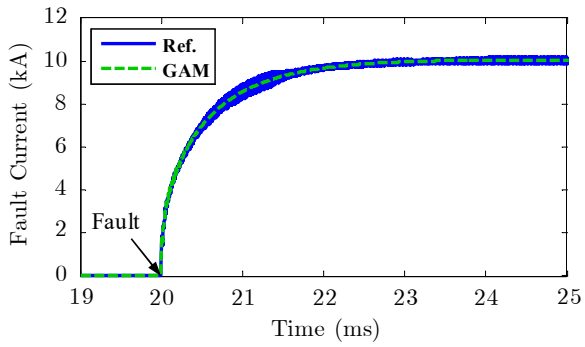

(b) Transient fault current at fault application

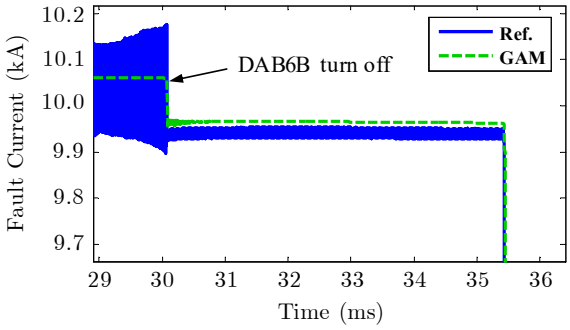

(c) Transient fault current after DAB6B turn off

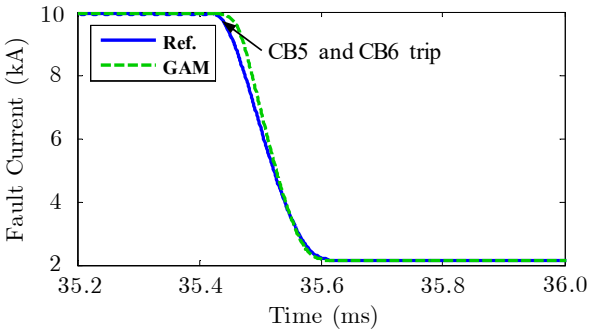

(d) Transient fault current during CB5 and CB6 arcing

Figure 4.13 : Analysis of the fault current at fault application and during fault clearing

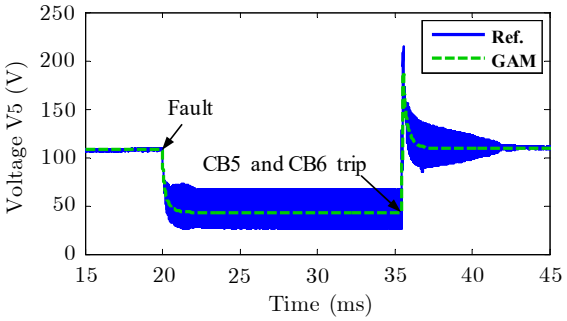

(a) Voltage at fault application and fault clearing

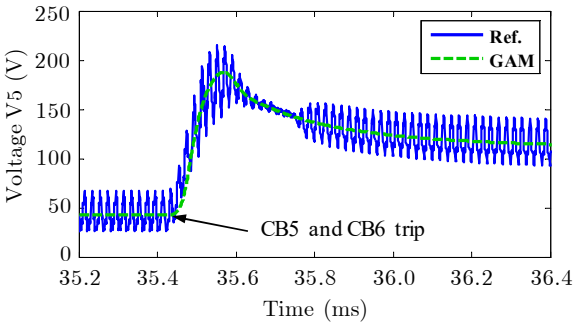

(b) Transient recovery voltage during arcing of CB5 and CB6

Figure 4.14 : Analysis of the voltage V5 during fault application and fault clearing

4.4.6 Performance comparison

Based on the results obtained in sections 4.4.1 to 4.4.5, the performance of the GAM model is now compared with the implemented ideal, SWF, and SSA models. The analysis mainly focuses on accuracy, frequency response as well as computational speed. The main outcomes regarding these three criteria are summarized in Table 4.1. It leads to the conclusion that the proposed GAM model offers the best compromise in terms of accuracy, speed and wideband response for system-level analysis. Further details on models' implementation are summarized in Table 4.2, while additional justifications are given below.

By first analyzing the time-domain simulation results, it is concluded that all the models accurately represent the averaged dynamic of the converter at the cross-over frequency $f_{\varphi \mathrm{m}}$ (Figure 4.4 e)). As for the SWF model, the GAM method also considers the transient component at the switching frequency f_{s} but it is not the case with SSA (Figure 4.4 c) and d)). The SWF model also considers the output ripple voltage at $6f_{\mathrm{s}}$ which is characteristic of the 3p-DAB while both GAM and SSA neglect this component (Figure 4.4 f)). Even if the transient responses of all the models are very similar for step-function perturbations (Figure 4.4 c) to e)), it can be seen from the frequency-domain analysis in Figure 4.11 that, unlike the SWF and GAM models, the SSA model is not accurate to reproduce the converter behavior for perturbations beyond $1/5^{\mathrm{th}}$ of f_{s}. These conclusions are summarized in Table 4.1.

Furthermore, from Figure 4.5 and Figure 4.7, it is concluded that both GAM and SSA provide a significant increase in computation speed when compared to the reference and SWF models. This is mainly explained by three fundamental differences. The primary reason is the fact that they both allow the use of larger simulation time-steps Δt which significantly increases the computation speed. It is also explained, to a lesser extent, by the reduction in the size of the network main system of equations (see Table 4.2), which follows the modified-augmented-nodal analysis (MANA) formulation approach [59], [86]. Finally, it is also attributed to the fact that, with the reference and SWF models, the modulator must be completely modeled to obtain the switching-functions, while, for GAM and SSA, it is simply modeled as a gain.

Table 4.1: Large-signal models comparison summary

Model	Accuracy[1]	Speed[2]	Frequency Response (up to)
Ideal-Model (Ref.)	1	4	$6f_s$
Switching-Function (SWF)	1	3	$6f_s$
Generalized Averaging (GAM)	2	2	f_s
State-Space Averaging (SSA)	3	1	$\sim 0.2f_s$

[1]Ranked from 1 (Most accurate) to 3 (Less accurate)
[2]Ranked from 1 (Fastest) to 4 (Slowest)

Table 4.2: Summary of 3p-DAB models' implementation in EMTP

Model	Network Nodes	Size of the network main system of equations	Number of non-zeros	Number of solution points in time-domain (n_{iter})	Size of the equivalent control system equations using state-space formulation
Ref.	16[1]	43[1]	162[1]	Eq. (4.27)	-
SWF	18	29	99	Eq. (4.26)	-
GAM	6	8	24	Eq. (4.26)	**A**:6x6, **B**:6x2 **C**:2x6, **D**=[0]
SSA	6	8	24	Eq. (4.26)	**A**=[0], **B**=[0] **C**=[0], **D**=2x2

[1] This assumes that each transistor is modeled with an ideal switch in parallel with an ideal free-wheeling diode.

However, as seen in Figure 4.5, for the same Δt, the benefit in computation speed of both the SSA and GAM approaches compared to the reference model is less significant than the reduction in the size of the network main system of equations given in Table 4.2. This is because the size of the network main system of equations cannot be used alone to conclude on the relative simulation speed between models since control system equations are also solved separately from network equations [82], [86]. For the GAM method, the computation burden of solving the larger non-linear and coupled set of control equations defined by (4.8)–(4.18) (as compared to (4.4)–(4.7) for SSA) also explains why, for the same Δt, the computation time in Figure 4.5 is higher with GAM as compared to SSA.

Finally, it is also worth mentioning that the SWF, GAM and SSA models all lead to a reduced number of solution points n_{iter} in time-domain as compared to the reference model (Table 4.2). In fact, for the simplest 3p-DAB model representation, the number of solution points for the SWF, GAM and SSA models is given by,

$$n_{\text{iter}} = t_{\text{sim}} / \Delta t \tag{4.26}$$

while, for the reference model, it is fundamentally higher by an additional term $12 t_{\text{sim}} f_{\text{s}}$,

$$n_{\text{iter}} = t_{\text{sim}} / \Delta t + 12 t_{\text{sim}} f_{\text{s}} \tag{4.27}$$

This difference is explained by the fact that, at each switching event, EMTP switches from a fixed time-step trapezoidal integration method to backward Euler with two half-step $\Delta t/2$ [87]. This feature helps reduce numerical oscillations when ideal switches are used. It is not required to solve the SWF, GAM, and SSA models because the circuit topology is time-invariant. Furthermore, the simultaneous-switching control algorithm [88], which allows a simultaneous solution of network and control system equations at switching events, also explains why, for the same Δt, the computation time is higher with the reference model.

Finally, the results of the short-circuit test cases (Figure 4.7, Figure 4.13 and Figure 4.14) also shows that the developed GAM model can effectively be used for accelerated grid-level analyses. The GAM model reduces the computation time by a factor of 1/30 in the test case of Figure 4.7, while still providing accurate results (error of less than 1% on the peak fault current). As seen in Figure 4.13 and Figure 4.14, the GAM model also provides accurate results for typical power system transient analyses such as the evaluation of transient fault current and transient recovery voltage during arcing of circuit breakers. It also provides a significant reduction in computation time for the large-scale test case (factor of 1/100: 45 s for the GAM model vs 4565 s for the reference model).

CHAPTER 5 OPEN-PHASE FAULT-TOLERANT OPERATION

In this chapter, a new mode for open-phase fault-tolerant operation of the 3p-DAB converter is proposed and confirmed experimentally on the closed-loop GaN-based small-scale prototype. Steady-state analysis is performed to evaluate the impact of open-phase operation on the converter voltage and current waveforms, and its power transfer and soft-switching capabilities. Small-signal analysis along with time-domain simulations and experimental results are also provided to assess the impacts on the converter stability and its transient dynamic performance. The adaptation of the steady-state (Chapter 2) and small-signal (Chapter 3) modeling strategies to open-phase operation is also highlighted.

5.1 Open-phase operation

Upon detection of a fault in a transistor module, intelligent gate drivers can interrupt the gating signals going to the faulty-leg and provide a feedback signal of the fault condition. In frozen leg operation [35] (Figure 5.1), following the detection of a fault in a transistor module, the two transistors of the same phase are open, leaving their free-wheeling diode self-commutated into the circuit. As shown in Figure 5.1, because the diodes are left into the circuit, reactive current can still circulate in the faulty-phase. As shown in Figure 5.2, it is proposed here to use the same fault signal to open the faulty-phase such that it eliminates the interaction of the faulty-leg free-wheeling diodes. As it will be shown in this chapter, due to the circulation of reactive current in the faulty-phase free-wheeling diodes in frozen leg operation, the power transfer capability is reduced, and the current stress in the faulty-bridge may be increased as compared to open-phase. The equivalent circuits for the 3p-DAB in frozen leg and open-phase operations (with phase C open) are shown in Figure 1.6 a) and b) respectively.

Since the prototype is fabricated with GaN FETs, it is important to note here that GaN FETs do not have a body diode, but the channel itself is bidirectional and behaves like a body diode when $V_{GS} = 0$ V, which is the prerequisite to frozen leg operation. However, this “equivalent body diode” can exhibit an important voltage drop. For example, as seen in Figure 5.3 for the EPC2022 (100 V, 90 A) GaN FET, the minimum forward voltage in reverse conduction is 2 V. If GaN FETs are expected to conduct large currents in the reverse direction when $V_{GS} = 0$ V, it may be difficult to

ensure that adequate cooling is provided due to their small size (see Appendix B for EPC2022 footprint). The open-phase operation is therefore even more advantageous with GaN FETs since it reduces the circulation of reactive current through the “equivalent body diodes”.

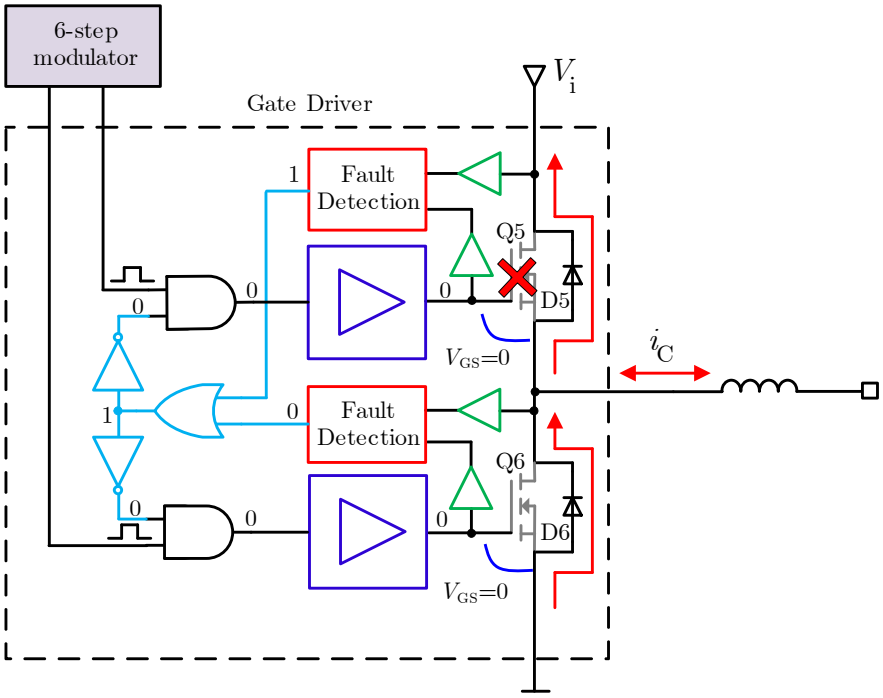

Figure 5.1 : Protection scheme concept for frozen-leg operation (e.g. Fault on Q5, phase C)

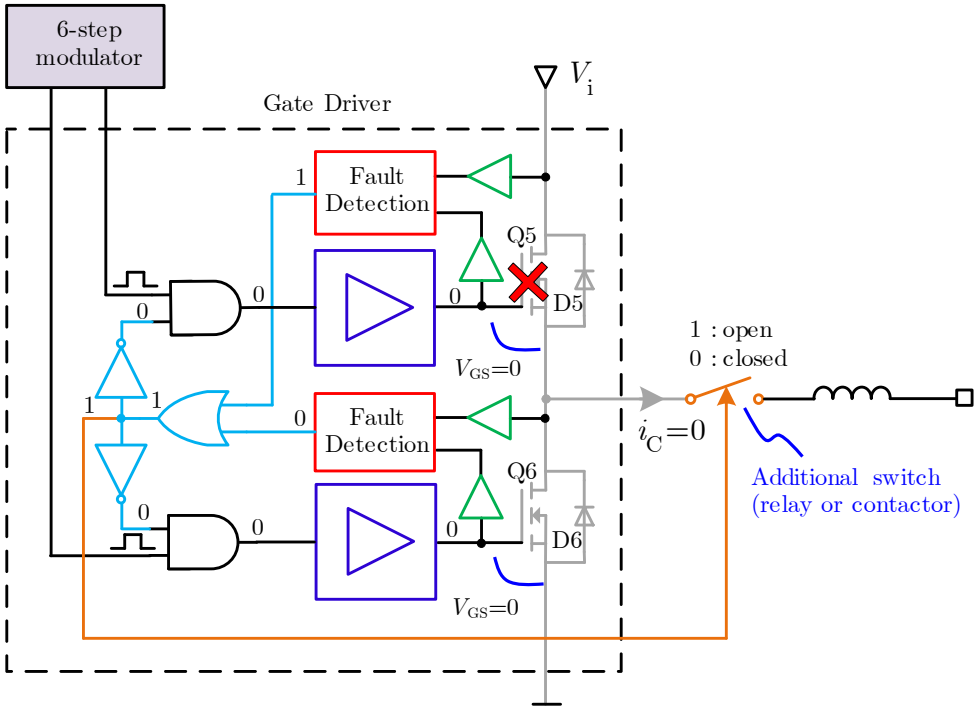

Figure 5.2 : Protection scheme concept for open-phase operation (e.g. Fault on Q5, phase C)

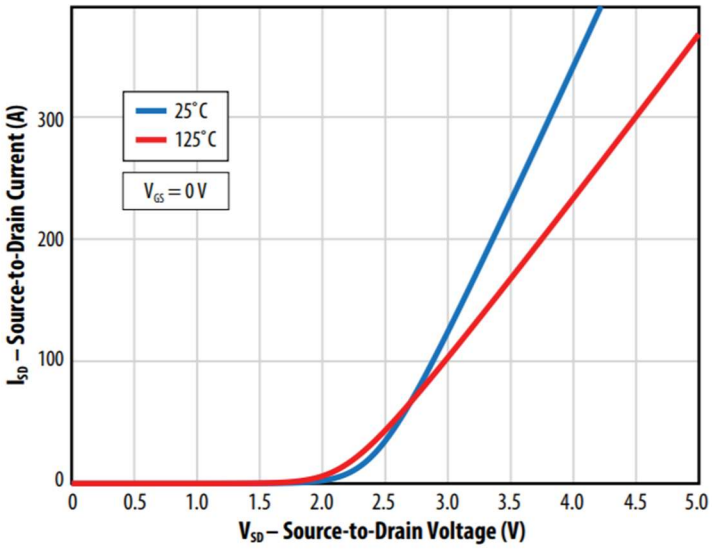

Figure 5.3 : Reverse drain-source characteristic of the EPC2022 GaN FET (100V, 90A) [89]

5.2 Steady-state analysis

5.2.1 Transformer voltage and current waveforms

The steady-state analysis of the 3p-DAB converter in normal operation using the piecewise-linear modeling (PLM) approach has been presented in section 2.2. In open-phase operation, the voltage waveforms are affected and differs from the normal case. As shown in Figure 5.4, if phase C is open, the current in phase C is zero ($i_{\mathrm{C}} = 0$). Knowing that the voltage across L_{s} on phase C must also be zero, and assuming that the output bridge is kept in operation, it can be concluded that the voltage v_{CN} on the primary side becomes a function of the output voltage v_{o} as well as the output bridge switching-functions. Following (2.32) given for the normal operation case, the new voltage v_{CN} in open-phase mode is defined as,

$$v_{\mathrm{CN}} = m v_{\mathrm{ca}} = m\left(\mathrm{s}_5^{'} - \mathrm{s}_1^{'}\right) v_{\mathrm{o}} \tag{5.1}$$

In open-phase operation, the output bridge is proposed to be kept operated with the same balanced set of switching-functions such that the following relationship still applies,

$$v_{\mathrm{ab}} + v_{\mathrm{bc}} + v_{\mathrm{ca}} = 0 \tag{5.2}$$

Therefore, v_{AN}, v_{BN} and v_{CN} remain balanced, and the definition of v_{NO} given in (2.22) for the normal operation case still stands in open-phase operation. While the voltages applied by the input

bridge on phases A and B (v_{AO} and v_{BO}) are still given by (2.23) and (2.24) respectively, the voltage v_{CO} is no longer applied by the input bridge since phase C is open. Nevertheless, the application of KVL on phase C still requires that,

$$v_{CO} = v_{CN} + v_{NO} \tag{5.3}$$

Inserting (2.23), (2.24) and (5.3) into the original definition of v_{NO} given in (2.22), with v_{CN} given by (5.1), the voltage v_{NO} for the open-phase operation is reduced to,

$$v_{NO} = \frac{\left(s_1 + s_3\right)v_i + m\left(s_5' - s_1'\right)v_o}{2} \tag{5.4}$$

Furthermore, inserting (5.4) into the definitions of v_{AN} and v_{BN} given by (2.19) and (2.20) respectively, the new voltages v_{AN} and v_{BN} are defined by,

$$v_{AN} = \frac{\left(s_1 - s_3\right)v_i + m\left(s_1' - s_5'\right)v_o}{2} \tag{5.5}$$

$$v_{BN} = \frac{\left(s_3 - s_1\right)v_i + m\left(s_1' - s_5'\right)v_o}{2} \tag{5.6}$$

The results obtained in (5.5) and (5.6) lead to an important conclusion: in open-phase operation, the voltages v_{AN} and v_{BN} are now dependent on the output bridge switching-functions and the output voltage v_o. This is a fundamental difference with normal operation for which v_{AN} and v_{BN} are only dependent on the input bridge switching-functions and the input voltage v_i.

Moreover, in open-phase operation, since the transformer primary winding is floating Y, the following relationship apply for both the normal and open-phase operation cases,

$$i_A + i_B + i_C = 0 \tag{5.7}$$

Since $i_C = 0$, it leads to the other important conclusion that the phase A and B currents are now out of phase,

$$i_A = -\,i_B \tag{5.8}$$

In Figure 5.5, the resulting theoretical waveforms for phase A in range 1 and range 2 are compared with the normal operation case. Phase B can be obtained by applying a similar procedure (not shown here). For the same voltage and loading conditions, experimental waveforms for phase A are provided to compare the normal (Figure 5.6) and open-phase (Figure 5.7) operations. The

results are in accordance with Figure 5.5 a) for the normal case and Figure 5.5 d) for the open-phase case. The operating points in Figure 5.6 and Figure 5.7 are referred in the next sections as the “main test cases”.

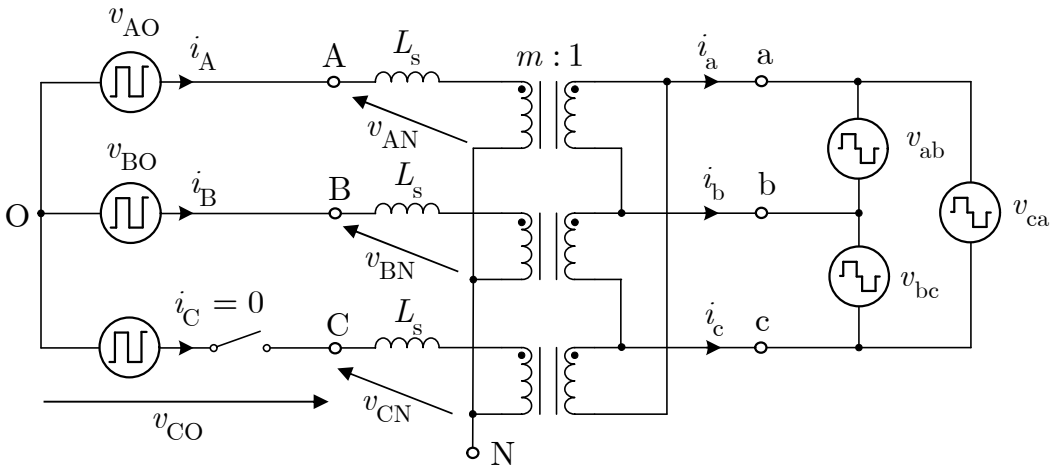

Figure 5.4 : Simplified representation of the Y-Δ 3p-DAB with phase C open

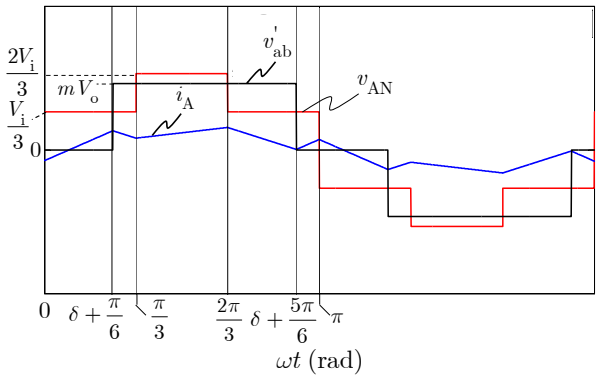

(a) Normal operation (range 1)

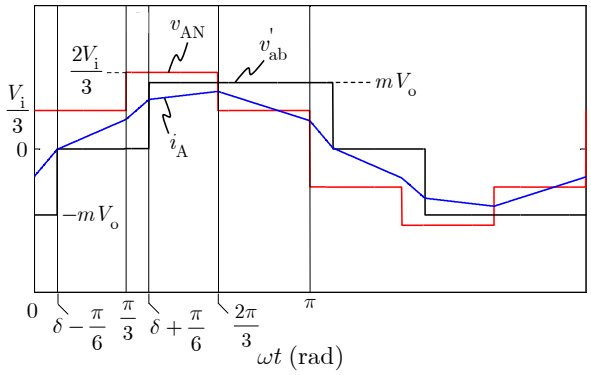

(b) Normal operation (range 2)

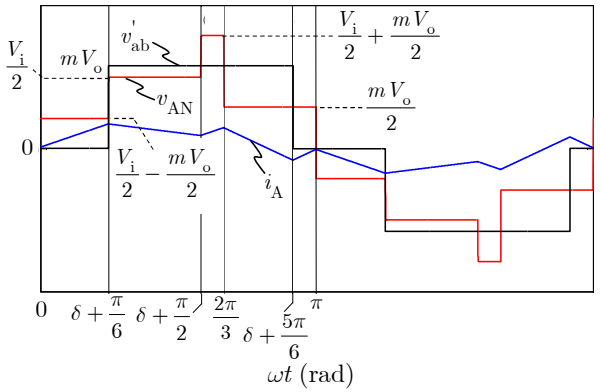

(c) Open-phase operation (range 1)

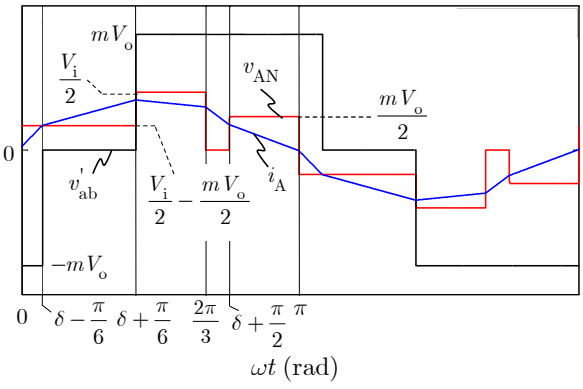

(d) Open-phase operation (range 2)

Figure 5.5 : Theoretical waveforms for phase A (normal vs open-phase)

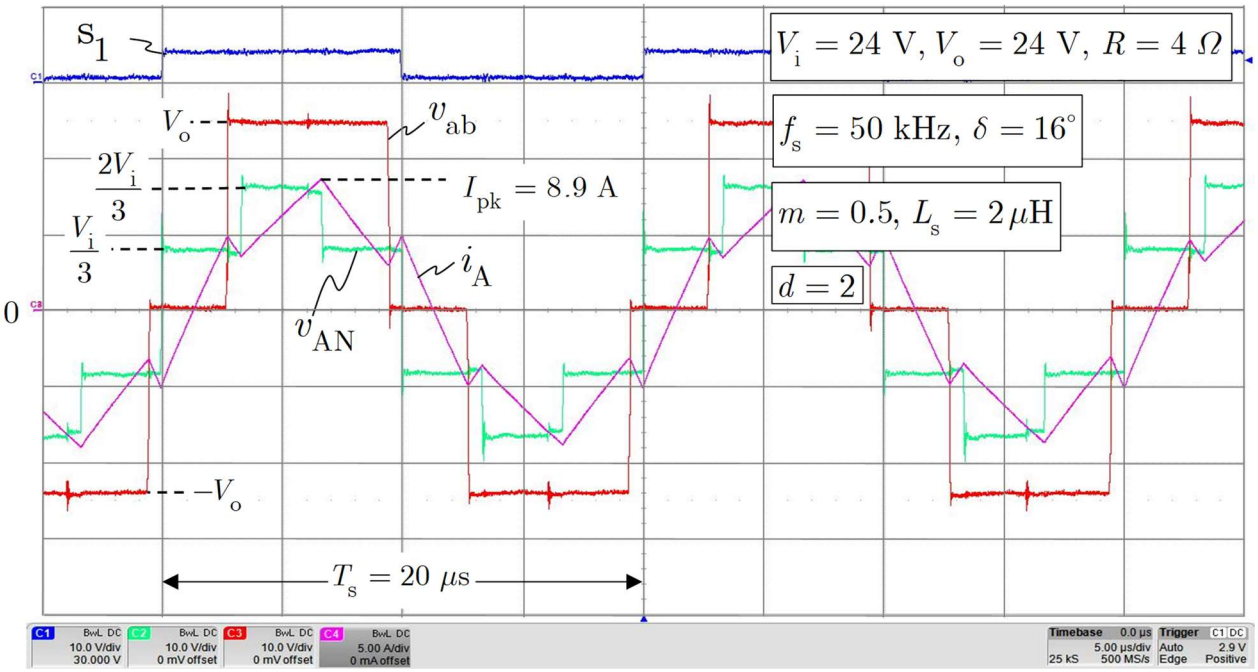

Figure 5.6 : Experimental waveforms for phase A in normal operation (prototype)

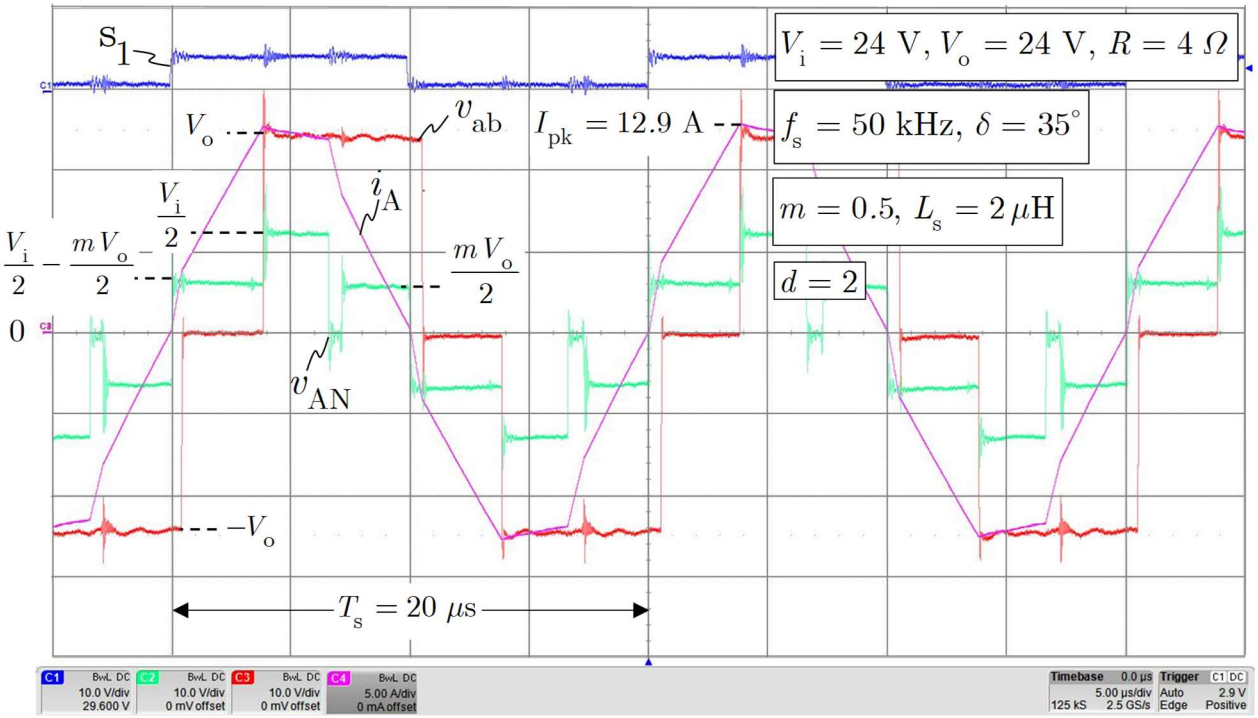

Figure 5.7 : Experimental waveforms for phase A in open-phase operation (prototype)

Knowing the values of the switching-functions (either 0 or 1) for each mode defined in Appendix F over $\theta = [0, \pi]$, and taking the assumption that the input and output voltages are constant, i.e. $v_i = V_i$ and $v_o = V_o$, it is possible to evaluate v_{AN}, v_{BN} and v_{CN} using (5.5), (5.6) and (5.1)

respectively. It then allows solving the current equations for phase A $i_{\mathrm{A}}(\theta)$ and phase B $i_{\mathrm{B}}(\theta)$ for each mode using (2.16) and (2.17). The resulting current equations for each mode, and for the two phase-shift δ operating ranges are given in Appendix F. From the knowledge of $i_{\mathrm{A}}(\theta)$, the output bridge currents can be derived. It can be demonstrated that,

$$i_{\mathrm{a}} = i_{\mathrm{c}} = m i_{\mathrm{A}} \tag{5.9}$$

$$i_{\mathrm{b}} = -2m i_{\mathrm{A}} \tag{5.10}$$

A similar steady-state analysis can be performed if one phase is open on the secondary side. In this case, it is the secondary voltage waveforms v'_{ab}, v'_{bc} and v'_{ca} that are modified instead of v_{AN}, v_{BN} and v_{CN}. For example, if phase c is open on the secondary side, the voltage v'_{ab} remains the same as in normal operation but v'_{bc} and v'_{ca} will depend on the input voltage v_{i} due to coupling with the voltages applied by the input bridge on the primary side of the three-phase transformer.

5.2.2 Power transfer relationship

The procedure to derive the power transfer relationship of the 3p-DAB in open-phase operation is similar to normal operation in section 2.2.3. It requires averaging the output current which is function of the transformer currents as well as the output bridge switching-functions given in Appendix F. In open-phase operation, because $i_{\mathrm{C}} = 0,$ equation (2.34) is reduced to,

$$i_{\mathrm{o}} = m\left[(\mathrm{s}'_1 - \mathrm{s}'_3) i_{\mathrm{A}} + (\mathrm{s}'_3 - \mathrm{s}'_5) i_{\mathrm{B}}\right] \tag{5.11}$$

Due to the symmetrical operation of the 3p-DAB in normal operation, the analysis in section 2.2.3 has been only performed over the interval $\theta = [0, \pi/3],$ i.e. for modes I and II. Because of the unbalanced operation in open-phase, it requires analyzing the transformer currents over the interval $\theta = [0, \pi],$ i.e. for modes I to V.

The procedure to calculate the average output current for each mode is similar to normal operation. The results are given in Appendix F. Knowing the average currents for modes I to V, the average output current I_{o} is calculated. For range 1, I_{o} is calculated by applying the following averaging operation,

$$I_{\mathrm{o}}=\frac{1}{\pi}\left[\begin{array}{l}\left(\delta+\frac{\pi}{6}\right)\cdot\left\langle i_{\mathrm{o}}\right\rangle\Big|_{\mathrm{I}}+\frac{\pi}{3}\cdot\left\langle i_{\mathrm{o}}\right\rangle\Big|_{\mathrm{II}}+\left(\frac{\pi}{6}-\delta\right)\cdot\left\langle i_{\mathrm{o}}\right\rangle\Big|_{\mathrm{III}} \\ \qquad\qquad +\left(\delta+\frac{\pi}{6}\right)\cdot\left\langle i_{\mathrm{o}}\right\rangle\Big|_{\mathrm{IV}}+\left(\frac{\pi}{6}-\delta\right)\cdot\left\langle i_{\mathrm{o}}\right\rangle\Big|_{\mathrm{V}}\end{array}\right] \tag{5.12}$$

which, using (F.25) to (F.29) yields to,

$$I_{\mathrm{o}}=\frac{mV_{\mathrm{i}}}{2\omega_{\mathrm{s}}L_{\mathrm{s}}}\delta \tag{5.13}$$

such that,

$$P_{\mathrm{o}}=V_{\mathrm{o}}I_{\mathrm{o}}=\frac{mV_{\mathrm{i}}V_{\mathrm{o}}}{2\omega_{\mathrm{s}}L_{\mathrm{s}}}\delta \tag{5.14}$$

Applying a similar procedure in range 2 with the use of (F.30) to (F.34), it leads to,

$$P_{\mathrm{o}}=\frac{mV_{\mathrm{i}}V_{\mathrm{o}}}{2\omega_{\mathrm{s}}L_{\mathrm{s}}}\left[\frac{3}{2}\left(\delta-\frac{\delta^2}{\pi}\right)-\frac{\pi}{24}\right] \tag{5.15}$$

By comparing (5.14) with (2.37), and (5.15) with (2.38), it is concluded that the power transfer capability of the 3p-DAB in open-phase operation is theoretically half the one in normal operation. For the experimental prototype parameters (model 4), the power transfer relationships in normal, frozen leg and open-phase operations are compared in Figure 5.8. Experimental results are included to validate the theoretical models. For the frozen leg mode, the power transfer capability is evaluated using time-domain simulations. For the normal and open-phase cases, the errors between the theoretical and the experimental results are mainly due to losses (5-10%) and the dead-time (0.1μs) which are both not considered in the theoretical model. As the power increases, losses reduce the accuracy of the theoretical models for the open-phase and frozen leg modes. The power transfer capability is also smaller than expected by the theoretical prediction.

As shown in Figure 5.8, when the converter is operated in closed-loop with regulated output voltage $v_{\mathrm{o}}=V_{\mathrm{o}}$ and a resistive load R, the output power P_{o} must remain constant, such that, in frozen leg and open-phase conditions, the control phase-shift δ will naturally be increased to meet the new operating conditions. In frozen leg operation, due to the circulation of reactive current in the faulty-phase free-wheeling diodes, the power transfer capability is reduced as compared to open-phase.

However, for conditions where there is no reactive current circulating in the faulty-phase, it can be demonstrated that frozen leg operation is virtually equivalent to open-phase operation, such that, in these conditions, the power transfer capabilities are the same.

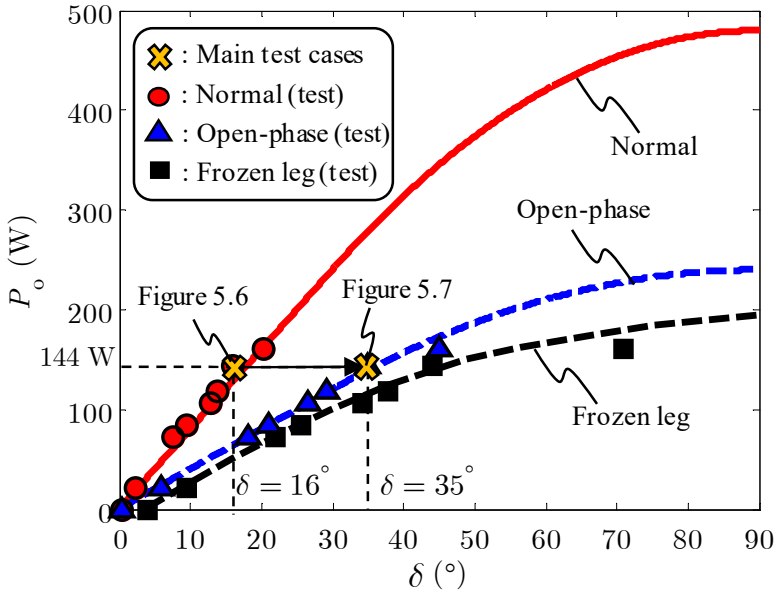

Figure 5.8 : Comparison of the power transfer capabilities (model 4/prototype)

5.2.3 Current stress in the faulty-bridge

The results in Figure 5.9 show the rms current stress for each phase in the faulty-bridge for different voltage and loading conditions. These results are obtained from time-domain simulations in EMTP. Experimental results are also added.

By analyzing the results for the currents in phase A and phase B, it is concluded that the current stress on the switches is higher in frozen leg operation as compared to the open-phase case due to reactive current circulating in the faulty phase C in frozen leg operation. It is also concluded that this advantage of open-phase over frozen leg increases as d decreases.

Moreover, it is remarked that the rms current in phase A and phase B is generally higher in frozen leg and open-phase operations as compared to normal operation. This is an intuitive result since the total active power is transmitted through the two remaining phases in frozen leg and open-phase operations. For low power, it can however be noted that the rms current in phase A and phase B can be lower in frozen leg and open-phase operations as compared to normal operation. This is a counterintuitive result, but this is due to modifications in the voltage and current waveforms.

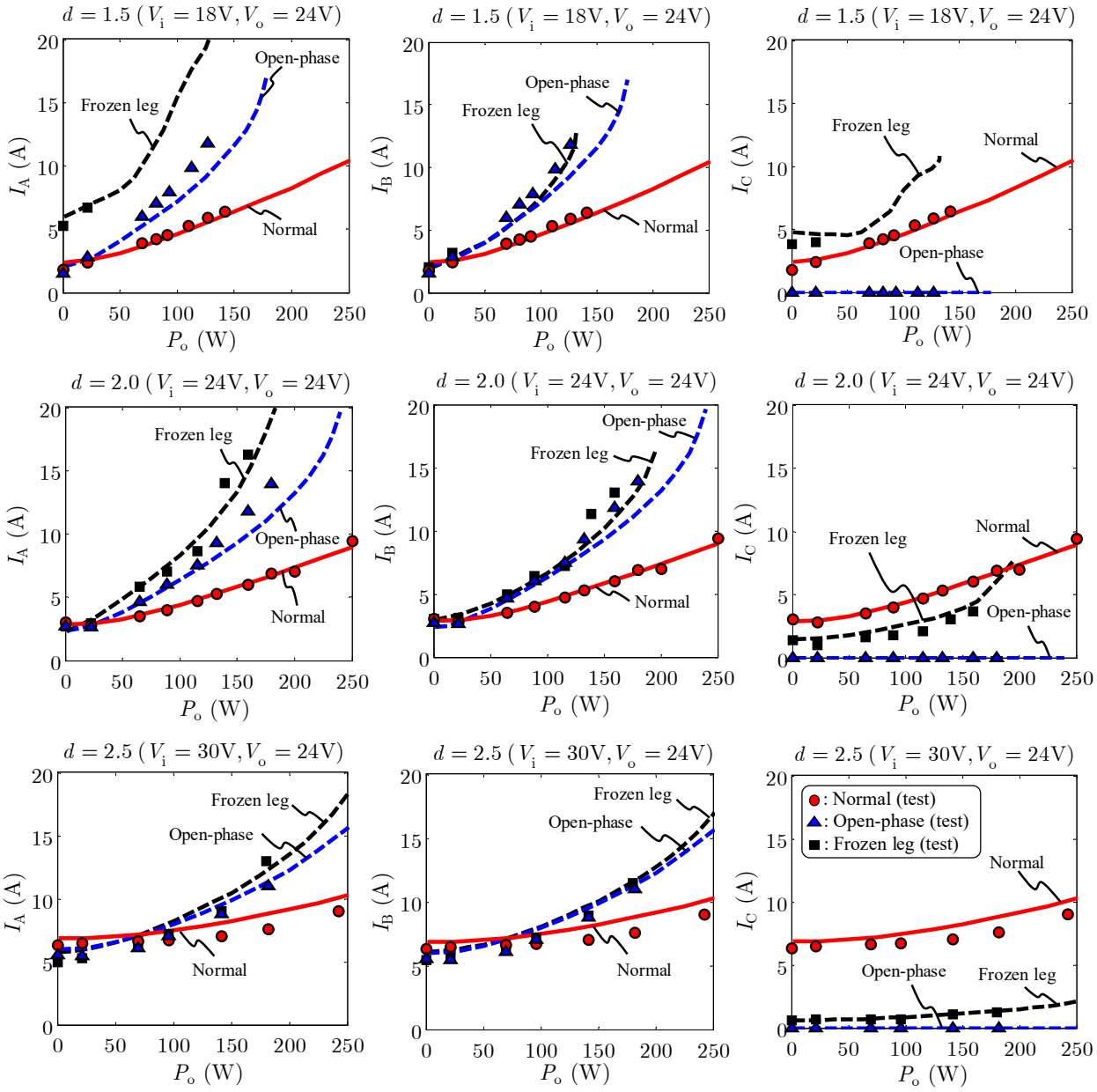

Figure 5.9 : RMS current for different voltage and loading conditions (model 4/prototype)

Note that, for $d = 1.5$, it was not possible to test the prototype for output power higher than 25 W because of the high reactive component circulating through the "equivalent body diodes" of the GaN transistors Q5 and Q6 in phase C. At this operating point, the conduction losses in Q5 and Q6 of phase C are estimated to 3.75 W/transistor as compared to 13 mW/transistor in normal operation. In frozen leg, this led to rapid failure of the GaN transistors because of the very high-power loss concentration (approximately 0.27 W/mm^2 for the EPC2022).

5.2.4 ZVS soft-switching regions

The procedure to evaluate the theoretical ZVS regions for the 3p-DAB in normal operation has been presented in section 2.2.4. The results are recalled here in Figure 5.10 a). A similar procedure can be applied in open-phase operation, but, since the currents are unbalanced, each phase must be studied independently. For phase A of the input bridge, it leads to the following ZVS boundaries. For range 1 ($0 \leq \delta \leq \pi/6$), it results in,

$$d > \frac{3\pi + 6\delta}{2\pi} \tag{5.16}$$

and for range 2 ($\pi/6 \leq \delta \leq \pi/2$), it yields to,

$$d > \frac{5\pi - 6\delta}{2\pi} \tag{5.17}$$

For phase a of the output bridge, it leads to the following ZVS boundary in range 1,

$$d < \frac{2\pi}{\pi - 6\delta} \tag{5.18}$$

For range 2, there is no ZVS boundary which means that ZVS is always provided in phase a of the output bridge for loading conditions where $\delta \geq \pi/6$. The results for phase A (input bridge) and phase a (output bridge) in open-phase are shown in Figure 5.10 b).

The theoretical results in Figure 5.10 are also compared with the main test case experimental results. As expected for the normal operation case in Figure 5.6 , i.e. that $i_{\mathrm{A}} < 0$ at turn-on of S1, the input bridge is soft-switched in Figure 5.10 a). Since it is operated far from its hard-switching boundary, the reactive component of i_{A} is significant in Figure 5.6. In open-phase operation, according to Figure 5.10. b), the phase A of the input bridge should be soft-switched but operated very close its hard-switching boundary. According to Figure 5.7, i_{A} is close to zero at turn-on of S1 which means that it is indeed operated close to its ZVS boundary.

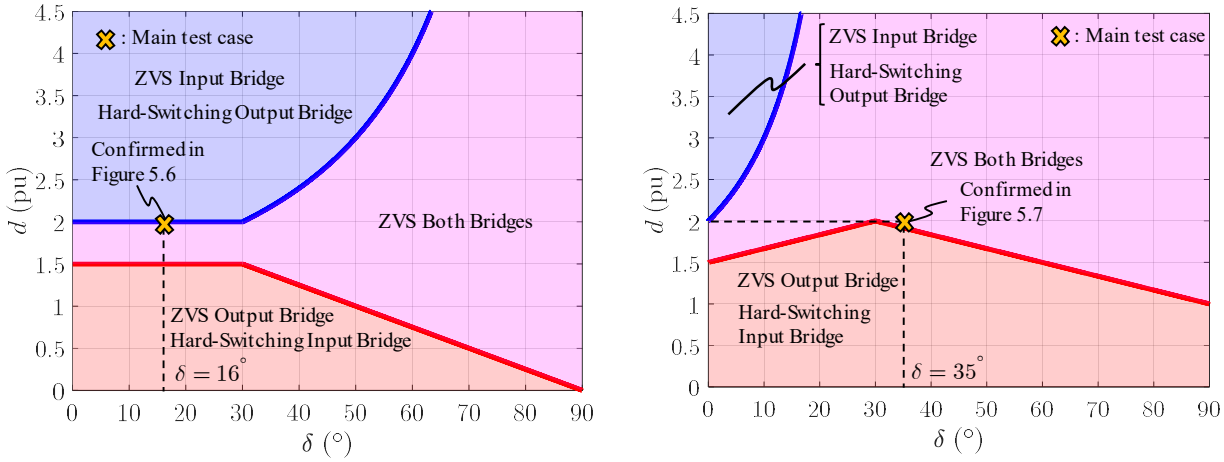

(a) Normal operation (b) Open-phase operation

Figure 5.10 : ZVS regions (normal vs open-phase)

The results in Figure 5.10 a) show that it is advantageous from a soft-switching standpoint to operate the 3p-DAB in normal operation with a voltage conversion ratio d ranging between 1.5 and 2. It is possible in applications where the input voltage V_{i} is tightly regulated by a pre-regulating stage and the output voltage V_{o} is held constant by the DAB converter.

In open-phase, a similar analysis can be performed for the other phases. In fact, ZVS happens in phase B of the input bridge if $i_{\mathrm{B}} < 0$ at turn-on of S3, and ZVS take place in phase b of the output bridge if $i_{\mathrm{b}} > 0$ at turn-on of S3'. Since phase C is open, the ZVS analysis is not applicable for phase C of the input bridge but ZVS occurs in phase c of the output bridge if $i_{\mathrm{c}} > 0$ at turn-on of S5'. Since $i_{\mathrm{A}} = -i_{\mathrm{B}}$ and $i_{\mathrm{C}} = 0$, it has been shown previously that the output bridge currents i_{a}, i_{b} and i_{c} can all be derived from the knowledge of i_{A}. This simplifies the ZVS analysis for the other phases. The results for all the phases are compared in Figure 5.11; the darker the region, the more phases are soft-switched. A detailed analysis of the relationship between the output power P_{o}, the conversion ratio d and the ZVS boundaries is also provided for all phases in Figure 5.12. For the per-unit conversion, the following bases are taken,

$$V_{\mathrm{b}} = mV_{\mathrm{o}}, \quad P_{\mathrm{b}} = \frac{\left(mV_{\mathrm{o}}\right)^2}{\omega_{\mathrm{s}} L_{\mathrm{s}}} \tag{5.19}$$

For the normal case, the results in Figure 5.12 a) are valid for all phases. In open-phase operation, the results are given in Figure 5.12 b) to d). From these results, it is concluded that, in open-phase

operation, for $d = 2$, the input bridge is always ZVS, but only phase a and phase b in the output bridge are ZVS. The whole output bridge is also always ZVS for a voltage conversion ratio $d < 1$.

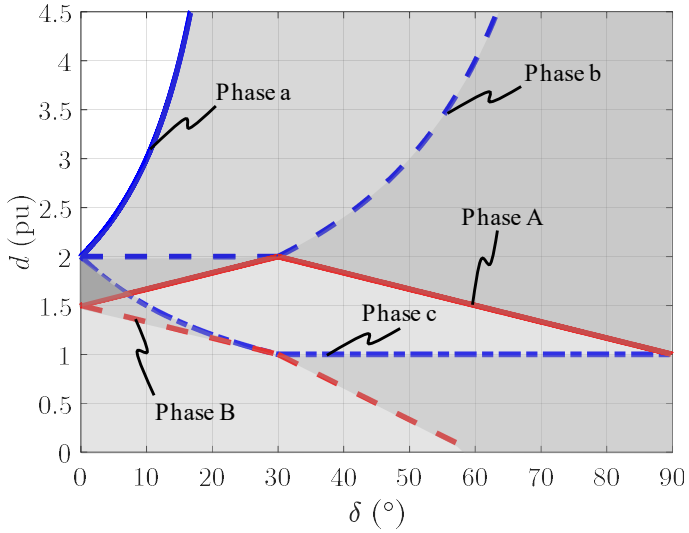

Figure 5.11 : ZVS regions for all phases in open-phase

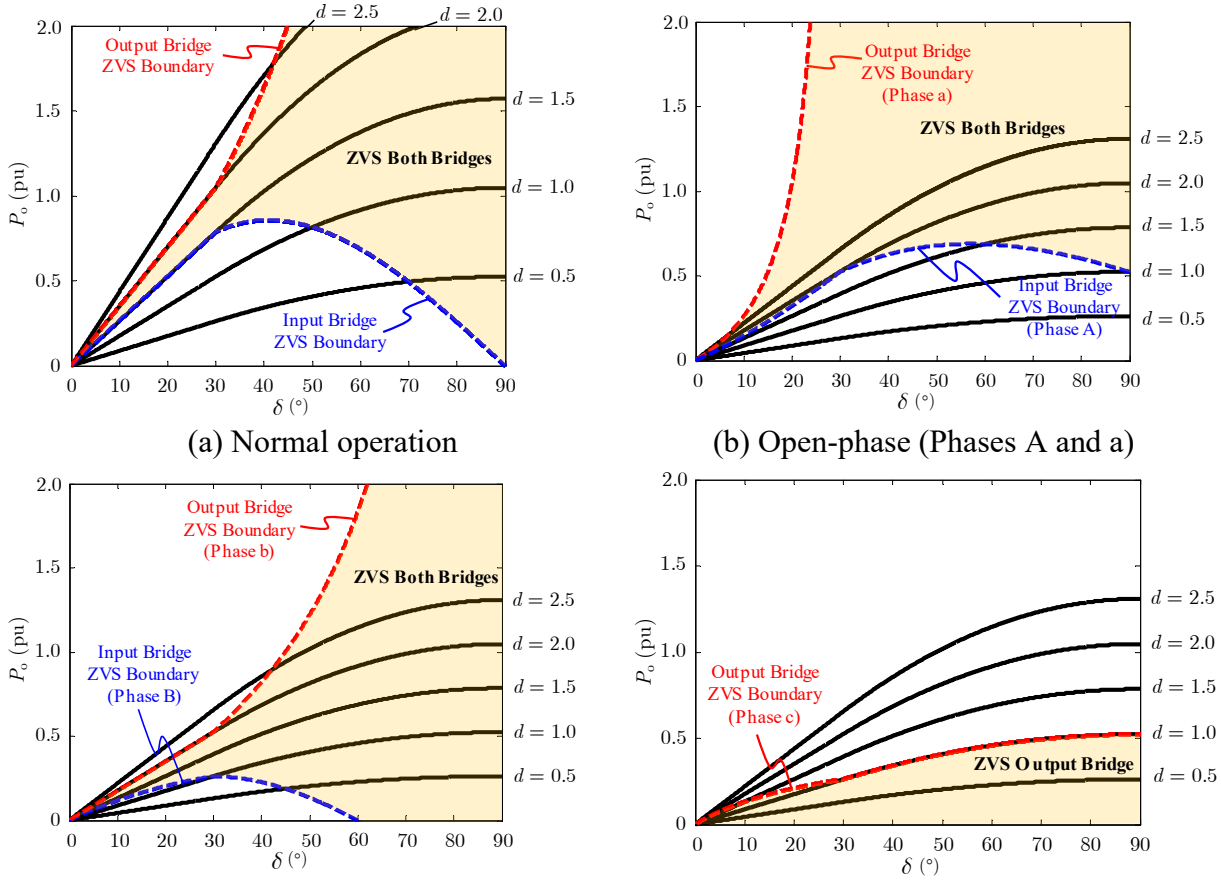

(a) Normal operation

(b) Open-phase (Phases A and a)

(c) Open-phase (Phases B and b)

(d) Open-phase (Phase c)

Figure 5.12 : Output power versus the control phase-shift with *d* as a parameter

5.3 Small-signal analysis

5.3.1 State-space averaging (SSA) model in open-phase

In this section, the state-space averaging (SSA) methodology presented in section 3.2 is extended for the determination of the transfer functions in open-phase operation. The model is still defined using the same general state-space formulation given in (3.6)–(3.8). The average input and output currents are still necessary to solve the output capacitor equation (3.9) as well as the input current equation (3.10). As for the PLM approach, due to the unbalanced operation of the 3p-DAB in open-phase operation, the procedure needs to be applied for modes I to V instead of modes I and II only. The average currents for modes I to V in open-phase operation are given in Appendix F. The averaged matrices $\mathbf{A}$, $\mathbf{B}$, $\mathbf{C}$, and $\mathbf{D}$ are then obtained by averaging their respective state-space matrices for modes I to V. Taylor's linearization technique is used afterward to linearize the non-linear terms around the operating point calculated using (5.14) or (5.15) depending on the control phase-shift range. It results in the following small-signal state-space equations. For range 1,

$$\frac{\mathrm{d}\hat{v}_\mathrm{o}(t)}{\mathrm{d}t}=\underbrace{\left(\frac{-1}{RC_\mathrm{o}}\right)}_{\hat{\mathbf{A}}}\hat{v}_\mathrm{o}(t)+\underbrace{\begin{bmatrix}\frac{mV_\mathrm{i}}{2\omega_\mathrm{s}L_\mathrm{s}C_\mathrm{o}} & \frac{m\delta}{2\omega_\mathrm{s}L_\mathrm{s}C_\mathrm{o}}\end{bmatrix}}_{\hat{\mathbf{B}}}\begin{bmatrix}\hat{\delta}(t)\\ \hat{v}_i(t)\end{bmatrix} \tag{5.20}$$

$$\begin{bmatrix}\hat{v}_\mathrm{o}(t)\\ \hat{i}_\mathrm{i}(t)\end{bmatrix}=\underbrace{\begin{bmatrix}1\\ \frac{m\delta}{2\omega_\mathrm{s}L_\mathrm{s}}\end{bmatrix}}_{\hat{\mathbf{C}}}\hat{v}_\mathrm{o}(t)+\underbrace{\begin{bmatrix}0 & 0\\ \frac{mV_\mathrm{o}}{2\omega_\mathrm{s}L_\mathrm{s}} & 0\end{bmatrix}}_{\hat{\mathbf{D}}}\begin{bmatrix}\hat{\delta}(t)\\ \hat{v}_\mathrm{i}(t)\end{bmatrix} \tag{5.21}$$

and range 2,

$$\frac{\mathrm{d}\hat{v}_\mathrm{o}(t)}{\mathrm{d}t}=\underbrace{\left(\frac{-1}{RC_\mathrm{o}}\right)}_{\hat{\mathbf{A}}}\hat{v}_\mathrm{o}(t)+\underbrace{\left(\frac{m}{2\omega_\mathrm{s}L_\mathrm{s}C_\mathrm{o}}\right)\begin{bmatrix}\left[\frac{3}{2}\left(1-\frac{2\delta}{\pi}\right)\right]V_\mathrm{i} & \left[\frac{3}{2}\left(\delta-\frac{\delta^2}{\pi}\right)-\frac{\pi}{24}\right]\end{bmatrix}}_{\hat{\mathbf{B}}}\begin{bmatrix}\hat{\delta}(t)\\ \hat{v}_i(t)\end{bmatrix} \tag{5.22}$$

$$\begin{bmatrix}\hat{v}_\mathrm{o}(t)\\ \hat{i}_\mathrm{i}(t)\end{bmatrix}=\underbrace{\begin{bmatrix}1\\ \frac{m}{2\omega_\mathrm{s}L_\mathrm{s}}\left[\frac{3}{2}\left(\delta-\frac{\delta^2}{\pi}\right)-\frac{\pi}{24}\right]\end{bmatrix}}_{\hat{\mathbf{C}}}\hat{v}_\mathrm{o}(t)+\underbrace{\begin{bmatrix}0 & 0\\ \frac{mV_\mathrm{o}}{2\omega_\mathrm{s}L_\mathrm{s}}\left[\frac{3}{2}\left(1-\frac{2\delta}{\pi}\right)\right] & 0\end{bmatrix}}_{\hat{\mathbf{D}}}\begin{bmatrix}\hat{\delta}(t)\\ \hat{v}_\mathrm{i}(t)\end{bmatrix} \tag{5.23}$$

By transferring (5.20)–(5.23) into the frequency-domain, the SSA model allows deriving the equivalent small-signal circuits for the 3p-DAB in open-phase operation (Figure 5.13). As for the normal operation case, these equivalent circuits are then used to derive the converter transfer functions G_{vd}, G_{vg}, Z_{D}, Z_{N} and Z_{o} in open-phase operation. The resulting transfer functions are compared with the normal operation case in Table 5.1.

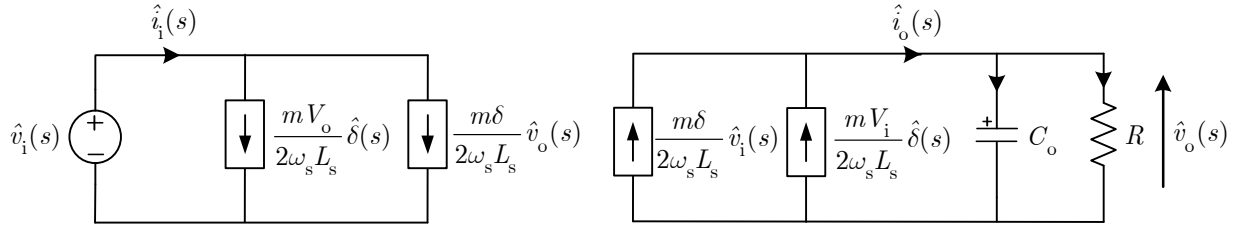

(a) Range 1

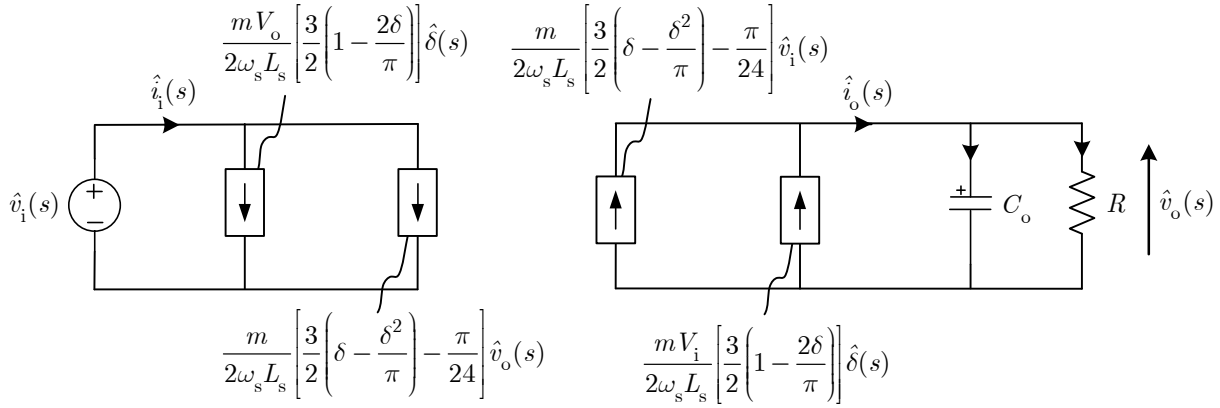

(b) Range 2

Figure 5.13 : Equivalent SSA small-signal circuits in open-phase operation

The analysis of the results given in Table 5.1 first shows that, in open-phase operation, the gain of the control-to-output transfer function G_{vd} is half the gain in normal operation. This means that, according to SSA, the gain of G_{vd} in open-phase is expected to be –6 dB inferior to the normal case. While it may look that it is also the case in range 2, the gain of G_{vd} depends on the control phase-shift δ which, as previously mentioned, for the same input and output voltages as well as loading conditions, must increase in open-phase condition as shown in Figure 5.8. Nevertheless, it is also concluded that the phase of G_{vd} is not affected in open-phase operation.

Moreover, the gain of the input-to-output transfer function G_{vg} in open-phase operation is also expected to be half (or –6 dB) the gain in normal operation. This suggests that perturbations on the

input voltage v_{i} should result in smaller consequences on the output voltage v_{o}. However, in both ranges, the gain of G_{vg} depends on the control phase-shift δ which increases in open-phase condition such that the conclusions may be different. This will be demonstrated in section 5.3.3.

Furthermore, according to the results in Table 5.1, the gain of the driving point input impedance Z_{D} is expected to increase by a factor 4 (+12 dB), and the gain of the null driving point input impedance Z_{N} is expected to increase by a factor 2 (+6 dB). As discussed in section 3.7, according to Middlebrook's theorem [55], for a given input filter, it suggests that the converter should be more stable in open-phase operation. In other words, this indicates that an input filter designed considering the normal conditions should not lead to instability in open-phase operation. However, it will also be shown in section 5.3.3 that the conclusions may be different if the increase in the control phase-shift δ in open-phase condition is considered.

Finally, according to the SSA model, the perturbation $\hat{\delta}$ that needs to be injected for the evaluation of Z_{N} can be calculated using the same relationships as for the normal operation case given in (3.24) and (3.25). Moreover, since the output impedance Z_{o} only depends on the load R and the output capacitor C_{o}, it is concluded that it is not affected in open-phase operation.

Table 5.1: Comparison of the transfer functions in normal and open-phase operations

Normal operation		**Open-phase operation**	
For range 1 ($0 \le \delta \le \pi/6$):			
$G_{vd}(s) = \left(\frac{mRV_i}{\omega_s L_s}\right)\frac{1}{sRC_o+1}$	(5.24)	$G_{vd}(s) = \left(\frac{mRV_i}{2\omega_s L_s}\right)\frac{1}{sRC_o+1}$	(5.25)
$G_{vg}(s) = \left(\frac{mR\delta}{\omega_s L_s}\right)\frac{1}{sRC_o+1}$	(5.26)	$G_{vg}(s) = \left(\frac{mR\delta}{2\omega_s L_s}\right)\frac{1}{sRC_o+1}$	(5.27)
$Z_D(s) = \left(\frac{\omega_s L_s}{m\delta}\right)^2 \frac{sRC_o+1}{R}$	(5.28)	$Z_D(s) = 4\left(\frac{\omega_s L_s}{m\delta}\right)^2 \frac{sRC_o+1}{R}$	(5.29)
$Z_N(s) = -\frac{\omega_s L_s V_i}{mV_o\delta}$	(5.30)	$Z_N(s) = -\frac{2\omega_s L_s V_i}{mV_o\delta}$	(5.31)
For range 2 ($\pi/6 \le \delta \le \pi/2$):			
$G_{vd}(s) = \frac{\left(\frac{mRV_i}{\omega_s L_s}\left[\frac{3}{2}\left(1-\frac{2\delta}{\pi}\right)\right]\right)}{sRC_o+1}$	(5.32)	$G_{vd}(s) = \frac{\left(\frac{mRV_i}{2\omega_s L_s}\left[\frac{3}{2}\left(1-\frac{2\delta}{\pi}\right)\right]\right)}{sRC_o+1}$	(5.33)
$G_{vg}(s) = \frac{\left(\frac{mR}{\omega_s L_s}\left[\frac{3}{2}\left(\delta-\frac{\delta^2}{\pi}\right)-\frac{\pi}{24}\right]\right)}{sRC_o+1}$	(5.34)	$G_{vg}(s) = \frac{\left(\frac{mR}{2\omega_s L_s}\left[\frac{3}{2}\left(\delta-\frac{\delta^2}{\pi}\right)-\frac{\pi}{24}\right]\right)}{sRC_o+1}$	(5.35)
$Z_D(s) = \frac{sRC_o+1}{R\left(\frac{m}{\omega_s L_s}\left[\frac{3}{2}\left(\delta-\frac{\delta^2}{\pi}\right)-\frac{\pi}{24}\right]\right)^2}$	(5.36)	$Z_D(s) = \frac{4\left(sRC_o+1\right)}{R\left(\frac{m}{\omega_s L_s}\left[\frac{3}{2}\left(\delta-\frac{\delta^2}{\pi}\right)-\frac{\pi}{24}\right]\right)^2}$	(5.37)
$Z_N(s) = \frac{\left(-\frac{\omega_s L_s V_i}{mV_o}\right)}{\left[\frac{3}{2}\left(\delta-\frac{\delta^2}{\pi}\right)-\frac{\pi}{24}\right]}$	(5.38)	$Z_N(s) = \frac{\left(-\frac{2\omega_s L_s V_i}{mV_o}\right)}{\left[\frac{3}{2}\left(\delta-\frac{\delta^2}{\pi}\right)-\frac{\pi}{24}\right]}$	(5.39)

Note: the differences between the normal and open-phase operation are marked in red.

5.3.2 Generalized state-space averaging (GSSA) model in open-phase

While SSA is derived in the previous section because it provides a better mathematical insight of the impacts of open-phase on the transfer functions, it has been concluded in section 3.5.2 that it is of limited use for small-signal modeling of the 3p-DAB at frequencies higher than 1/5$^{\text{th}}$ of f_{s}. SSA is generally precise enough for controller sizing with G_{vd} and for the evaluation of Z_{o}, but it lacks precision for the evaluation of G_{vg}, Z_{D}, and Z_{N}.

As discussed before, to overcome the limitations of SSA for DAB converters, the generalized state-space averaging (GSSA) approach [56] is used. Since GSSA is valid for the unbalanced case, it may be tempted to think that the open-phase case simply consists in replacing L_{A}, L_{B}, or L_{C} by a large value and recalculate the operating point using (5.14) and (5.15) to consider the fact that one phase is open. This has been proved not to be the case.

In fact, in open-phase operation, since the primary voltages v_{AN} and v_{BN} both depend on the output bridge switching-functions as well as the output voltage v_{o} the derivation of the GSSA model for the open-phase case requires to rewrite the converter differential equations. Using (2.30), (2.31), (5.5), and (5.6) for defining the voltages applied to L_{A} and L_{B} the following current differential equations are obtained,

$$\frac{di_{\text{A}}}{dt}=\frac{1}{2L_{\text{s}}}\left(\left[\text{s}_1-\text{s}_3\right]v_{\text{i}}-m\left[\text{s}_1^{'}-2\text{s}_3^{'}+\text{s}_5^{'}\right]v_{\text{o}}\right) \tag{5.40}$$

$$\frac{di_{\text{B}}}{dt}=\frac{1}{2L_{\text{s}}}\left(\left[\text{s}_3-\text{s}_1\right]v_{\text{i}}+m\left[\text{s}_1^{'}-2\text{s}_3^{'}+\text{s}_5^{'}\right]v_{\text{o}}\right) \tag{5.41}$$

It must be noted in (5.40) and (5.41) that it is assumed that the series inductance is the same for phases A and B, i.e. that, $L_{\text{A}}=L_{\text{B}}=L_{\text{s}}$. Then, using (5.11), the output capacitor voltage differential equation given in (3.9) is obtained,

$$\frac{dv_{\text{o}}}{dt}=\frac{m}{C_{\text{o}}}\left(\left[\text{s}_1^{'}-\text{s}_3^{'}\right]i_{\text{A}}+\left[\text{s}_3^{'}-\text{s}_5^{'}\right]i_{\text{B}}\right)-\frac{v_{\text{o}}}{RC_{\text{o}}} \tag{5.42}$$

As for the normal operation case, it is also convenient to add the input current equation into the GSSA model. In open-phase operation, it is reduced to,

$$i_{\text{i}}=\text{s}_1 i_{\text{A}}+\text{s}_3 i_{\text{B}} \tag{5.43}$$

By making similar assumptions as for the normal case, the model considers the index $k = 0$ (dc) term of v_{i}, i_{i}, and v_{o}, and the index $k = \pm 1$ (fundamental frequency) terms of i_{A} and i_{B}. Therefore, in open-phase operation, the following assumptions are made for the GSSA model,

$$v_{\mathrm{i}} = \left\langle v_{\mathrm{i}} \right\rangle_0, i_{\mathrm{i}} = \left\langle i_{\mathrm{i}} \right\rangle_0, v_{\mathrm{o}} = \left\langle v_{\mathrm{o}} \right\rangle_0 \tag{5.44}$$

$$\begin{aligned} i_{\mathrm{A}} &= \left\langle i_{\mathrm{A}} \right\rangle_1 = \left\langle i_{\mathrm{A}} \right\rangle_1^{\mathrm{R}} + j\left\langle i_{\mathrm{A}} \right\rangle_1^{\mathrm{I}} = \left\langle i_{\mathrm{A}} \right\rangle_{-1}^{*} \\ i_{\mathrm{B}} &= \left\langle i_{\mathrm{B}} \right\rangle_1 = \left\langle i_{\mathrm{B}} \right\rangle_1^{\mathrm{R}} + j\left\langle i_{\mathrm{B}} \right\rangle_1^{\mathrm{I}} = \left\langle i_{\mathrm{B}} \right\rangle_{-1}^{*} \end{aligned} \tag{5.45}$$

Since the there is no change to the switching-pattern, there is also no change in the switching-functions definition such that (3.54) and (3.55) still apply. Consequently, their average values are still given by (3.74)–(3.79).

By taking the average on both sides of (5.42) and (5.43), and using property 1 (*differentiation with respect to time*), the index-0 averaged model equations are obtained,

$$\frac{\mathrm{d}\left\langle v_{\mathrm{o}} \right\rangle_0}{\mathrm{d}t} = \frac{m}{C_{\mathrm{o}}}\left[\left\langle \mathrm{s}_1' i_{\mathrm{A}} \right\rangle_0 - \left\langle \mathrm{s}_3' i_{\mathrm{A}} \right\rangle_0 + \left\langle \mathrm{s}_3' i_{\mathrm{B}} \right\rangle_0 - \left\langle \mathrm{s}_5' i_{\mathrm{B}} \right\rangle_0\right] - \frac{\left\langle v_{\mathrm{o}} \right\rangle_0}{RC_{\mathrm{o}}} \tag{5.46}$$

$$\left\langle i_{\mathrm{i}} \right\rangle_0 = \left\langle \mathrm{s}_1 i_{\mathrm{A}} \right\rangle_0 + \left\langle \mathrm{s}_3 i_{\mathrm{B}} \right\rangle_0 \tag{5.47}$$

Similarly, by taking the average on both sides of (5.40) and (5.41), and using property 1 (*differentiation with respect to time*), the index-1 averaged model equations are given by,

$$\frac{\mathrm{d}\left\langle i_{\mathrm{A}} \right\rangle_1}{\mathrm{d}t} = \frac{1}{2L_{\mathrm{s}}}\left[\left\langle \mathrm{s}_1 v_{\mathrm{i}} \right\rangle_1 - \left\langle \mathrm{s}_3 v_{\mathrm{i}} \right\rangle_1 - m\left(\left\langle \mathrm{s}_1' v_{\mathrm{o}} \right\rangle_1 - 2\left\langle \mathrm{s}_3' v_{\mathrm{o}} \right\rangle_1 + \left\langle \mathrm{s}_5' v_{\mathrm{o}} \right\rangle_1\right)\right] - j\omega_{\mathrm{s}}\left\langle i_{\mathrm{A}} \right\rangle_1 \tag{5.48}$$

$$\frac{\mathrm{d}\left\langle i_{\mathrm{B}} \right\rangle_1}{\mathrm{d}t} = \frac{1}{2L_{\mathrm{s}}}\left[\left\langle \mathrm{s}_3 v_{\mathrm{i}} \right\rangle_1 - \left\langle \mathrm{s}_1 v_{\mathrm{i}} \right\rangle_1 + m\left(\left\langle \mathrm{s}_1' v_{\mathrm{o}} \right\rangle_1 - 2\left\langle \mathrm{s}_3' v_{\mathrm{o}} \right\rangle_1 + \left\langle \mathrm{s}_5' v_{\mathrm{o}} \right\rangle_1\right)\right] - j\omega_{\mathrm{s}}\left\langle i_{\mathrm{B}} \right\rangle_1 \tag{5.49}$$

Applying property 2 (*average of product*) to (5.46)–(5.49), writing the system of equation using the state-space formulation, and linearizing the resulting set of equations, it results in the following averaged small-signal state-space matrices,

$$\hat{\mathbf{A}}=\begin{bmatrix} \dfrac{-1}{RC_{\mathrm{o}}} & A_{12} & A_{13} & A_{14} & A_{15} \\ A_{21} & 0 & \omega_{\mathrm{s}} & 0 & 0 \\ A_{31} & -\omega_{\mathrm{s}} & 0 & 0 & 0 \\ A_{41} & 0 & 0 & 0 & \omega_{\mathrm{s}} \\ A_{51} & 0 & 0 & -\omega_{\mathrm{s}} & 0 \end{bmatrix}, \hat{\mathbf{B}}=\begin{bmatrix} B_{11} & 0 \\ B_{21} & \dfrac{\sqrt{3}}{4\pi L_{\mathrm{s}}} \\ B_{31} & \dfrac{-3}{4\pi L_{\mathrm{s}}} \\ B_{41} & \dfrac{-\sqrt{3}}{4\pi L_{\mathrm{s}}} \\ B_{51} & \dfrac{3}{4\pi L_{\mathrm{s}}} \end{bmatrix}, \hat{\mathbf{C}}=\begin{bmatrix} 1 & 0 & 0 & 0 & 0 \\ 0 & 0 & -\dfrac{2}{\pi} & -\dfrac{\sqrt{3}}{\pi} & \dfrac{1}{\pi} \end{bmatrix}, \hat{\mathbf{D}}=\begin{bmatrix} 0 & 0 \\ 0 & 0 \end{bmatrix} \tag{5.50}$$

The $\hat{\mathbf{A}}$ matrix terms are given as follows,

$$A_{12}=\frac{2S_{12}}{C_{\mathrm{o}}},\ A_{13}=\frac{2S_{13}}{C_{\mathrm{o}}},\ A_{14}=\frac{2S_{14}}{C_{\mathrm{o}}},\ A_{15}=\frac{2S_{15}}{C_{\mathrm{o}}} \tag{5.51}$$

with,

$$\begin{aligned} S_{12}&=\frac{m}{\pi}\left[\sin\left(\delta+\frac{7\pi}{6}\right)-\sin\left(\delta+\frac{11\pi}{6}\right)\right],\ S_{13}=\frac{m}{\pi}\left[\cos\left(\delta+\frac{7\pi}{6}\right)-\cos\left(\delta+\frac{11\pi}{6}\right)\right] \\ S_{14}&=\frac{m}{\pi}\left[\sin\left(\delta+\frac{11\pi}{6}\right)-\sin\left(\delta+\frac{\pi}{2}\right)\right],\ S_{15}=\frac{m}{\pi}\left[\cos\left(\delta+\frac{11\pi}{6}\right)-\cos\left(\delta+\frac{\pi}{2}\right)\right] \end{aligned} \tag{5.52}$$

and,

$$A_{21}=\frac{-S_{21}}{L_{\mathrm{s}}},A_{31}=\frac{-S_{31}}{L_{\mathrm{s}}},\ A_{41}=\frac{S_{41}}{L_{\mathrm{s}}},\ A_{51}=\frac{S_{51}}{L_{\mathrm{s}}} \tag{5.53}$$

$$\begin{aligned} S_{21}&=S_{41}=\frac{m}{2\pi}\left[\sin\left(\delta+\frac{7\pi}{6}\right)-3\sin\left(\delta+\frac{11\pi}{6}\right)\right] \\ S_{31}&=S_{51}=\frac{m}{2\pi}\left[\cos\left(\delta+\frac{7\pi}{6}\right)-\cos\left(\delta+\frac{11\pi}{6}\right)\right] \end{aligned} \tag{5.54}$$

The $\hat{\mathbf{B}}$ matrix terms are given as follow,

$$B_{21}=\frac{-S_{31}\mathrm{V}_{\mathrm{o}}}{L_{\mathrm{s}}},\ B_{31}=\frac{S_{21}\mathrm{V}_{\mathrm{o}}}{L_{\mathrm{s}}},\ B_{41}=\frac{S_{31}\mathrm{V}_{\mathrm{o}}}{L_{\mathrm{s}}},\ B_{51}=\frac{-S_{21}\mathrm{V}_{\mathrm{o}}}{L_{\mathrm{s}}} \tag{5.55}$$

$$B_{11}=\frac{2}{C_{\mathrm{o}}}\sum_{n=1}^{4}B_{11}(n) \tag{5.56}$$

with the $B_{11}(n)$ terms being defined as,

$$B_{11}(1)=S_{13}\left\langle I_{\mathrm{A}}\right\rangle_1^{\mathrm{R}},\ B_{11}(2)=-S_{12}\left\langle I_{\mathrm{A}}\right\rangle_1^{\mathrm{I}},\ B_{11}(3)=S_{15}\left\langle I_{\mathrm{B}}\right\rangle_1^{\mathrm{R}},\ B_{11}(4)=-S_{14}\left\langle I_{\mathrm{B}}\right\rangle_1^{\mathrm{I}} \tag{5.57}$$

In this case, the resulting vectors of small-signal state-variables, and inputs and outputs are given by,

$$\left\langle \hat{\mathbf{x}} \right\rangle = \left[\left\langle \hat{v}_{\mathrm{o}} \right\rangle_0 \ \left\langle \hat{i}_{\mathrm{A}} \right\rangle_1^{\mathrm{R}} \ \left\langle \hat{i}_{\mathrm{A}} \right\rangle_1^{\mathrm{I}} \ \left\langle \hat{i}_{\mathrm{B}} \right\rangle_1^{\mathrm{R}} \ \left\langle \hat{i}_{\mathrm{B}} \right\rangle_1^{\mathrm{I}} \right]^T \tag{5.58}$$

$$\left\langle \hat{\mathbf{u}} \right\rangle = \left[\left\langle \hat{\delta} \right\rangle_0 \ \ \left\langle v_{\mathrm{i}} \right\rangle_0 \right]^T, \ \left\langle \hat{\mathbf{y}} \right\rangle = \left[\left\langle \hat{v}_{\mathrm{o}} \right\rangle_0 \ \ \left\langle \hat{i}_{\mathrm{i}} \right\rangle_0 \right]^T \tag{5.59}$$

5.3.3 Small-signal characteristics of the 3p-DAB in open-phase

The SSA and GSSA models developed in the previous sections are now used to analyze the small-signal characteristics of the 3p-DAB in open-phase operation. This section has two main objectives: 1) evaluate the impacts of open-phase operation on the transient response and the stability of the 3p-DAB, and 2) compare the SSA and GSSA modeling methods for the analysis of the 3p-DAB in the open-phase case. The focus is on the transfer functions G_{vd}, G_{vg}, and Z_{D}. The parameters of model 4 (prototype) given in Appendix A are used in this section.

Analysis of G_{vd}:

First, from Figure 5.14 a) to c), it is concluded that the open-phase operation does reduce the magnitude of control-to-output transfer function G_{vd}. According to the GSSA model, this difference is equal to –7.5 dB at low frequency and decreases as the frequency increases toward the switching frequency f_{s}. However, according to the SSA model, the difference between the normal and the open-phase cases is constant to –7 dB over the entire frequency range. This is slightly different from the –6 dB difference expected in section 5.3.1. This is explained by the fact that the gain of G_{vd} depends on the control phase-shift δ, which, as mentioned before, increases in open-phase condition for the same voltage and loading conditions. Regarding the change in the control phase-shift δ between the two operating modes, two different cases are possible as shown in Figure 5.15. They are explained below.

> **Case #1:** At low power, if the converter is operated in range 1 in the normal operation mode, it may stay in range 1 in open-phase. The condition that must be met is the following,

$$P_{\mathrm{o}} \leq \frac{m\pi V_{\mathrm{i}} V_{\mathrm{o}}}{12\omega_{\mathrm{s}} L_{\mathrm{s}}} \tag{5.60}$$

This leads to the following relationship between the phase-shift in normal operation $\delta_{3\varphi}$ and the phase-shift in open-phase operation $\delta_{2\varphi}$,

$$\delta_{3\varphi} = \frac{\delta_{2\varphi}}{2} \tag{5.61}$$

Case #2: At high power, if the converter is operated in range 1 in the normal operation mode, it may need to be operated in range 2 in open-phase. The condition that must be met in this case is the following,

$$P_{\mathrm{o}} > \frac{m\pi V_{\mathrm{i}} V_{\mathrm{o}}}{12\omega_{\mathrm{s}} L_{\mathrm{s}}} \tag{5.62}$$

This leads to the following relationship between the phase-shift in normal operation $\delta_{3\varphi}$ and the phase-shift in open-phase operation $\delta_{2\varphi}$,

$$\delta_{3\varphi} = \frac{3}{4}\left(\delta_{2\varphi} - \frac{\left(\delta_{2\varphi}\right)^2}{\pi}\right) - \frac{\pi}{48} \tag{5.63}$$

Note that, for a given loading condition, if the converter is operated in range 2 in normal operation, it cannot be operated in open-phase condition for the same voltage and loading conditions. As shown in Figure 5.15, the test case analyzed in Figure 5.14 meets case #2 conditions; the phase-shift must be increased from $\delta_{3\varphi}$ = 18° (range 1) to $\delta_{2\varphi}$ = 36.3° (range 2) to keep the same output power P_{o} = 144 W. In the particular case of the SSA model, this means that the transfer function G_{vd} is given by (5.24) in normal operation (range 1), but it is given by (5.33) in open-phase operation (range 2) instead of (5.25) which applies to range 1 in open-phase. As a remark here, the –6 dB rule discussed in section 5.3.1 for G_{vd} evaluated with SSA only applies under case #1 conditions.

Furthermore, as shown in Figure 5.14 d), the GSSA model results confirm that the phase of G_{vd} is not affected in open-phase operation. Overall, since the gain of G_{vd} is reduced in open-phase but not its phase, for the same controller G_{c}, a degradation in the closed-loop transient response is expected. This will be confirmed experimentally in section 5.4.

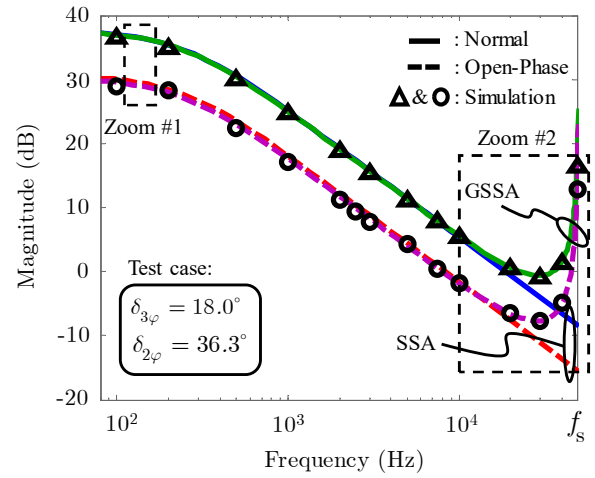

(a) Magnitude of G_{vd}

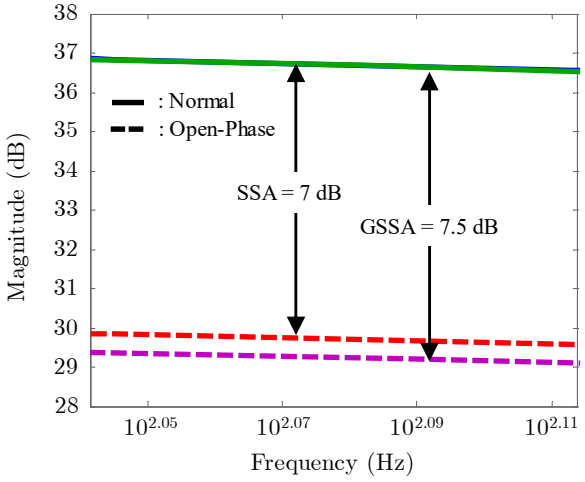

(b) Zoom #1 on the magnitude of G_{vd}

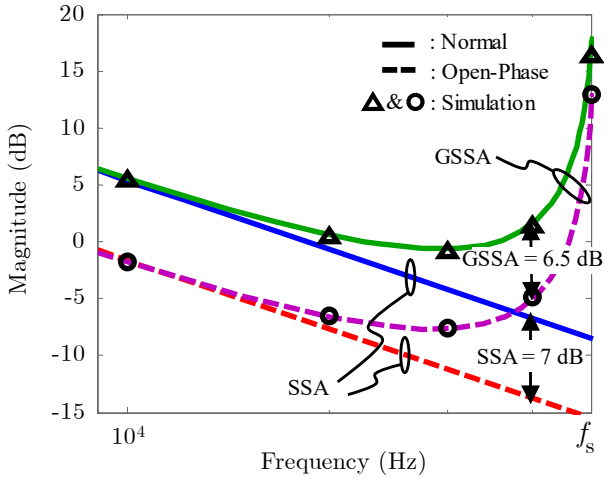

(c) Zoom #2 on the magnitude of G_{vd}

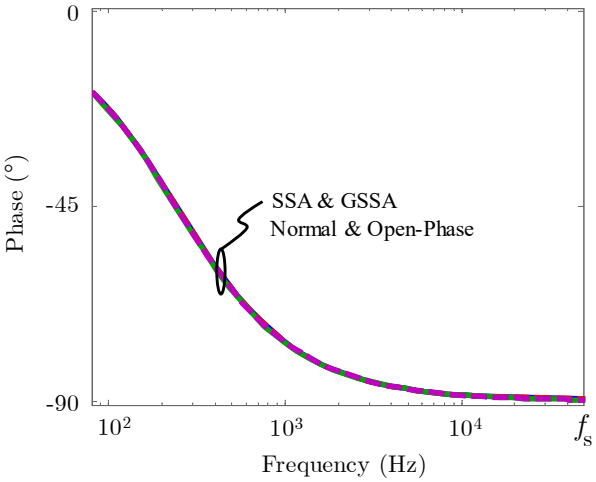

(d) Phase of G_{vd}

Figure 5.14 : Impact of open-phase on the control-to-output transfer function (model 4)

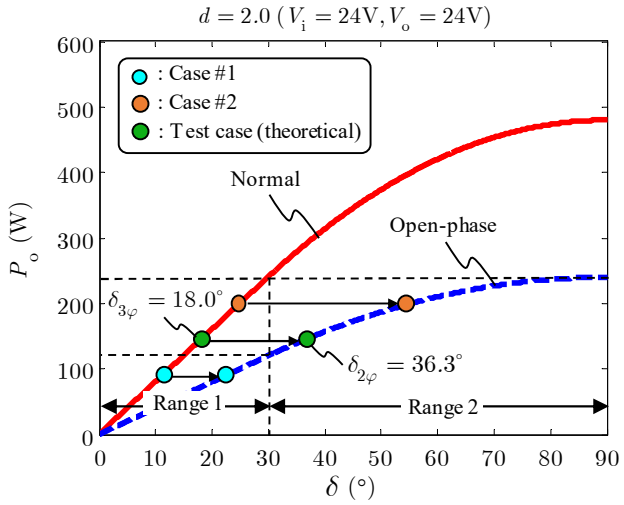

Figure 5.15 : Impact of open-phase on the control phase-shift (model 4)

Analysis of G_{vg}:

From Figure 5.16 a), it is also observed that SSA leads to the false conclusion that, for the same voltage and loading conditions, the transfer function G_{vg} is not affected in open-phase operation. In fact, according to GSSA in Figure 5.16 b), open-phase operation slightly reduces the magnitude of G_{vg} at low frequencies. As seen in Figure 5.16 a), this difference is, however, very small up to around 1/5th of the switching frequency f_s. For the test case parameters, the maximum reduction in the magnitude of G_{vg} is –4.5 dB at a frequency f = 30 kHz.

The error with the SSA model can be explained mathematically using the definitions of G_{vg} given in Table 5.1, and the equations for the calculation of the operating points for the normal and open-phase cases. The analysis is done here for range 1. In range 1, for normal operation, the required phase-shift δ is obtained by solving (2.37) for δ. It leads to,

$$\delta_{3\varphi} = \frac{\omega_s L_s P_o}{m V_i V_o} \tag{5.64}$$

Inserting (5.64) into the definition of the transfer function G_{vg} given by (5.26), and simplifying, it results in the following simplified version of the transfer function G_{vg},

$$G_{vg,3\varphi}(s) = \left(\frac{V_o}{V_i}\right)\frac{1}{sRC_o + 1} \tag{5.65}$$

Similarly, in range 1, for open-phase operation, the required phase-shift δ is obtained by solving (5.14) for δ. It leads to,

$$\delta_{2\varphi} = \frac{2\omega_s L_s P_o}{m V_i V_o} \tag{5.66}$$

Inserting (5.66) into the definition of the transfer function G_{vg} given by (5.27) and simplifying lead to the conclusion that,

$$G_{vg,2\varphi}(s) = G_{vg,3\varphi}(s) = \left(\frac{V_o}{V_i}\right)\frac{1}{sRC_o + 1} \tag{5.67}$$

It can also be demonstrated that (5.67) is also valid in range 2 for both the normal and open-phase cases. This explains why, for the same input and output voltages V_i and V_o as well as the same

loading condition R, the magnitude of G_{vg} in Figure 5.16 is the same in normal and open-phase operations according to SSA.

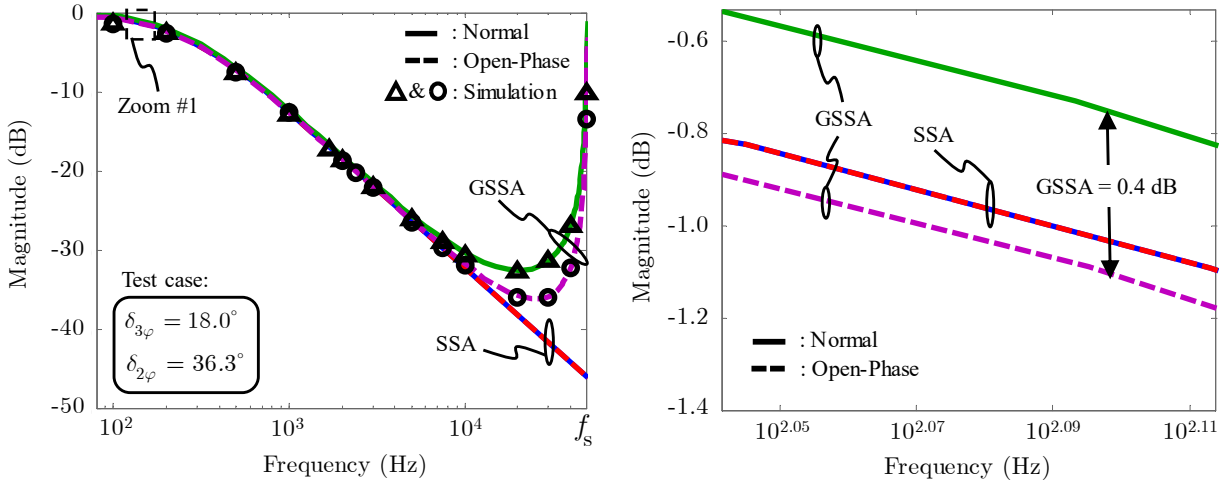

(a) Magnitude of G_{vg} (b) Zoom #1 on the magnitude of G_{vg}

Figure 5.16 : Impact of open-phase on the input-to-output transfer function (model 4)

Analysis of Z_D:

From Figure 5.17 a), it is concluded that SSA also leads to the false conclusion that, for the same input and output voltages as well as loading conditions, the input impedance Z_D is not affected in open-phase operation. In fact, according to the GSSA model in Figure 5.17 b), the peak gain frequency is shifted from 1.8 kHz to 2.5 kHz in open-phase operation. According to Middlebrook's theorem [55], for a given input filter, it suggests that it tends to be less stable between 1 kHz and 2.1 kHz, but to be more stable at frequencies higher than 2.1 kHz.

As for G_{vg}, the error with the SSA model can be explained mathematically using the definitions of Z_D given in Table 5.1, and using equations (5.64) and (5.66) for the calculation of the control phase-shift for the normal and open-phase cases respectively. It leads to,

$$Z_{D,2\varphi}(s) = Z_{D,3\varphi}(s) = \left(\frac{RV_i^2}{V_o^2}\right)\left[sRC_o + 1\right] \tag{5.68}$$

Again, it can also be demonstrated that (5.68) is valid in range 2. As for G_{vg}, it explains why, for the same voltages V_i and V_o as well as the same loading condition R, the magnitude of Z_D in Figure 5.17 is the same in normal and open-phase operations according to SSA.

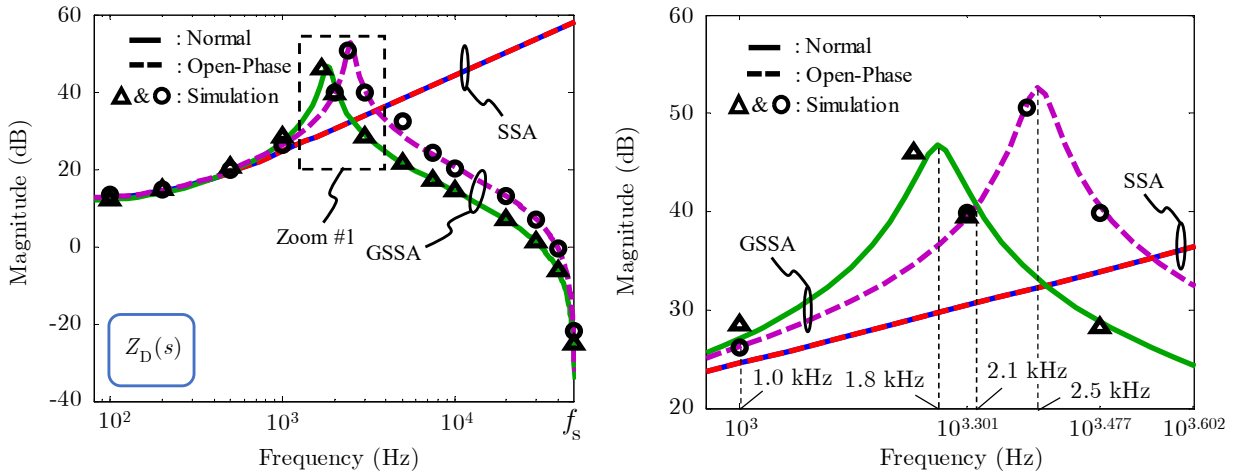

(a) Magnitude of Z_D (b) Zoom #1 on the magnitude of Z_D

Figure 5.17 : Impact of open-phase on the input impedance (model 4)

5.4 Closed-loop transient analysis in open-phase

When switching from normal to open-phase operation with the same voltage and the same loading conditions, it must also be determined if the controller parameters need to be adjusted to keep an acceptable transient dynamic response.

To answer this question, the PI-controller G_c sized in section 3.6.2 using the transfer function G_{vd} of the 3p-DAB in normal operation is used. The characteristics of the designed PI-controller G_c are given in Figure 5.18. This controller is used for both simulation and experimental analyses. The impacts of keeping the same controller G_c when passing from normal to open-phase operation on the cross-over frequency $f_{\varphi m}$ and the phase-margin φ_m are also highlighted in Figure 5.18. Overall, it is concluded that the cross-over frequency $f_{\varphi m}$ is reduced from 1 kHz in normal operation to 535 Hz in open-phase operation. The phase-margin φ_m also slightly decreases from 65° to 63°.

By applying a step from 0 V to 24 V in the reference voltage on the prototype, the overall result is a higher overshoot (15% against less than 9%) and a slower transient response (time-to-peak of 1.6 ms against 0.5 ms). This is due to the reduced ability of the same PI-controller G_c to deal with disturbances in open-phase. This is mainly due to the important reduction in the cross-over frequency $f_{\varphi m}$. This situation can be considered acceptable in some practical applications, but the controller parameters may need to be adjusted in some cases.

Furthermore, the simulation results in Figure 5.21 a) show that the designed controller allows a transition from normal to frozen leg and from frozen leg to open-phase without interruption. From Figure 5.21 b), it is also concluded that open-phase operation provides reduced current stress over the frozen leg operation. The results in Figure 5.21 c) also confirm that open-phase operation provides an increased power transfer capability over frozen leg operation because, for the same output power, the control phase-shift δ is smaller in open-phase than in frozen leg.

Moreover, experimental results also confirm that the converter can transition from normal to frozen leg (Figure 5.22), from frozen leg to open-phase (Figure 5.23), and from normal to open-phase (Figure 5.24) without interruption. The normal to frozen leg transition is performed by disabling the phase C gating signals s_5 and s_6. The frozen leg to open-phase and normal to open-phase transitions are validated by opening the normally closed (NC) contact of a relay inserted in the phase C. The relay coil signal is used to trigger the oscilloscope and capture the event. A delay of 2.8 ms between the coil opening signal and the actual phase opening is introduced by the relay.

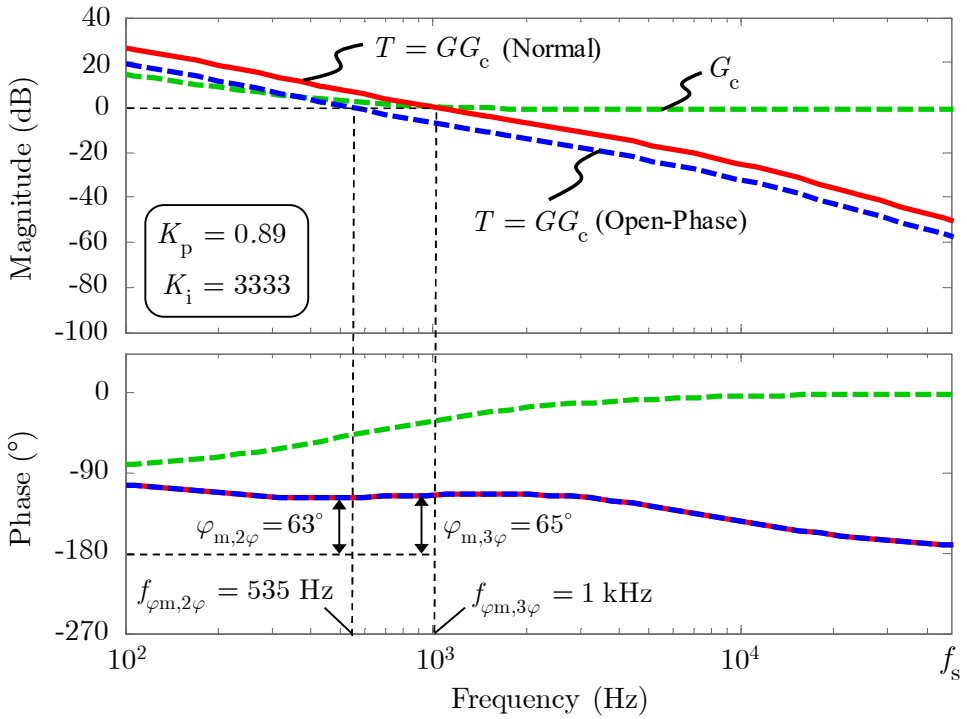

Figure 5.18 : Closed-loop small-signal characteristics in open-phase (model 4)

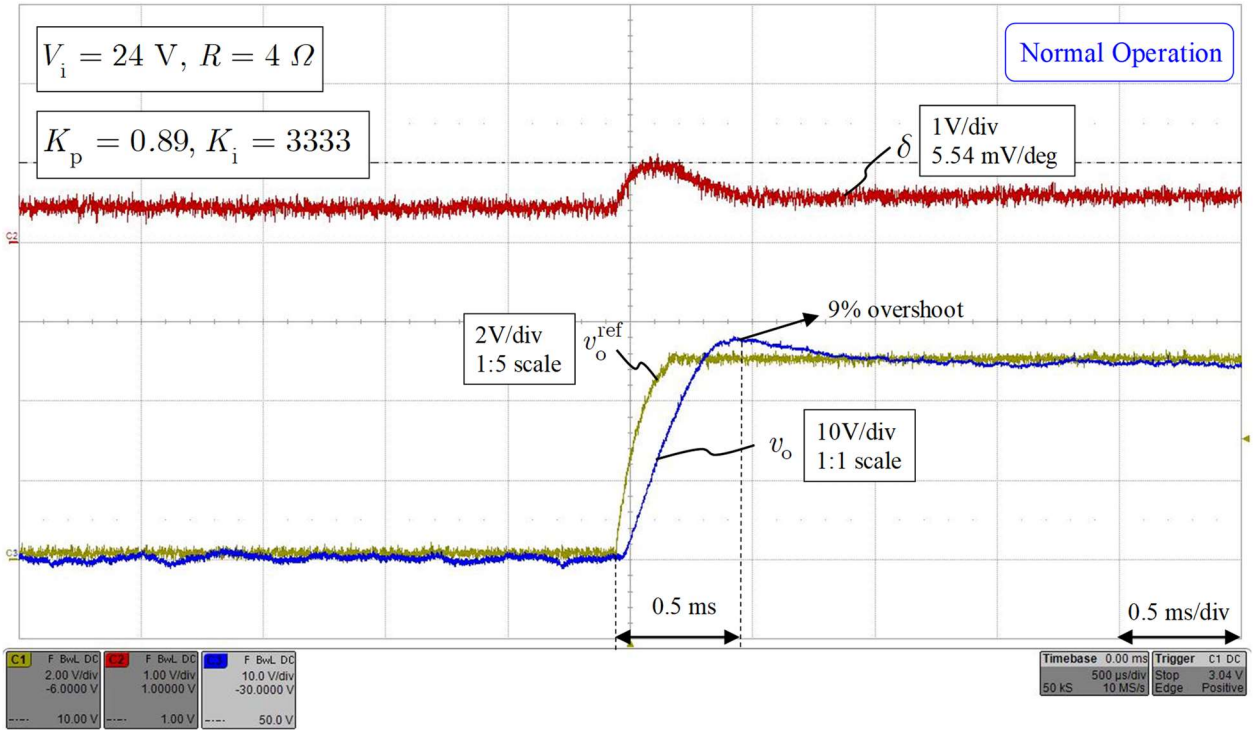

Figure 5.19 : Closed-loop response for the normal operation case (prototype)

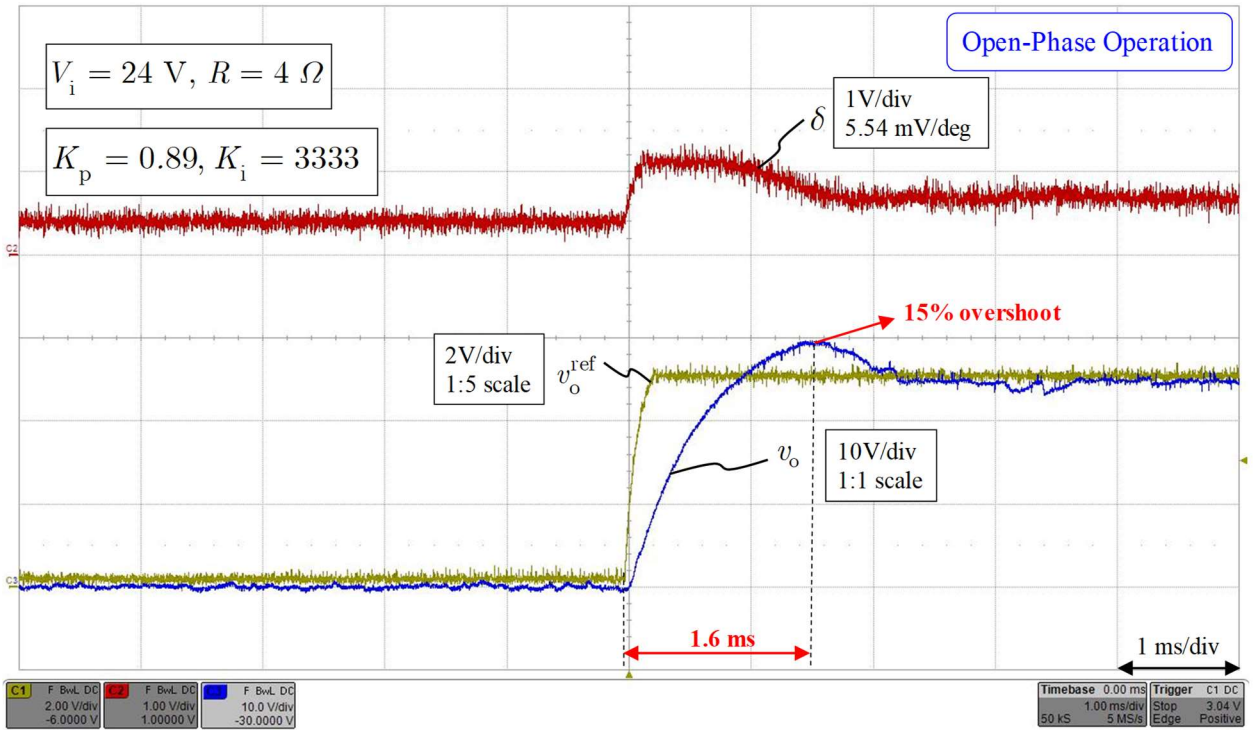

Figure 5.20 : Closed-loop response for the open-phase operation case (prototype)

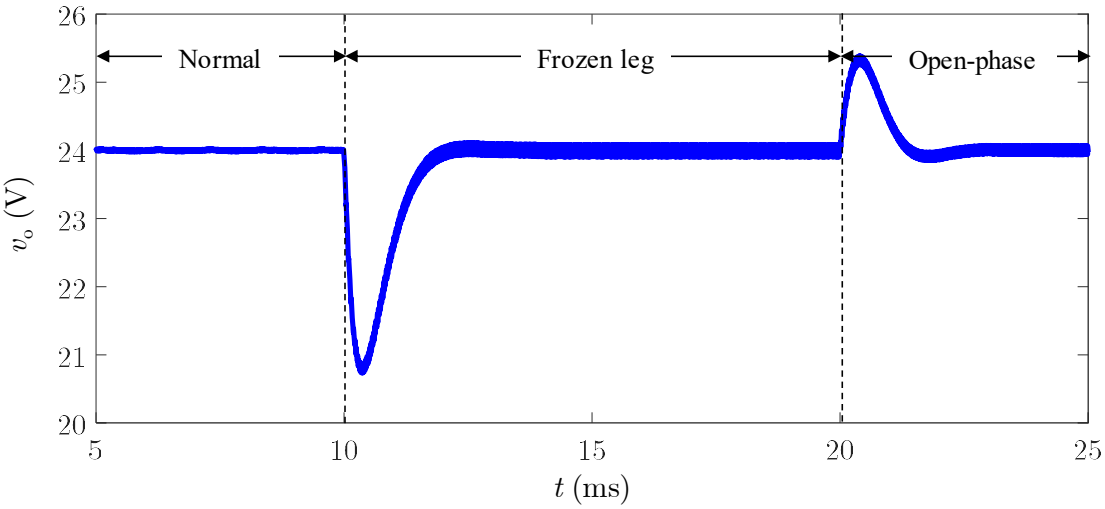

(a) Output voltage

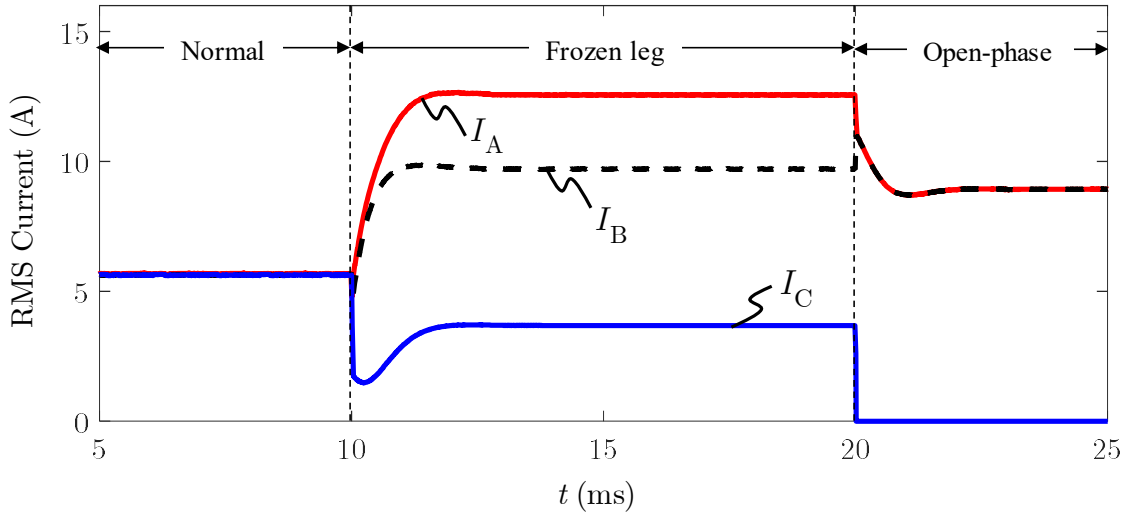

(b) Transformer RMS currents

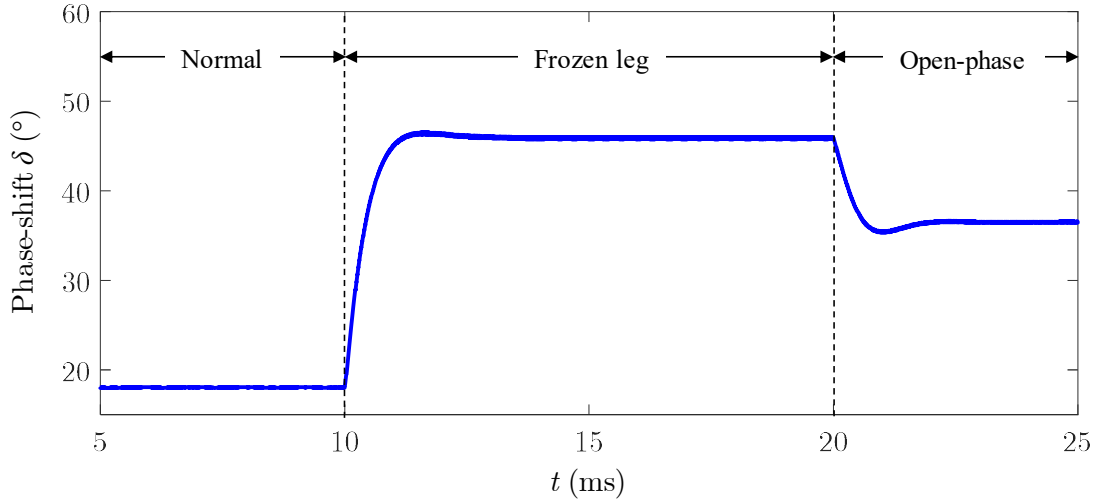

(c) Control phase-shift

Figure 5.21 : Simulation results for the transitions between the operating modes (model 4)

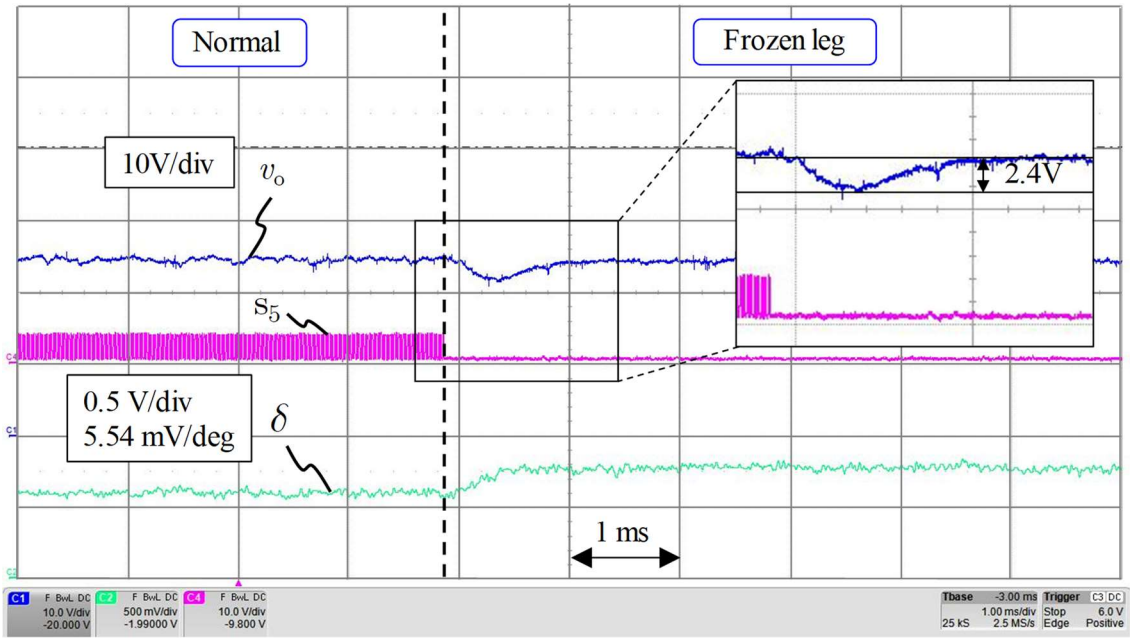

Figure 5.22 : Transition from normal to frozen leg (prototype)

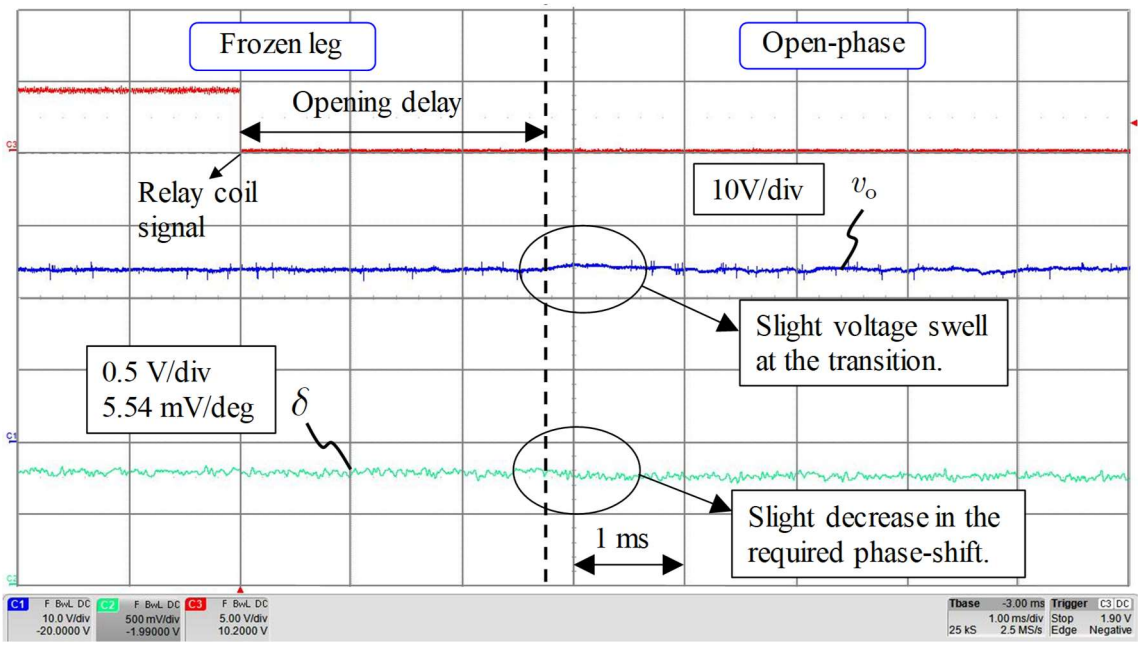

Figure 5.23 : Transition from frozen leg to open-phase (prototype)

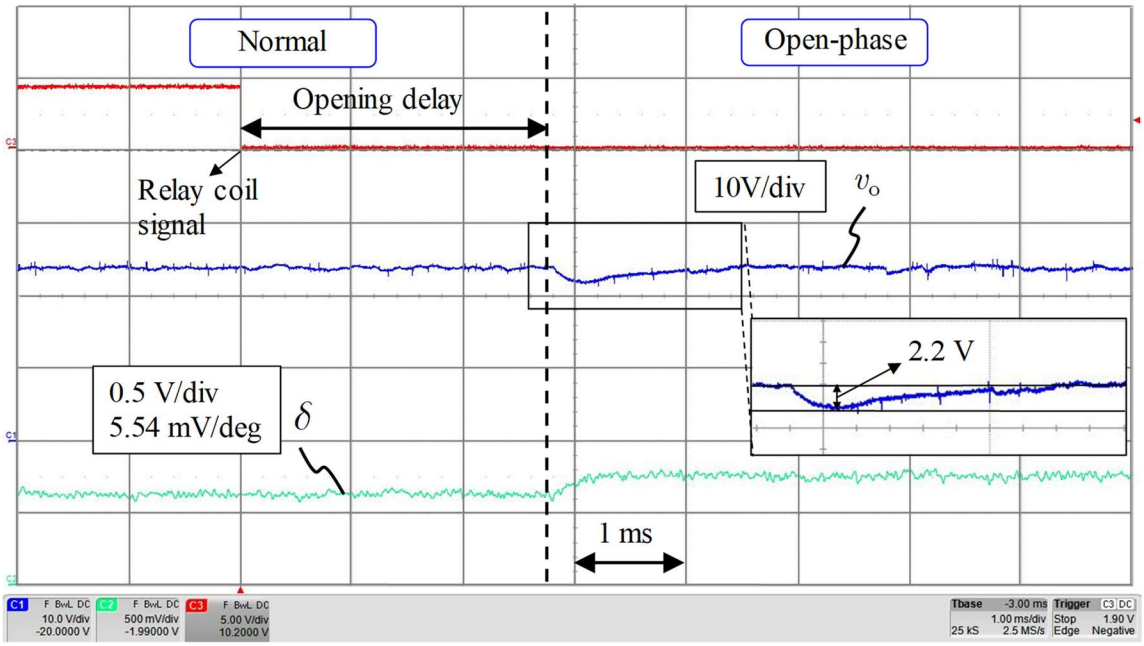

Figure 5.24 : Transition from normal to open-phase (prototype)

CHAPTER 6 CONCLUSIONS AND RECOMMENDATIONS

6.1 Summary of this thesis

The main objective of this thesis was to develop and validate accurate models for the analysis of integration of 3p-DAB converters into dc-grids. It fills gaps in the literature by demonstrating the efficiency, accuracy and usefulness of the developed small- and large-signal models. It is a key step forward toward describing the behavior of 3p-DAB converters for their integration in next-generation dc power systems. By comparing different modeling strategies, this thesis provides a comprehensive review of the advantages and limitations of different modeling approaches for simulation and analysis of 3p-DAB converters. Furthermore, it has been discovered that the 3p-DAB can be operated with one phase open. By studying the open-phase operation mode, this thesis shows how the investigated modeling strategies can be adapted to the analysis of the 3p-DAB in degraded operation. The main contributions and conclusions of this thesis are summarized as follows.

Small-signal modeling of the 3p-DAB

The successful integration of the 3p-DAB with other power systems components requires determining its frequency-domain small-signal characteristics accurately. The standard approach for small-signal modeling of the 3p-DAB converter is to use the state-space averaging (SSA) method. SSA benefits from being easier in representing the small-signal model as an equivalent circuit. It also provides a better insight of parameters influence. For the 3p-DAB, SSA leads to a dc-averaged model which neglects the ac dynamic of the three-phase transformer currents as well as the impact of the input and output bridges switching-functions. As shown in this thesis, SSA is generally precise enough for controller sizing using the control-to-output transfer function G_{vd} in addition to determining the output impedance Z_{o} of the converter. However, SSA is not accurate for the stability analysis of the 3p-DAB because it lacks precision in evaluating the driving point input impedance Z_{D} and the null driving point input impedance Z_{N}. These two transfer functions are necessary for the application of Middlebrook's extra element theorem (EET) which is broadly used in practice by power electronic designers to avoid dynamic performance degradation or instability conditions in the presence of an additional input filter.

To overcome the limitations of SSA in stability analysis, a hybrid SSA and generalized state-space averaging (GSSA) model is proposed in this thesis. The GSSA model is used to calculate the driving point input impedance Z_{D} while the proposed hybrid model is used to evaluate the null driving point input impedance Z_{N}. The proposed approach allows reducing the number of time-domain simulation runs and experimental tests required to predict dynamic performance degradation and instability conditions. The main outcomes have been published in [50].

Large-signal modeling of the 3p-DAB

Previous work has shown that large-signal time-domain modeling of 3p-DAB converters is not trivial. The only resource in the literature proposed a discretized switching-function model in the αβ frame which reduces the number of electrical nodes while preserving the switching-effect [62]. However, the reduction in the computation time compared to the ideal-model approach is not shown. Furthermore, although the reduction in the number of electrical nodes is a sign of a reduced computational effort, it cannot be used alone as an indicator for the reduction in computation time.

As a response to this breach in the literature, large-signal models of the 3p-DAB converter are developed, analyzed and implemented in EMTP. Three modeling strategies are investigated in this thesis: 1) the switching-function (SWF), 2) the generalized average modeling (GAM) and 3) the state-space averaging (SSA). The results showed that, even if SSA significantly reduces the computation time, it has a limited precision for studying phenomena beyond $1/5^{\mathrm{th}}$ of the converter switching frequency f_{s}. Because they allow higher time-steps, the SWF and GAM models both offer significant reduction in the computation time compared to the ideal-model, while still preserving the converter frequency characteristics up to its switching frequency f_{s}. However, the maximum time-step with the SWF model is limited by the inclusion of the switching-effect, which, still leads to a high computation time for system-level studies. Overall, the proposed GAM model offers the best compromise in terms of accuracy, speed and wideband response. It is a key step toward efficient and accurate time-domain system-level simulation of next-generation dc-grids based on the 3p-DAB topology. The main results have been published in [61].

Open-phase degraded-operation of the 3p-DAB converter

Preceding research showed that the 3p-DAB converter can be operated in a frozen leg degraded-mode [35]. However, the analytical characterization of the converter behavior under all voltage and loading conditions is not shown due to the important impact of the reactive current circulation in the faulty-phase on the voltage and current waveforms. In this thesis, open-phase fault-tolerant operation of the 3p-DAB converter has been proposed as an upgrade to frozen leg. It is confirmed experimentally on a closed-loop EPC2022 GaN-based small-scale prototype. The first benefit of open-phase operation is to simplify the analytical characterization of the 3p-DAB. The results presented in this thesis also showed that, even if it requires an additional switch (relay or contactor) to open the faulty-phase, the open-phase operation provides practical advantages over the frozen leg operation.

Steady-state analysis is performed to evaluate the impact of open-phase operation on the converter voltage and current waveforms, and its power transfer and ZVS capabilities. Small-signal analysis along with time-domain simulations are also provided to assess the impacts on the converter stability and its dynamic performance. The most important conclusions are as follows. 1) Open-phase operation requires no change to the modulation pattern. 2) Open-phase operation provides reduced current stress and an increased power transfer capability over frozen leg operation. 3) The power transfer capability in open-phase is theoretically half the normal operation, such that, for the same voltage and loading conditions, the control phase-shift needs to increase. 4) The stability of the 3p-DAB can be positively and/or negatively affected in open-phase operation. 5) For the same PI-controller, the transient response is negatively affected in open-phase operation such that the controller parameters may need to be adjusted if the dynamic of the converter is a metric that must be preserved in degraded-operation.

Overall, using a fault-tolerant topology, which provides intrinsic redundancy upon failure of switches, will undeniably facilitate the industrial acceptation of emerging semiconductor technologies such as silicon carbide (SiC) and gallium nitride (GaN). Accurate characterization of the 3p-DAB behavior in degraded-mode is also crucial for the development of reliable and resilient dc-grids which utilizes 3p-DAB as central elements. The main results have been submitted in IEEE Transactions on Power Electronics. The paper is currently accepted with major mandatory changes.

6.2 Future work

The recommendations for future areas of research are divided into two main categories: 1) improvements to the small- and large-signal models of the 3p-DAB, and 2) development and implementation of switch failure diagnosis schemes for the post-fault open-phase operation of the 3p-DAB converter.

6.2.1 Improvements to the developed small- and large-signal models

Inclusion of filters, losses, and higher harmonics in the small- and large-signal models

In this thesis, filters and losses (conduction and core losses, and capacitor ESR) are neglected in the proposed small- and large-signal models of the 3p-DAB converter. Furthermore, only the fundamental-frequency component of the transformer current is included in the generalized averaging small- and large-signal models.

The inclusion of filters increases the order of the small-signal models using the state-space averaging (SSA) method [90]. The inclusion of filters with the generalized averaging approach applied to the 3p-DAB is not shown in the literature. The inclusion of filters in the converter small-signal model is fundamentally different from the application of Middlebrook's theorem [55] which separates a priori the design of the converter from the input filter. In large-signal models implemented in time-domain simulation tools, filters can be considered as discrete RLC-elements or directly included in the converter model equations. When modeled as discrete RLC-elements, it increases the burden to solve the network equations. Conversely, when included in the converter model equations, it increases the control system equations solver task. The comparison of the computation time t_{cpu} with these two approaches is not provided in the literature.

Previous work on the 1p-DAB also showed that, neglecting losses, can reduce the accuracy of the 1p-DAB small-signal model [57]. However, when considering conduction losses with the SSA method, the equations describing the transformer current waveforms become piecewise exponentials instead of piecewise-linear. In this case, the calculation of the average value of the input and output currents is more complex. Its application to the 3p-DAB is not trivial. Conduction losses can also be considered with the generalized averaging approach as shown in [53] and [58]

for the 1p-DAB and the 3p-DAB respectively. The inclusion of core losses is not shown in these references. Furthermore, as shown in [53], the inclusion of the capacitor ESR with the generalized averaging method also increases the order of the resulting system of equations.

Neglecting higher harmonics with the generalized averaging method can also lead to errors in the determination of the steady-state operating point, which, further impacts the accuracy of the resulting small-signal models [58], [91]. Including higher harmonics in the generalized averaging method for large-signal analysis of the 3p-DAB will increase the computation time t_{cpu}, but the real impact is unknown.

Modeling of the 3p-DAB with constant power loads (CPLs)

In this thesis, the 3p-DAB converter under study is always supplying power to a purely resistive load R. However, in dc-grids, tightly regulated power electronics converter can act, within their control bandwidth, as constant power loads (CPLs) [26], [81]. As a consequence, CPLs behave as negative incremental resistances seen from their input terminals. Because of the presence of LC filters, the system can oscillate and becomes unstable [92].

As seen in this thesis, the load R is part of all the 3p-DAB transfer functions (G_{vd}, G_{vg}, Z_{D}, Z_{N}, and Z_{o}). When loaded with CPLs, it has been shown in [93] using the state-space averaging (SSA) method, that the control-to-output transfer function G_{vd} of the 3p-DAB is modified. The conclusion is that the small-signal stability is affected by the percentage of CPLs against resistive loads R. The impact on other transfer functions is not shown. The inclusion of CPLs in the generalized averaging approach applied to the 3p-DAB is also the ground for further research.

Modeling of the 3p-DAB with variable switching frequency

In this thesis, all the developed models assume that the 3p-DAB is controlled with a fixed switching frequency f_{s} modulation scheme. The phase-shift δ is the only controlled variable to regulate the output voltage v_{o}. Previous work on the 1p-DAB showed that the converter soft-switching operation may benefit from adjusting the switching frequency f_{s} [94], [95]. By analyzing the 3p-DAB converter transfer functions given in this thesis, it must be recognized that interactions between the control of f_{s} and δ is unavoidable. In other words, changing f_{s} impacts the operating

point of the converter which further influence the control-to-output transfer function G_{vd} relating the output voltage v_{o} to the phase-shift δ. High bandwidth control of both f_{s} and δ requires an accurate characterization of the converter small-signal characteristics with f_{s} considered as a control variable. Considering f_{s} as a control variable with the state-space averaging (SSA) method is quite trivial. If f_{s} is not slowly varied, the inclusion of f_{s} as a control variable is, however, challenging with the generalized averaging methodology [56].

6.2.2 Diagnosis of switch failure for post-fault open-phase operation

Fault-tolerant (FT) operation relies on effective fault-diagnosis (FD) methodologies [37]. In this thesis, post-fault open-phase FT operation is proposed to be triggered by a feedback fault signal coming from the gate drivers, similarly to previous work on frozen leg operation [35]. This covers only a limited number of failure cases in the 3p-DAB. Because it requires opening the faulty-phase, the detection and the identification of the faulty-phase is an important step to increase the potential use of the proposed open-phase FT operation. Recent work investigated the possibility to detect an open-circuit condition of one transistor using the polarity of the dc component in the transformer currents [96]. The detection of other conditions such as transistor short-circuit or failed diodes remains unaddressed. Since the 3p-DAB converter is composed of two three-phase inverters, many of the FD strategies and remedial actions proposed for three-phase inverters in the literature [97] are potential candidates for application with the 3p-DAB.

BIBLIOGRAPHY

[1] T. Dragicevic, X. Lu, J.C.Vasquez, and J.M.Guerrero, "DC Microgrids—Part II: A review of power architectures, applications, and standardization issues," *IEEE Trans. Power Electron.*, vol. 31, no. 5, pp. 3528–3549, May 2016.

[2] D. Boroyevich, I. Cvetkovic, D. Dong, R. Burgos, F. Wang, and F. Lee, "Future electronic power distribution systems a contemplative view," in *Proc. 12th Int. Conf. Optim. Elect. Electron. Equip. (OPTIM)*, May 2010, pp. 1369–1380.

[3] J. A. Rosero, J. A. Ortega, E. Aldabas, and L. Romeral, "Moving towards a more electric aircraft," *IEEE Aerosp. Electron. Syst. Mag.*, vol. 22, no. 3, pp. 3–9, Mar. 2007.

[4] M. Berger, C. Lavertu, I. Kocar, and J. Mahseredjian, "Proposal of a time-domain platform for short-circuit protection analysis in rapid transit train DC auxiliary systems," *IEEE Trans. Ind. Appl.*, vol. 52, no. 6, pp. 5295–5304, Nov./Dec. 2016.

[5] A. Sannino, G. Postiglione, and M. H. J. Bollen, "Feasibility of a DC network for commercial facilities," *IEEE Trans. Ind. Appl.*, vol. 39, no. 5, pp. 1499–1507, Sep./Oct. 2003.

[6] M. E. Baran and N. R. Mahajan, "DC distribution for industrial systems: Opportunities and challenges," *IEEE Trans. Ind. Appl.*, vol. 39, no. 6, pp. 1596–1601, Nov./Dec. 2003.

[7] D. J. Becker and B. J. Sonnenberg, "DC microgrids in buildings and data centers," in *Proc. IEEE Int. Telecom. Energy Conf.*, Oct. 2011, pp. 1–7.

[8] A. Berizzi, A. Silvestri, D. Zaninelli, and S. Massucco, "Short-circuit current calculations for DC systems," *IEEE Trans. Ind. Appl.*, vol. 32, no. 5, pp. 990–997, Sep./Oct. 1996.

[9] J. Robinson, D. Jovcic, and G. Joos, "Analysis and design of an offshore wind farm using a MV DC grid," *IEEE Trans. Power Del.*, vol. 25, no. 4, pp. 2164–2173, Oct. 2010.

[10] G. S. Thandi, R. Zhang, K. Xing, F. C. Lee, and D. Boroyevich, "Modeling, control and stability analysis of a PEBB based DC DPS," *IEEE Trans. Power Del.*, vol. 14, no. 2, pp. 497–505, Apr. 1999.

[11] B. Zhao, Q. Song, W. Liu, and Y. Sun, "Overview of Dual-Active-Bridge Isolated Bidirectional DC–DC Converter for High-Frequency-Link Power-Conversion System," *IEEE Trans. Power Electron.*, vol. 29, no. 8, pp. 4091–4106, Aug. 2014.

[12] R. W. A. A. De Doncker, D. M. Divan, and M. H. Kheraluwala, "A three-phase soft-switched high-power-density DC/DC converter for high-power applications," *IEEE Trans. Ind. Appl.*, vol. 27, no. 1, pp. 63–73, Jan/Feb 1991.

[13] M. N. Kheraluwala, R. W. Gascoigne, D. M. Divan, and E. D. Baumann, "Performance characterization of a high-power dual active bridge DC-to-DC converter," *IEEE Trans. Ind. Appl.*, vol. 28, no. 6, pp. 1294–1301, Nov/Dec 1992.

[14] N. M. L. Tan, T. Abe, and H. Akagi, "Design and Performance of a Bidirectional Isolated DC–DC Converter for a Battery Energy Storage System," *IEEE Trans. Power Electron.*, vol. 27, no. 3, pp. 1237–1248, Mar. 2012.

[15] B. Zhao, Q. Song, W. Liu, and Y. Xiao, "Next-Generation Multi-Functional Modular Intelligent UPS System for Smart Grid," *IEEE Trans. Ind. Electron.*, vol. 60, no. 9, pp. 3602–3618, Sept. 2013.

[16] G. J. Su and L. Tang, "A Three-Phase Bidirectional DC-DC Converter for Automotive Applications," in *Proc. IEEE Ind. Appl. Soc. Annu. Meet.*, 2008, pp.1–7.

[17] H. van Hoek, M. Neubert, and R. W. De Doncker, “Enhanced Modulation Strategy for a Three-Phase Dual Active Bridge-Boosting Efficiency of an Electric Vehicle Converter,” *IEEE Trans. Power Electron.*, vol. 28, no. 12, pp. 5499–5507, Dec. 2013.

[18] N. H. Baars, J. Everts, H. Huisman, J. L. Duarte, and E. A. Lomonova, “A 80-kW Isolated DC–DC Converter for Railway Applications,” *IEEE Trans. Power Electron.*, vol. 30, no. 12, pp. 6639–6647, Dec. 2015.

[19] X. She, A. Q. Huang, and R. Burgos, “Review of Solid-State Transformer Technologies and Their Application in Power Distribution Systems,” *IEEE J. of Emerg. Sel. Topics in Power Electron.*, vol. 1, no. 3, pp. 186–198, Sept. 2013.

[20] C. Gammeter, F. Krismer, and J. W. Kolar, “Comprehensive conceptualization, design, and experimental verification of a weight-optimized all-sic 2 kV/700 V DAB for an airborne wind turbine,” *IEEE J. Emerg. Sel. Topics Power Electron.*, vol. 4, no. 2, pp. 638–656, Jun. 2016.

[21] H. Y. Kanaan, M. Caron, and K. Al-Haddad, “Design and Implementation of a Two-Stage Grid-Connected High Efficiency Power Load Emulator,” *IEEE Trans. Power Electron.*, vol. 29, no. 8, pp. 3997–4006, Aug. 2014.

[22] R. W. DeDoncker, M. H. Kheraluwala, and D. M. Divan, “Power conversion apparatus for DC/DC conversion using dual active bridges,” U.S. Patent 5027264, Jun. 25, 1991.

[23] R. W. De Doncker, “Power electronic technologies for flexible DC distribution grids,” in *Proc. IEEE Int. Power Electron. Conf.,* 2014, pp. 736–743.

[24] N. H. Baars, J. Everts, C. G. E. Wijnands, and E. A. Lomonova, “Performance Evaluation of a Three-Phase Dual Active Bridge DC–DC Converter With Different Transformer Winding Configurations,” *IEEE Trans. Power Electron.*, vol. 31, no. 10, pp. 6814–6823, Oct. 2016.

[25] D. G. Shah and M. L. Crow, “Stability Design Criteria for Distribution Systems With Solid-State Transformers,” *IEEE Trans. Power Del.*, vol. 29, no. 6, pp. 2588–2595, Dec. 2014.

[26] A. Emadi, A. Khaligh, C. H. Rivetta, and G. A. Williamson, “Constant power loads and negative impedance instability in automotive systems: Definition, modeling, stability, and control of power electronic converters and motor drives,” *IEEE Trans. Veh. Technol.*, vol. 55, no. 4, pp. 1112–1125, July 2006.

[27] A. Riccobono *et al*., “Stability of Shipboard DC Power Distribution: Online Impedance-Based Systems Methods,” *IEEE Elect. Mag.*, vol. 5, no. 3, pp. 55–67, Sept. 2017.

[28] S. Chiniforoosh, J. Jatskevich, A. Yazdani, V. Sood, V. Dinavahi, J. A. Martinez, and A. Ramirez, “Definitions and applications of dynamic average models for analysis of power systems,” *IEEE Trans. Power Del.*, vol. 25, no. 4, pp. 2655–2669, Oct. 2010.

[29] M. Hamzeh, M. Ghafouri, H. Karimi, K. Sheshyekani, and J. M. Guerrero, “Power Oscillations Damping in DC Microgrids,” *IEEE Trans. Energy Convers.*, vol. 31, no. 3, pp. 970–980, Sept. 2016.

[30] R. W. Erickson and D. Maksimovic, *Fundamental of Power Electronics*. 2nd ed., Norwell, MA, USA: Kluwer, 2001.

[31] N. Mohan, W. P. Robbins, T. M. Undeland, R. Nilssen, and O. Mo,“Simulation of power electronic and motion control systems – An overview,” *Proc. IEEE*, vol. 82, no. 8, Aug. 1994, pp. 1287–1302.

[32] H. Jin, “Behavior-mode simulation of power electronic circuits,” *IEEE Trans. Power Electron.*, vol. 12, no. 3, pp. 443–452, May 1997.

[33] D. Maksimovic, A. M. Stankovic, V. J. Thottuvelil, and G. C. Verghese, "Modeling and simulation of power electronic converters," *Proc. IEEE*, vol. 89, no. 6, pp. 898–912, June 2001.

[34] Q. Ye, R. Mo, and H. Li, "Low-Frequency Resonance Suppression of a Dual-Active-Bridge DC/DC converter Enabled DC Microgrid," *IEEE J. of Emerg. Sel. Topics Power Electron.*, vol. 5, no. 3, pp. 982–994, Sep. 2017.

[35] S. Haghbin, F. Blaabjerg, and A. S. Bahman, "Frozen Leg Operation of a Three-Phase Dual Active Bridge Converter," *IEEE Trans. Power Electron.*, vol. 34, no. 5, pp 4239–4248, May 2019.

[36] L. Ferreira Costa and M. Liserre, "Failure Analysis of the dc-dc Converter: A Comprehensive Survey of Faults and Solutions for Improving Reliability," *IEEE Power Electron. Mag.*, vol. 5, no. 4, pp. 42–51, Dec. 2018.

[37] Y. Song and B. Wang, "Survey on Reliability of Power Electronic Systems," *IEEE Trans. Power Electron.*, vol. 28, no. 1, pp. 591–604, Jan. 2013.

[38] F. Krismer, "Modeling and optimization of bidirectional dual active bridge dc–dc converter topologies," Ph.D. dissertation, Power Electron. Syst. Lab. (PES), ETH Zurich, Zurich, Switzerland, 2010.

[39] F. Krismer, S. Round, and J. W. Kolar, "Performance optimization of a high current dual active bridge with a wide operating voltage range," in *Proc. IEEE Power Electron. Spec. Conf.*, 2006, pp. 1–7.

[40] H. van Hoek, M. Neubert, A. Kroeber, and R. W. De Doncker, "Comparison of a single-phase and a three-phase dual active bridge with low-voltage, high-current output," in *Proc. Int. Conf. Renewable Energy Res. Appl.*, Nov. 2012, pp. 1–6.

[41] B. Zhao, Q. Yu, and W. Sun, "Extended-phase-shift control of isolated bidirectional dc-dc converter for power distribution in microgrid," *IEEE Trans. Power Electron.*, vol. 27, no. 11, pp. 4667–4680, Nov. 2012.

[42] H. Bai, Z. Nie, and C. C. Mi, "Experimental Comparison of Traditional Phase-Shift, Dual-Phase-Shift, and Model-Based Control of Isolated Bidirectional DC–DC Converters," *IEEE Trans. Power Electron.*, vol. 25, no. 6, pp. 1444–1449, June 2010.

[43] F. Krismer and J. W. Kolar, "Closed form solution for minimum conduction loss modulation of DAB converters," *IEEE Trans. Power Electron.*, vol. 27, no. 1, pp. 174–188, Jan. 2012.

[44] Z. Li, Y. Wang, L. Shi, J. Huang, and W. Lei, "Optimized modulation strategy for three-phase dual-active-bridge DC-DC converters to minimize RMS inductor current in the whole load range," in *Proc. IEEE Int. Power Electron. Mot. Cont. Conf., May* 2016, pp. 2787–2791.

[45] G. Waltrich, M. A. M. Hendrix, and J. L. Duarte, "Three-Phase Bidirectional DC/DC Converter With Six Inverter Legs in Parallel for EV Applications," *IEEE Trans. Ind. Electron.*, vol. 63, no. 3, pp. 1372–1384, Mar. 2016.

[46] K. Jin and C. Liu, "A Novel PWM High Voltage Conversion Ratio Bidirectional Three-Phase DC/DC Converter With Y–Δ Connected Transformer," *IEEE Trans. Power Electron.*, vol. 31, no. 1, pp. 81–88, Jan. 2016.

[47] Z. Wang and H. Li, "A Soft Switching Three-phase Current-fed Bidirectional DC-DC Converter With High Efficiency Over a Wide Input Voltage Range," *IEEE Trans. Power Electron.*, vol. 27, no. 2, pp. 669–684, Feb. 2012.

[48] S. Baek, S. Roy, S. Bhattacharya, and S. Kim, “Power flow analysis for 3-port 3-phase dual active bridge dc/dc converter and design validation using high frequency planar transformer,” in *Proc. IEEE Energy Convers. Congr. Expo.*, Sep. 2013, pp. 388–395.

[49] S. Baek, S. Dutta, and S. Bhattacharya, “Characterization of a three-phase dual active bridge dc/dc converter in wye-delta connection for a high frequency and high power applications,” in *Proc. IEEE Energy Convers. Congr. Expo.*, Sep. 2011, pp. 4183–4188.

[50] M. Berger, I. Kocar, H. Fortin-Blanchette, and C. Lavertu, “Hybrid Average Modeling of Three-Phase Dual Active Bridge Converters for Stability Analysis,” *IEEE Trans. Power Del.*, vol. 33, no. 4, pp. 2020–2029, Aug. 2018.

[51] R. D. Middlebrook and S. Cùk, “A general unified approach to modelling switching-converter power stages,” in *Proc. IEEE Power Electron. Spec. Conf.*, pp. 18–34, June 1976.

[52] J. A. Mueller and J. W. Kimball, “Model-based determination of closed-loop input impedance for dual active bridge converters,” in *Proc. IEEE Appl. Power Electron. Conf. and Expo.*, pp. 1039–1046, Mar. 2017.

[53] H. Qin and J. W. Kimball, “Generalized average modeling of dual active bridge DC-DC converter,” *IEEE Trans. Power Electron*., vol. 27, no. 4, pp. 2078–2084, Apr. 2012.

[54] S. P. Engel, N. Soltau, H. Stagge, and R. W. De Doncker, “Dynamic and Balanced Control of Three-Phase High-Power Dual-Active Bridge DC–DC Converters in DC-Grid Applications,” *IEEE Trans. Power Electron.*, vol. 28, no. 4, pp. 1880–1889, April 2013.

[55] R. D. Middlebrook, “Input filter considerations in design and application of switching regulators,” in *Proc. IEEE Industrial Applications Soc. Conf.*, Oct. 1976, pp. 91–107.

[56] S. Sanders, J. Noworolski, X. Liu, and G. Verghese, “Generalized averaging method for power conversion circuits,” *IEEE Trans. Power Electron.*, vol. 6, no. 2, pp. 251–259, Apr. 1991.

[57] K. Zhang, Z. Shan, and J. Jatskevich, “Large- and small-signal average value modeling of dual-active-bridge DC-DC converter considering power losses,” *IEEE Trans. Power Electron.*, vol. 32, no. 3, pp. 1964–1974, Mar. 2017.

[58] Z. Li, Y. Wang, L. Shi, J. Huang, Y. Cui, and W. Lei, “Generalized averaging modeling and control strategy for three-phase dual-active-bridge DC-DC converters with three control variables,” in *Proc. IEEE Appl. Power Electron. Conf. Expo.*, Mar. 2017, pp. 1078–1084.

[59] J. Mahseredjian, S. Dennetiere, L. Dube, B. Khodabakhchian, and L. Gerin-Lajoie, “On a new approach for the simulation of transients in power systems,” *Electr. Power Syst. Res.*, vol. 77, no. 11, pp. 1514–1520, Sep. 2007.

[60] A. Riccobono and E. Santi, “Comprehensive Review of Stability Criteria for DC Power Distribution Systems,” *IEEE Trans. Ind. Appl.*, vol. 50, no. 5, pp. 3525–3535, Sept.–Oct. 2014.

[61] M. Berger, I. Kocar, H. Fortin-Blanchette, and C. Lavertu, “Large-signal modeling of three-phase dual active bridge converters for electromagnetic transient analysis in DC grids,” *J. of Mod. Power Syst. and Clean Energy*, pp. 1–13, May 2019.

[62] R. Uhl, A. Arasteh, A. Monti, A. Hinz and R. W. De Doncker, “Nodal-reduced modeling of three-phase dual-active bridge converters for EMTP-type simulations,” in *Proc. IEEE 26th Int. Symp. Ind. Electron.*, 2017, pp. 787–792.

[63] L. Salazar and G. Joos, “PSPICE simulation of three-phase inverters by means of switching functions,” *IEEE Trans. Power Electron.*, vol. 9, no. 1, pp. 35–42, Jan 1994.

[64] T.A. Short, *Electric Power Distribution Handbook*., Boca Raton, FL, USA: CRC Press, 2004.

[65] D. Hirschmann, D. Tissen, S. Schroder and R. W. De Doncker, "Reliability Prediction for Inverters in Hybrid Electrical Vehicles," *IEEE Trans. Power Electron.*, vol. 22, no. 6, pp. 2511–2517, Nov. 2007.

[66] D. Tan, "Transportation Electrification: Challenges and opportunities," *IEEE Power Electron. Magazine*, vol. 3, no. 2, pp. 50–52, June 2016.

[67] R. V. White and F. M. Miles, "Principles of fault tolerance," in *Proc. IEEE Appl. Power Electron. Conf.*, 1996, pp. 18–25.

[68] H. van Hoek, K. Jacobs, and R. W. De Doncker, "Performance analysis of an analytical calculation tool for dual-active-bridge converters," in *Proc. IEEE Int. Conf. Power Electron. and Drive Syst.*, June 2015, pp. 1130–1137.

[69] W. M. Mordey, "On testing and working alternators," *J. of the Institution of Elect. Eng.*, vol. 22, no. 104, pp. 116–132, April 1893.

[70] Y. Lee, G. Vakil, R. Feldman, A. Goodman, and P. Wheeler, "Design optimization of a high-power transformer for three-phase dual active bridge DC-DC converter for MVDC grids," in *IET 8th Int. Conf. Power Electron., Machines and Drives*, April 2016, pp. 1–6.

[71] Y. Lee, A. J. Watson, G. Vakil and P. W. Wheeler, "Design considerations for a high-power dual active bridge DC-DC converter with galvanically isolated transformer," in *Proc. IEEE Energy Convers. Congr. Expo.*, Oct. 2017, pp. 4531–4537.

[72] Z. Yang, J. Hu, G. C. Pasupuleti, and R. W. De Doncker, "Operation-Oriented Design Procedure of a Three-Phase Dual-Active Bridge Converter for a Wide Operation Range," in *Proc. IEEE Energy Convers. Congr. Expo.,* Sept. 2018, pp. 2835–2842.

[73] D. Wang, F. Peng, J. Ye, Y. Yang, and A. Emadi, "Dead-time effect analysis of a three-phase dual-active bridge DC/DC converter," *IET Power Electron.*, vol. 11, no. 6, pp. 984–994, May 2018.

[74] C. Zhao, S. D. Round, and J. W. Kolar, "An Isolated Three-Port Bidirectional DC-DC Converter With Decoupled Power Flow Management," *IEEE Trans. Power Electron.*, vol. 23, no. 5, pp. 2443–2453, Sept. 2008.

[75] H. Li and F. Peng, "Modeling of a new ZVS bi-directional dc-dc converter," *IEEE Trans. Aerosp. Electron. Syst.*, vol. 40, no. 1, pp. 272–283, Jan. 2004.

[76] S. Chandrasekar and R. Gokaraju, "Dynamic Phasor Modeling of Type 3 DFIG Wind Generators (Including SSCI Phenomenon) for Short-Circuit Calculations," *IEEE Trans. Power Del.*, vol. 30, no. 2, pp. 887–897, April 2015.

[77] C. Liu, A. Bose, and P. Tian, "Modeling and Analysis of HVDC Converter by Three-Phase Dynamic Phasor," *IEEE Trans. Power Del.*, vol. 29, no. 1, pp. 3–12, Feb. 2014.

[78] Y. Huang, L. Dong, S. Ebrahimi, N. Amiri, and J. Jatskevich, "Dynamic Phasor Modeling of Line-Commutated Rectifiers With Harmonics Using Analytical and Parametric Approaches," *IEEE Trans. Energy Convers.*, vol. 32, no. 2, pp. 534–547, June 2017.

[79] A. M. Stankovic, S. R. Sanders, and T. Aydin, "Dynamic phasors in modeling and analysis of unbalanced polyphase AC machines," *IEEE Trans. Energy Convers.,* vol. 17, no. 1, pp. 107–113, Mar. 2002.

[80] A. M. Stankovic, B. C. Lesieutre, and T. Aydin, "Modeling and analysis of single-phase induction machines with dynamic phasors," *IEEE Trans. Power Syst.*, vol. 14, no. 1, pp. 9–14, Feb. 1999.

[81] Y. Jang and R. W. Erickson, "Physical origins of input filter oscillations in current programmed converters," *IEEE Trans. Power Electron.*, vol. 7, no. 4, pp. 725–733, Oct. 1992.

[82] J. Mahseredjian, L. Dube, Ming Zou, S. Dennetiere, and G. Joos, "Simultaneous solution of control system equations in EMTP," *IEEE Trans. Power Syst.*, vol. 21, no. 1, pp. 117–124, Feb. 2006.

[83] M. Berger, J. M. Grave, C. Lavertu, I. Kocar, J. Mahseredjian, and D. Ferrara, "Modeling, Simulation, and Testing of Switching Surge Transients in Rapid Transit Vehicles DC Power Systems," *IEEE Trans. Ind. Appl.*, vol. 54, no. 1, pp. 822–831, Jan.–Feb. 2018.

[84] O. Tremblay and L.-A. Dessaint, "Experimental validation of a battery dynamic model for EV applications," *World Electr. Veh. J.*, vol. 3, no. 1, pp. 1–10, 2009.

[85] H. Wu, L. Yuan, L. Sun, and X. Li, "Modeling of current-limiting circuit breakers for the calculation of short-circuit current," *IEEE Trans. Power Del.*, vol. 30, no. 2, pp. 652–656, Apr. 2015.

[86] J. Mahseredjian, V. Dinavahi and J. A. Martinez, "Simulation Tools for Electromagnetic Transients in Power Systems: Overview and Challenges," *IEEE Trans. Power Del.*, vol. 24, no. 3, pp. 1657–1669, July 2009.

[87] J. R. Marti and J. Lin, "Suppression of numerical oscillations in the EMTP power systems," *IEEE Trans. Power Syst.*, vol. 4, no. 2, pp. 739–747, May 1989.

[88] M. Zou, J. Mahseredjian, G. Joos, B. Delourme, and L. Gerin-Lajoie, "Interpolation and reinitialization in time-domain simulation of power electronic circuits," *Electr. Power Syst. Res.*, vol. 76, no. 8, pp. 688–694, May 2006.

[89] Efficient Power Conversion, EPC2022–*Enhancement mode power transistor* [Online]. Available: www.epc-co.com.

[90] F. Krismer and J. W. Kolar, "Accurate small-signal model for the digital control of an automotive bidirectional dual active bridge," *IEEE Trans. Power Electron.*, vol. 24, no. 12, pp. 2756–2768, Dec. 2009.

[91] J. M. Ramos, J. Diaz, A. M. Pernia, F. Nuno, and J. M. Lopera, "Dynamic and steady-state models for the PRC-LCC resonant topology with a capacitor as output filter," *IEEE Trans. Ind. Electron.*, vol. 54, no. 4, pp. 2262–2275, Aug. 2007.

[92] N.O. Sokal, "System oscillations from negative input resistance at power input port of switching-mode regulator, amplifier, DC/DC converter, or DC/DC inverter," *Power Electron. Specialists Conf.,* June 1973, pp.138–140.

[93] E. De Din, H. A. B. Siddique, M. Cupelli, A. Monti and R. W. De Doncker, "Voltage Control of Parallel-Connected Dual-Active Bridge Converters for Shipboard Applications," *IEEE J. of Emerg. Sel. Topics Power Electron.*, vol. 6, no. 2, pp. 664–673, June 2018.

[94] J. Hiltunen, V. Vaisanen, R. Juntunen and P. Silventoinen, "Variable-Frequency Phase Shift Modulation of a Dual Active Bridge Converter," *IEEE Trans. Power Electron.*, vol. 30, no. 12, pp. 7138–7148, Dec. 2015.

[95] F. Jauch and J. Biela, “Generalized modeling and optimization of a bidirectional dual active bridge DC-DC converter including frequency variation,” in *Proc. Int. Power Electron. Conf.*, May 2014, pp. 1788–1795.

[96] A. Davoodi, N. Noroozi and M. R. Zolghadri, “A Fault-Tolerant Strategy for Three-Phase Dual Active Bridge Converter,” in *Proc. Int. Power Electron., Drive Syst. Tech. Conf.*, Feb. 2019, pp. 253–258.

[97] B. Mirafzal, “Survey of Fault-Tolerance Techniques for Three-Phase Voltage Source Inverters,” *IEEE Trans. Ind. Electron.*, vol. 61, no. 10, pp. 5192–5202, Oct. 2014.

APPENDIX A – CONVERTER MODEL PARAMETERS

Description	Symbol	Model 1	Model 2	Model 3	Model 4 (Proto.)
Referenced in Chapter	-	3, 4	4	4	2, 3, 4, 5
Nominal Input Voltage	$V_{\mathrm{i}}^{\mathrm{nom}}$	600 V	750 V	380 V	24 V
Nominal Output Voltage	$V_{\mathrm{o}}^{\mathrm{nom}}$	37.5 V	380 V	110 V	24 V
Nominal Output Power	$P_{\mathrm{o}}^{\mathrm{nom}}$	1 kW	100 kW	10 kW	–
Load Resistor	R	–	–	–	4 Ω
Input Filter Inductor	L_{i}	–	100 µH	50 µH	–
Input Filter Capacitor	C_{i}	–	1100 µF	150 µF	164 µF
Output Capacitor	C_{o}	150 µF	2200 µF	150 µF	164 µF
Transformer Series Inductance	L_{s}	420 µH	10 µH	12 µH	2 µH
Transformer Ratio	M	16	1.732	3.45	0.866
Nominal Switching Frequency	f_{s}	50 kHz	20 kHz	50 kHz	50 kHz
G_{c} Cross-Over frequency	$f_{\varphi\mathrm{m}}$	1.5 kHz	1.5 kHz	2.5 kHz	1 kHz
G_{c} Phase-Margin	φ_{m}	45°	45°	45°	65°
G_{f} Cut-Off Frequency	f_{o}	5 kHz	5 kHz	5 kHz	7.9 kHz
Maximum Output Current (see figure below)	$I_{\mathrm{o}}^{\mathrm{max}}$	30 A		100 A	–
Modulator gain	K_{m}	-11.4 dB	-13.4 dB	-11.4 dB	-11.4 dB

VI-characteristic for output current limitation:

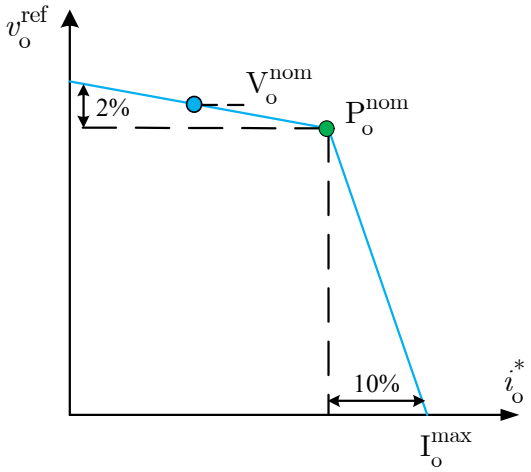

APPENDIX B – SMALL-SCALE PROTOTYPE

In this appendix, additional information on the EPC2022 GaN-based Y-Δ 3p-DAB prototype is provided. The figure below shows a simplified schematic of the prototype main elements:

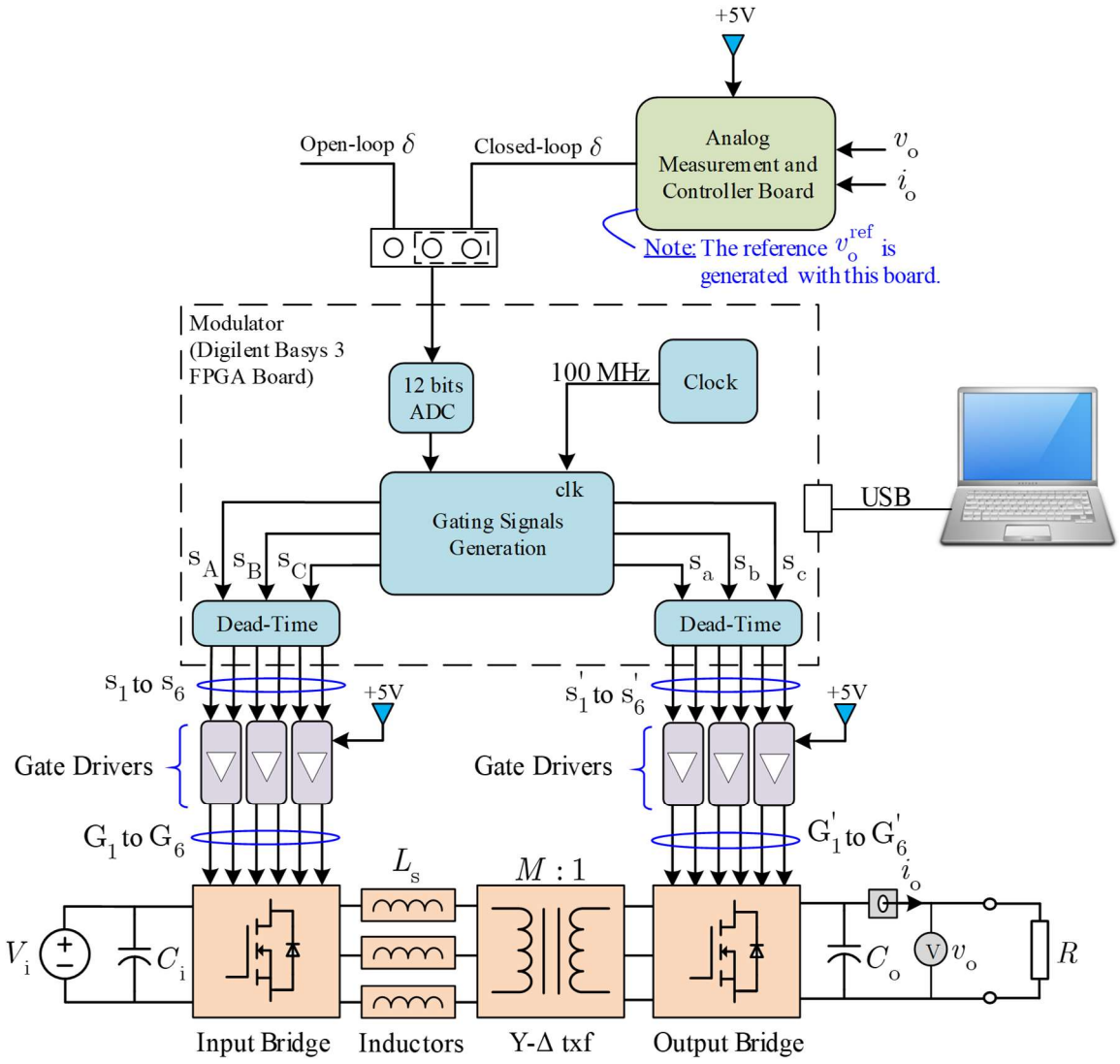

The prototype is composed of two three-phase inverters using EPC2022 (100V, 90A) [89] GaN FET as switching elements. The series inductors are custom-built for the application. The three-phase transformer is fabricated using three custom-built single-phase transformers. The output voltage v_o is fed back to an analog control board which filters, calculates the error between v_o and v_o^{ref}, and generates the control phase-shift δ with a PI-controller. The analog value of the phase-shift δ is digitized using a 12 bits analog-to-digital converter (ADC). The digital value of

the control phase-shift δ is transformed by the FPGA into gating signals for each leg at the switching frequency f_s. Note that the refreshing rate of the control phase-shift δ is $T_s = 1 / f_s$, i.e. that the FPGA read the new value of δ once every cycle T_s. The FPGA code includes a dead-time t_{dead} between the signals going to the upper and lower transistors of the same leg. Since the clock frequency of the Basys 3 board is f_{clk} = 100 MHz, the minimum theoretical dead-time is $1 / f_{clk}$ = 0.01 µs. For all the experiments, the dead-time t_{dead} has been set to 0.1 µs. The gating signals at the output of the Basys 3 board are then sent to the gate drivers (one gate driver for each leg) which isolate and amplify the signals going to the gate of the transistors. The gate driver design is based on Texas Instruments reference design TIDA-00785. It has been adapted to ensure compatibility with the Basys 3 board output signals.

The figure below shows an overview of the main hardware components:

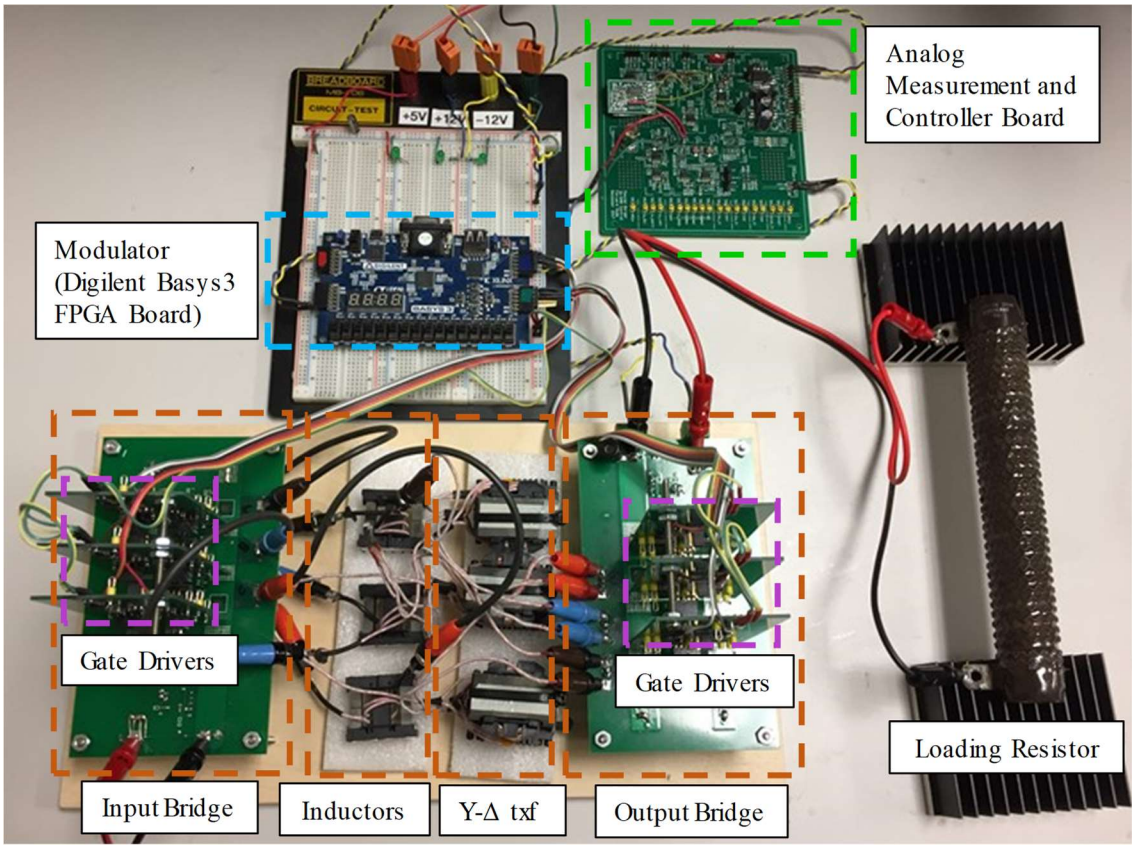

The power supply used for all the experiments is an EMS 40-25 (40VDC, 25A). The measurements are taken using a LeCroy HDO6104 oscilloscope with CP150 current probes and ADP305 differential voltage probes.

The figure below shows an example of the top layer of the three-phase output bridge. The input bridge is identical to the output bridge. The output capacitor C_o is made of two 82 µF film capacitors (Vishay MKT1820682015), such that C_o = 164 µF.

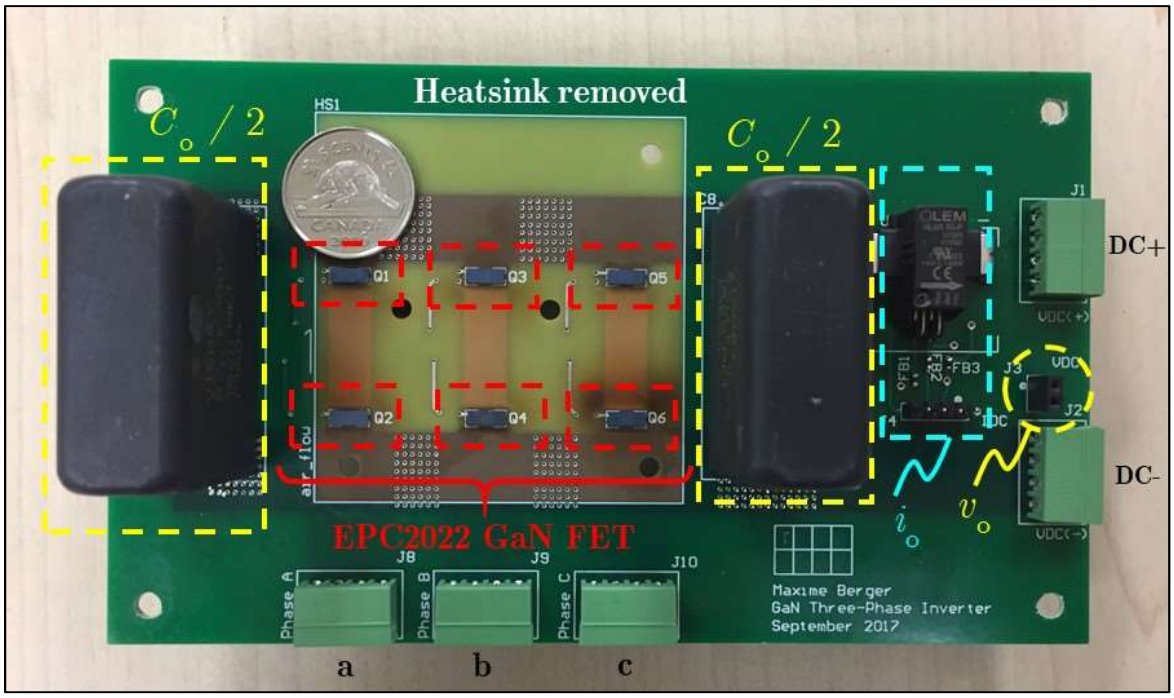

The figure below shows the footprint for the EPC2022 GaN FETs. It shows the arrangement of the gate (G), drain (D), source (S) and substrate (SS) pads as well as the main dimensions of the EPC2022 footprint.

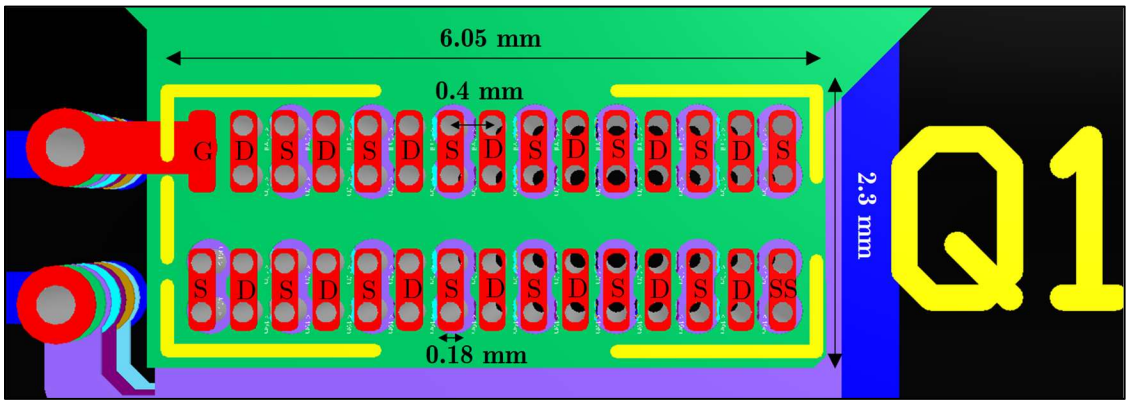

The inverter board is composed of 8 layers to allow a better extraction of both the heat and the current from the GaN FET pads. The layers connecting the drain (D) and the source (S) pads are interleaved to reduce the risk of short-circuit during the fabrication process:

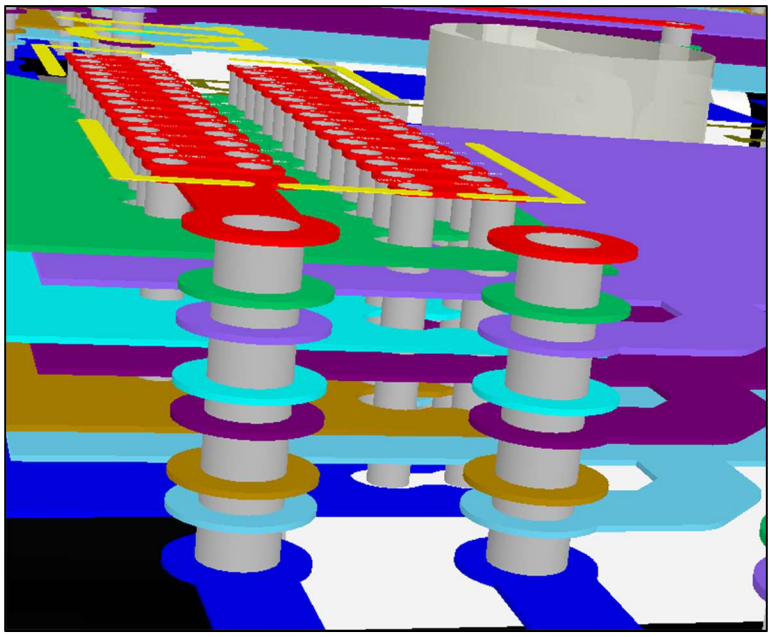

The figures below show an example of the gate driver board for the phase a of the output bridge:

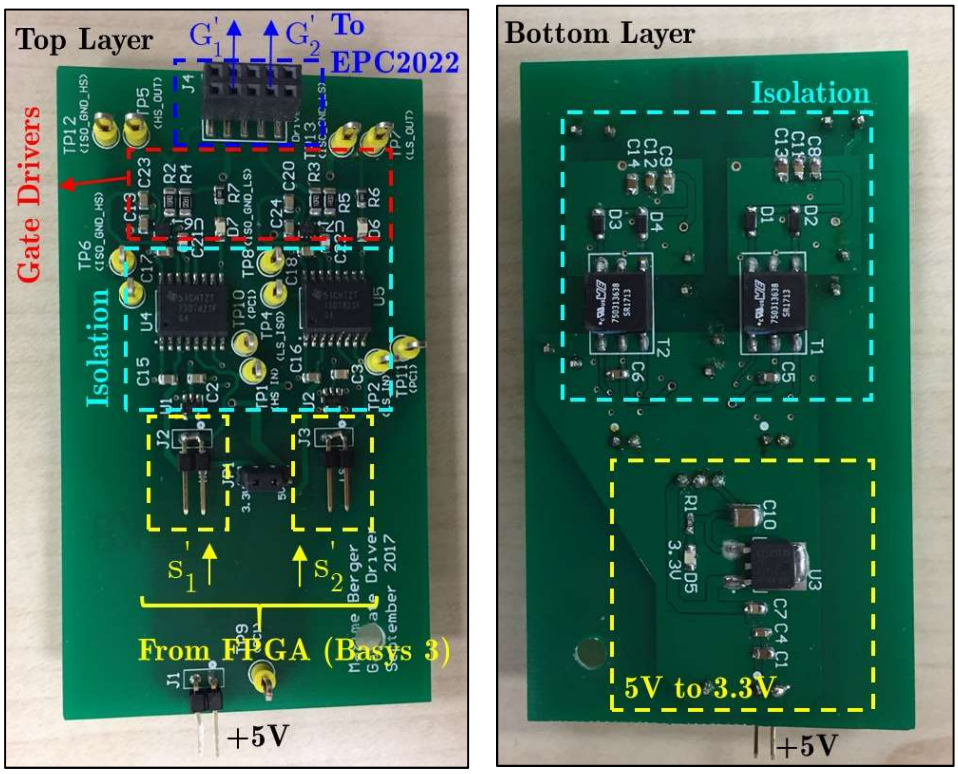

The figure below shows the analog measurement and controller board:

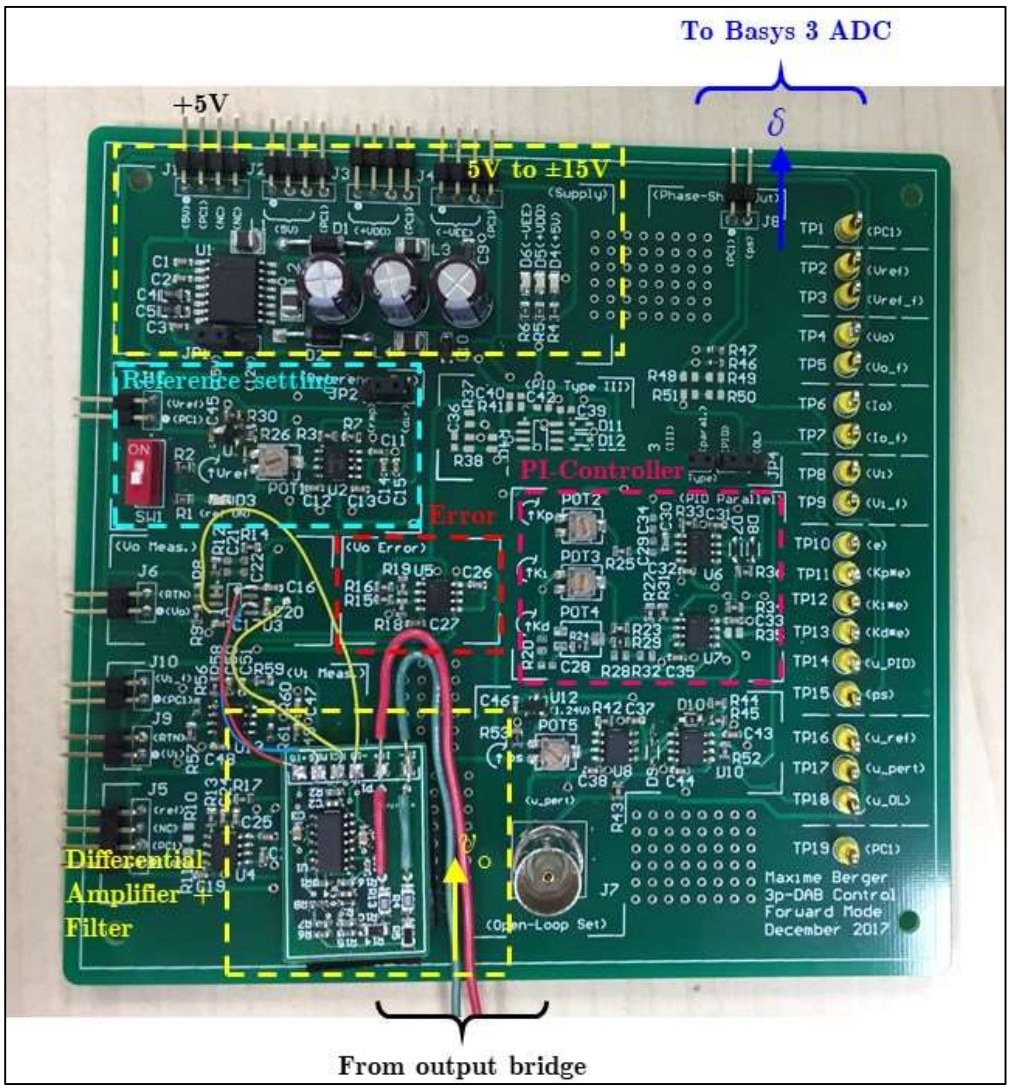

APPENDIX C – PIECEWISE-LINEAR MODEL IN NORMAL OPERATION

C.1 Mode definition and switching-functions:

Legend : X = 1, (empty) = 0

Mode	$0 \le \delta \le \frac{\pi}{6}$	s_1	s_3	s_5	s_1'	s_3'	s_5'
I	$0 \le \theta \le \delta + \frac{\pi}{6}$	X		X			X
II	$\delta + \frac{\pi}{6} \le \theta \le \frac{\pi}{3}$	X		X	X		X
III	$\frac{\pi}{3} \le \theta \le \delta + \frac{\pi}{2}$	X			X		X
IV	$\delta + \frac{\pi}{2} \le \theta \le \frac{2\pi}{3}$	X			X		
V	$\frac{2\pi}{3} \le \theta \le \delta + \frac{5\pi}{6}$	X	X		X		
VI	$\delta + \frac{5\pi}{6} \le \theta \le \pi$	X	X		X	X	

Mode	$\frac{\pi}{6} \le \delta \le \frac{\pi}{2}$	s_1	s_3	s_5	s_1'	s_3'	s_5'
I	$0 \le \theta \le \delta - \frac{\pi}{6}$	X		X		X	X
II	$\delta - \frac{\pi}{6} \le \theta \le \frac{\pi}{3}$	X		X			X
III	$\frac{\pi}{3} \le \theta \le \delta + \frac{\pi}{6}$	X					X
IV	$\delta + \frac{\pi}{6} \le \theta \le \frac{2\pi}{3}$	X			X		X
V	$\frac{2\pi}{3} \le \theta \le \delta + \frac{\pi}{2}$	X	X		X		X
VI	$\delta + \frac{\pi}{2} \le \theta \le \pi$	X	X		X		

C.2 Piecewise-linear current equations:

For range 1 ($0 \le \delta \le \pi/6$):

- Phase A:

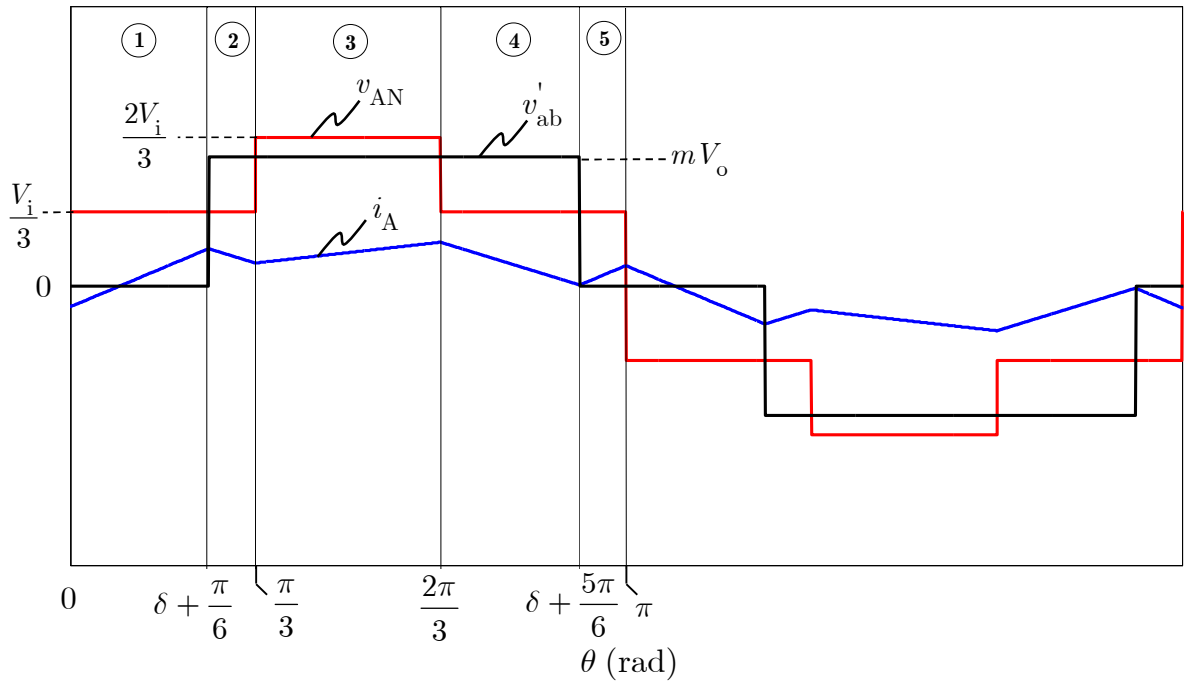

Interval	Range	$i_A(\theta)$	
1	$0 \le \theta \le \delta + \frac{\pi}{6}$	$i_A(\theta) = \frac{V_i}{3\omega_s L_s}\theta + i_A(0)$	(C.1)
2	$\delta + \frac{\pi}{6} \le \theta \le \frac{\pi}{3}$	$i_A(\theta) = \frac{V_i - 3mV_o}{3\omega_s L_s}(\theta - \delta - \frac{\pi}{6}) + i_A(\delta + \frac{\pi}{6})$	(C.2)
3	$\frac{\pi}{3} \le \theta \le \frac{2\pi}{3}$	$i_A(\theta) = \frac{2V_i - 3mV_o}{3\omega_s L_s}(\theta - \frac{\pi}{3}) + i_A(\frac{\pi}{3})$	(C.3)
4	$\frac{2\pi}{3} \le \theta \le \delta + \frac{5\pi}{6}$	$i_A(\theta) = \frac{V_i - 3mV_o}{3\omega_s L_s}(\theta - \frac{2\pi}{3}) + i_A(\frac{2\pi}{3})$	(C.4)
5	$\delta + \frac{5\pi}{6} \le \theta \le \pi$	$i_A(\theta) = \frac{V_i}{3\omega_s L_s}(\theta - \delta - \frac{5\pi}{6}) + i_A(\delta + \frac{5\pi}{6})$	(C.5)

Initial current:

$$i_A(0) = \frac{\left[3mV_o - 2V_i\right]\pi}{9\omega_s L_s} \tag{C.6}$$

○ Phase B:

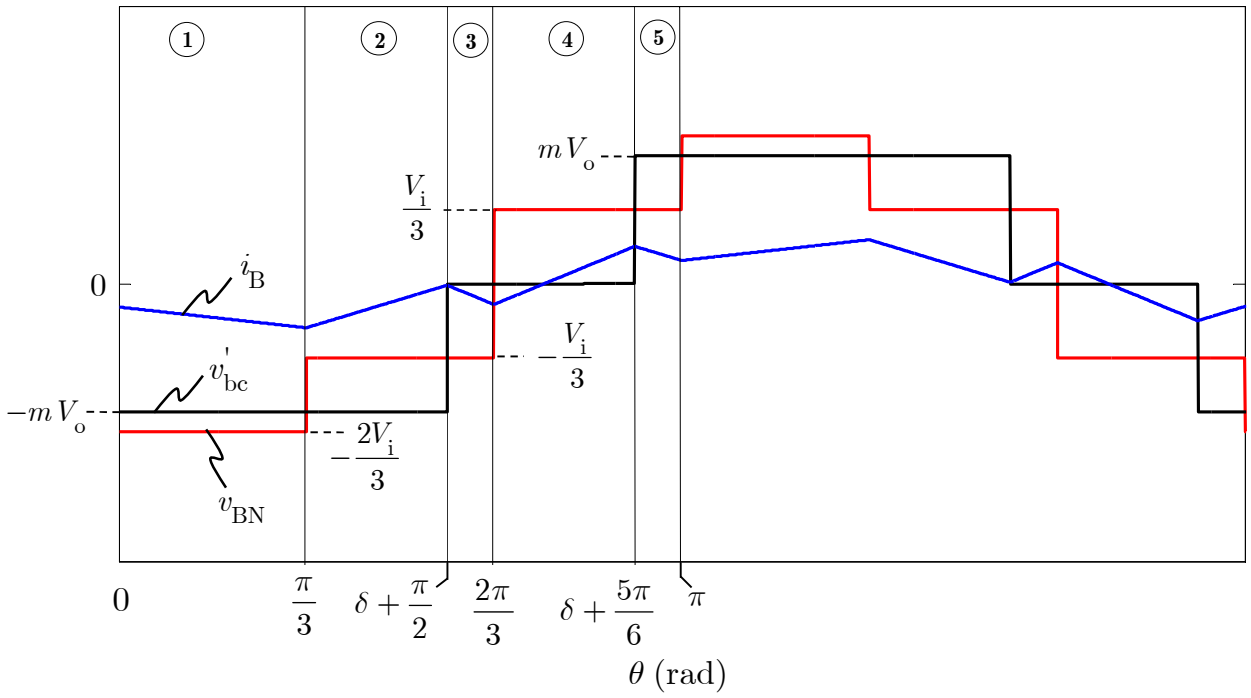

Interval	Range	$i_B(\theta)$	
1	$0 \le \theta \le \frac{\pi}{3}$	$i_B(\theta)=\frac{-2V_i+3mV_o}{3\omega_s L_s}\theta + i_B(0)$	(C.7)
2	$\frac{\pi}{3} \le \theta \le \delta+\frac{\pi}{2}$	$i_B(\theta)=\frac{-V_i+3mV_o}{3\omega_s L_s}(\theta-\frac{\pi}{3}) + i_B(\frac{\pi}{3})$	(C.8)
3	$\delta+\frac{\pi}{2} \le \theta \le \frac{2\pi}{3}$	$i_B(\theta)=\frac{-V_i}{3\omega_s L_s}(\theta-\delta-\frac{\pi}{2}) + i_B(\delta+\frac{\pi}{2})$	(C.9)
4	$\frac{2\pi}{3} \le \theta \le \delta+\frac{5\pi}{6}$	$i_B(\theta)=\frac{V_i}{3\omega_s L_s}(\theta-\frac{2\pi}{3}) + i_B(\frac{2\pi}{3})$	(C.10)
5	$\delta+\frac{5\pi}{6} \le \theta \le \pi$	$i_B(\theta)=\frac{V_i-3mV_o}{3\omega_s L_s}(\theta-\delta-\frac{5\pi}{6}) + i_B(\delta+\frac{5\pi}{6})$	(C.11)

Initial current:

$$i_B(0) = \frac{\pi V_i - 3mV_o\left[3\delta+\frac{\pi}{2}\right]}{9\omega_s L_s} \tag{C.12}$$

- Phase C:

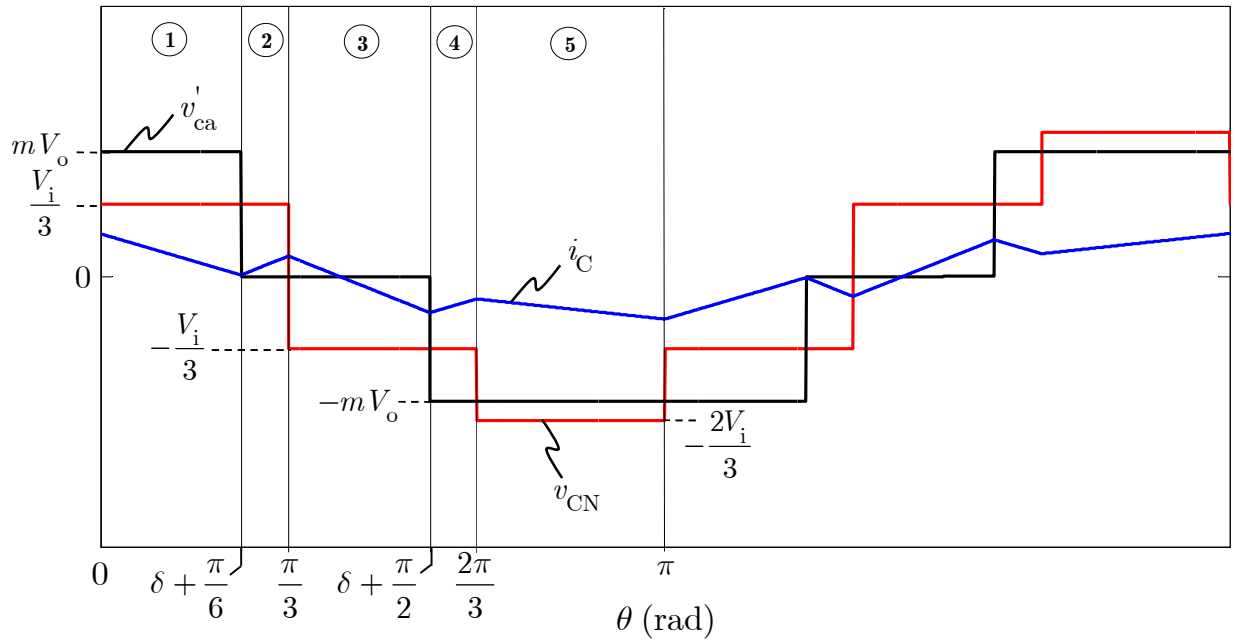

Interval	Range	$i_C(\theta)$	
1	$0 \le \theta \le \delta + \frac{\pi}{6}$	$i_C(\theta) = \frac{V_i - 3mV_o}{3\omega_s L_s}\theta + i_C(0)$	(C.13)
2	$\delta + \frac{\pi}{6} \le \theta \le \frac{\pi}{3}$	$i_C(\theta) = \frac{V_i}{3\omega_s L_s}(\theta - \delta - \frac{\pi}{6}) + i_C(\delta + \frac{\pi}{6})$	(C.14)
3	$\frac{\pi}{3} \le \theta \le \delta + \frac{\pi}{2}$	$i_C(\theta) = \frac{-V_i}{3\omega_s L_s}(\theta - \frac{\pi}{3}) + i_C(\frac{\pi}{3})$	(C.15)
4	$\delta + \frac{\pi}{2} \le \theta \le \frac{2\pi}{3}$	$i_C(\theta) = \frac{-V_i + 3mV_o}{3\omega_s L_s}(\theta - \delta - \frac{\pi}{2}) + i_C(\delta + \frac{\pi}{2})$	(C.16)
5	$\frac{2\pi}{3} \le \theta \le \pi$	$i_C(\theta) = \frac{-2V_i + 3mV_o}{3\omega_s L_s}(\theta - \frac{2\pi}{3}) + i_C(\frac{2\pi}{3})$	(C.17)

Initial current:

$$i_C(0) = \frac{\pi V_i + 3mV_o\left[3\delta - \frac{\pi}{2}\right]}{9\omega_s L_s} \tag{C.18}$$

For range 2 ($\pi/6 \le \delta \le \pi/2$):

- Phase A:

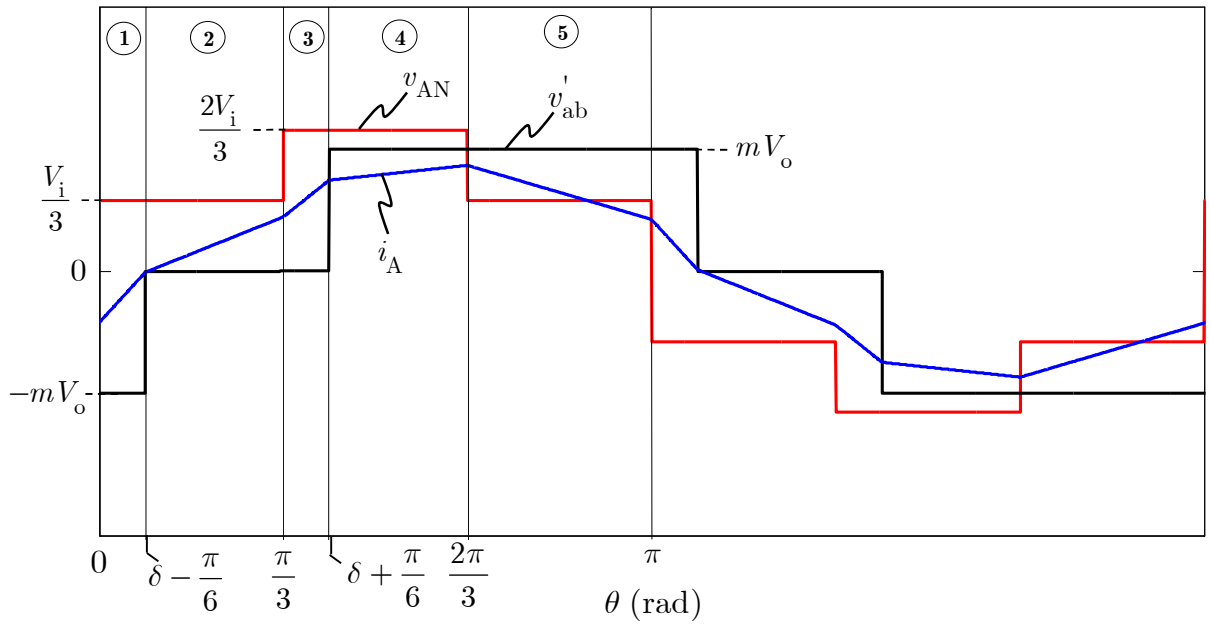

Interval	Range	$i_A(\theta)$	
1	$0 \le \theta \le \delta - \frac{\pi}{6}$	$i_A(\theta) = \frac{V_i + 3mV_o}{3\omega_s L_s}\theta + i_A(0)$	(C.19)
2	$\delta - \frac{\pi}{6} \le \theta \le \frac{\pi}{3}$	$i_A(\theta) = \frac{V_i}{3\omega_s L_s}(\theta - \delta + \frac{\pi}{6}) + i_A(\delta - \frac{\pi}{6})$	(C.20)
3	$\frac{\pi}{3} \le \theta \le \delta + \frac{\pi}{6}$	$i_A(\theta) = \frac{2V_i}{3\omega_s L_s}(\theta - \frac{\pi}{3}) + i_A(\frac{\pi}{3})$	(C.21)
4	$\delta + \frac{\pi}{6} \le \theta \le \frac{2\pi}{3}$	$i_A(\theta) = \frac{2V_i - 3mV_o}{3\omega_s L_s}(\theta - \delta - \frac{\pi}{6}) + i_A(\delta + \frac{\pi}{6})$	(C.22)
5	$\frac{2\pi}{3} \le \theta \le \pi$	$i_A(\theta) = \frac{V_i - 3mV_o}{3\omega_s L_s}(\theta - \frac{2\pi}{3}) + i_A(\frac{2\pi}{3})$	(C.23)

Initial current:

$$i_A(0) = \frac{-2\pi V_i + 9mV_o\left[\frac{\pi}{2} - \delta\right]}{9\omega_s L_s} \tag{C.24}$$

- Phase B:

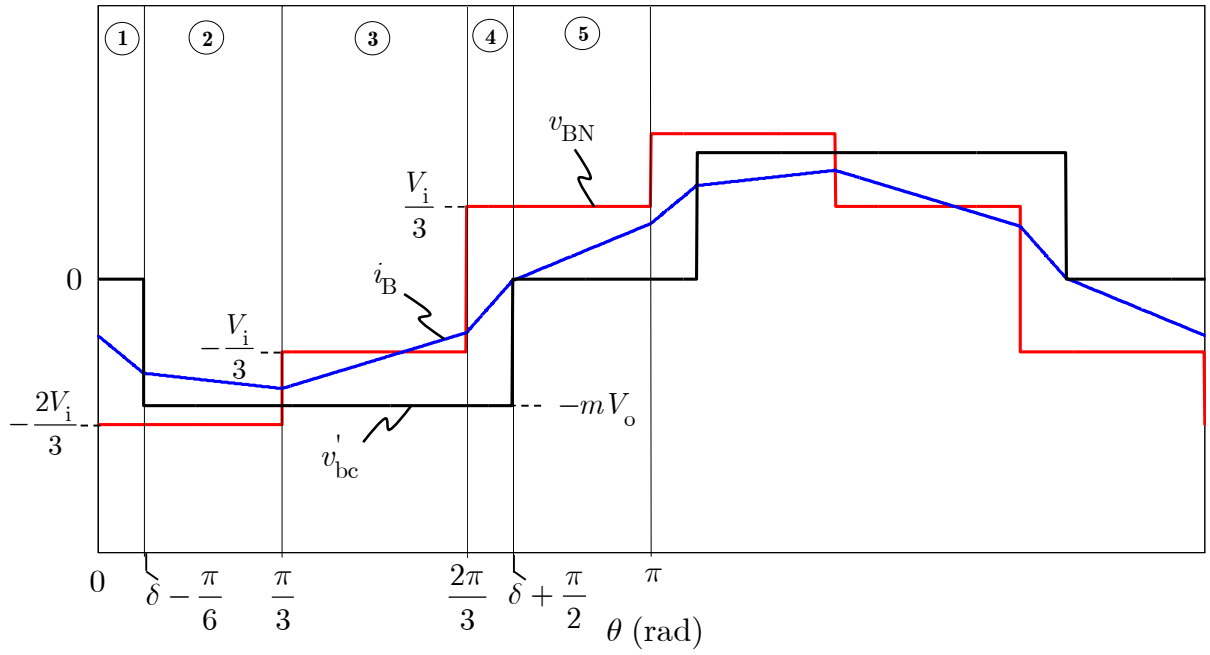

Interval	Range	$i_B(\theta)$	
1	$0 \le \theta \le \delta - \frac{\pi}{6}$	$i_B(\theta) = \frac{-2V_i}{3\omega_s L_s}\theta + i_B(0)$	(C.25)
2	$\delta - \frac{\pi}{6} \le \theta \le \frac{\pi}{3}$	$i_B(\theta) = \frac{-2V_i + 3mV_o}{3\omega_s L_s}(\theta - \delta + \frac{\pi}{6}) + i_B(\delta - \frac{\pi}{6})$	(C.26)
3	$\frac{\pi}{3} \le \theta \le \frac{2\pi}{3}$	$i_B(\theta) = \frac{-V_i + 3mV_o}{3\omega_s L_s}(\theta - \frac{\pi}{3}) + i_B(\frac{\pi}{3})$	(C.27)
4	$\frac{2\pi}{3} \le \theta \le \delta + \frac{\pi}{2}$	$i_B(\theta) = \frac{V_i + 3mV_o}{3\omega_s L_s}(\theta - \frac{2\pi}{3}) + i_B(\frac{2\pi}{3})$	(C.28)
5	$\delta + \frac{\pi}{2} \le \theta \le \pi$	$i_B(\theta) = \frac{V_i}{3\omega_s L_s}(\theta - \delta - \frac{\pi}{2}) + i_B(\delta + \frac{\pi}{2})$	(C.29)

Initial current:

$$i_B(0) = \frac{\left[V_i - 3mV_o\right]\pi}{9\omega_s L_s} \tag{C.30}$$

○ Phase C:

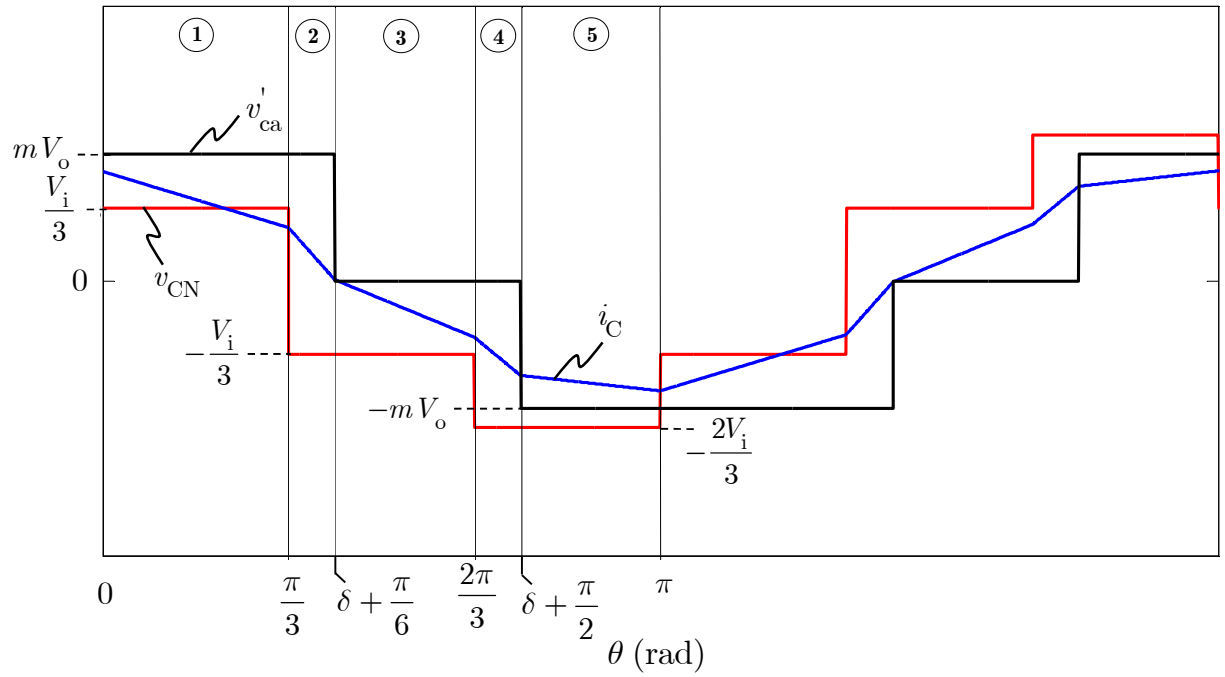

Interval	Range	$i_C(\theta)$	
1	$0 \le \theta \le \frac{\pi}{3}$	$i_C(\theta)=\frac{V_i - 3mV_o}{3\omega_s L_s}\theta + i_C(0)$	(C.31)
2	$\frac{\pi}{3} \le \theta \le \delta+\frac{\pi}{6}$	$i_C(\theta)=\frac{-V_i - 3mV_o}{3\omega_s L_s}(\theta-\frac{\pi}{3}) + i_C(\frac{\pi}{3})$	(C.32)
3	$\delta+\frac{\pi}{6} \le \theta \le \frac{2\pi}{3}$	$i_C(\theta)=\frac{V_i}{3\omega_s L_s}(\theta-\delta-\frac{\pi}{6}) + i_C(\delta+\frac{\pi}{6})$	(C.33)
4	$\frac{2\pi}{3} \le \theta \le \delta+\frac{\pi}{2}$	$i_C(\theta)=\frac{-2V_i}{3\omega_s L_s}(\theta-\frac{2\pi}{3}) + i_C(\frac{2\pi}{3})$	(C.34)
5	$\delta+\frac{\pi}{2} \le \theta \le \pi$	$i_C(\theta)=\frac{-2V_i + 3mV_o}{3\omega_s L_s}(\theta-\delta-\frac{\pi}{2}) + i_C(\delta+\frac{\pi}{2})$	(C.35)

Initial current:

$$i_C(0) = \frac{\pi V_i + 3mV_o\left[3\delta - \frac{\pi}{2}\right]}{9\omega_s L_s} \tag{C.36}$$

C.3 Output current equations:

For range 1 ($0 \le \delta \le \pi/6$):

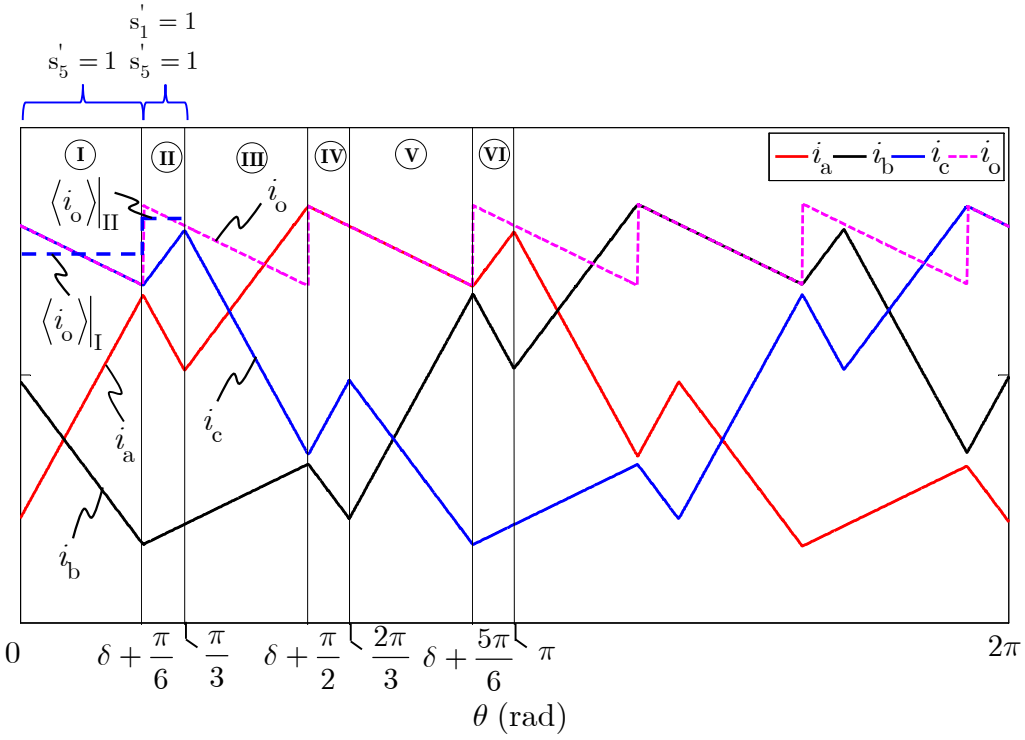

- For Mode I:

  The output current is given by,

$$i_o = i_c = m\left(i_C - i_B\right) \tag{C.37}$$

  From (C.7) and (C.12), the current i_B is given by,

$$i_B(\theta) = \frac{-2V_i + 3mV_o}{3\omega_s L_s}\theta + \frac{\pi V_i - 3mV_o\left[3\delta + \frac{\pi}{2}\right]}{9\omega_s L_s} \tag{C.38}$$

  and from (C.13) and (C.18), the current i_C is given by,

$$i_C(\theta) = \frac{V_i - 3mV_o}{3\omega_s L_s}\theta + \frac{\pi V_i + 3mV_o\left[3\delta - \frac{\pi}{2}\right]}{9\omega_s L_s} \tag{C.39}$$

  Inserting (C.38) and (C.39) into (C.37), and simplifying, it results that,

$$i_o(\theta) = m\left[\frac{V_i - 2mV_o}{\omega_s L_s}\theta + \frac{2\delta m V_o}{\omega_s L_s}\right] \tag{C.40}$$

Then, since the current is assumed linear, it can be written that,

$$\left\langle i_{\mathrm{o}} \right\rangle\Big|_{\mathrm{I}} = \frac{i_{\mathrm{o}}(0) + i_{\mathrm{o}}(\delta + \frac{\pi}{6})}{2} \tag{C.41}$$

Using (C.40) to solve (C.41), it finally leads to,

$$\left\langle i_{\mathrm{o}} \right\rangle\Big|_{\mathrm{I}} = \left(\frac{m}{9\omega_{\mathrm{s}} L_{\mathrm{s}}}\right) \cdot \left[\left(\frac{9}{2}\delta + \frac{3\pi}{4}\right) V_{\mathrm{i}} + \left(9\delta - \frac{3\pi}{2}\right) m V_{\mathrm{o}}\right] \tag{C.42}$$

- For Mode II:

The output current is given by,

$$i_{\mathrm{o}} = i_{\mathrm{a}} + i_{\mathrm{c}} = m\left(i_{\mathrm{A}} - i_{\mathrm{B}}\right) \tag{C.43}$$

such that,

$$\left\langle i_{\mathrm{o}} \right\rangle\Big|_{\mathrm{II}} = m\left(\left\langle i_{\mathrm{A}} \right\rangle\Big|_{\mathrm{II}} - \left\langle i_{\mathrm{B}} \right\rangle\Big|_{\mathrm{II}}\right) \tag{C.44}$$

with,

$$\left\langle i_{\mathrm{A}} \right\rangle\Big|_{\mathrm{II}} = \frac{i_{\mathrm{A}}(\delta + \frac{\pi}{6}) + i_{\mathrm{A}}(\frac{\pi}{3})}{2} \tag{C.45}$$

$$\left\langle i_{\mathrm{B}} \right\rangle\Big|_{\mathrm{II}} = \frac{i_{\mathrm{B}}(\delta + \frac{\pi}{6}) + i_{\mathrm{B}}(\frac{\pi}{3})}{2} \tag{C.46}$$

Using (C.1), (C.2) and (C.6) for determining $\left\langle i_{\mathrm{A}} \right\rangle\Big|_{\mathrm{II}}$, and using (C.7) and (C.12) for determining $\left\langle i_{\mathrm{B}} \right\rangle\Big|_{\mathrm{II}}$, equations (C.45) and (C.46) are reduced to,

$$\left\langle i_{\mathrm{A}} \right\rangle\Big|_{\mathrm{II}} = \frac{1}{9\omega_{\mathrm{s}} L_{\mathrm{s}}}\left(\left[\frac{3}{2}\delta - \frac{5\pi}{4}\right] V_{\mathrm{i}} + \left[\frac{9}{2}\delta + \frac{9\pi}{4}\right] m V_{\mathrm{o}}\right) \tag{C.47}$$

$$\left\langle i_{\mathrm{B}} \right\rangle\Big|_{\mathrm{II}} = \frac{1}{9\omega_{\mathrm{s}} L_{\mathrm{s}}}\left(-\left[3\delta + \frac{\pi}{2}\right] V_{\mathrm{i}} + \left[\frac{3\pi}{4} - \frac{9}{2}\delta\right] m V_{\mathrm{o}}\right) \tag{C.48}$$

Injecting (C.47) and (C.48) into (C.44), and simplifying, it yields that,

$$\left\langle i_{\mathrm{o}} \right\rangle\Big|_{\mathrm{II}} = \frac{m}{9\omega_{\mathrm{s}} L_{\mathrm{s}}}\left[\left(\frac{9}{2}\delta - \frac{3\pi}{4}\right) V_{\mathrm{i}} + \left(9\delta + \frac{3\pi}{2}\right) m V_{\mathrm{o}}\right] \tag{C.49}$$

For range 2 ($\pi/6 \leq \delta \leq \pi/2$):

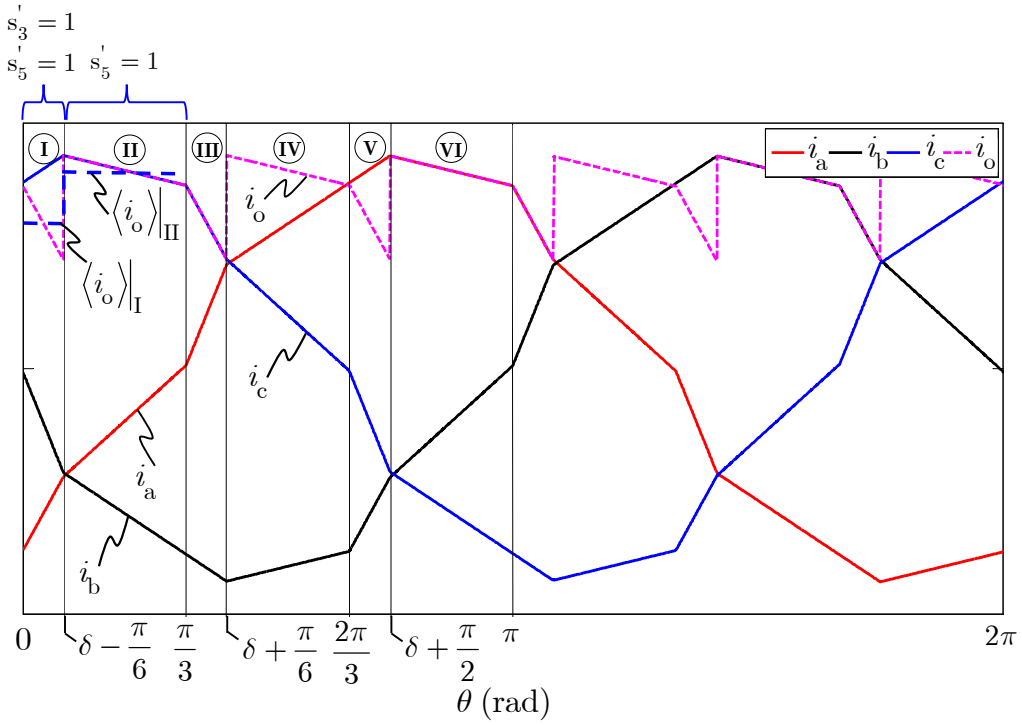

- <u>For Mode I:</u>

  Applying a similar procedure as for range 1, it can be demonstrated that $\langle i_o \rangle|_I$ is given by,

$$\langle i_o \rangle|_I = \left(\frac{m}{9\omega_s L_s}\right) \cdot \left[3\pi V_i + 9m V_o \left(\delta - \frac{\pi}{2}\right)\right] \tag{C.50}$$

- <u>For Mode II:</u>

  As for range 1, it can be demonstrated that $\langle i_o \rangle|_{II}$ is given by,

$$\langle i_o \rangle|_{II} = \frac{m}{9\omega_s L_s}\left[\left(\frac{9}{2}\delta + \frac{3\pi}{4}\right)V_i + \left(9\delta - \frac{3\pi}{2}\right)m V_o\right] \tag{C.51}$$

C.4 Input current equations:

For range 1 ($0 \leq \delta \leq \pi/6$):

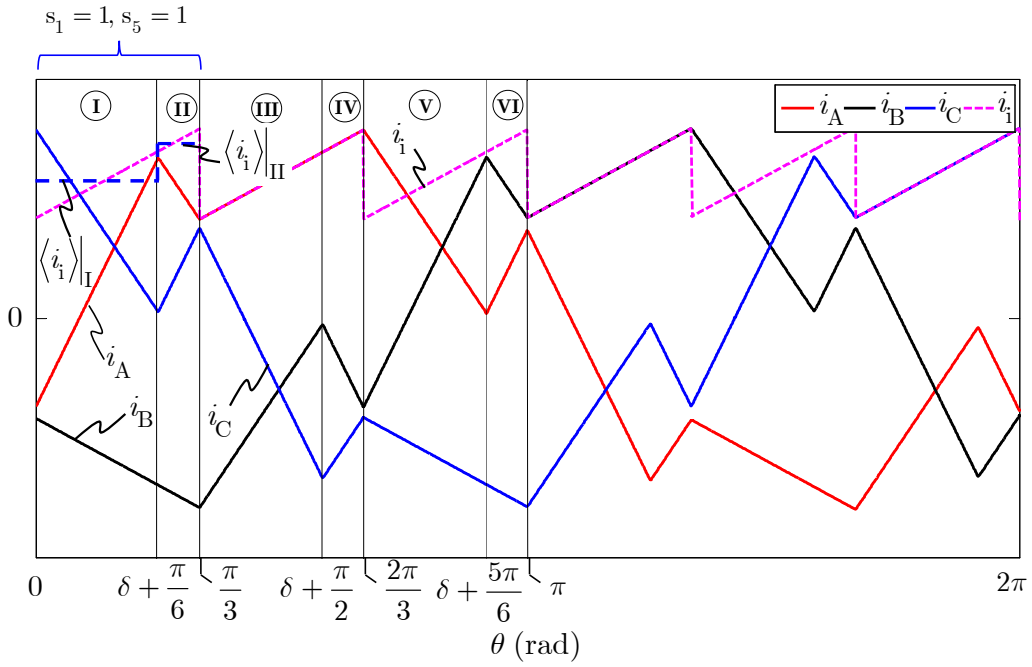

- For Mode I:

  The input current is given by,

$$i_i = i_A + i_C = -i_B \tag{C.52}$$

  with the current i_B given by (C.38). Since the current is linear, it can be written that,

$$\langle i_i \rangle|_I = -\langle i_B \rangle|_I = -\frac{i_B(0) + i_B(\delta + \frac{\pi}{6})}{2} \tag{C.53}$$

  Using (C.38) and simplifying, it yields to,

$$\langle i_i \rangle|_I = \left(\frac{1}{9\omega_s L_s}\right) \cdot \left[\left(3\delta - \frac{\pi}{2}\right) V_i + \left(\frac{9}{2}\delta + \frac{3\pi}{4}\right) m V_o\right] \tag{C.54}$$

- For Mode II:

  The input current is also given by (C.52), such that,

$$\langle i_i \rangle|_I = -\langle i_B \rangle|_I = -\frac{i_B(\delta + \frac{\pi}{6}) + i_B(\frac{\pi}{3})}{2} \tag{C.55}$$

  with the current i_B also given by (C.38). Simplifying, it yields to,

$$\langle i_i \rangle|_I = \left(\frac{1}{9\omega_s L_s}\right) \cdot \left[\left(3\delta + \frac{\pi}{2}\right) V_i + \left(\frac{9}{2}\delta - \frac{3\pi}{4}\right) m V_o\right] \tag{C.56}$$

For range 2 ($\pi/6 \leq \delta \leq \pi/2$):

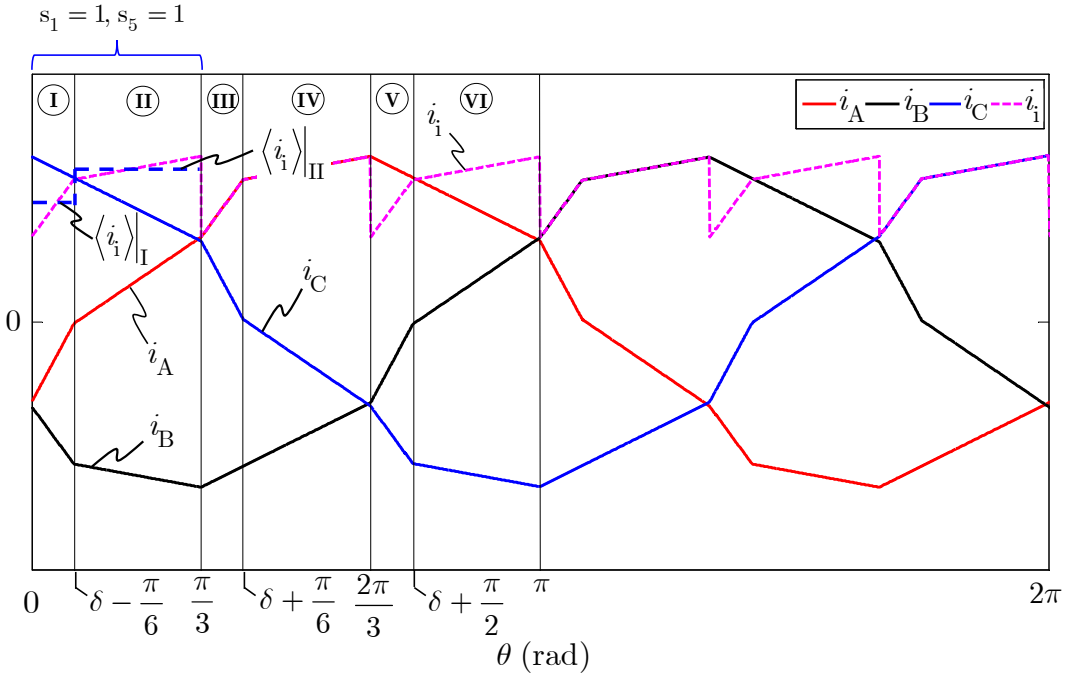

- For Mode I:

  Applying a similar procedure as for range 1, it can be demonstrated that $\langle i_i \rangle|_I$ is given by,

$$\langle i_i \rangle|_I = \left(\frac{1}{9\omega_s L_s}\right) \cdot \left[\left(3\delta - \frac{3\pi}{2}\right) V_i + 3\pi m V_o\right] \tag{C.57}$$

- For Mode II:

  Similarly, it can be demonstrated that $\langle i_i \rangle|_{II}$ is given by,

$$\langle i_i \rangle|_{II} = \left(\frac{1}{9\omega_s L_s}\right) \cdot \left[\left(3\delta - \frac{\pi}{2}\right) V_i + \left(\frac{9}{2}\delta + \frac{3\pi}{4}\right) m V_o\right] \tag{C.58}$$

APPENDIX D – COMPLEMENT TO THE SSA MODEL IN NORMAL OPERATION

D.1 State-space equations for mode I and mode II:

- For range 1 ($0 \le \delta \le \pi/6$):
  - For Mode I:

    Inserting (C.42) into (3.9), it results in,

$$\frac{\mathrm{d}v_{\mathrm{o}}(t)}{\mathrm{d}t}=\underbrace{\left(\frac{1}{9\omega_{\mathrm{s}}L_{\mathrm{s}}C_{\mathrm{o}}}\right)\left[9\delta m^2-\frac{3\pi}{2}m^2-\frac{9\omega_{\mathrm{s}}L_{\mathrm{s}}}{R}\right]}_{\mathbf{A}_{\mathrm{I}}}v_{\mathrm{o}}(t)+\underbrace{\left(\frac{m}{9\omega_{\mathrm{s}}L_{\mathrm{s}}C_{\mathrm{o}}}\right)\left[\frac{9}{2}\delta+\frac{3\pi}{4}\right]}_{\mathbf{B}_{\mathrm{I}}}v_{\mathrm{i}}(t) \tag{D.1}$$

    Inserting (C.54) into (3.10), it leads to,

$$i_{\mathrm{i}}(t)=\underbrace{\left(\frac{m}{9\omega_{\mathrm{s}}L_{\mathrm{s}}}\right)\left[\frac{9}{2}\delta+\frac{3\pi}{4}\right]}_{\mathbf{C}_{\mathrm{I}}}v_{\mathrm{o}}(t)+\underbrace{\left(\frac{1}{9\omega_{\mathrm{s}}L_{\mathrm{s}}}\right)\left[3\delta-\frac{\pi}{2}\right]}_{\mathbf{D}_{\mathrm{I}}}v_{\mathrm{i}}(t) \tag{D.2}$$

  - For Mode II:

    Inserting (C.49) into (3.9), it results in,

$$\frac{\mathrm{d}v_{\mathrm{o}}(t)}{\mathrm{d}t}=\underbrace{\left(\frac{1}{9\omega_{\mathrm{s}}L_{\mathrm{s}}C_{\mathrm{o}}}\right)\left[9\delta m^2+\frac{3\pi}{2}m^2-\frac{9\omega_{\mathrm{s}}L_{\mathrm{s}}}{R}\right]}_{\mathbf{A}_{\mathrm{II}}}v_{\mathrm{o}}(t)+\underbrace{\left(\frac{m}{9\omega_{\mathrm{s}}L_{\mathrm{s}}C_{\mathrm{o}}}\right)\left[\frac{9}{2}\delta-\frac{3\pi}{4}\right]}_{\mathbf{B}_{\mathrm{II}}}v_{\mathrm{i}}(t) \tag{D.3}$$

    Inserting (C.56) into (3.10), it leads to,

$$i_{\mathrm{i}}(t)=\underbrace{\left(\frac{m}{9\omega_{\mathrm{s}}L_{\mathrm{s}}}\right)\left[\frac{9}{2}\delta-\frac{3\pi}{4}\right]}_{\mathbf{C}_{\mathrm{II}}}v_{\mathrm{o}}(t)+\underbrace{\left(\frac{1}{9\omega_{\mathrm{s}}L_{\mathrm{s}}}\right)\left[3\delta+\frac{\pi}{2}\right]}_{\mathbf{D}_{\mathrm{II}}}v_{\mathrm{i}}(t) \tag{D.4}$$

- For range 2 ($\pi/6 \le \delta \le \pi/2$):
  - For Mode I:

    Inserting (C.50) into (3.9), it results in,

$$\frac{\mathrm{d}v_{\mathrm{o}}(t)}{\mathrm{d}t}=\underbrace{\left(\frac{1}{9\omega_{\mathrm{s}}L_{\mathrm{s}}C_{\mathrm{o}}}\right)\left[9\delta m^2-\frac{9\pi}{2}m^2-\frac{9\omega_{\mathrm{s}}L_{\mathrm{s}}}{R}\right]}_{\mathbf{A}_{\mathrm{I}}}v_{\mathrm{o}}(t)+\underbrace{\left(\frac{m}{9\omega_{\mathrm{s}}L_{\mathrm{s}}C_{\mathrm{o}}}\right)\left[3\pi\right]}_{\mathbf{B}_{\mathrm{I}}}v_{\mathrm{i}}(t) \tag{D.5}$$

    Inserting (C.57) into (3.10), it leads to,

$$i_{\mathrm{i}}(t)=\underbrace{\left(\frac{m}{9\omega_{\mathrm{s}}L_{\mathrm{s}}}\right)\left[3\pi\right]}_{\mathbf{C}_{\mathrm{I}}}v_{\mathrm{o}}(t)+\underbrace{\left(\frac{1}{9\omega_{\mathrm{s}}L_{\mathrm{s}}}\right)\left[3\delta-\frac{3\pi}{2}\right]}_{\mathbf{D}_{\mathrm{I}}}v_{\mathrm{i}}(t) \tag{D.6}$$

- For Mode II:
  Inserting (C.51) into (3.9), it results in,

$$\frac{\mathrm{d}v_{\mathrm{o}}(t)}{\mathrm{d}t}=\underbrace{\left(\frac{1}{9\omega_{\mathrm{s}}L_{\mathrm{s}}C_{\mathrm{o}}}\right)\left[9\delta m^2-\frac{3\pi}{2}m^2-\frac{9\omega_{\mathrm{s}}L_{\mathrm{s}}}{R}\right]}_{\mathbf{A}_{\mathrm{II}}}v_{\mathrm{o}}(t)+\underbrace{\left(\frac{m}{9\omega_{\mathrm{s}}L_{\mathrm{s}}C_{\mathrm{o}}}\right)\left[\frac{9}{2}\delta+\frac{3\pi}{4}\right]}_{\mathbf{B}_{\mathrm{II}}}v_{\mathrm{i}}(t) \tag{D.7}$$

  Inserting (C.58) into (3.10), it leads to,

$$i_{\mathrm{i}}(t)=\underbrace{\left(\frac{m}{9\omega_{\mathrm{s}}L_{\mathrm{s}}}\right)\left[\frac{9}{2}\delta+\frac{3\pi}{4}\right]}_{\mathbf{C}_{\mathrm{II}}}v_{\mathrm{o}}(t)+\underbrace{\left(\frac{1}{9\omega_{\mathrm{s}}L_{\mathrm{s}}}\right)\left[3\delta-\frac{\pi}{2}\right]}_{\mathbf{D}_{\mathrm{II}}}v_{\mathrm{i}}(t) \tag{D.8}$$

D.2 Averaged state-space matrices:

The averaged state-space matrices $\mathbf{A}$, $\mathbf{B}$, $\mathbf{C}$ and $\mathbf{D}$ in (3.15)–(3.18) are obtained by averaging their respective state-space matrices for modes I and II. For range 1, it is done by solving the following equations,

$$\begin{aligned}\mathbf{A}&=\frac{3}{\pi}\left(\mathbf{A}_{\mathrm{I}}\left[\delta+\frac{\pi}{6}\right]+\mathbf{A}_{\mathrm{II}}\left[\frac{\pi}{6}-\delta\right]\right),\ \mathbf{B}=\frac{3}{\pi}\left(\mathbf{B}_{\mathrm{I}}\left[\delta+\frac{\pi}{6}\right]+\mathbf{B}_{\mathrm{II}}\left[\frac{\pi}{6}-\delta\right]\right)\\ \mathbf{C}&=\frac{3}{\pi}\left(\mathbf{C}_{\mathrm{I}}\left[\delta+\frac{\pi}{6}\right]+\mathbf{C}_{\mathrm{II}}\left[\frac{\pi}{6}-\delta\right]\right),\ \mathbf{D}=\frac{3}{\pi}\left(\mathbf{D}_{\mathrm{I}}\left[\delta+\frac{\pi}{6}\right]+\mathbf{D}_{\mathrm{II}}\left[\frac{\pi}{6}-\delta\right]\right),\end{aligned} \tag{D.9}$$

and the resulting averaged state-space matrices are given in (3.15) and (3.16).

For range 2, it requires solving the following equations,

$$\begin{aligned}\mathbf{A}&=\frac{3}{\pi}\left(\mathbf{A}_{\mathrm{I}}\left[\delta-\frac{\pi}{6}\right]+\mathbf{A}_{\mathrm{II}}\left[\frac{\pi}{2}-\delta\right]\right),\ \mathbf{B}=\frac{3}{\pi}\left(\mathbf{B}_{\mathrm{I}}\left[\delta-\frac{\pi}{6}\right]+\mathbf{B}_{\mathrm{II}}\left[\frac{\pi}{2}-\delta\right]\right)\\ \mathbf{C}&=\frac{3}{\pi}\left(\mathbf{C}_{\mathrm{I}}\left[\delta-\frac{\pi}{6}\right]+\mathbf{C}_{\mathrm{II}}\left[\frac{\pi}{2}-\delta\right]\right),\ \mathbf{D}=\frac{3}{\pi}\left(\mathbf{D}_{\mathrm{I}}\left[\delta-\frac{\pi}{6}\right]+\mathbf{D}_{\mathrm{II}}\left[\frac{\pi}{2}-\delta\right]\right)\end{aligned} \tag{D.10}$$

and the resulting averaged state-space matrices are given in (3.17) and (3.18).

APPENDIX E – COMPLEMENT TO THE GSSA MODEL IN NORMAL OPERATION

In this appendix, the procedure to linearize the system of equations defined by (3.61)–(3.69) and (3.74)–(3.79) is summarized.

Linearizing the switching-functions:

Because of the sine and cosine terms in the definition of the output bridge averaged switching-functions, they must be first linearized. The procedure is shown here for $\left\langle \hat{s}_1^{'} \right\rangle_1^{\mathrm{R}}$ and $\left\langle \hat{s}_1^{'} \right\rangle_1^{\mathrm{I}}$.

- For the real part $\left\langle \hat{s}_1^{'} \right\rangle_1^{\mathrm{R}}$:

First, recall from (3.75) that,

$$\left\langle s_1^{'} \right\rangle_1^{\mathrm{R}} = \frac{1}{\pi}\sin\left(\left\langle \delta \right\rangle_0 + \frac{7\pi}{6}\right) \tag{E.1}$$

Applying the following perturbation $\left\langle \delta \right\rangle_0 = \delta + \left\langle \hat{\delta} \right\rangle_0$, it yields to,

$$\left\langle \hat{s}_1^{'} \right\rangle_1^{\mathrm{R}} = \frac{1}{\pi}\sin\left(\left(\delta + \frac{7\pi}{6}\right) + \left\langle \hat{\delta} \right\rangle_0\right) \tag{E.2}$$

Using the following trigonometric identity $\sin(\mathrm{A}+\mathrm{B}) = \sin(\mathrm{A})\cos(\mathrm{B}) + \cos(\mathrm{A})\sin(\mathrm{B})$, the above equation can be developed into,

$$\left\langle \hat{s}_1^{'} \right\rangle_1^{\mathrm{R}} = \frac{1}{\pi}\left[\sin\left(\delta + \frac{7\pi}{6}\right)\cos\left(\left\langle \hat{\delta} \right\rangle_0\right) + \cos\left(\delta + \frac{7\pi}{6}\right)\sin\left(\left\langle \hat{\delta} \right\rangle_0\right)\right] \tag{E.3}$$

Assuming that $\left\langle \hat{\delta} \right\rangle_0$ is small, it can be approximated that $\cos\left(\left\langle \hat{\delta} \right\rangle_0\right) \approx 1$ and $\sin\left(\left\langle \hat{\delta} \right\rangle_0\right) \approx \left\langle \hat{\delta} \right\rangle_0$, such that (E.3) becomes,

$$\left\langle \hat{s}_1^{'} \right\rangle_1^{\mathrm{R}} = \frac{1}{\pi}\left[\sin\left(\delta + \frac{7\pi}{6}\right) + \cos\left(\delta + \frac{7\pi}{6}\right)\left\langle \hat{\delta} \right\rangle_0\right] \tag{E.4}$$

- For the imaginary part $\left\langle \hat{s}_1^{'} \right\rangle_1^{\mathrm{I}}$:

Recall from (3.75) that,

$$\left\langle s_1^{'} \right\rangle_1^{\mathrm{I}} = \frac{1}{\pi}\cos\left(\left\langle \delta \right\rangle_0 + \frac{7\pi}{6}\right) \tag{E.5}$$

Applying the same perturbation $\left\langle \delta \right\rangle_0 = \delta + \left\langle \hat{\delta} \right\rangle_0$, it yields to,

$$\left\langle \hat{\mathrm{s}}_1^{'} \right\rangle_1^{\mathrm{I}} = \frac{1}{\pi} \cos\left(\left(\delta + \frac{7\pi}{6} \right) + \left\langle \hat{\delta} \right\rangle_0 \right) \tag{E.6}$$

Using the following trigonometric identity $\cos(\mathrm{A}+\mathrm{B}) = \cos(\mathrm{A})\cos(\mathrm{B}) - \sin(\mathrm{A})\sin(\mathrm{B})$, the above equation can be developed into,

$$\left\langle \hat{\mathrm{s}}_1^{'} \right\rangle_1^{\mathrm{I}} = \frac{1}{\pi} \left[\cos\left(\delta + \frac{7\pi}{6} \right) \cos\left(\left\langle \hat{\delta} \right\rangle_0 \right) - \sin\left(\delta + \frac{7\pi}{6} \right) \sin\left(\left\langle \hat{\delta} \right\rangle_0 \right) \right] \tag{E.7}$$

Again, assuming that $\left\langle \hat{\delta} \right\rangle_0$ is small, such that $\cos\left(\left\langle \hat{\delta} \right\rangle_0 \right) \approx 1$ and $\sin\left(\left\langle \hat{\delta} \right\rangle_0 \right) \approx \left\langle \hat{\delta} \right\rangle_0$, the final result is the following,

$$\left\langle \hat{\mathrm{s}}_1^{'} \right\rangle_1^{\mathrm{I}} = \frac{1}{\pi} \left[\cos\left(\delta + \frac{7\pi}{6} \right) - \sin\left(\delta + \frac{7\pi}{6} \right) \left\langle \hat{\delta} \right\rangle_0 \right] \tag{E.8}$$

By applying a similar procedure to $\left\langle \mathrm{s}_3^{'} \right\rangle_1^{\mathrm{R}}$, $\left\langle \mathrm{s}_3^{'} \right\rangle_1^{\mathrm{I}}$, $\left\langle \mathrm{s}_5^{'} \right\rangle_1^{\mathrm{R}}$ and $\left\langle \mathrm{s}_5^{'} \right\rangle_1^{\mathrm{I}}$, it can be demonstrated that,

$$\left\langle \hat{\mathrm{s}}_3^{'} \right\rangle_1^{\mathrm{R}} = \frac{1}{\pi} \left[\sin\left(\delta + \frac{11\pi}{6} \right) + \cos\left(\delta + \frac{11\pi}{6} \right) \left\langle \hat{\delta} \right\rangle_0 \right] \tag{E.9}$$

$$\left\langle \hat{\mathrm{s}}_3^{'} \right\rangle_1^{\mathrm{I}} = \frac{1}{\pi} \left[\cos\left(\delta + \frac{11\pi}{6} \right) - \sin\left(\delta + \frac{11\pi}{6} \right) \left\langle \hat{\delta} \right\rangle_0 \right] \tag{E.10}$$

$$\left\langle \hat{\mathrm{s}}_5^{'} \right\rangle_1^{\mathrm{R}} = \frac{1}{\pi} \left[\sin\left(\delta + \frac{\pi}{2} \right) + \cos\left(\delta + \frac{\pi}{2} \right) \left\langle \hat{\delta} \right\rangle_0 \right] \tag{E.11}$$

$$\left\langle \hat{\mathrm{s}}_5^{'} \right\rangle_1^{\mathrm{I}} = \frac{1}{\pi} \left[\cos\left(\delta + \frac{\pi}{2} \right) - \sin\left(\delta + \frac{\pi}{2} \right) \left\langle \hat{\delta} \right\rangle_0 \right] \tag{E.12}$$

Linearization of the system of equations:

An example of the procedure to linearize the terms in (3.61)–(3.69) is shown here. The other terms can be obtained by applying a similar procedure. Let's develop the following term in (3.65),

$$-\frac{m}{L_{\mathrm{A}}} \left\langle S_{13}^{'} \right\rangle_1^{\mathrm{R}} \tag{E.13}$$

Since it is located in the first column of the matrix $\mathbf{A}$, it multiplies the output voltage $\left\langle v_{\mathrm{o}}\right\rangle_0$ in the vector of state-variables $\left\langle \mathbf{x}(t)\right\rangle$, such that,

$$\left\langle i_{\mathrm{A}}\right\rangle_1^{\mathrm{R}} = -\frac{m}{L_{\mathrm{A}}}\left\langle S_{13}^{'}\right\rangle_1^{\mathrm{R}}\left\langle v_{\mathrm{o}}\right\rangle_0 \;+\; [...] \tag{E.14}$$

Knowing from (3.66) that $\left\langle S_{13}^{'}\right\rangle_1^{\mathrm{R}} = \left\langle \mathrm{s}_1^{'}\right\rangle_1^{\mathrm{R}} - \left\langle \mathrm{s}_3^{'}\right\rangle_1^{\mathrm{R}}$, and applying the following perturbations $\left\langle v_{\mathrm{o}}\right\rangle_0 = V_{\mathrm{o}} + \left\langle \hat{v}_{\mathrm{o}}\right\rangle_0$, $\left\langle i_{\mathrm{A}}\right\rangle_1^{\mathrm{R}} = \left\langle I_{\mathrm{A}}\right\rangle_1^{\mathrm{R}} + \left\langle \hat{i}_{\mathrm{A}}\right\rangle_1^{\mathrm{R}}$, it leads to,

$$\left\langle I_{\mathrm{A}}\right\rangle_1^{\mathrm{R}} + \left\langle \hat{i}_{\mathrm{A}}\right\rangle_1^{\mathrm{R}} = -\frac{m}{L_{\mathrm{A}}}\left(\left\langle \hat{\mathrm{s}}_1^{'}\right\rangle_1^{\mathrm{R}} - \left\langle \hat{\mathrm{s}}_3^{'}\right\rangle_1^{\mathrm{R}}\right)\cdot\left(V_{\mathrm{o}} + \left\langle \hat{v}_{\mathrm{o}}\right\rangle_0\right) + \; [...] \tag{E.15}$$

Knowing that $\left\langle \hat{\mathrm{s}}_1^{'}\right\rangle_1^{\mathrm{R}}$ and $\left\langle \hat{\mathrm{s}}_3^{'}\right\rangle_1^{\mathrm{R}}$ are given by (E.4) and (E.9) respectively, the above equation can be developed into,

$$\begin{aligned} = -\frac{m}{\pi L_{\mathrm{A}}}\left(\left[\sin\left(\delta+\frac{7\pi}{6}\right) - \sin\left(\delta+\frac{11\pi}{6}\right)\right] + \left[\cos\left(\delta+\frac{7\pi}{6}\right) - \cos\left(\delta+\frac{11\pi}{6}\right)\right]\left\langle\hat{\delta}\right\rangle_0\right) \\ \times\left(V_{\mathrm{o}} + \left\langle \hat{v}_{\mathrm{o}}\right\rangle_0\right) + \; [...] \end{aligned} \tag{E.16}$$

which can be further expanded to,

$$\left\langle I_{\mathrm{A}}\right\rangle_1^{\mathrm{R}} + \left\langle \hat{i}_{\mathrm{A}}\right\rangle_1^{\mathrm{R}} = -\frac{m}{\pi L_{\mathrm{A}}}\left(\begin{array}{l} \left[\sin\left(\delta+\frac{7\pi}{6}\right) - \sin\left(\delta+\frac{11\pi}{6}\right)\right]V_{\mathrm{o}} + \ldots \\ \quad \ldots + \left[\cos\left(\delta+\frac{7\pi}{6}\right) - \cos\left(\delta+\frac{11\pi}{6}\right)\right]V_{\mathrm{o}}\left\langle\hat{\delta}\right\rangle_0 + \ldots \\ \quad \ldots + \left[\sin\left(\delta+\frac{7\pi}{6}\right) - \sin\left(\delta+\frac{11\pi}{6}\right)\right]\left\langle \hat{v}_{\mathrm{o}}\right\rangle_0 + \ldots \\ \quad \ldots + \left[\cos\left(\delta+\frac{7\pi}{6}\right) - \cos\left(\delta+\frac{11\pi}{6}\right)\right]\left\langle\hat{\delta}\right\rangle_0\left\langle \hat{v}_{\mathrm{o}}\right\rangle_0 \end{array}\right) + [...] \tag{E.17}$$

Neglecting the constant terms related to the operating point and neglecting the second order term, (E.17) can be simplified to,

$$\left\langle \hat{i}_{\mathrm{A}} \right\rangle_1^{\mathrm{R}} = -\frac{m}{\pi L_{\mathrm{A}}} \begin{pmatrix} \left[\sin\left(\delta + \frac{7\pi}{6}\right) - \sin\left(\delta + \frac{11\pi}{6}\right) \right] \left\langle \hat{v}_{\mathrm{o}} \right\rangle_0 + \ldots \\ \ldots + \left[\cos\left(\delta + \frac{7\pi}{6}\right) - \cos\left(\delta + \frac{11\pi}{6}\right) \right] V_{\mathrm{o}} \left\langle \hat{\delta} \right\rangle_0 \end{pmatrix} + [\ldots] \tag{E.18}$$

Equation (E.18) can be further rearranged into,

$$\left\langle \hat{i}_{\mathrm{A}} \right\rangle_1^{\mathrm{R}} = -\frac{1}{L_{\mathrm{A}}} \left(S_1 \left\langle \hat{v}_{\mathrm{o}} \right\rangle_0 + S_2 V_{\mathrm{o}} \left\langle \hat{\delta} \right\rangle_0 \right) + [\ldots] \tag{E.19}$$

with,

$$S_1 = \frac{m}{\pi} \left[\sin\left(\delta + \frac{7\pi}{6}\right) - \sin\left(\delta + \frac{11\pi}{6}\right) \right] \tag{E.20}$$

$$S_2 = \frac{m}{\pi} \left[\cos\left(\delta + \frac{7\pi}{6}\right) - \cos\left(\delta + \frac{11\pi}{6}\right) \right] \tag{E.21}$$

The term $-\frac{1}{L_{\mathrm{A}}} S_1$ becomes A_{21} in the matrix $\hat{\mathbf{A}}$ given in (3.87) and the term $-\frac{V_{\mathrm{o}}}{L_{\mathrm{A}}} S_2$ becomes B_{12} in the matrix $\hat{\mathbf{B}}$ given in (3.88).

APPENDIX F – PIECEWISE-LINEAR MODEL IN OPEN-PHASE OPERATION

F.1 Mode definition and switching-functions:

Legend : X = 1, (empty) = 0

Mode	$0 \le \delta \le \frac{\pi}{6}$	s_1	s_3	s_1'	s_3'	s_5'
I	$0 \le \theta \le \delta + \frac{\pi}{6}$	X				X
II	$\delta + \frac{\pi}{6} \le \theta \le \delta + \frac{\pi}{2}$	X		X		X
III	$\delta + \frac{\pi}{2} \le \theta \le \frac{2\pi}{3}$	X		X		
IV	$\frac{2\pi}{3} \le \theta \le \delta + \frac{5\pi}{6}$	X	X	X		
V	$\delta + \frac{5\pi}{6} \le \theta \le \pi$	X	X	X	X	

Mode	$\frac{\pi}{6} \le \delta \le \frac{\pi}{2}$	s_1	s_3	s_1'	s_3'	s_5'
I	$0 \le \theta \le \delta - \frac{\pi}{6}$	X			X	X
II	$\delta - \frac{\pi}{6} \le \theta \le \delta + \frac{\pi}{6}$	X				X
III	$\delta + \frac{\pi}{6} \le \theta \le \frac{2\pi}{3}$	X		X		X
IV	$\frac{2\pi}{3} \le \theta \le \delta + \frac{\pi}{2}$	X	X	X		X
V	$\delta + \frac{\pi}{2} \le \theta \le \pi$	X	X	X		

F.2 Piecewise-linear current equations:

For range 1 ($0 \le \delta \le \pi/6$):

- Phase A:

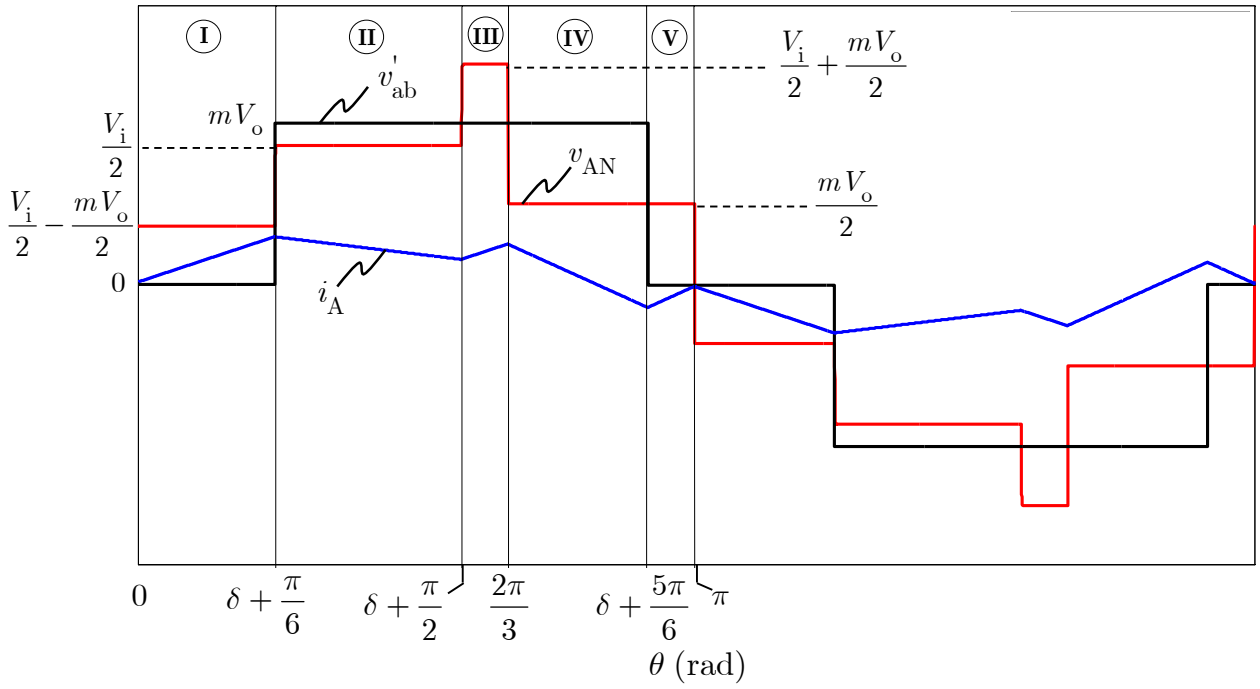

Mode	$i_A(\theta)$	
I	$i_A(\theta) = \frac{V_i - mV_o}{2\omega_s L_s}\theta + i_A(0)$	(F.1)
II	$i_A(\theta) = \frac{V_i - 2mV_o}{2\omega_s L_s}(\theta - \delta - \frac{\pi}{6}) + i_A(\delta + \frac{\pi}{6})$	(F.2)
III	$i_A(\theta) = \frac{V_i - mV_o}{2\omega_s L_s}(\theta - \delta - \frac{\pi}{2}) + i_A(\delta + \frac{\pi}{2})$	(F.3)
IV	$i_A(\theta) = \frac{-mV_o}{2\omega_s L_s}(\theta - \frac{2\pi}{3}) + i_A(\frac{2\pi}{3})$	(F.4)
V	$i_A(\theta) = \frac{mV_o}{2\omega_s L_s}(\theta - \delta - \frac{5\pi}{6}) + i_A(\delta + \frac{5\pi}{6})$	(F.5)

Initial current:

$$i_A(0) = \frac{\left[\left(3\pi + 6\delta\right)mV_o - 2\pi V_i\right]}{12\omega_s L_s} \qquad \text{(F.6)}$$

- Phase B:

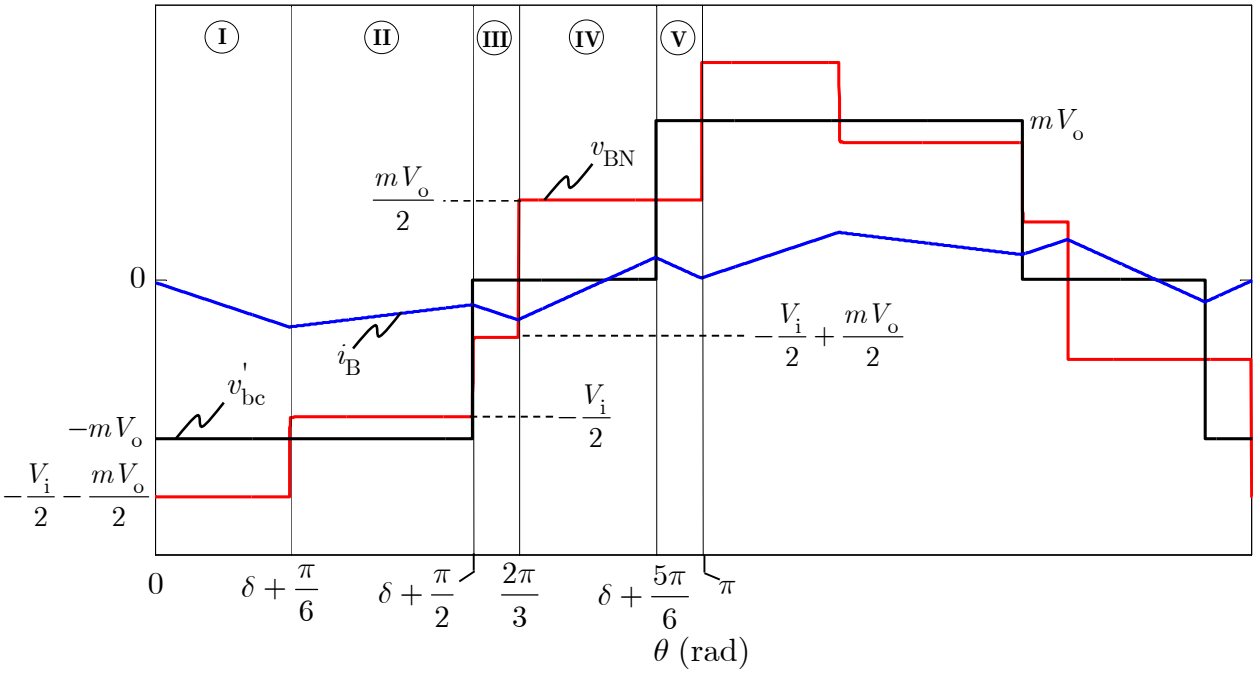

Mode	$i_B(\theta)$	
I	$i_B(\theta)=\frac{-V_i+mV_o}{2\omega_s L_s}\theta+i_B(0)$	(F.7)
II	$i_B(\theta)=\frac{-V_i+2mV_o}{2\omega_s L_s}(\theta-\delta-\frac{\pi}{6})+i_B(\delta+\frac{\pi}{6})$	(F.8)
III	$i_B(\theta)=\frac{-V_i+mV_o}{2\omega_s L_s}(\theta-\delta-\frac{\pi}{2})+i_B(\delta+\frac{\pi}{2})$	(F.9)
IV	$i_B(\theta)=\frac{mV_o}{2\omega_s L_s}(\theta-\frac{2\pi}{3})+i_B(\frac{2\pi}{3})$	(F.10)
V	$i_B(\theta)=\frac{-mV_o}{2\omega_s L_s}(\theta-\delta-\frac{5\pi}{6})+i_B(\delta+\frac{5\pi}{6})$	(F.11)

Initial current:

$$i_B(0)=-i_A(0) \tag{F.12}$$

For range 2 ($\pi/6 \leq \delta \leq \pi/2$):

- Phase A:

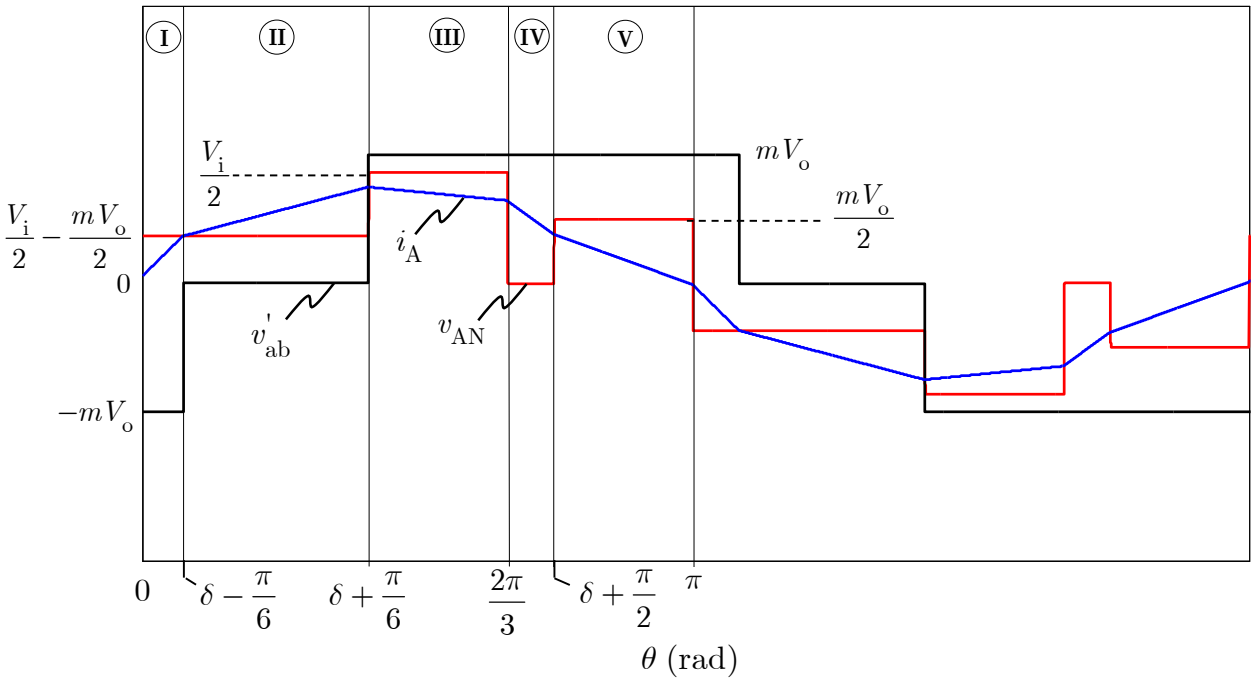

Mode	$i_A(\theta)$	
I	$i_A(\theta) = \frac{V_i + mV_o}{2\omega_s L_s}\theta + i_A(0)$	(F.13)
II	$i_A(\theta) = \frac{V_i - mV_o}{2\omega_s L_s}(\theta - \delta + \frac{\pi}{6}) + i_A(\delta - \frac{\pi}{6})$	(F.14)
III	$i_A(\theta) = \frac{V_i - 2mV_o}{2\omega_s L_s}(\theta - \delta - \frac{\pi}{6}) + i_A(\delta + \frac{\pi}{6})$	(F.15)
IV	$i_A(\theta) = \frac{-2mV_o}{2\omega_s L_s}(\theta - \frac{2\pi}{3}) + i_A(\frac{2\pi}{3})$	(F.16)
V	$i_A(\theta) = \frac{-mV_o}{2\omega_s L_s}(\theta - \delta - \frac{\pi}{2}) + i_A(\delta + \frac{\pi}{2})$	(F.17)

Initial current:

$$i_A(0) = \frac{\left[\left(5\pi - 6\delta\right)mV_o - 2\pi V_i\right]}{12\omega_s L_s} \tag{F.18}$$

- Phase B:

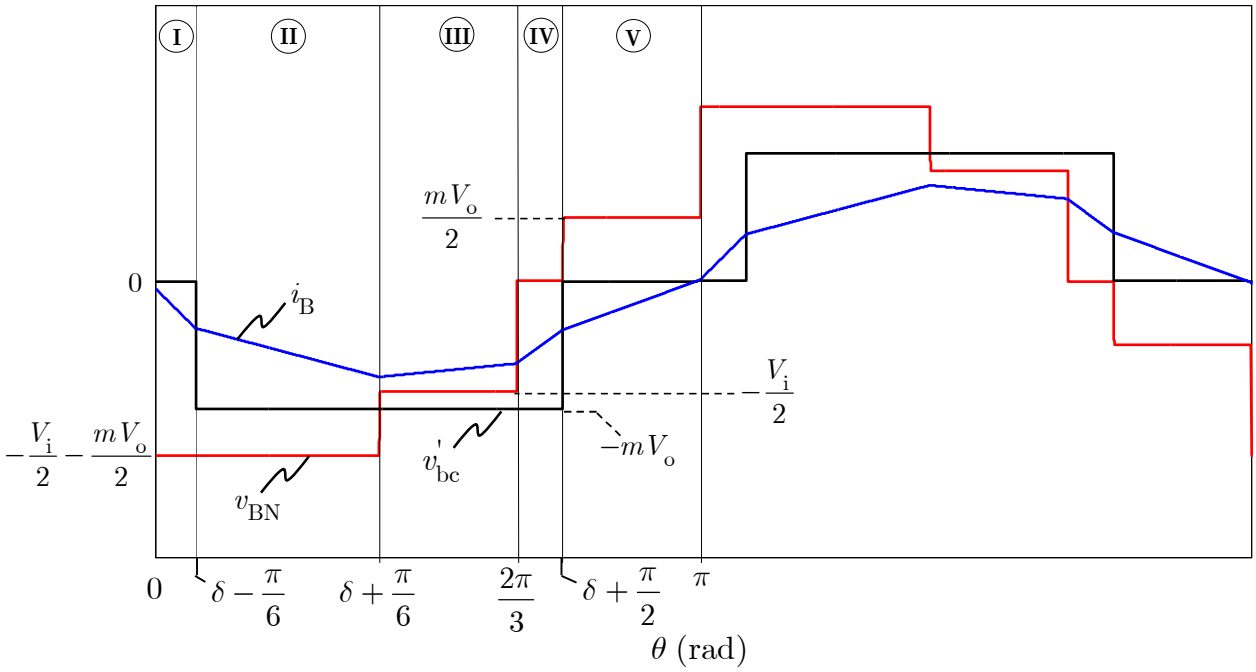

Mode	$i_B(\theta)$	
I	$i_B(\theta)=\frac{-V_i-mV_o}{2\omega_s L_s}\theta+i_B(0)$	(F.19)
II	$i_B(\theta)=\frac{-V_i+mV_o}{2\omega_s L_s}(\theta-\delta+\frac{\pi}{6})+i_B(\delta-\frac{\pi}{6})$	(F.20)
III	$i_B(\theta)=\frac{-V_i+2mV_o}{2\omega_s L_s}(\theta-\delta-\frac{\pi}{6})+i_B(\delta+\frac{\pi}{6})$	(F.21)
IV	$i_B(\theta)=\frac{2mV_o}{2\omega_s L_s}(\theta-\frac{2\pi}{3})+i_B(\frac{2\pi}{3})$	(F.22)
V	$i_B(\theta)=\frac{mV_o}{2\omega_s L_s}(\theta-\delta-\frac{\pi}{2})+i_B(\delta+\frac{\pi}{2})$	(F.23)

Initial current:

$$i_B(0)=-i_A(0) \tag{F.24}$$

F.3 Output current equations:

For range 1 ($0 \le \delta \le \pi/6$):

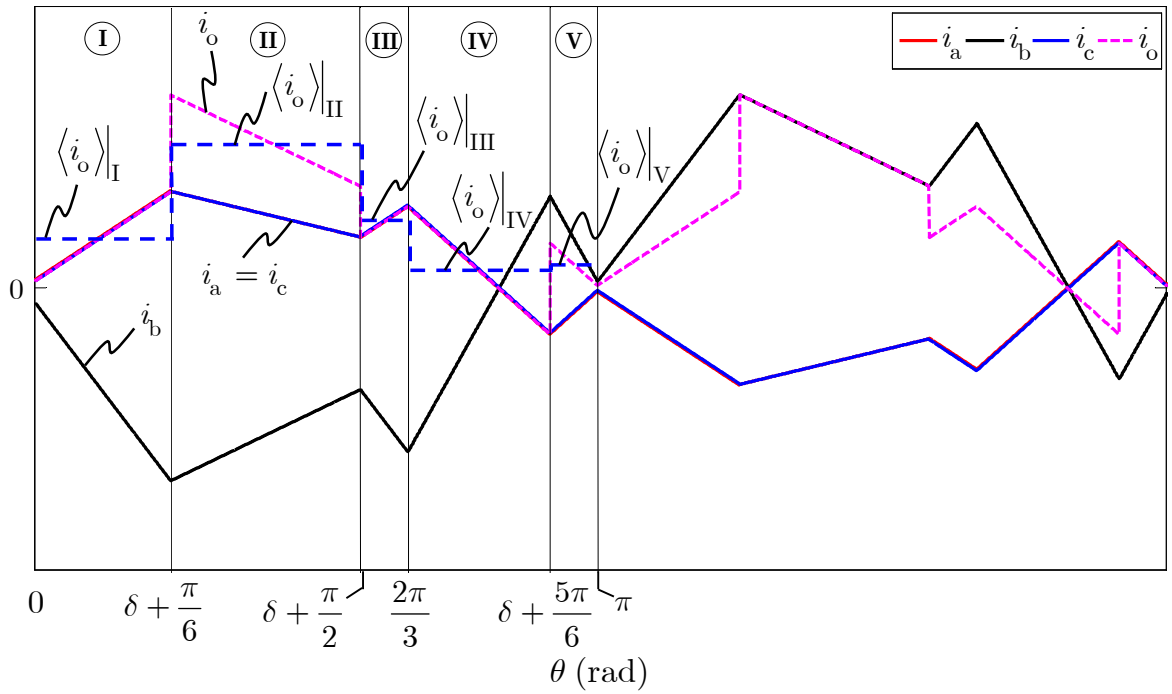

Mode	$\langle i_o(\theta) \rangle$	
I	$\langle i_o(\theta) \rangle\|_I = \left(\frac{m}{12\omega_s L_s}\right) \cdot \left[\left(\frac{5\pi}{2} + 3\delta\right) m V_o - \left(\frac{3\pi}{2} - 3\delta\right) V_i\right]$	(F.25)
II	$\langle i_o(\theta) \rangle\|_{II} = \left(\frac{m}{12\omega_s L_s}\right) \left[12\delta V_i\right]$	(F.26)
III	$\langle i_o(\theta) \rangle\|_{III} = \left(\frac{m}{12\omega_s L_s}\right) \cdot \left[\left(3\delta - \frac{5\pi}{2}\right) m V_o + \left(3\delta + \frac{3\pi}{2}\right) V_i\right]$	(F.27)
IV	$\langle i_o(\theta) \rangle\|_{IV} = \left(\frac{m}{12\omega_s L_s}\right) \cdot \left[\left(3\delta - \frac{7\pi}{2}\right) m V_o + 2\pi V_i\right]$	(F.28)
V	$\langle i_o(\theta) \rangle\|_V = \left(\frac{m}{12\omega_s L_s}\right) \cdot \left[\left(3\delta + \frac{7\pi}{2}\right) m V_o - 2\pi V_i\right]$	(F.29)

For range 2 ($\pi/6 \leq \delta \leq \pi/2$):

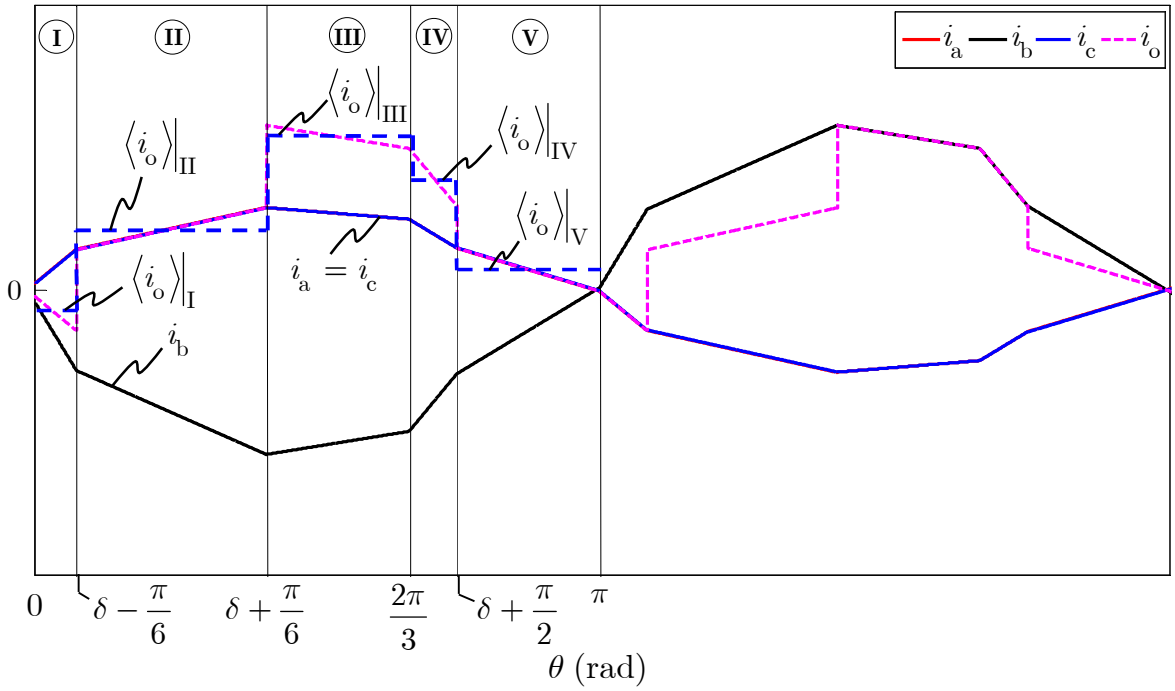

Mode	$\langle i_o(\theta) \rangle$	
I	$\langle i_o(\theta) \rangle\|_I = \left(\frac{m}{12\omega_s L_s}\right) \cdot \left[\left(3\delta - \frac{9\pi}{2}\right) m V_o + \left(\frac{5\pi}{2} - 3\delta\right) V_i\right]$	(F.30)
II	$\langle i_o(\theta) \rangle\|_{II} = \left(\frac{m}{12\omega_s L_s}\right) \cdot \left[3\pi m V_o + \left(6\delta - 2\pi\right) V_i\right]$	(F.31)
III	$\langle i_o(\theta) \rangle\|_{III} = \left(\frac{m}{12\omega_s L_s}\right) \cdot \left[\left(12\delta - 2\pi\right) m V_o + \left(6\delta + \pi\right) V_i\right]$	(F.32)
IV	$\langle i_o(\theta) \rangle\|_{IV} = \left(\frac{m}{12\omega_s L_s}\right) \cdot \left[\left(12\delta - 6\pi\right) m V_o + 4\pi V_i\right]$	(F.33)
V	$\langle i_o(\theta) \rangle\|_{V} = \left(\frac{m}{12\omega_s L_s}\right) \cdot \left[\left(\frac{7\pi}{2} - 3\delta\right) m V_o - 2\pi V_i\right]$	(F.34)

F.4 Input current equations:

For range 1 ($0 \leq \delta \leq \pi/6$):

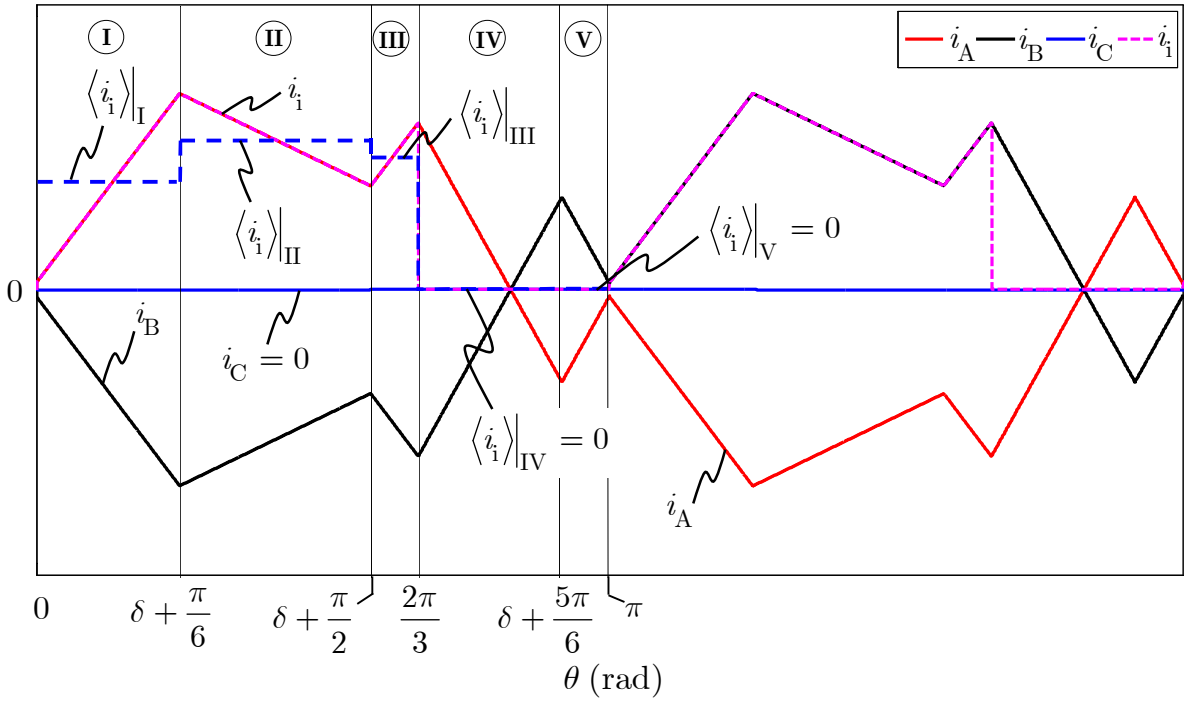

Mode	$\langle i_i(\theta) \rangle$	
I	$\langle i_i(\theta) \rangle\|_I = \left(\frac{1}{12\omega_s L_s}\right) \cdot \left[\left(\frac{5\pi}{2} + 3\delta\right) m V_o - \left(\frac{3\pi}{2} - 3\delta\right) V_i\right]$	(F.35)
II	$\langle i_i(\theta) \rangle\|_{II} = \left(\frac{1}{12\omega_s L_s}\right) [6\delta V_i]$	(F.36)
III	$\langle i_i(\theta) \rangle\|_{III} = \left(\frac{1}{12\omega_s L_s}\right) \cdot \left[\left(3\delta - \frac{5\pi}{2}\right) m V_o + \left(3\delta + \frac{3\pi}{2}\right) V_i\right]$	(F.37)
IV	$\langle i_i(\theta) \rangle\|_{IV} = 0$	(F.38)
V	$\langle i_i(\theta) \rangle\|_V = 0$	(F.39)

For range 2 ($\pi/6 \le \delta \le \pi/2$):

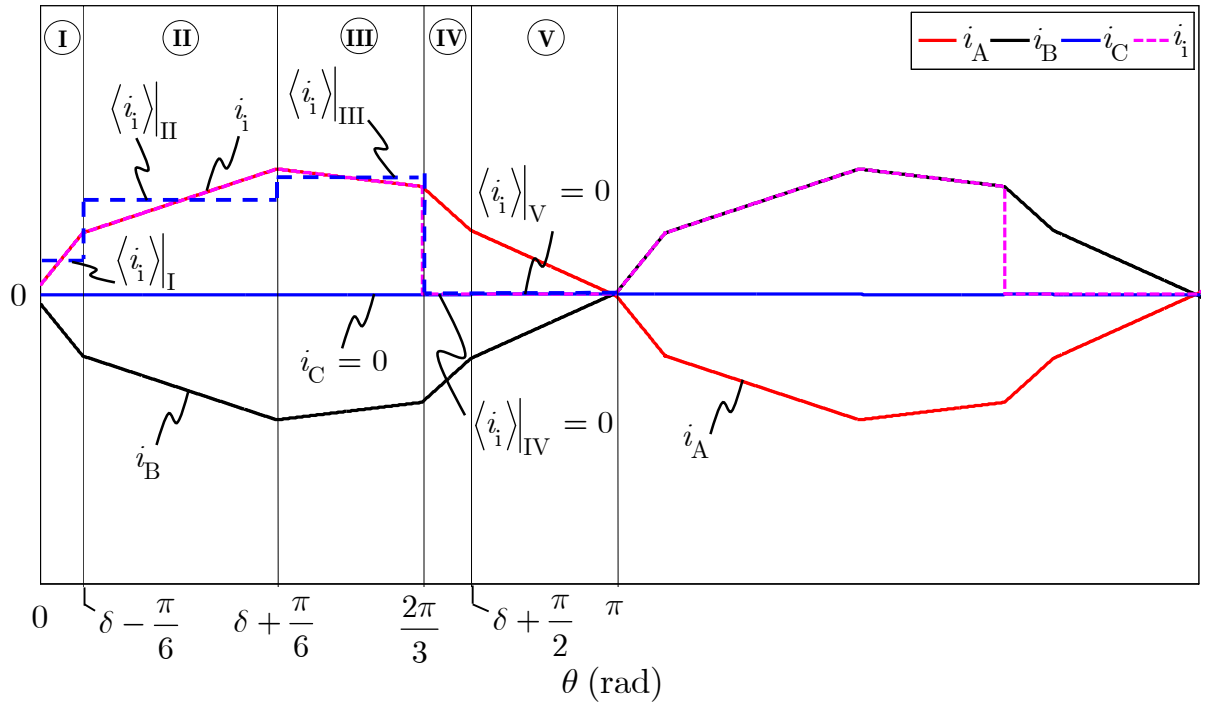

Mode	$\langle i_i(\theta) \rangle$	
I	$\langle i_i(\theta) \rangle\|_I = \left(\frac{1}{12\omega_s L_s}\right) \cdot \left[\left(\frac{9\pi}{2} - 3\delta\right) m V_o + \left(3\delta - \frac{5\pi}{2}\right) V_i\right]$	(F.40)
II	$\langle i_i(\theta) \rangle\|_{II} = \left(\frac{1}{12\omega_s L_s}\right) \cdot \left[3\pi m V_o + (6\delta - 2\pi) V_i\right]$	(F.41)
III	$\langle i_i(\theta) \rangle\|_{III} = \left(\frac{1}{12\omega_s L_s}\right) \cdot \left[(6\delta - \pi) m V_o + \left(3\delta + \frac{\pi}{2}\right) V_i\right]$	(F.42)
IV	$\langle i_i(\theta) \rangle\|_{IV} = 0$	(F.43)
V	$\langle i_i(\theta) \rangle\|_{V} = 0$	(F.44)